Defect Modulation Doping for Transparent Conducting Oxide Materials

By

Getnet Kacha Deyu

Born in Addis Ababa, Ethiopia

European Joint Double Doctoral Thesis (EJD-FunMat)

The Department of Material and Geosciences of the Technical University of Darmstadt, Germany in Fulfillment of the Requirements for the Degree of Doctor in Engineering (Dr.-Ing.)

The Doctoral School of Industrial, Materials, Mechanical and Process Engineering (I-MEP2) Univ. Grenoble Alpes, France in Fulfillment of the Requirements for the Degree of Doctor with specialty Materials, Mechanics, Civil Engineering, Electrochemistry (2MGE).

February 12, 2020

THÈSE

Pour obtenir le grade de

DOCTEUR DE LA COMMUNAUTE UNIVERSITE GRENOBLE ALPES

préparée dans le cadre d'une cotutelle *entre la Communauté Université Grenoble Alpes* Technische Universität Darmstadt

Spécialité : **Matériaux, Mécanique, Génie civil, Electrochimie**

Arrêté ministériel : le 6 janvier 2005 – 25 mai 2016

Présentée par

Getnet Kacha DEYU

Thèse dirigée par **Andreas KLEIN** et **Daniel BELLET** codirigée par **David MUNOZ-ROJAS**

préparée au sein des **Electronic Structure of Materials (ESM), Darmstadt Allemagne** et **Laboratoire des Matériaux et du Génie Physique (LMGP), Grenoble France**

dans **l'IMEP-2**

Defect Modulation Doping for Transparent Conducting Oxide Materials

Thèse soutenue publiquement le **06 December 2019**,
devant le jury composé de :

Tomas HEISER
Professeur Uni. of Strasbourg France, Président du jury
Ngoc Duy NGUYEN
Professeur Uni. of Liége Belgique, Extérieur, Rapporteur pour UGA
Michel AILLERIE
Professeur Uni. Mitz, Extérieur, Rapporteur pour UGA
Lambert ALFF
Professeur Uni. Tech. Darmstadt Allemagne Extérieur Examinateur
Oliver CLEMENS
Ass. Professeur Uni. Tech. Darmstadt Allemagne, Extérieur Examinateur
Dr. Daniel BELLET
Professeur Uni. Grenoble Alpes, Co-Directeur de thèse et représentant d'UGA
Dr. Andreas KlEIN
Professeur Uni. Tech. Darmstadt Allemagne, Co-Directeur de thèse

Defect Modulation Doping for Transparent Conducting Oxide Materials

Approved dissertation by Getnet Kacha Deyu (M.Sc.) from Addis Ababa, Ethiopia

Double doctoral thesis joined by

Technische Universität Darmstadt and University of Grenoble Alpes; under the framework of European Joint Doctoral programme in the field of functional materials (EJD-FunMAT)

Supervisors: Prof. Dr. Andreas Klein (Technische Universität Darmstadt)

Prof. Dr. Daniel Bellet (University of Grenoble Alpes)

Co-supervisor: Dr. David Muñoz-Rojas (University of Grenoble Alpes)

Date of Submission: October 02, 2019

Date of defense: December 06, 2019

Please cite this document as:

URN: urn:nbn:de:tuda-tuprints-97008

URI: https://tuprints.ulb.tu-darmstadt.de/id/eprint/9700

Declaration of Authorship

I hereby confirm that I have written the present thesis independently and without illicit aid from third parties, using solely the aids mentioned. All passages from other sources are marked as such. This work has not been presented to an examination office before in this or a similar form.

Déclaration sur la Dissertation

Je déclare par la présente que la thèse a été rédigée sans l'aide d'un tiers et que toutes les aides et supports ont été mentionnés. Toutes les sources ont été indiquées. Ce travail n'a pas été présenté antérieurement devant un comité d'examen, que ce soit en totalité ou en partie,

Erklärung zur Dissertation

Hiermit versichere ich, die vorliegende Dissertation ohne Hilfe Dritter nur mit den angegebenen Quellen und Hilfsmitteln angefertigt zu haben. Alle Stellen, die aus Quellen entnommen wurden, sind als solche kenntlich gemacht. Diese Arbeit hat in gleicher oder ähnlicher Form noch keiner Prüfungsbehörde vorgelegen.

Darmstadt, 30th September 2019

Getnet Kacha Deyu

Dedication

ለ እናቴ ወ/ሮ የሺ መኩሪያ መንግስቱ

Yeshi Mekuria Mengistu

Contents

Contents

Abstract

English:

The doping of semiconductor materials is a fundamental part of modern technology. Transparent conducting oxides (TCOs) are a group of semiconductors, which holds the features of being transparent and electrically conductive. The high electrical conductivity is usually obtained by typical doping with heterovalent substitutional impurities like in Sn-doped In_2O_3 (ITO), fluorine-doped SnO_2 (FTO) and Al-doped ZnO (AZO). However, these classical approaches have in many cases reached their limits both in regard to achievable charge carrier density, as well as mobility. Modulation doping, a mechanism that exploits the energy band alignment at an interface between two materials to induce free charge carriers in one of them, has been shown to avoid the mobility limitation. However, the carrier density limit cannot be lifted by this approach, as the alignment of doping are limited by intrinsic defects. The goal of this work was to implement the novel doping strategy for TCO materials. The strategy relies on using of defective wide band gap materials to dope the surface of the TCO layers, which results Fermi level pinning at the dopant phase and Fermi level positions outside the doping limit in the TCOs. The approach is tested by using undoped In_2O_3, Sn-doped In_2O_3 and SnO_2 as TCO host phase and Al_2O_3 and SiO_{2-x} as wide band gap dopant phase.

The study was divided into two parts by the approaches followed experimentally. The first part deals with physical approach, in which sputtered TCOs are used as a host materials and covered with dopant layers. To test the versatility of the approach the second part deals with a chemical approach, in which SnO_2 based nanocomposite films produced in spray pyrolysis deposition.

In the physical approach, ITO/ALD-Al_2O_3, In_2O_3/ALD-Al_2O_3 and In_2O_3/sputtered SiO_{2-x} thin film systems were exploited. The study was conducted mostly by photoelectron spectroscopy and Hall effect measurements. ITO films prepared in different conditions showed an increase of conductivity after ALD-Al_2O_3 deposition at 200 °C. This was mostly due to an increase of carrier concentrations. However, Al_2O_3 deposition also resulted a chemical reduction of ITO. The diffusivity of compensating oxygen

interstitial (O_i) defects at 200 °C is sufficiently screen the high Fermi level induced by Al_2O_3, which disable the use of defect modulation doping at this temperature. The results indicate that achieving higher carrier concentration in ITO thin films requires a control of the oxygen pressure in combination with low temperature ALD process. Undoped In_2O_3 films also showed an increase of conductivity upon deposition of upto 10-cycles of ALD-Al_2O_3. These increases indicate the occurrence of defect modulation doping. However, in order to improve the interface properties and firmly prove the modulation doping effect, more detailed studies required on the doped interfaces. The approach was further examined by depositing reactively sputtered SiO_{2-x} dopant phase from Si target on the top of In_2O_3 films. The resulting conductivity of In_2O_3/sputtered SiO_{2-x} do not show enhancement of electrical properties. This is due to the implantation of oxygen species during SiO_2 deposition on the surface of In_2O_3, which counteract the defect modulation doping by reducing concentration of oxygen vacancies (V_O) in In_2O_3. Therefore, further studies on the deposition conditions of the dopant phase is still vital to see enhanced electrical properties.

In the chemical approach two different routes were followed: embedding nanoparticles in TCO host matrix and formation of demixed composite films. In the first route, Al_2O_3 and TiO_2 nanoparticles (NPs) were chosen as dopant phases and were deposited together with SnO_2 TCO precursors. Different characterization of the produced films do not confirm the presence nanoparticles into tin oxide films. Therefore to realise modulation effect further optimization deposition conditions and sample preparation techniques are needed. For the second route, mixture of $SnCl_4 \cdot 5(H_2O)$ and $Al(acac)_3$ precursor solutions in different composition are used to produce SnO_2/Al_2O_3 demixed composite films. Different physicochemical studies shows that under the deposition conditions followed during this study Al^{3+} preferably substitute Sn^{4+} than forming another Al_2O_3 separated phase. Al was acting as an acceptor doping on SnO_2 films. Therefore, enhanced conductivity was not observed on the probed samples. For this route further optimization of deposition condition is clearly required.

The results of this dissertation are relevant for the usage of TCOs in the emerging field of oxide thin film electronics in particular in field where the surface to bulk ratio is much higher than in conventional films, as the approach is near surface phenomena. However, further utilization of both the processing conditions and material selection are vital.

Français:

Le dopage des matériaux semi-conducteurs est une partie fondamentale de la technologie moderne. Les oxydes conducteurs transparents (TCO) constituent une famille de semi-conducteurs, qui sont optiquement transparents et électriquement conducteurs. La conductivité électrique élevée est généralement obtenue grâce à un dopage associant des impuretés de substitution hétérovalentes comme dans In_2O_3 dopé au Sn (ITO), SnO_2 dopé au fluor (FTO) et ZnO dopé à l'Al (AZO). Cependant, ces approches classiques ont dans de nombreux cas atteint leurs limites tant en ce qui concerne la densité de porteurs de charge atteignable, que pour la valeur de la mobilité des porteurs de charge. Le dopage par modulation est un mécanisme qui exploite l'alignement de la bande d'énergie à une interface entre deux matériaux pour induire une densité de porteurs de charges libres dans l'un d'entre eux ; un tel mécanisme a permis de montrer dans certains cas que la limitation liée à la mobilité pouvait ainsi était évitée. Cependant, la limite de densité de porteuse ne peut pas être levée par cette approche, du fait de l'alignement des limites de dopage par défauts intrinsèques. Le but de ce travail était de mettre en œuvre cette nouvelle stratégie de dopage pour les TCO. La stratégie repose sur l'utilisation de large bande interdite pour doper la surface des couches de TCO, ce qui résulte à un piégeage du niveau de Fermi pour la phase dopante et à un positionnement du niveau de Fermi en dehors de la limite de dopage dans les TCO. La méthode est testée en utilisant un TCO comme In_2O_3 non dopé, In_2O_3 dopé au Sn et SnO_2 phase hôte et Al_2O_3 et SiO_{2-x} en tant que phase de dopant gap à large bande.

L'étude était divisée en deux parties au travers des deux approches expérimentales différentes. La première partie traite de l'approche physique, dans laquelle les TCO dont la croissance a été effectuée par pulvérisation sont utilisés en tant que matériau hôte et recouvert de couches dopantes. Pour tester la polyvalence de l'approche, la deuxième partie traite d'une approche chimique dans laquelle des films nano-composites à base de SnO_2 sont produits par dépôt spray pyrolyse. Par conséquent, de nouvelles études sur les conditions de dépôt de la phase dopante restent vitales pour voir l'éventuelle amélioration des propriétés électriques.

Dans l'approche physique, les couches minces étudiées furent: ITO/ALD-Al_2O_3, In_2O_3/ ALD-Al_2O_3 and In_2O_3/sputtered SiO_{2-x}. L'étude a été menée principalement par spectroscopie de photoélectrons (XPS) et mesures d'effet Hall. Les films ITO préparés dans différentes conditions ont montré une augmentation de la conductivité après le dépôt d'ALD-Al_2O_3 à 200 °C. Cela était principalement dû à une augmentation des concentrations de porteurs. Cependant, le dépôt d'Al_2O_3 a également entraîné une réduction chimique de l'ITO. La diffusivité de défauts comme l'oxygène interstitiels (O_i) compensateur à 200 °C écrante suffisamment le niveau élevé de Fermi induit par Al_2O_3, empêchant ainsi le dopage par modulation de défauts à cette température. Les résultats du indiquent que pour atteindre une concentration plus élevée en porteurs dans les films minces ITO, il faut un contrôle de la pression d'oxygène en combinaison avec le procédé ALD à basse température. Les films d'In_2O_3 non dopés ont également montré une augmentation de la conductivité lors du dépôt de 10 cycles d'ALD-Al_2O_3. Ces augmentations indiquent que le dopage par modulation de défaut a bien eu lieu. Cependant, afin d'améliorer les propriétés de l'interface et de prouver définitivement l'effet de dopage par modulation, des études plus détaillées sont nécessaires sur les interfaces dopées. L'approche a ensuite été examinée en déposant une phase dopante SiO_{2-x} pulvérisée de manière réactive sur une cible Si sur films d'In_2O_3. La conductivité résultante In_2O_3/pulvérisée SiO_{2-x} ne montre pas d'amélioration des propriétés électriques. Ceci est dû à l'implantation des espèces d'oxygène lors du dépôt de SiO_2 à la surface de In_2O_3, qui contrecarre le dopage par modulation des défauts en réduisant la concentration des lacunes en oxygène (V_O) dans In_2O_3.

Dans l'approche chimique, deux voies différentes ont été suivies: l'inclusion de nanoparticules dans la matrice hôte TCO et la formation de films composites démixés. Dans la première approche, les nanoparticules d' Al_2O_3 et de TiO_2 (NP) ont été choisies comme phases dopantes et ont été déposées avec les précurseurs utilisés lors du dépôt du TCO SnO_2. Différentes caractérisations des films produits ne confirment pas la présence de nanoparticules dans des films d'oxyde d'étain. Donc si l'on veut obtenir un effet de modulation une optimisation supplémentaire des conditions de dépôt et de préparation des échantillons techniques s'avèrent nécessaires. Pour la seconde voie, le mélange des solutions des précurseurs de composition différente de $SnCl_4 \cdot 5(H_2O)$ et $Al(acac)_3$ ont été utilisées pour produire du SnO_2/Al_2O_3 démixé au sein de films composites. Différentes études physico-chimiques montrent que dans les conditions de dépôt suivies pendant cette étude,Al^{3+} substitue de préférence Sn^{4+} formant ainsi une autre phase de Al_2O_3. Al agissait en tant que dopeur accepteur sur des films de SnO_2. Par conséquent, une conductivité accrue n'a pas été observée sur les échantillons étudiés. Afin de poursuivre dans cette démarche, une future optimisation supplémentaire des conditions de dépôt est clairement requise.

Les résultats de cette thèse sont pertinents pour l'utilisation des TCO dans le domaine émergeant de l'électronique des couches minces d'oxyde, en particulier dans les domaines où le rapport surface / volume est beaucoup plus élevé que dans les films conventionnels, car l'approche visée est un phénomène actif au voisinage immédiat de la surface. Cependant, Il sera essentiel de continuer à optimiser les conditions de dépôt ainsi que le choix des matériaux à utiliser.

Deutsch:

Die Dotierung von Halbleitermaterialien ist ein fundamentaler Bestandteil der modernen Technologie. Transparente leitfähige Oxide (TCOs) sind eine Gruppe von Halbleitern, mit den Eigenschaften, transparent und elektrisch leitfähig zu sein. Die hohe elektrische Leitfähigkeit wird in der Regel durch Dotieren mit heterovalenten, substitutionellen Fremdatomenerreicht. Beispiele hierfür sind Sn dotiertes In_2O_3 (ITO), F dotiertes SnO_2 (FTO) und Al dotiertes ZnO (AZO). Allerdings stößt dieser klassiche Ansatz in vielen Fällen an seine Grenzen, und zwar sowohl in Bezug auf erreichbare Ladungsträgerdichte, als auch Mobilität. Es hat sich gezeigt, die Mobilitätsbeschränkung durch Modulationsdotierung überwunden werden kann. Hierbei handelt es sich um einen Mechanismus der die Energiebandanpassung an einer Grenzfläche zwischen zwei Materialien ausnutzt, um Ladungsträger in einem von ihnen freizusetzen. Die Begrenzung in der Ladungsträgerdichte kann durch diesen Ansatz jedoch nicht aufgehoben werden, da die Bandanpassung durch intrinsische Defekte begrenzt ist. Ziel dieser Arbeit war die Umsetzung dieser neuartigen Dotierstrategie für TCO-Materialien. Die Strategie beruht auf der Verwendung von defekthaltigen Halbleitern mit großer Bandlücke (Wide-Bandgap-Halbleiter) als Dotierphase um die Oberfläche der TCO Schichten zu dotieren. Aufgrund des hohen, nach unten begrenzten Ferminiveaus (Fermi level pinning) in der Dotierphase kann das Fermi-Niveau der TCOs an der Grenzfläche oberhalb der Dotiergrenze liegen. Der Ansatz der Modulationsdotierung von TCOs wird untersucht, indem undotiertes In_2O_3, Sn-dotiertes In_2O_3 und SnO_2 als TCO-Wirtsphase und Al_2O_3 und SiO_{2-x} als Dotierphase verwendet werden.

Die Arbeit wurde anhand der experimentell verfolgten Ansätze in zwei Teile aufgeteilt. Der erste Teil befasst sich mit einem physikalischen Ansatz. Hierbei werden gesputterte TCOs als Wirtsmaterial verwendet und dünne Schichten der Dotierphase aufgebracht. Um die Vielseitigkeit des Ansatzes zu untersuchen, befasst sich der zweite Teil mit einem chemischen Ansatz, bei dem auf SnO2 basierende Nanokompositfilme durch Sprühpyrolyseabscheidung hergestellt werden.

Bei dem physikalischen Ansatz wurden ITO/ALD-Al_2O_3, In_2O_3/ALD-Al_2O_3 und In_2O_3 / gesputterte SiO_{2-x}-Dünnschichtsysteme genutzt. Die Studie wurde hauptsächlich mittels Photoelektronenspektroskopie und Hall-Effekt-Messungen durchgeführt. Unter verschiedenen Bedingungen hergestellte ITO-Schichten zeigten eine Erhöhung der Leitfähigkeit nach der ALD-Al_2O_3-Abscheidung bei 200 °C. Dies war hauptsächlich auf eine Erhöhung der Ladungsträgerkonzentrationen zurückzuführen. Die Al_2O_3-Abscheidung führte jedoch auch zu einer chemischen Reduktion des ITO. Das Diffusionsvermögen der kompensierenden, Sauerstoff-Interstitial (O_i)-interstitiellen Sauerstoff Defekte ist bei 200 °C hoch genug um das, durch das Al_2O_3 induzierte hohe Fermi-Niveau ausreichend abzuschirmen. Somit ist die Defektmodulationsdotierung von ITO bei dieser Temperatur nicht möglich. Die Ergebnisse zeigen, dass für die Erzielung einer höheren Ladungsträgerkonzentration in ITO-Dünnschichten eine Kontrolle des Sauerstoffpartialdrucks in Kombination mit dem Niedertemperatur-ALD-Prozess erforderlich ist. Undotierte In_2O_3 Filme zeigten auch ebenfalls eine Erhöhung der Leitfähigkeit bei der Abscheidung von bis zu 10 Zyklen ALD-Al_2O_3. Diese Erhöhungen deuten auf das Auftreten einer Defektmodulationsdotierung hin. Um die Grenzflächeneigenschaften weiter zu verbessern und den Modulationsdotierungseffekt sicher nachzuweisen, sind jedoch weitere Untersuchungen an den dotierten Grenzflächen erforderlich. Der physikalische Ansatz wurde weiter untersucht, indem, von einem Si-Target, reaktiv gesputtertes SiO_{2-x} als Dotierungsphase auf die Oberfläche der In_2O_3-Schichten aufgebracht wurde. Die resultierende Leitfähigkeit von der In_2O_3/gesputtertem SiO_{2-x} Struktur zeigt keine Verbesserung der elektrischen Eigenschaften. Dies ist auf die Implantation von Sauerstoffspezies während der SiO_2-Abscheidung auf der Oberfläche von In_2O_3 zurückzuführen, die der Dotierung der Defektmodulationsdotierung entgegenwirken, indem sie die Konzentration der Sauerstoffleerstellen (V_O) in In_2O_3 reduzieren. Daher sind weitere Studien über die Abscheidungsbedingungen der Dotierungsphase nach wie vor unerlässlich, um verbesserte elektrische Eigenschaften zu erzielen.

Beim chemischen Ansatz wurden zwei verschiedene Wege beschritten: Einbettung von Nanopartikeln in die TCO-Wirtsmatrix und Herstellung von entmischten Kompositfilmen. Für den ersten Weg wurden Al_2O_3- und TiO_2-Nanopartikel (NPs) als Dotierphasen ausgewählt und zusammen mit SnO_2-TCO Precursor abgeschieden. Verschiedene Charakterisierungsmethoden konnten die Existenz von Nanopartikeln in den Zinnoxidschichten nicht bestätigen. Daher sind zur Modulationsdotierung weitere Optimierungen der Abscheidungsbedingungen und der Probenpräparationstechniken erforderlich. Für den zweiten Weg wird eine Mischung aus $SnCl_4$ -5(H_2O) und Al(acac)$_3$ Percursorlösungen in unterschiedlicher Zusammensetzung verwendet, um entmischte SnO_2/Al_2O_3 kompositschichten herzustellen. Verschiedene physikalisch-chemische Studien zeigen, dass unter den in dieser Studie verfolgten Abscheidungsbedingungen Al^{3+} vorzugsweise Sn^{4+} ersetzt, anstatt eine weitere Al_2O_3-getrennte Phase zu bilden. Al wirkte als Akzeptor in SnO_2-Filmen. Daher wurde an den untersuchten Proben keine erhöhte Leitfähigkeit beobachtet. Für diesen Weg ist eine weitere Optimierung der Abscheidungsbedingungen eindeutig erforderlich.

Die Ergebnisse dieser Dissertation sind relevant für die Verwendung von TCOs im aufstrebenden Bereich der Oxid-Dünnschichtelektronik, insbesondere in Bereichen, in denen das Verhältnis von Oberfläche zu Volumen viel höher ist als bei konventionellen Schichten, da der hier verfolgte Ansatz ein oberflächennahes Phänomene ist. Die weitere Untersuchung sowohl der Herstellungsbedingungen als auch der Materialauswahl ist jedoch von entscheidender Bedeutung.

Preface

This doctoral thesis is under the framework of the European Joint Doctorate for Multi-functional Materials (EJD-FunMat:http://idsfunmat.u-bordeaux.fr/ejd-home). It is co-supervised by Professor Dr. Andreas Klein from Technische Universität Darmstadt (TU Darmstadt, Germany), and Professor Dr. Daniel Bellet from Institut polytechnique de Grenoble (Grenoble INP, France), as well co-supervised by Dr David Muñoz-Rojas (CNRS, France). The main work in this thesis has been conducted in two laboratories: ESM (electronic structure of materials, https://www.mawi.tu-darmstadt.de/esm) in the department of Materials and Earth Sciences of TU Darmstadt, which is expert in the electronic structure of materials and their functional properties with emphasis on defects and surface/interface properties and at LMGP (Laboratoire des Matériaux et du Génie Physique, http://www.lmgp.grenoble-inp.fr, which is expert in deposition and characterization of functional thin film materials.

The controlled doping of semiconductors is a prerequisite for modern technology. The amount of charge carriers that can be introduced into the host material by conventional substitutional doping is known to be restricted by material-specific doping limits, which are caused by the formation of compensating defects due to the Fermi level dependent defect formation energies [1, 2]. Another drawback of the classical doping approach by elemental substitution is the decrease of charge carrier mobility (μ) with increasing charge carrier density (n), caused by ionized impurity scattering [3]. In the field of transparent oxide semiconductors, these physical limits have precluded a significant increase of achievable film conductivity for the past 3 decades [4, 5].

Transparent conducting oxide (TCO) semiconductors, which hold the features of being transparent and electrically conductive, are used as electrodes in solar cells, touch screens, transparent heaters and flat-panel displays [6]. For this group of semiconductors, the high electrical conductivity is usually obtained by typical doping with heterovalent substitutional impurities like in Sn-doped In_2O_3 (ITO), fluorine-doped SnO_2 (FTO) and Al-doped ZnO (AZO) [4]. For future applications in solid state lighting materials, higher conductivities than those available today are desirable. If we see today's smart phone technology, the display is the most expensive part of the phone as its production cost is higher than all other parts together (battery, camera, CPU, and memory). Moreover, the TCO with the best performance to date is ITO, which suffers from limited resources of indium. The lower conductivites of FTO and AZO are caused by lower dopant solubility or grain boundary barriers, which are a direct consequence of the applied substitutional doping [5].

Modulation doping (MD) is already used successfully in semiconductor (opto-)electronics and has also been discussed as a potential route to overcome conductivity limits. This technique has its origin in heterostrutures and superlattices of semiconductors, which demonstrate charge carrier confinement by heterojunctions and showed that in layers which are sufficiently thin the carriers occupy quantized energy states. Modulation doping was first introduced by Dingle et al. in 1978 [7], using molecular beam epitaxy (MBE) grown GaAs/GaAs-$Al_xGa_{1-x}As$ superlattices with modulated silicon doping. It employs the concept of spatial separation between ionized (parent) donor impurities and the electrons in 2D electron system. Therefore, the technique can alleviate the carrier mobility restriction in highly doped semiconductors. However, this conventional approach of modulation doping is not suitable for increasing the conductivity of TCOs. This is related to the intrinsic defect formation, which determines the maximum possible carrier concentrations. This restriction is caused by the general use of two materials of similar chemical and lattice structure for the formation of doped interface and the alignment of pinning level [1].

This thesis is dedicated to elucidate the practical limits of modulation doping by implementing a novel doping strategy, which relies on defect related Fermi level pinning in insulators as dopant phase namely "*defect modulation doping*". This approach uses two chemically and structurally dissimilar materials to circumvent the alignment of doping limits. The use of dissimilar materials, which do not have to be conducting on their own, removes the constraint of aligned doping limits. By aligning two dissimilar materials it is therefore, in principle, possible to obtain Fermi levels outside the doping limits in the host material. This is possible by a careful control of the interface properties used to induce previously unattainable charge carrier densities in one of them. Such a situation can, from a thermodynamic point of view, only be achieved if defects in the host material cannot form spontaneously when the Fermi energy is raised during deposition of a modulation layer. The viability of this approach has already been demonstrated by Weidner [8, 9] during his PhD work. He deposited a defective and amorphous insulator material Al_2O_3 on sputtered SnO_2 thin films, in which the Fermi level in defective Al_2O_3 pinned and resulted in a Fermi level position outside of the doping limit in SnO_2. In this work, electrically conducting TCOs[1] shall be obtained by employing modulation doping of sputtered thin films and nanocomposite materials synthesized from undoped TCO hosts and embedded dopant nanoparticles. The defect modulation doping is schematically illustrated in Fig. 1.

[1] with mitigation of both carrier concentration and mobility restrictions

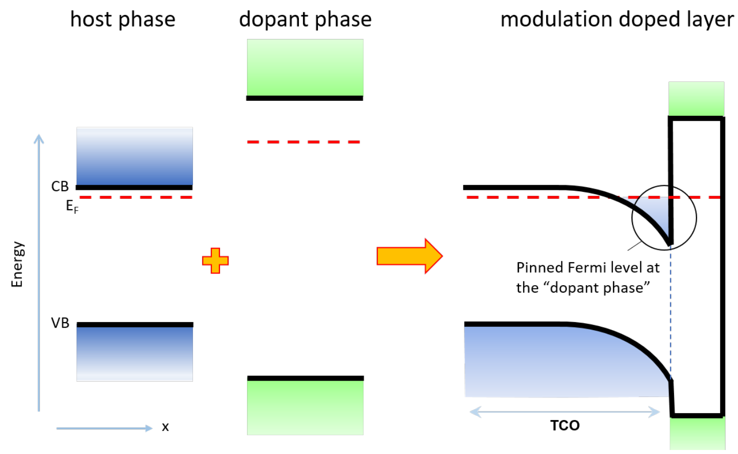

Figure 1: *Schematic illustration of defect modulation doping, in which the host phase is representing undoped TCOs and dopant phase that of wide band gap potential dopants.*

Structure of this thesis

This work is separated into two parts. In Part I, the scientific foundations of relevant topics will be introduced. In Part II, the attempts followed to demonstrate defect modulation doping on TCO materials will be discussed with experimental results and interpretations.

Part I, "Background and Fundamentals", is divided into four chapters. In *chapter 1*, the fundamental properties of semiconductors, starting from an ideal semiconductor will be outlined. Subsequently, the formation of point defects and their influence on dopability will be presented. *Chapter 2*, starts with Transparent conducting oxides (TCO) by reviewing the relevant literature. In section 2.1, electrical properties of TCOs with limitations of carrier concentration and carrier mobility will be discussed. The optical properties of TCOs will be reviewed in section 2.2 and that of their applications will be described briefly in section 2.3. Section 2.4 will be focused on the alternative doping strategy for semiconductors, namely modulation doping. First the concept of modulation doping will be introduced in classical case with a set of examples. Then, previous works on attempting to implement modulation doping for TCO materials will be reviewed. Finally, in the last subsection the novel approach, namely defect modulation doping, which is the foundation of this work will be introduced. In *chapter 3*, the materials In_2O_3, Sn-doped In_2O_3, SnO_2, and Al_2O_3 used during this study will be introduced in detail, with focusing on their electronic, crystal, and defect structures. Finally, *chapter 4* outlines specifics of experimental approaches used in the present work.

Part II, "Results, discussion, and considerations" is separated into two sub-parts based on the experimental strategies followed during this work.

- **Part II-A** ”Physical Approach” will focus on sputtered TCO thin films with coating of different dopant insulators on the top surface of TCO. In *chapter 5*, differently prepared Sn-doped In_2O_3 used as TCO host and 5-cycles of ALD-Al_2O_3 used as a dopant are described. The doped interface is then investigated to prove the viability of the approach. In *chapter 6*, undoped In_2O_3 sputtered films used as TCO host and different cycles of ALD-Al_2O_3 as dopant. Here, the influence of dopant layer thickness will also be investigated. *Chapter 7* focuses on the viability of using different a wide band gap material, namely SiO_2, as a potential dopant. For this purpose, different SiO_{2-x} layers were sputtered from a Si target on top of In_2O_3 substrates. The results are complemented with interfacial and electrical studies.

- **Part II-B** ”Chemical Approach” will focus on testing defect modulation doping on nanocomposite thin films prepared by the ultrasonic spray pyrolysis deposition method. Nominally undoped SnO_2 is used as TCO host and the sub-part is divided into three chapters based on type and form of potential dopant used. In *chapter 8*, TiO_2 nanoparticles (NPs) are used as a potential dopant and intended to embed them into SnO_2 host matrix. The case for composite films of SnO_2 (TCO host)/ Al_2O_3 (dopant) from $SnCl_4 \cdot 5H_2O/Al(acac)_3$ precursors respectively, will be covered in *chapter 9*. Finally, *Chapter 10* discusses the approach followed to embed dopant Al_2O_3 NPs into a SnO_2 host for realization of defect modulation doping.

  At the end, the key points related to this thesis work have been selected and summarized together with future perspectives in ”Closing Remarks and Outlook”.

Part I

Background and Fundamentals

Chapter 1

Fundamentals of Semiconductors

Semiconductors are identified as a unique material group on the basis of their common macroscopic properties, as is done for metals, dielectrics and magnetic materials. The name 'semiconductor' stems from the fact that such materials have moderately good conductivity, higher than that of insulators, and lower than that of metals. The conductivity of these materials strongly depends on the state of material including chemical purity and of temperature. For sufficiently pure semiconductors, the conductivity decays by orders of magnitude by cooling down from room temperature to liquid helium temperature. At absolute zero temperature, semiconductor conductivity vanishes and it acts like insulators: In contrast, the conductivity of metals increases with lowering of temperature and reaches its maximum at low temperature. The electrical conductivity of semiconductors can also be altered by many orders of magnitude by introducing a small quantities of other substances. At a very pure state they resemble an insulator, while in high polluted state they act like a metal, with other peculiarities. These impurities also determine whether the conductivity is electron or hole character. The entire field of solid state electronics relies on this particular properties of semiconductors.

In this chapter, the basic properties of semiconductors will be introduced very briefly. First the electronic band structure and its influence on electrical properties will be explained. Subsequently, point defects, concept of doping and doping limits will be presented. The concepts presented in this chapter are taken from the following references [10, 11, 12, 13, 14].

1.1 Band Model

Core level electrons are tightly bounded electrons, which localized close to the atomic nucleus of an atom and having higher binding energy. Due to the strong localization close to the core, the broadening of the binding energy is defined by the Heisenberg uncertainty principle [15]. Less tightly bound electrons may also be present close to the boundaries of an atom, which are called valence electrons. Due to the weak spatial localization, the corresponding energy level is sharp. When a solid is formed, individual atoms are approximated until an equilibrium between attraction and repulsion is reached. Valence electrons interact with each other and the occupancy of energy levels by an electron is limited by the Pauli principle [16]. This means that a spatial vicinity of energetically similar orbitals leads to a dispersion in energy. This dispersion is the origin of the formation of what is referred to as an energy band.

Under some circumstances, valence electrons enable charge transport and electrical current, which is why they are further discussed in the following. The solution of the Schrödinger equation for a quasi-free electron in the periodic potential of a crystal leads to degeneracy at the Brillouin zone boundaries. This degeneracy is forbidden by the Pauli principle. An adequate correction to the calculation results in energies, for which no eigenvalues exist. This energy range is thus referred to as the forbidden energy band gap E_{g}. In a perfect crystal, the change in density of states at the band edges is described by a step function. The energetically highest occupied band is referred to as the valence band, whereas the lowest (completely) unoccupied band is called the conduction band. If a band is partially occupied, it can allow a transport of charges, as it is the case for a metal. The band gap is defined as the energy difference between the valence band maximum $E_{\mathrm{V}B}$ and the conduction band minimum $E_{\mathrm{C}B}$. Pure insulators and semiconductors are characterized by a fully occupied valence band and a $T = 0$ K. Very often a material is called a semiconductor when the band gap is greater than 0 eV but does not exceed 3 eV. The electronic band structure of these materials is shown in in Fig. 1.1.

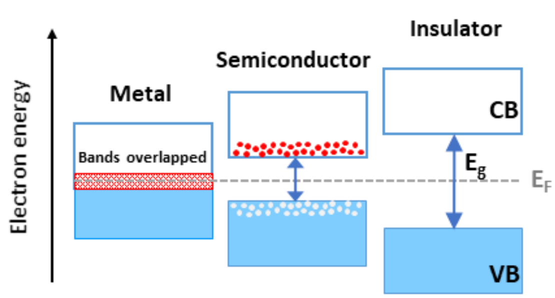

Figure 1.1: *Schematic representation of electronic band structures of solids at 300 K. Red and white dots represent electrons and holes, respectively.*

General Definitions of Energy Parameters

As briefly introduced above, a semiconductor has a fundamental energy gap E_{g} between two energy bands of valence band maximum with energy ($E_{\mathrm{V}BM}$) which is fully occupied and conduction band minimum with energy ($E_{\mathrm{C}BM}$) - is unoccupied. The basic principles of the band structure of semiconductors are illustrated in Fig. 1.2. The important energy quantities of the semiconductor are shown in Fig. 1.2 a) and are defined as follow:

Electron affinity (X)

$$X = E_{\mathrm{v}ac} - E_{\mathrm{C}B} \tag{1.1}$$

Work function (ϕ)

$$\phi = E_{\mathrm{v}ac} - E_{\mathrm{F}} \tag{1.2}$$

Ionization potential (E_{I})

$$E_{\mathrm{I}} = E_{\mathrm{v}ac} - E_{\mathrm{V}B} \tag{1.3}$$

Band gap (E_{g})

$$E_{\mathrm{g}} = E_{\mathrm{C}B} - E_{\mathrm{V}B} \tag{1.4}$$

The energy E of electrons in solids is related via dispersion relation $E(k)$ with the wave vectors k of the electron waves , which corresponds to the momentum of the electrons $\hbar k$. This is schematically depicted in Fig. 1.2 b) and is also referred to as the band structure of the semiconductor. It therefore represents all the possible states of electrons in the solid. The dispersion curvature of the valence and conduction bands are usually not identical.

The densities of states in the conduction band ($N_{\mathrm{C}B}$) and in that of valence band ($N_{\mathrm{V}B}$) are obtained by the number of states at a certain energy and are schematically represented in Fig. 1.2 c). The density of states can take different shapes, but are approximated in the vicinity of the band edges $E_{\mathrm{V}BM}$ and $E_{\mathrm{C}BM}$ with the behavior of free electrons. This is also called approximation of parabolic bands, since for this purpose E $\propto \pm$ K applies. For the density of states of the bands, this result in a square root dependence of the energy and is given by Eq. 1.5 and Eq. 1.6 for conduction and valence bands respectively.

$$N_{CB}(E) \approx \frac{1}{2\pi^2}\left(\frac{2m_e^*}{\hbar^2}\right)^{3/2}\sqrt{E - E_{\mathrm{C}BM}} \tag{1.5}$$

$$N_{VB}(E) \approx \frac{1}{2\pi^2}\left(\frac{2m_\hbar^*}{\hbar^2}\right)^{3/2}\sqrt{E_{\mathrm{V}BM} - E} \tag{1.6}$$

where, $\hbar$ is the Planck constant, m_e^* is the effective mass of an electron, and m_h^* is the effective mass of a hole.

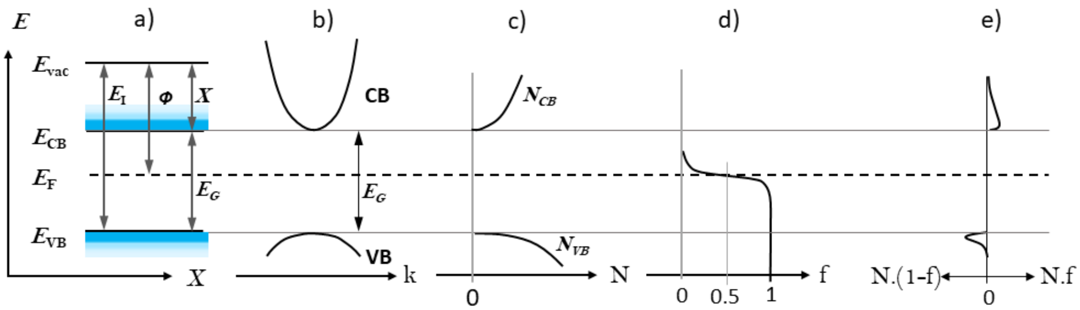

Figure 1.2: *a) Energy band diagram of semiconductor with the energy quantities, b) Energetic dispersion of valence and conduction bands, c) Density of states of valence and conduction band, d) Fermi distribution function f(E) of electrons , e) Number of occupied states.*

Fermi Distribution: In thermodynamic equilibrium, the distribution function for electrons is given by the Fermi–Dirac distribution (Fermi function) f(E):

$$f(E) = \frac{1}{1 + \exp(\frac{E - E_F}{\mathrm{K}T})} \tag{1.7}$$

Where, k (or k_B) denotes the Boltzmann constant, T the temperature, and E_F the Fermi level.

The distribution function gives the probability that a state at energy E is populated in thermodynamic equilibrium. For $E = E_\mathrm{F}$ the population is 1/2 for all temperatures. At (the unrealistic case of) T = 0K , f (E) makes a step from 1 (for$E < E_\mathrm{F}$) to 0. At $T > 0$K, it becomes smoother with higher temperature. The energy interval around E_F, which is affected by the smoothening is $\approx 6\mathrm{k}T$; the shape of f(E) is schematically represented in Fig. 1.2 d.

The high-energy tail of the Fermi distribution, i.e. for $E - E_\mathrm{F} >> \mathrm{kT}$ can be approximated by the Boltzmann distribution;

$$f(E) \approx \exp(-\frac{E - E_\mathrm{F}}{\mathrm{K}T}) \tag{1.8}$$

If the Boltzmann distribution is a good approximation, the carrier distribution is called nondegenerate. If the Fermi distribution needs to be invoked, the carrier ensemble is called degenerate. If the Fermi level is within the band the ensemble is highly degenerate.

Carrier Concentration: The possibility of changing the conductivity of semiconductors from insulating to conducting material is mainly governed by the distance between the Fermi energy and one of the band edges E_{VB} and E_{CB}.

The density of free carrier electrons (n) in the conduction band is given by:

$$n = \int_{E_{CB}}^{\infty} N(E) f(E) dE \tag{1.9}$$

and accordingly the density of holes (p) in the valence band is given by:

$$p = \int_{-\infty}^{E_{VB}} N(E)(1 - f(E)) d(E) \tag{1.10}$$

Where, $N(E)$ is the density of states. If E_{F} is more than 3kT from the band edges, Eq. 1.9 and Eq. 1.10 can be simplified by the Boltzmann statistics and resulting Equations 1.11 and 1.12. In addition, $N(E)$ is approximated by the density of states at the conduction band minimum CBM and valence band maximum VBM, respectively.

$$n = N_{\mathrm{C}B} \cdot \exp\left(\frac{-(E_{\mathrm{C}B} - E_{\mathrm{F}})}{KT}\right) \; with \; N_{\mathrm{C}B} = 2\left(\frac{2\pi m_e^* KT}{\hbar^2}\right)^{3/2} \tag{1.11}$$

$$p = N_{\mathrm{V}B} \cdot \exp\left(\frac{-(E_{\mathrm{F}} - E_{VB})}{\mathrm{KT}}\right) \; with \; N_{\mathrm{V}B} = 2\left(\frac{2\pi m_h^* KT}{\hbar^2}\right)^{3/2} \tag{1.12}$$

Where, $N_{\mathrm{C}B}$ and $N_{\mathrm{V}B}$ are the effective density of states of conduction and valence bands respectively. The states occupied by carriers are schematically represented in Fig. 1.2 e). It should be noted that the effective mass of charged carriers plays an important role for carrier transport, since it is inversely proportional to the charge carrier mobility of the material μ.

In thermodynamic equilibrium, charge neutrality is obeyed, which means n = p. Therefore the intrinsic density (n_i) of a charge carrier is given by the following equation:

$$n \cdot p = n_i^2 = N_{CB} \cdot \exp\left(\frac{-(E_{CB} - E_F)}{KT}\right) \cdot N_{VB} \cdot \exp\left(\frac{-(E_F - E_{VB})}{KT}\right)$$

$$= N_{CB} N_{VB} \exp\left(\frac{-(E_{CB} - E_{VB})}{KT}\right) = N_{CB} N_{VB} \exp\left(\frac{-E_g}{KT}\right) \tag{1.13}$$

The Fermi level of an intrinsic semiconductor can also be calculated when the charge neutrality is obeyed :

$$E_{\mathrm{F}} = \frac{1}{2}E\mathrm{g} + \frac{3}{4}\mathrm{K}T \ln\left(\frac{m_h^*}{m_e^*}\right) \tag{1.14}$$

If $m_e^* \approx m_h^*$, the Fermi energy of an intrinsic semiconductor is found in the middle of the band gap neglecting the second part of Eq. 1.14, which only takes into account the influence of temperature and the different masses of holes and electrons.

1.2 Defects

In the discussion above, only perfect intrinsic semiconductors with Fermi energy at mid-gap $E_{\mathrm{g}}/2$ and n=p were considered. However, many semiconductors applied in devices have majority and minority carriers. If electrons are majority carriers they are called n-type semiconductors, while if the holes are dominating carriers they are called p-type semiconductors. This preferred conduction is generally caused by localized impurities or defects, which have charge transition states inside the band gap.

1.2.1 Description of Defects in Semiconductors

Defects play an important role in the functionality of semiconductor devices. According to the dimensions of the defect, a classification can be made between three-dimensional defects (inclusions, secondary phases, pores, etc.), two-dimensional defects (e.g. surfaces, interfaces, grain boundaries), one-dimensional defects (dislocation), and zero-dimensional defects, also known as point defects.

Point defects play an important role in semiconductor's conductivity. Some typical point defects in semiconductors and the usual nomenclature for them using a binary compound AB are presented below.

If an atom A is missing at a lattice position where it is intended to be by the crystal symmetry, this is referred to as vacancy with a symbol V_{A}. On the other hand, if an atom A is found at an interstitial position of the crystal, is called an interstitial atom with a symbol A_i. If an atom A occupies a B position in the crystal lattice, this is called A_{B}; such defect types, which are formed from the atoms of the semiconducting material itself, are called *intrinsic defects*. In addition, impurities can form *extrinsic* *point defects* in the crystals. For example, an atom C can form an interstitial atom C_i in the compound AB or occupy B-place as C_B. It is important to note that both intrinsic and extrinsic point defects have great importance for electrical behavior of semiconductors.

The Kröger-Vink notation [17] is usually used to describe point defects with respect to their position in the crystal lattice and their charge, which can be denoted as $X^{charge}_{position}$. Here, X is the element in use. If there is an empty space on a regular atomic position, this is marked with "V"[1]. The subscript indicates the location where the defect is placed in the lattice. If it is at an interstitial position, this is marked with "i". The superscript indicates the charge of the defect with respect to the regular (perfect) position. If the defect is positively charged with respect to the lattice, this is indicated by "$^\bullet$" (for every additional positive charge, one additional "$^\bullet$"). If the charge is negative with respect to the lattice, it is indicated by "'". If the defect is neutral relative the lattice, the value is "x".

For illustration purpose an example of Sn - doped In_2O_3 is given below:

- In^x_{In} $\cdots\cdots$ an indium ion located on regular indium lattice
- $V^{\bullet\bullet}_O$ $\cdots\cdots$ doubly positively charged oxygen vacancy
- O''_i $\cdots\cdots$ a double negatively charged oxygen ion in an interstitial position (oxygen interstitial)
- $Sn^{\bullet}_{In}$ $\cdots\cdots$ a tin atom placed on an indium position with a single positive charge (donor doping, an electron is transferred to the lattice).

1.2.2 Electronic properties of Defects in Semiconductors

1.2.2.1 Dopants

The selective contamination of a semiconductor with foreign atoms is called doping. To generate extrinsic charge carriers, the dopant element must have more or less valence electrons than the host lattice. If the dopant atom has one more valence electron than the one to be replaced in the lattice it is a donor and an n-doping is achieved. While, if the dopant has one less valence electron, it represents an acceptor and correspondingly a p-doping achieved.

[1]Vacancy

Doping is associated with an introduction of defect states in the band gap. If the defect states are found within 3kT from one of the band edges, they are called *shallow dopants* and the ionization is possible so that the electron or hole will contribute to free carrier density. *Deep dopants* on the other hand cannot directly contribute to free charge carrier density, but have an influence as compensating defect. Depending on the position of the Fermi level, the defect states could be occupied or not occupied. An example of this is shown in the Fig. 1.3 a), on the basis of an energy band diagram with a donor and an acceptor defect level. A simple donor is neutral if it is occupied by an electron, when an electron is removed from the dopant the state will become positively charged. On the other hand an acceptor state is unoccupied in the neutral state and becomes negatively charged when it is occupied. The total density of donors N_{D} then consists of the density of neutral donors N_{D}^0 and positively charged donors N_{D}^+ (Eq. 1.15) . Similarly, Eq. 1.16 applies to acceptors.

$$N_{\mathrm{D}} = N_D^+ + N_{\mathrm{D}}^0 \tag{1.15}$$

$$N_{\mathrm{A}} = N_{\mathrm{A}}^- + N_{\mathrm{A}}^0 \tag{1.16}$$

For each dopant, the density of ionized dopants N_{D}^+ and N_{A}^- with respect to the total dopant density N_D and N_{A} is governed by the distance of the Fermi energy to the respective dopant level E_{D} and E_A according to equations Eq. 1.17 and Eq. 1.18.

$$N_{\mathrm{D}}^+ = \frac{N_D}{1 + g_{\mathrm{D}} \exp \frac{(E_F - E_{\mathrm{D}})}{\mathrm{K}T}} \tag{1.17}$$

$$N_{\mathrm{A}}^- = \frac{N_{\mathrm{A}}}{1 + g_A \exp \frac{(E_{\mathrm{A}} - E_{\mathrm{F}})}{KT}} \tag{1.18}$$

The symbols g_{D} and g_{A} are the respective ground-state degeneracy of the impurity level. This shall be shortly explained for a monovalent dopant: Such a level can be occupied by electrons with two types of spins, so it appears as two available sites in carrier statistics while it is unoccupied. However once occupied, it holds its maximum charge and appears in carrier statistics as a single level. Consequently g_{D} for donors becomes 1/2 whereas g_A for acceptors is equal to 2.

After doping the semiconductor remains electrically neutral, thus the total charge neutrality must be maintained under the condition:

$$n + N_{\mathrm{A}}^- = p + N_{\mathrm{D}}^+ \tag{1.19}$$

For shallow dopants, it is usually assumed that the donors (N_{D}) and acceptors (N_{A}) are almost completely ionized at room temperature, namely, $n \approx N_{\mathrm{D}}^+ \approx {}_{\mathrm{D}}$ for n-doped semiconductor and $p \approx N_{\mathrm{A}}^{-} \approx N_{\mathrm{A}}$ for p-doped semiconductors. Due to the change of carrier concentrations by doping, the Fermi level positions in doped semiconductor also change: increasing electron concentrations brings the E_{F} closer to band edges.

For n-type semiconductor

$$E_{\mathrm{F}} = E_{\mathrm{C}B} - kT \ln \frac{N_{\mathrm{C}B}}{n} \tag{1.20}$$

For p-type semiconductor

$$E_{\mathrm{F}} = E_{\mathrm{V}B} + kT \ln \frac{N_{\mathrm{V}B}}{p} \tag{1.21}$$

The exact position of the Fermi level for n-type semiconductors depends on the temperature, the position of donor level, effective mass of electrons in the conduction band, and the density of donors according to Eq. 1.20: Similarly, Eq. 1.21 applied for p-type doping.

1.2.2.2 Intrinsic point defects

An intentional introduction of defects for the doping of a semiconductor can only lead to a shift of the Fermi level position within or beyond the band gap within certain limits. These limits are very different for different materials, which is directly related to the *intrinsic defects* of the material: as a result of a shift in the Fermi level, intrinsic defects can be formed when their formation enthalpy $\Delta\mathrm{H}_x$ depends on the position of the Fermi level E_{F}. This is the case for charged defects (donors and acceptors). This mechanism stems from the fact that a defect after its formation can contribute to the reduction of the total energy of the crystal by releasing a charge q to the crystal. The energy gain per unit charge is the energy difference between defect level and Fermi level, since the mean energy of the charge carriers in the crystal is E_{F}, while the charge carrier on the defect state has the energy E_{x} [18, 19].

The defect formation enthalpy ΔH_x, can then be calculated as follow:

$$\Delta H_x = \Delta H + q(E_{\mathrm{F}} - E_{\mathrm{V}B}) \tag{1.22}$$

Where, q is charge of the defect (positive for donors and negative for acceptors), ΔH is the defect formation enthalpy of the defect at $\mathrm{E_F} = \mathrm{E}_{\mathrm{V}B}$.

Whether a defect exists in its charged or uncharged state depends on the defect state, which has the lower formation enthalpy. According to Eq. 1.22 the defect formation enthalpy of a charged defect depends on the position of the Fermi level. The cause for

Fermi level dependent formation enthalpy is the charge transfer from the defect into the charge reservoir of the solid, resulting in an energy gain.

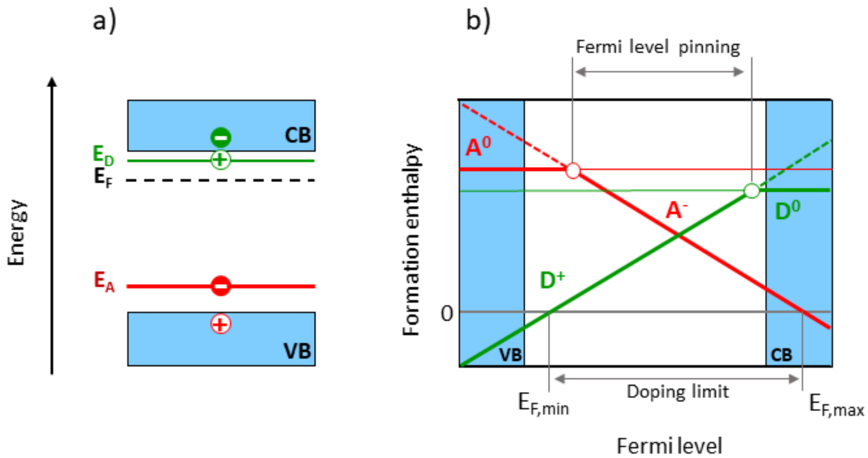

Figure 1.3: *a) Energy band diagram of a semiconductor with an donor and an acceptor defect levels. Both defects are charged at the indicated position of the Fermi level; b) Defect formation energies of defects shown in the left plot as a function of Fermi level position. The stable charged state are marked with solid lines, while unstable charged states are represented by dashed lines. In addition, the doping limit and the area to which the Fermi level is pinned are also marked (assuming identical defect concentrations) [14].*

An illustration on how the defect formation entalpies behave for a donor/acceptor pair versus Fermi energy is given in Fig. 1.3. Furthermore the terms self compensation, doping limits and Fermi level pinning will be discussed.

A semiconductor with an acceptor defect whose energy level is slightly above the valence band maximum and a donor defect with an energy level just below the conduction band minimum, is shown in Fig. 1.3 a). The defects have the charge states of 0 and +1 (donor) or 0 and -1 (acceptor). The defect formation enthalpy as a function of the position of Fermi level of the semiconductor is also shown in Fig. 1.3 b). The transfer points (marked with circle) of the defects are located at the energetic positions of the defect levels in the band diagram.

The charged state with the lower defect enthalpy is always stable. However, the Fermi level cannot be shifted arbitrarily far in the direction of conduction band or valence band by doping. Furthermore, for values of the Fermi level $\mathrm{E_F} > \mathrm{E}_{\mathrm{F},max}$ and $E_\mathrm{F} < E_{\mathrm{F},min}$, the defect formation enthalpy of one of the defect's becomes negative. Thus, this defect is formed spontaneously and contributes to the fact that the Fermi level cannot exceed or fall below this value. This energetic limit corresponds to the *doping limit of the material*: Thus, the Fermi level is thermodynamically fixed to the range $\mathrm{E}_{\mathrm{F},min} < \mathrm{E_F} < E_{\mathrm{F},max}$ and cannot be shifted beyond this range by doping with foreign atoms (or applying an electrical voltage). This effect is called *self-compensation*.

Assuming the same defect concentrations N_D and N_A in the example discussed above, charge neutrality is only obtained if both defects are charged. This corresponds to the area between the transfer points. The Fermi level range is thus limited to the range of transfer points and pinned onto this area. However, for high defect concentrations and $N_\mathrm{D} \neq N_\mathrm{A}$, the charge neutrality condition can be valid only for a single point. The Fermi level can then be determined by high density of the defect in the material at this point. This is called *Fermi level pinning*.

In contrast to the solid body shown here, there are often more than two defects in real materials, which have different charge states and formation enthalpies. The defect formation enthalpy diagrams are therefore more complicated.

Self-compensation is the most important limiting factor of doping. Other limitations of dopability may result from a reduced solubility of the dopant element and from the energetic position of the dopant level [20]. If the doping level is far away from the band, the ionization is energetically unfavorable, one speaks of deep impurities.

Chapter 2

Transparent Conducting Oxides (TCO)

Optical transparency is often incompatible with high electronic conduction, since optical transparency requires band gaps larger than 3 eV and such a large gap makes carrier doping very difficult. In this sense, transparent conductive oxides (TCOs) are exceptional materials. They have high optical transmission at visible wavelengths and as well high electrical conductivity. They also reflect near infrared and infrared (i.e., heat) wavelengths, and are used in products ranging from energy efficient low-e windows to photovoltaics. Virtually all applications involve thin films. TCO's range from simple binary compounds to exotic ternary and quaternary compounds. Examples of TCO's include indium oxide (In_2O_3), indium tin oxide (ITO), zinc oxide (ZnO), tin oxide (SnO_2), aluminum doped zinc oxide (AZO), and cadmium oxide (CdO). TCO's are generally n-type wide bandgap semiconductors (although p-type materials are now being developed) with a relatively high concentration of free electrons in the conduction band. The wide bandgap is responsible for high optical transmittance and free electrons increase electrical conductivity.

In this section, the fundamental electrical and optical properties, limits for electrical conductivity, and most important applications of TCO materials will be introduced. In addition, the conventional approach followed to overcome the doping limitations namely modulation doping will be explained. Furthermore, different trials reported in literature to implement the modulation doping concept for TCO materials will also be reviewed. Finally, the new concept of a doping strategy for modulation doping of TCO materials, namely "*defect related modulation doping*" will be introduced.

2.1 Electrical Properties

TCOs are wide band gap semiconducting oxides, with conductivity σ in the range 10^2 – 1.2×10^4 S/cm. The conductivity is due to doping either by oxygen vacancies or by extrinsic dopants. In the absence of doping, these oxides become very good insulators, with resistivity ρ up to 10^{10} Ωcm. Most of the TCOs are n-type semiconductors. The electrical conductivity of n-type TCO thin films depends on the electron density in the conduction band and on their mobility and is given by the Eq. 2.1:

$$\sigma = \mu n e \tag{2.1}$$

where, μ is the electron mobility, n is its density, and e is the electron charge.

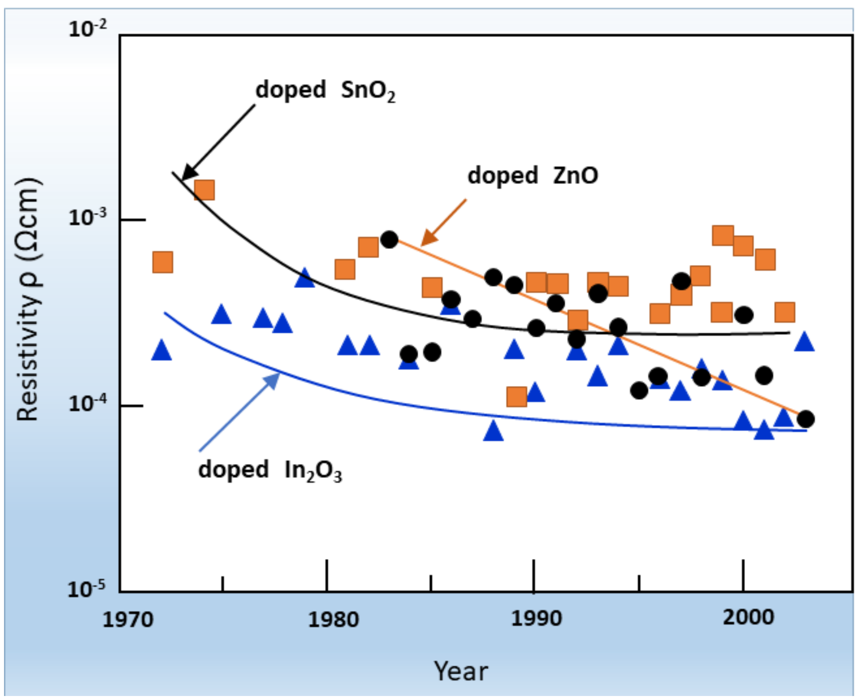

Figure 2.1: *Reported electrical resistivity of impurity -doped binary compound TCO films; impurity-doped SnO_2 (square), In_2O_3 (triangle), and ZnO(circle). (Redrawn from [4]).*

2.1.1 Electrical Conductivity Limits of TCOs

TCO materials should be sufficiently conductive to be used for the desired applications. Minami [4] reviewed the changes in minimum resistivity of impurity-doped binary compounds of SnO_2, In_2O_3, and ZnO reported over the years and shown in Fig. 2.1.

The reported minimum resistivities of these TCO compounds did not change for more than the past two decades. Thus, obtaining an improved conductivity of these materials is still one of biggest challenge for the researchers in this area.

The electrical behavior of differently doped In_2O_3 films, which are prepared in different conditions at TU Darmstadt [21] and carrier mobility versus concentration of these films is shown in Fig. 2.2. In the plot, the carrier concentration of In_2O_3 increased by several orders of magnitude by doping with different impurities, and n could reach up to 10^{21} cm^{-3}. This is the maximum carrier concentration for doped In_2O_3 films and further increase is not possible as indicated by red vertical line. Similarly, the carrier mobility μ values vary depending on carrier concentration. At lower concentrations, the mobility depends on grain boundary scattering and at higher n values mobility depends more on impurity doping, which can not be surmounted for homogeneously doped films. This limitation is a universal property of semiconductors and has been found before for silicon [22], GaAs [23] and other semiconductors.

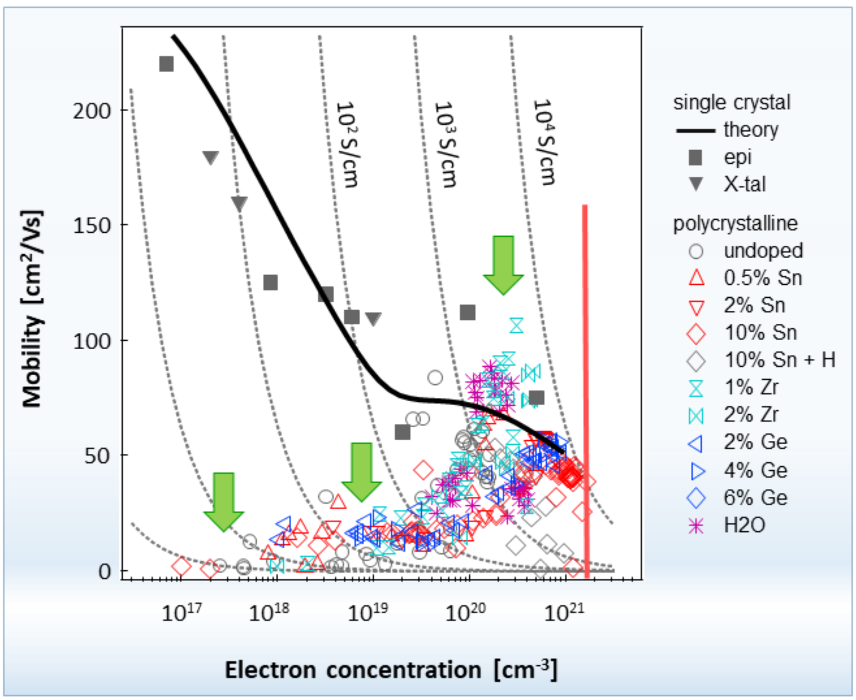

Figure 2.2: *Charge carrier mobity in dependence on carrier concentration for differently doped -In_2O_3 thin films. The solid black line is a calculated dependence of $\mu(n)$ for single crystal In_2O_3. The vertical red line is the limit for carrier concentration and the green arrows indicates different scattering mechanims which limits mobilities of carriers. Data collected in Electronic Structure of Materials Group at TU Darmstadt by M. Frischbier, A. Wachau, H. Wardenga, A. Hubmann and K. Hoyer. Results are published in [21, 24].*

In this section, the universal limitations of carrier concentration (doping limit) and barriers for carrier transports will be discussed.

2.1.1.1 Limits in Carrier Concentration - Doping Limitation

The ability to dope a material effectively could be limited by three main factors: a lack of dopant solubility, the dopant level being too deep and unionizable, or the dopant being compensated by intrinsic defects. Among these factors, compensation by intrinsic defects is the key limitation. This occur if moving the Fermi energy towards a band edge causes the spontaneous formation of compensating defects because the formation energy of that defect has fallen to zero at that Fermi energy [20].

The chemical trends of limits to doping of many semiconducting metal oxides is analyzed in terms of the formation energies needed to form the compensating defects. The n-type oxides are found to have high electron affinities and charge neutrality levels that lie in midgap or the upper part of their gap, whereas p-type oxides have small photoionization potentials and charge neutrality levels lying in the lower gap [20, 25].

The concentration of intrinsic defects does not only affect the carrier concentration, it also depends on it. This is related to the dependence of the formation enthalpies of charged intrinsic defects on the Fermi energy, which is a consequence of the removal/addition of electrons from/to the defect [12, 25]. The energy gain is given by the difference between the defect energy, which corresponds to the Fermi level position at which the defect changes its charge state, and the actual Fermi energy position. An important consequence of this relation is known as self-compensation and the situation is illustrated in Fig. 2.3.

The limit of doping of semiconductors, particularly for materials with larger energy gaps or ionic bonding like TCOs, is determined by self-compensation [2, 20, 26]. Intentional insertion of donor impurities nominally increases the electron concentration and therefore raises the Fermi energy. Consequently, the formation energy for compensating intrinsic acceptor defects is lowered and their concentration increases. The highest possible Fermi level position ($E_{\mathrm{F},max}$) is reached when the acceptor formation enthalpy approaches zero. Any additional donors do not raise the Fermi level further, but just lead to complete ionic compensation, i.e., the charges of the additional donors are 100% compensated by the charges of the automatically generated intrinsic acceptor defects. Thereby the generation of intrinsic acceptor defects in response to a rising Fermi energy limits the electron concentration in a semiconductor. In the other case, the generation of intrinsic donor defects in response to a lowering of the Fermi energy leads to a minimum Fermi energy position ($E_{\mathrm{F},min}$) and limits the hole concentration. These both situations are depicted in top right plot of Fig. 2.3.

As the defect formation enthalpies also depend on the chemical potentials ($\Delta\mu$) of the constituents, the maximum and minimum Fermi energies can be adjusted by the chemical potentials. In oxides, these are directly related to the oxygen partial pressure

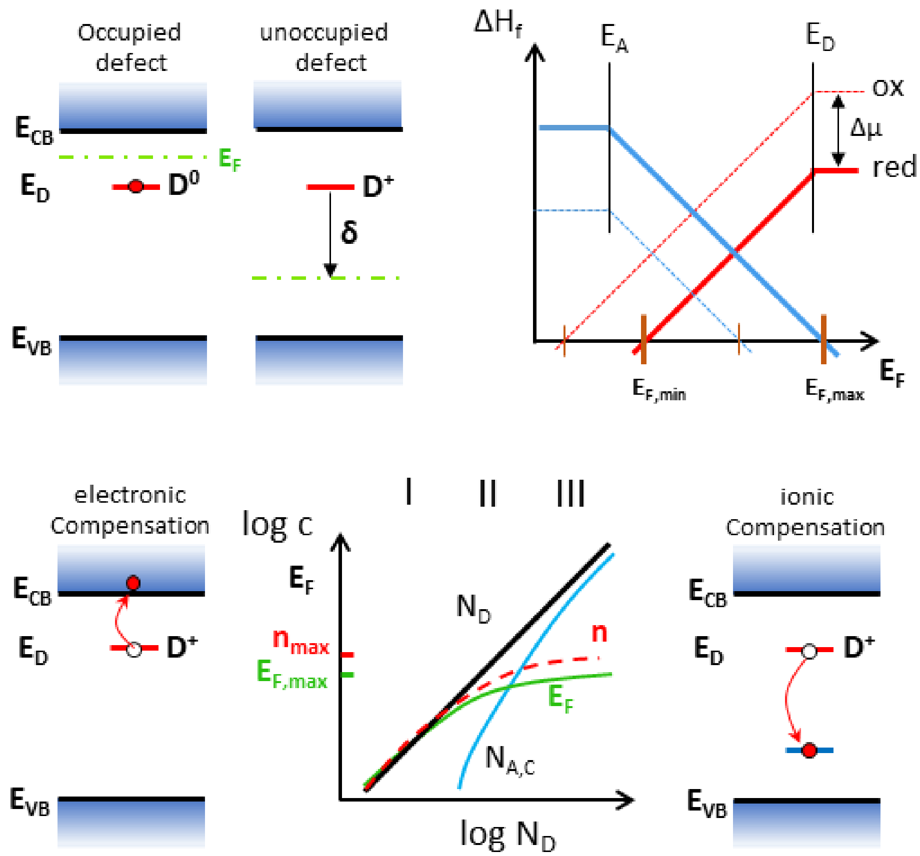

Figure 2.3: *The self-compensation mechanism: (left top) charge states of a donor defect in dependence on Fermi energy and energy gain δ by removing an electron during formation of an intrinsic donor; (top right) schematic defect formation enthalpies as a function of Fermi energy and chemical potential. Lower/higher Fermi energies are possible for oxidizing/reducing conditions; (bottom) transition from electronic (region I where $N_D \approx n$) into ionic compensation (region III where $N_D \approx N_A$) with increasing donor concentration [12].*

[12]. Most important intrinsic donor defects in oxides are oxygen vacancies (V_O) and cation interstitials, whereas acceptor defects are oxygen interstitials (O_i) and cation vacancies. Also antisites may need to be considered [27], although they are less important than in III–V materials due to the higher charge. Particular oxygen interstitial defects may also form oxygen dimers on regular oxygen lattice sites (also called dumbbells or split interstitials), which can be amphoteric, i.e., act as well as donors and as acceptors depending on the Fermi energy [27]. While these defects do not seem to limit the range of possible Fermi energies, they are essential for oxygen diffusion [12].

The dependence of $E_{\mathrm{F},max}$ on oxygen partial pressure causes the variation in film properties with deposition conditions. The dependence of defect formation energies on the chemical potential ($\Delta\mu$) is indicated in top right plot of Fig. 2.3 by the solid and dashed curves of the defect formation enthalpies [25]. An increase in oxygen pressure during deposition raises the formation enthalpy of donor defects (oxygen vacancies and cation interstitials) and lowers those of acceptors. Consequently, the range of accessible Fermi energies is shifting to lower values with increasing oxygen pressure as indicated in Fig. 2.3. The lowering of the Fermi energy with increasing oxygen concentration during film deposition is then caused by an increase in compensating acceptor concentration [12].

For ITO, the compensating acceptors are oxygen interstitials [27, 28, 29, 30, 31] whereas Zn vacancies are the respective defects for donor-doped ZnO [28, 32]. As oxygen interstitials and cation vacancies have comparatively large formation energies in SnO_2, higher Fermi energies and therefore larger electron concentrations compared with In_2O_3 and ZnO are expected [29]. However, the highest carrier concentrations and electrical conductivities achieved with doped SnO_2 films [33] are still lower than those of ITO [34], suggesting that additional compensation mechanisms, e.g., involving planar instead of point defects, may also be important [12].

Dopants may also become inactive when not incorporated into appropriate lattice sites. In particular for higher dopant concentrations, phase separation may occur. Such effects have been reported for Sn-doped In_2O_3 [35], Sb-doped SnO_2 [36], and Al-doped ZnO [37]. As for the formation of compensating intrinsic defects, the solubility of a dopant depends on the chemical potentials. In general, more oxidizing conditions favor the incorporation of donors and reducing conditions those of acceptors. This has been demonstrated, e.g., by the dependence of surface Sn concentration at ITO surfaces on oxygen pressure [12].

The Fermi level positions determined for a number of doped In_2O_3, SnO_2, and ZnO films are shown in Fig. 2.4. In all cases, the Fermi energy is found in the upper half of the energy gap, which clearly expresses the preference for n-type conductivity of these materials. However, the data obtained in Fig. 2.4 are mostly from undoped or intentionally donor doped materials. The highest possible Fermi level position $E_{F,max}$ of these films is indicated by red dashed lines. Due to the presence of intrinsic compensating defects, further inrease of Fermi energy was not not possible and doping is limited [12].

The doping limitation of In_2O_3 films is shown in Fig. 2.5. Introduction of Sn donor dopants increases the electronic concentration of In_2O_3 and therefore raise the Fermi energy. Further increase of Sn donors lead to the formation of acceptor type compensation intrinsic defect (O_i) [27, 28, 29, 30, 31], the formation energy of this defect will lowered and their concentration increases.

When the formation energy of acceptor O_i approaches zero, the highest possible Fermi level position will be reached (3.5 eV [38]). Any further addition of Sn donors do not raise the Fermi energy, but lead to complete ionic compensation Sn donors and form neutral

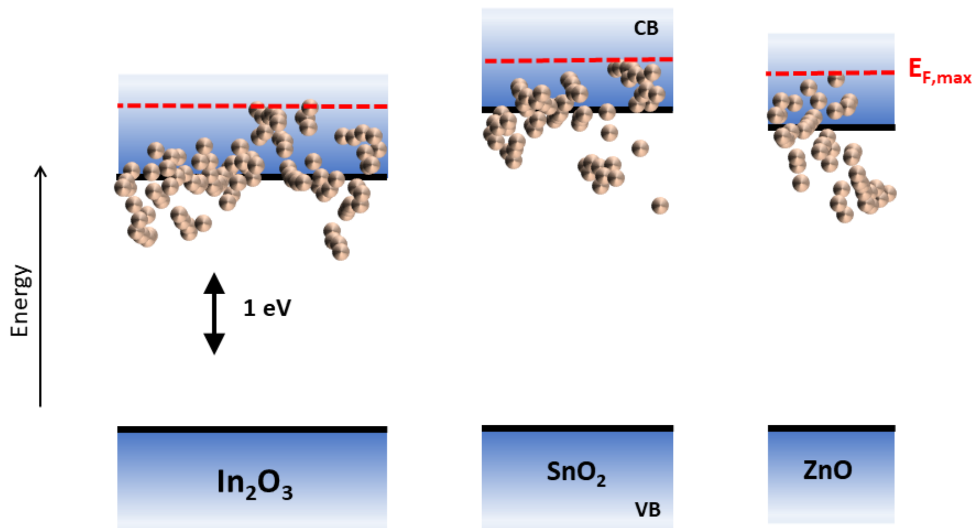

Figure 2.4: *Fermi levels of In_2O_3, SnO_2 and ZnO determined from in situ photoelectron spectroscopy measurements of films prepared by magnetron sputtering. Each data point has been recorded from a separate film. The order of the data points is arbitrary. The maximum Fermi level position's of each films marked by red dashed line [12].*

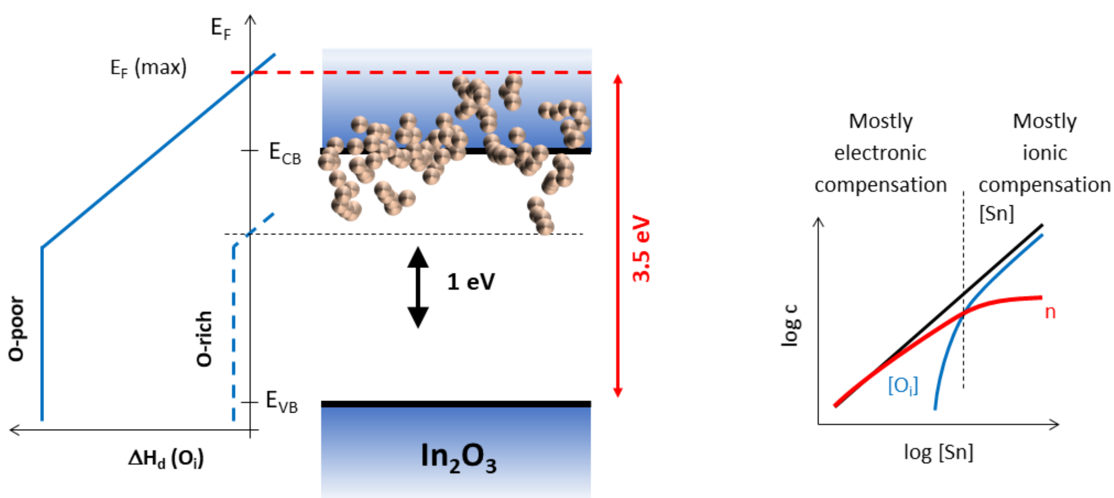

Figure 2.5: *Left: The Fermi energies of differently doped In_2O_3 films determined from in-situ photoelectron spectroscopy measurements which prepared by magnetron sputtering; in addition the maximum Fermi level position ever reported for In_2O_3 films with 10 % Sn doping of 3.5 eV [38] also indicated by red arrow. The adjustment of Fermi level positions by chemical potentials (oxygen partial pressure) is also shown. Right: The relation between Sn donor concentration and carrier concentration of In_2O_3, in the plot the transition from electronic to ionic compensation with increasing Sn concentration is shown [12].*

tin complex $(2\mathrm{Sn}^{\bullet}_{In}\mathrm{O}''_{i})^{X}$ [1]. The Fermi level position of In_2O_3 also depends on the oxygen partial pressure (oxidized /reduced condition) during film production. As can be seen in Fig. 2.5, oxygen-rich conditions lowers the Fermi energy and lead to minimum Fermi energy position ($E_{\mathrm{F},min}$); while in oxygen-poor condition the Fermi energy will be higher and lead to the maximum Fermi energy position ($E_{\mathrm{F},min}$). Therefore manipulation of Fermi energy of In_2O_3 is possible within the doping limit ranges [12].

2.1.1.2 Limits in Carrier Transport / Carrier Mobility

The carrier mobilities of TCO thin films measured by Hall effect can be explained by considering different scattering mechanisms. The possible scattering mechanisms, which could limit the carrier transport includes: ionized impurity scattering, grain boundary scattering, neutral impurity scattering, phonon scattering, and dislocation scattering. In this section, these different scattering mechanisms will be outlined with some considerations. Most of the informations in this section are adapted from the book "Handbook of Transparent Conductors" [39].

Grain boundary barrier limited transport

Polycrystalline films exhibit a vast amount of grain boundaries, which constitute crystallographically disturbed regions, leading to electronic defects in the band gap of semiconductor [39]. These defects are charged by carriers from the interior of the grains. Depending on the type of carriers (electrons or holes) and that of defects (electron trap or hole trap) charge balance causes depletion or accumulation zones around the barrier. In n-type TCO films a depletion zone is generated on both sides of a grain barrier accompanied by an energetic barrier of height Φ_b for the electrons. This is due to the electron trap character of the defects [39].

Seto [40] proposed a grain bounday model based on polycrystalline silicon. He assumed a δ-shaped density of electron trap states in the band gap, which are completely filled and foreign atoms or other defects at grain boundaries induce these electron traps. A schematic band diagram according to Seto's model is shown in Fig. 2.6.

The carrier transport across the grain boundary barriers is described by the classical thermionic emission (TE) theory. For very high carrier concentrations in the grains, the depletion width is very narrow, thus enabling quantum-mechanical tunneling of the

[1] The detail of defect structure of ITO is discussed in Chapter 3.1.4

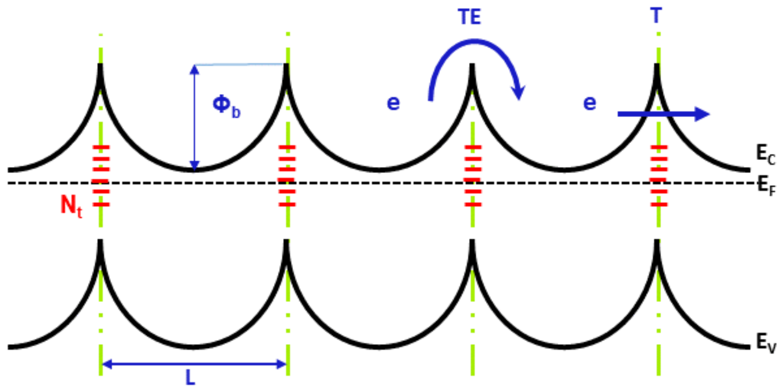

Figure 2.6: *Schematic band diagram of a linear row of grains of identical length L, doping N and with grain barriers of height ϕ_b caused by a continuous distribution of electron trap states of density N_t [40]. Two different transport paths for electrons are indicated: TE-thermionic emission across the barrier, T-tunnelling through the barrier. Inspired by [39]*

barriers by the electrons, represented as "T".

Baccarani et al. [41] improved Seto's model by considering a continuous energy distribution of trap states in the band gap. In addition, the possibility of traps to be only partially filled was treated. Seto's and Baccarani et al.'s models yield an effective mobility (μ_{eff}), which is dominated by thermionic emission across the grain barriers with an energetic height Φ_b:

$$\mu_{eff} = \mu_0 exp(-\Phi_b/\mathrm{K}T) \tag{2.2}$$

Where, T is the sample temperature, and k is the Boltzmann constant, respectively. The prefactor μ_0, which is the mobility inside the grain is obtained within Seto's model as by:

$$\mu_0 = \frac{eL}{\sqrt{2\Pi m^* \mathrm{K}T}} \tag{2.3}$$

where L is the grain size. Depending on the doping concentration in grains, two equations for the barrier height can be derived:

$$\Phi_b = \frac{e^2 N_t^2}{8\varepsilon\varepsilon_0 N} \quad for\ \ LN > N_t, \tag{2.4}$$

$$\Phi_b = \frac{e^2 L^2 N}{8\varepsilon\varepsilon_0} \quad for\ \ LN < N_t, \tag{2.5}$$

Where, e is the elementary charge, N_t is the charge carrier trap density at the boundary, $\varepsilon\varepsilon_0$ is the static dielectric constant, N is the carrier density in the bulk of the grain and

L is the grain size.

For LN > N_t, the traps are only partially filled and hence the crystallites are completely depleted; While for LN < N_t, only part of the grain is depleted and the traps are filled completely. The maximum barrier height Φ_{bmax} occurs for a doping concentration of $N(\Phi_{bmax}) = N_t/L$, accompanied by a minimum of the effective mobility according to Eq. 2.2.

The band structure at the grains with low, medium, and high carrier concentrations is schematically depicted in Fig. 2.7 (a-c). In Seto's [40] and Baccarani et al.'s [41] models only thermionic emission was considered. For very high carrier concentrations N ($> 10^{20}$cm^{-3}) additional tunneling through the barriers takes place, which increases the current flow between the grains. If thermionic model is applied for such high concentrations low Φ_b can be calculated [39].

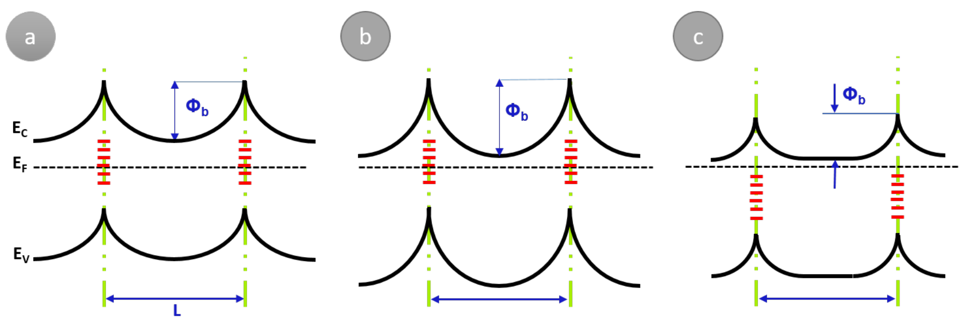

Figure 2.7: *Schematic band diagrams in the grains for different doping concentrations N in grains of identical size L, according to [42]. The situations a–c correspond to low, medium and high carrier concentrations. The barrier height increases with increasing N up to a maximum at $N_{max} = N_t/L$. Further increasing of N decreases the barrier height*

Ionized impurity limited transport

This is a scattering process, which is caused by ionized dopant atoms and dominates for carriers concentrations $> 5 \times 10^{18}$ cm^{-3}. Conwell and Weisskopf [43] were pioneers to describe the theory of ionized impurity limited mobility (μ_{ii}) and derive a formula for it.

An analytical expression for the mobility μ_{ii} of degenerately doped semiconductors, taking into account the non-parabolicity of the conduction band was given by Zawadzki [44] and refined by Pisarkiewicz et al. [45].

$$\mu_{ii} = \frac{3(\varepsilon_r\varepsilon_0)^2\hbar^3}{Z^2m^{*2}e^3}\frac{n}{N_i}\frac{1}{F_{ii}^{np}(\xi_d)} \quad with \quad \xi_d = (3\pi^2)^{1/3}\frac{\varepsilon_r\varepsilon_0\hbar^2 n^{1/3}}{m^*e^2}, \tag{2.6}$$

where the screening function F_{ii}^{np} is given by:

$$F_{ii}^{np} = \left[1 + \frac{4\xi_{np}}{\xi_d}\left(1 - \frac{\xi_{np}}{8}\right)\right] \cdot ln(1+\xi_d) - \frac{\xi_d}{1+\xi_d} - 2\xi_{np}\left(1 - \frac{5\xi_{np}}{16}\right) \tag{2.7}$$

where: ε_r is the relative dielectric constant, ξ_{np} = 1- m_0^*/m^* a parameter, which describes the non parabolicity of the conduction band (where m_0^* is effective mass in conduction band edge and m^* effective mass of conduction band). The non-parabolicity is usually described by the dependence m^*/m_0^* =1 + 2β(E-E_c); where β is the non-parabolicity parameter and E and E_c are the energies of the carriers in the conduction band and at its edge. The other symbols ε_0 and e have their usual meaning. The prefactor in Eq. 2.6 shows, that the ionized-impurity limited mobility depends as $\mu_{ii} \sim (\varepsilon_r/m^*)^2$ on the material constants of the semiconductor and as $\mu_{ii} \sim Z^{-2}$ on the charge of the dopants.

Bellingham et al. [46] were the first who stated that the mobility and hence the resistivity of transparent conductive oxides (ITO, SnO_2, and ZnO) is limited by ionized impurity scattering for carrier concentrations above 10^{20} cm^{-3}. The limitation of carrier mobility in heavily doped semiconductors by ionized impurity scattering can not be surmounted in homogeneously doped films. This limitation is a universal property of semiconductors and has been found before for silicon [22], GaAs [23] and other semiconductors. Generally, for ionized impurity scattering it is assumed that the ionized dopant atoms are homogeneously distributed in the semiconductor. The above theoretical model, as well as models of Conwell and Weisskopf [43], Dingle [3], and Shockley [47], are based on the same assumptions of a statistically homogeneous distribution of scattering centers. However, for extremely high dopant concentrations (above 10^{20} cm^{-3}) this is not necessarily valid, as the dopants may form clusters due to their higher charge. This may further reduce the mobilities $\mu_{ii} \sim Z^{-2}$. Dakhovskii et al. [48] has proposed this cluster model effect in 1971 and Klaassen applied the model to fit accurate measurements of mobilities in 1992 [49]. Recently, Ebert et al. [50] were able to visualize impurity clusters in Zn doped GaAs by cross-sectional tunneling microscopy. Due to the inverse dependence of the ionized impurity scattering on the square of the charge of the scattering centers, this clustering reduces the mobility significantly. The third effect, further reducing the mobility is the non-parabolicity of the conduction band, which has to be taken into account for degenerately doped semiconductors with its filled conduction band. In order to overcome this mobility limit, the principle of modulation doping, which has been introduced by Dingle et al. [7] in 1978 for GaAs/GaAlAs multi layers, has been suggested also for heavily doped TCO films.

Neutral impurity limited transport

This scattering mechanism occur at low temperature particularly for semiconductors showing small degree of ionization. The mobility due to neutral impurity scattering was first derived by Erginsoy [51], who scaled the electron scattering at hydrogen atoms to a semiconductor by using its dielectric constant and carrier effective mass, which leads to the following equation:

$$\mu_n = \frac{m^* e^3}{A(T) 4\pi\varepsilon\varepsilon_0 \hbar^3 N_n} \tag{2.8}$$

Where, A(T) is the scattering cross section factor and N_n is the density of neutral scattering centers. Erginsoy [51] calculated a temperature independent value A= 20, which is mostly used. The concentration of neutral impurities is given by $N_n = N_D - N_A - n(T)$, where N_D and N_A are the donor and acceptor concentrations, respectively.

Since the shallow donors in TCO materials exhibit ionization energies around about 50 meV, the concentrations of neutral donors at room temperature are very low, taking into account the further reduction of the ionization energy for degenerately doped semiconductors [39, 52].

Defect-limited transport / Dislocation scattering

Dislocation scattering seems to be a natural scattering process in polycrystalline materials. The dislocations generated by plastic deformation can introduce acceptor centers along the dislocation line, which capture electrons from the conduction band of an n-type semiconductor. The dislocation line becomes negatively charged and a space charge is formed around it. The resulting potential field scatters the conduction electrons and so reduces the electron mobility [53].

However, this process is rarely used in explaining experimental data of carrier transport in polycrystalline semiconductors and especially transparent conducting oxides. Pödör [54] investigated bended Ge crystals with a dislocation density around 10^7 cm^{-2} and his results could be described by Eq. 2.9, taking into account scattering by charged dislocations:

$$\mu_{disl} = \frac{30\sqrt{2\pi}(\varepsilon_r\varepsilon_0)^{3/2}a^2\sqrt{n}\mathrm{K}T}{e^3 f^2\sqrt{m^*}N_{disl}} \tag{2.9}$$

where, a is the distance between acceptor centers along the dislocation line, f is the occupation rate of these acceptors and N_{disl} is the density of dislocations.

Lattice vibration limited scattering

This scattering process is determined by scattering at acoustic and polar-optical phonons as well as by piezoelectric scattering from the phonon-induced electrical fields. The brief overview of these scattering processes is given below.

Optical mode scattering is due to the interaction of electrons with the electric field, induced by the lattice vibration polarization (polar longitudinal-optical phonons) occurring in polar semiconductors with partial ionic bonding [55]. The corresponding Hall mobility can be calculated by:

$$\mu_{Hopt} = r_{Hopt}\phi\frac{e}{2\alpha\omega_0 m^*}\left[\exp\left(\frac{\hbar\omega_0}{KT}\right) - 1\right] \tag{2.10}$$

where; the polaron coupling constant α is given by

$$\alpha = \left(\frac{1}{\varepsilon_\infty} - \frac{1}{\varepsilon_s}\right)\sqrt{\frac{m^* E_H}{m_e\hbar\omega_0}} \tag{2.11}$$

ε_∞ and ε_s are the high frequency and the static dielectric constants and E_H is the first ionization energy of the hydrogen atom (13.595 eV), $\hbar\omega_0$ is the energy of the longitudinal optical phonon. r_{Hopt} is the Hall coefficient factor for optical mode scattering and Φ is a slowly varying function of the temperature.

Acoustical mode scattering is a lattice deformation scattering process due to a local energetic shift of the band edges originating from acoustical phonons. According to Bardeen et al. [56], the acoustical lattice mode Hall mobility is given by the equation below:

$$\mu_{Hac} = r_{Hac}\frac{\sqrt{8\pi}\hbar^4 c_1 e}{3E_1^2\sqrt{m^{*5}(KT)^3}} \tag{2.12}$$

Where; c_1 is the averaged longitudinal elastic constant, E_1 is the deformation potential, $r_{Hac}= 3\pi/8 = 1.1178$ is the Hall coefficient for acoustic phonon scattering.

Piezoelectric mode scattering occurs only in piezoelectric materials, i.e., in crystals without inversion symmetry, and is caused by the electric field associated with acoustical phonons. It becomes important at low temperatures, where in pure samples it competes with the acoustic scattering due to deformation potential. Zook [57] calculated the piezoelectrically limited mobility as:

$$\mu_{Hpie} = r_{Hpie}\frac{16\sqrt{2\pi}\hbar^2\varepsilon\varepsilon_0}{3eP_{\perp}^2,\prod\sqrt{m^{*3}KT}} \tag{2.13}$$

Where; $r_{Hpie}= 45\pi/128 = 1.1045$ is Hall coefficient for piezoelectric mode scattering and $P_{\perp}^2,\prod$ is the piezoelectric electro-mechanical coupling coefficients.

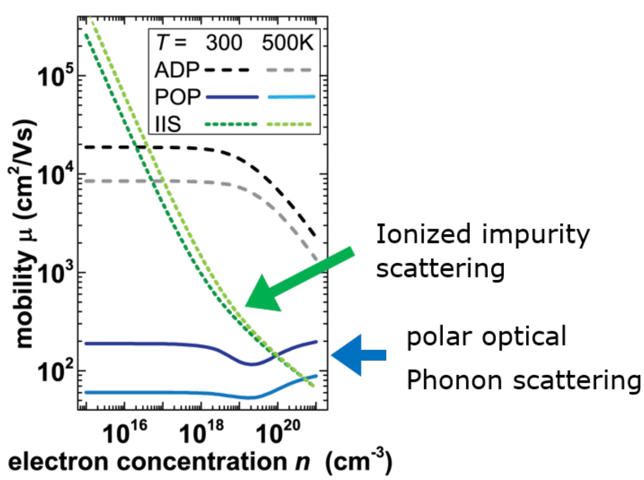

Figure 2.8: *Overview for individual scattering mechanisms of single crystal In_2O_3 showing modeled at 300 K and 500 K. Mobilities as a function of electron concentration of single crystal In_2O_3 for different scattering mechanisms: ADP = acoustic deformation potential; POP = polar optical phonon; IIS = ionized impurity scattering (Redrawn from [58]).*

Preissler et al. [58] reported a model for the dominant intrinsic scattering mechanisms, i.e. scattering by phonons and by the ionized donors, in single crystal In_2O_3, see Fig. 2.8. In the model, it is clearly seen that polar optical phonon scattering, best described by a Debye temperature of $\Theta_D = 700$ K and N_{OPML} is the dominant phonon scattering mechanism, which limits the room-temperature drift mobility to 190 cm^2/Vs. Acoustic deformation potential scattering is negligible. Since the donors are fairly shallow, almost all the donors are ionized and it even increases towards higher doping levels (where impurity scattering becomes more important) as sample becomes degenerate. Because the number of neutral donors is negligible in this case, neutral impurity scattering can be neglected [58].

2.2 Optical Properties

Transparent conductive oxides are remarkable materials since they present both a transparency in the visible wavelength range (λ = 400 - 800 nm), which is rather a characteristic of insulators, and an important electrical conductivity, which is generally a characteristic of metals. In order to obtain these properties, the band gap E_{g} of a semiconductor must be greater than the energy of the photons E_{ϕ} used in a visible range. This allows visible photons not to be absorbed through electronic transitions from the valence band to the conduction band. These transitions result an intense absorption when $E_{\phi} > E_{\mathrm{g}}$. The maximum energy of a visible photon is; $E_{\phi}(\lambda = 400 \text{ nm}) = 3.1$ eV. Therefore, to use TCOs for optical application in visible range, it is advisable to use materials with E_g greater than 3.1 eV.

Doping and Transparency

In order to be sufficiently conductive, most TCOs are heavily doped to degeneracy so that the Fermi level is positioned above the conduction band edge. The doping thus change the optical behavior of the material as illustrated in Fig. 2.9; in which the transmittance and reflectance spectra of Sn-doped In_2O_3 films with different doping levels are depicted.

The transmission window is defined by two imposed boundaries. The first is in near-UV region determined by the effective band gap, in which the transparency limit λ_g of the TCO is shifted to the shorter wavelengths. Since the conduction band is being partially occupied, photons needed a larger energy than the fundamental band gap E_g to excite transitions from the valence band to the unoccupied states in the conduction band. The required additional energy is called the Burstein-Moss shift [59]. Owing to higher electron concentrations involved, the absorption edge is shifted to higher photon energies. The sharp absorption edge near the band edge typically corresponds to the direct transition of electrons from the valence band to the conduction band.

The second phenomenon occurs in the near-infrared (NIR) region due to the increase in reflectance caused by the plasma resonance of electron gas in the conduction band. Consequently, the boundary in NIR region also shifts towards shorter wavelengths with increasing of the free carrier concentration. The shift in this region is more pronounced than that in the near UV-region. Therefore, the transmission window becomes narrower as the carrier concentration increases [60].

The response of carriers to an electromagnetic field is divided into two different domains in accordance with the wavelength of the photons considered. At short wavelength the TCO behaves like a dielectric and is transparent. On the contrary, at the longer wavelengths the TCO behaves like a metal and reflects or absorbs light; this is due to the collective oscillations of conduction band electrons known as plasma oscillations or plasmons in short, which are at the origin of substantial absorption at larger wavelength. The wavelength transition characteristic between these two regimes is known as the plasma wavelength λ_p, which can be calculated as follows:

$$\lambda_p = \sqrt{\frac{4\pi^2 c^2 \varepsilon_0 \varepsilon_\infty m^*}{ne^2}} \tag{2.14}$$

Where ε^0 permittivity of free space, ε_∞ the high frequency dielectric constant, c the speed of light, n the carrier concentration, and the m^* effective mass of free carriers. For functional TCOs, the plasma wavelength is typically between 1 to 2 μm. Thus, the transparency range of a TCO, between λ_g and λ_p, can cover the near UV, visible and near infrared regions depending on the material usage and its doping.

In Fig. 2.9, the evolution of transmittance and reflectance of differently doped ITO films are depicted with the carrier concentration n_c varied in the following range (1 - 30) $\times$ 10^{20} cm^{-3}. As it can be seen clearly in the top plot of the figure, an increase of carrier concentration by Sn doping shifts λ_p to the shorter wavelengths and reduces the transparency of ITO in the infrared region. In addition, due to an increased plasmonic reflection by free electrons in heavily doped ITO films, light reflection increases, see the bottom plot in the same figure. Similar observations are reported on other TCOs including; FTO [62], AZO [63], GZO [64], and yttrium-doped CdO [65]. Although heavy doping improves the concentration of free carriers and the conductivity, it also is at the disadvantage to the film transparency. This means both the conductivity and the transmittance window are interconnected. Thus, a compromise between material conductivity and transmittance window must be considered depending on the material usage [60].

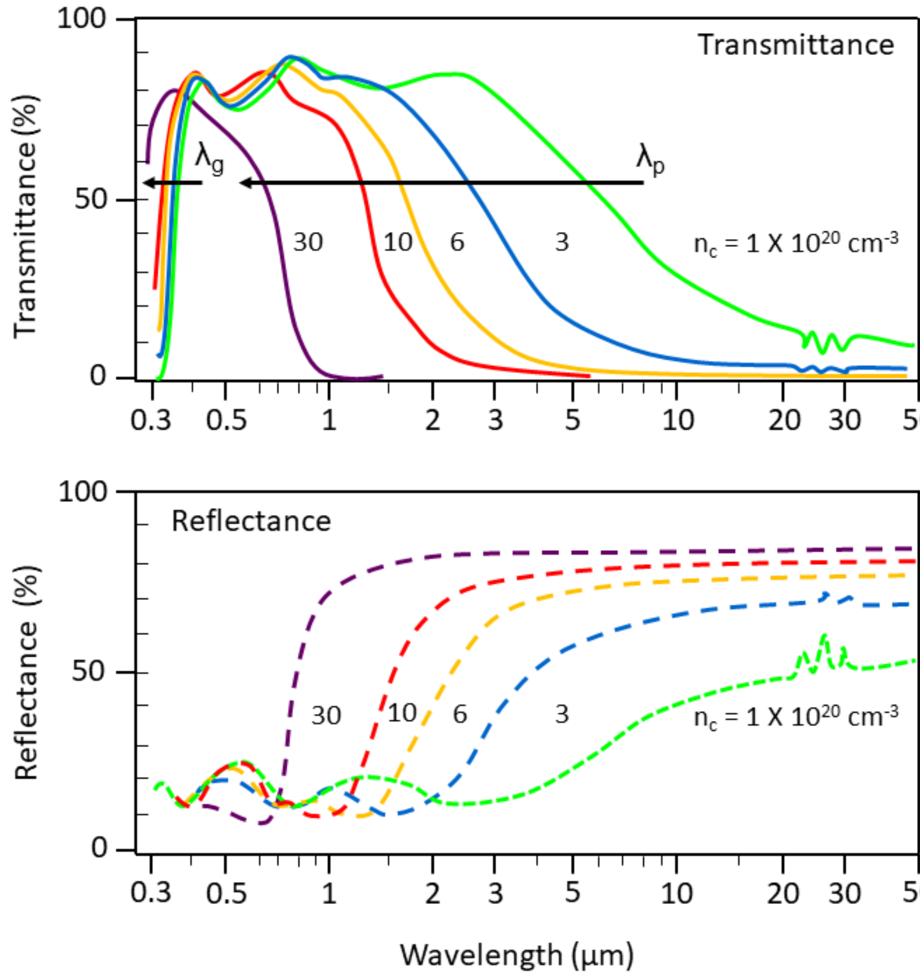

Figure 2.9: *Evolution of transmittance (top) and reflectance (bottom) of Sn-doped In_2O_3 thin films as a function of density of carrier concentration. (Redrawn from [61]).*

2.3 Applications

Transparent conductive oxides are used in a wide range of applications, including transparent electronics, gas sensing, and catalysis. From which, most of the demand goes to transparent electronics industry. This industry includes low-e windows, transparent contacts for solar cells, optoelectronic devices, flat panel displays, liquid crystal devices, touch screens, EMI shielding, and automobile window deicing and defogging. Other than the most commonly used TCOs (ITO, AZO, and FTO), a number of ternary compounds have been developed over the last decade, which becomes critical for different energy efficiency applications including Zn_2SnO_4, $ZnSnO_3$, $MgIn_2O_4$, $(GaIn)_2O_3$, $Zn_2In_2O_5$, and $In_4Sn_3O_{12}$ [66]. In this section, the importance of these TCO materials in some of the applications listed above will be highlighted.

- **Transparent Contact for Photovoltaics**: TCOs are an increasingly important component of photovoltaic (PV) devices, where they act as electrode element, structural templates, and diffusion barriers, and their work function controls the open-circuit device voltage [6]. They are employed in applications that range from crystalline - Si heterojunction with intrinsic thin layer (HIT) cells to organic PV polymer solar cells. The desirable characteristics of TCO materials that are common to all PV technologies include high optical transmissivity across the solar spectrum and low resistivity, which allow the TCO based electrode to transmit light and collect photogenerated current [12]. Additionally, TCOs for terrestrial PV applications must use low cost materials, and some may require device technology specific properties. Fortunato et al. [6] reported a review on TCOs employed in different current and future PV technologies with the required processing and properties, and it is summarized in Tab. 2.1.

- **Transparent Contact for Liquid Crystal Display (LCD)**: In LCDs, TCO films are needed for both electrodes in order to allow backlighting to pass through the liquid crystal while applying voltage to various pixels. Generally, these electrodes are aligned in the form of a perpendicular pattern of lines to each others. This allows to address individual pixels by applying a voltage to the two lines which intersect at a given pixel. ITO is the best candidate for this application due to its electro-optical properties and relative ease for pattering [55].

- **Low-emittance Energy Efficient Windows**: One of the major application area of TCOs in terms of the surface area coverage and their total volume is in energy efficient architectural windows, often as part of multi-layer stacks. For this application, the conductivity of TCO is usually irrelevant, but rather the control of free charge carriers in order to move the plasmon energy between the visible and IR region is pivotal to have high infra-red reflectivity [67]. The coated glass will then have good light transmission in visible range and minimized heat transmission. This feature is used to minimize costs of air conditioning in summer and heating in winter, in buildings equipped with appropriately coated windows. SnO_2:F, is the most common TCO used in this application.

- **Gas Sensing Application**: TCOs are also widely used as chemical gas sensors for detection of combustible and reducing gases. The sensor function is typically described in terms of a variation in band bending at the surface in response to adsorption of oxidizing or reducing gases, which affects the overall electrical conductivity of a film by switching on and off the contribution of the surface region to the electrical current parallel to the surface [68, 69].

Table 2.1: Review for TCOs employed in photovoltaics devices [6]

Cell Type	TCO in current use	TCO Needs	Materials Goals
Heterojunction with intrinsic thin layer (HIT) cell	ITO	smooth, good interfacial properties very good conductivity, low temperature deposition, light trapping	Indium zinc oxide (IZO) indium-free materials, ZnO
Copper indium gallium selenide (CIGS)	Intrinsic-ZnO/Al:ZnO	Interfacial stability to CdS, low-temperature deposition, resistance to diffusion and shorting, need to make/improve the junction	Single-layer TCO to replace two layers and CdS layer
CdTe	SnO_2 Zn_2SnO_4 /Cd_2SnO_4	Stable interface to CdS/CdTe at temperature, diffusion barrier	Doping of $ZnSnO_X$ materials, single-layer TCO
Nano-hybrid polymer cell	ZnO, SnO_2, TiO_2	Nanostructure with right length scale, work-function matching interface with organic, correct doping level for for carrier transport	Self-organized structures core–shell structures, new nonconventional TCO
Grätzel cell	TiO_2	Nanostructure with high electron mobility	Improved TiO_2 morphology and possible use of doped materials new non-TiO_2 materials
Amorphous Si	SnO_2, ITO, and ZnO; many cells employ two TCOs	Temperature stability, chemical stability, and appropriate texture for both TCO layers	Higher conductivity, texture, and ohmic contact for both TCO layers

2.4 Modulation Doping

2.4.1 Classical Modulation Doping

Modulation doping (MD) technique trace its origin to study heterostructures and superlattices of semiconductors, which demonstrates charge carrier confinement by heterojunctions and showed that in layers, which are sufficiently thin the carriers occupy quantized energy states. Modulation doping was first introduced by Dingle et al. in 1978 [7] using molecular beam epitaxy (MBE) grown GaAs/GaAs-Al$_x$Ga$_{1-x}$As superlattices with modulated silicon doping. It employs the concept of spatial separation between ionized (parent) donor impurities and the electrons in 2D electron system. The structures were designed to separate donors from mobile electrons in superlattices in order to increase the scattering time as schematically depicted in Fig. 2.10.

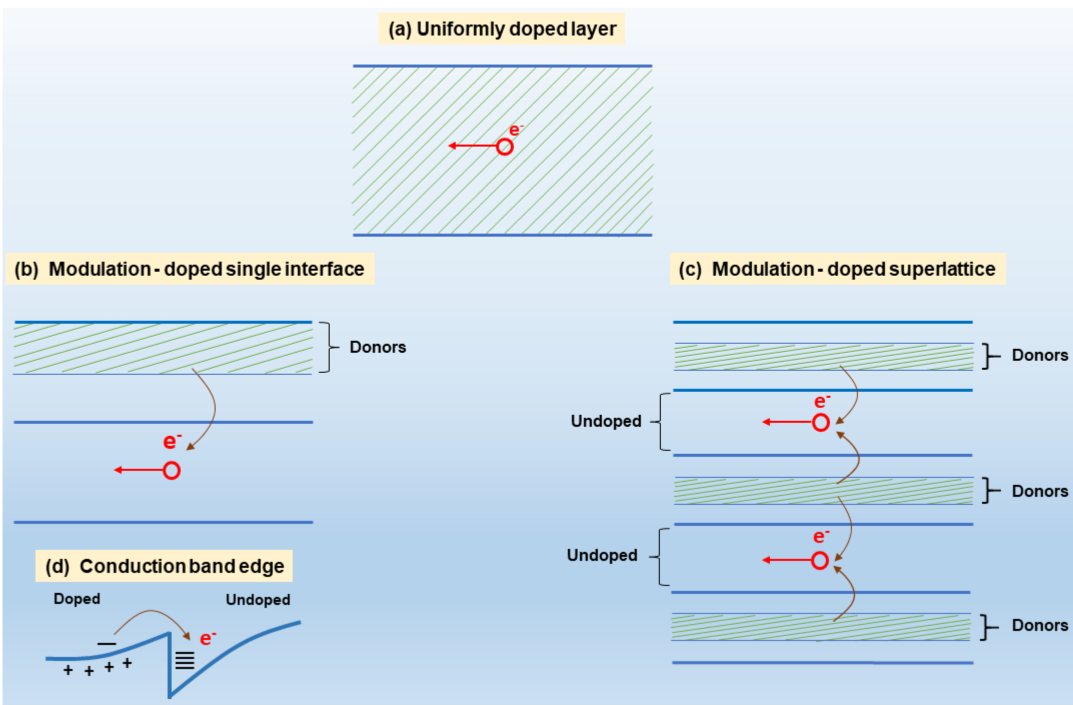

Figure 2.10: *Schematical illustration of spatial arrangement of layers in GaAs modulation-doped structures: (a), uniformly doped layer (b), modulation doped single interface layer, (c) modulation doped superlattice, and (d) the band structure at the heterointerface. Inspired by [70].*

For uniformly doped layers, the carrier electron mobility is limited by scattering due to ionized and neutral impurities, see Fig. 2.10(a). In the case of MD[2] single interface

[2]Modulation Doped

structure, see Fig. 2.10(b), the carrier electrons are separated from their parent dopants and are confined at the hetrojunction potential step by electric field of ionized donors; so electrons can travel a longer time between scattering event occurs. For MD superlattice structure, electron confinement occur at each sides of undoped layer by heterojunction potential step between undoped and doped material as shown in Fig. 2.10(c). The band structure of a heterointerface with a triangular potential step is also shown in Fig. 2.10(d). Theoretically, as long as the donor energy is larger than the conduction-band energy of the smaller-bandgap material, the electrons diffuse into the smaller-bandgap material [70].

Most of the modulation doping effects in heterostructures are based on charge transfer and carrier confinement, which are produced by the step in band energies occuring at the heterojunctions. This step can be probed in several ways: Optical determination of confined particle energy levels allows a determination of confining potential barrier heights. The energy levels can be deducted from interband optical absorption spectra, photoluminesccence excitation spectra, or from intersubband Raman scattering spectra [71, 72].

In GaAs/GaAs-Al$_x$Ga$_{1-x}$As heterostructure system, the band gap difference between the two layers is 1.247× electron volts. Thus, carrier electrons experience a conduction band-edge discontinuity and that of holes valence band-edge discontinuity. It must be noted that most of (≈ 85%) the band gap difference occurs in the conduction band and only a smaller (≈ 15%) in the valence band. These band-edge discontinuities form an upper limit for the energy difference between electrons bounded to a donor in the doped layer near the interface and electrons in the undoped layer.

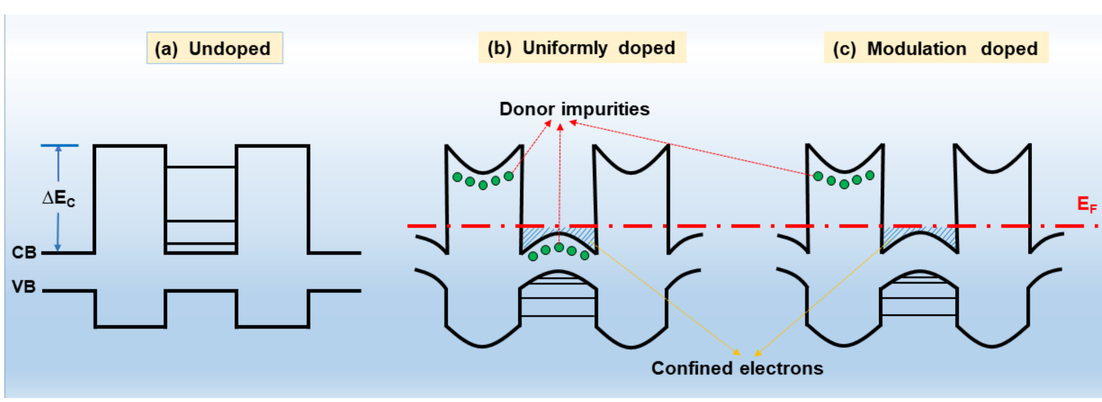

Figure 2.11: *Schematical illustration of band edges, donor states, and electron states in (a), undoped layer (b), uniformly doped layer, and (c) modulation doped Semicondutor system. Inspired by [7].*

Figure 2.11 represents the model for conduction edge structures of undoped, uniformly doped (UD), and modulation doped (MD) GaAs/GaAs-$Al_xGa_{1-x}As$ superlattice structures. The band gap discontinuities of the two materials is shown in Fig. 2.11(a). By the way of introducing dopants into the heterostructure, we can have either uniform doping or modulation doping. In case of MD structure, all mobile carriers (confined in undoped layer) and their parent donor impurities are spatially separated from each other in an irreversible manner as shown in Fig. 2.11(c). In the UD structure the separation of electrons from their parent donors is not possible, see Fig. 2.11(b). For both UD and MD structures, the GaAs-$Al_xGa_{1-x}As$ regions are depleted in order to satisfy the requirement of a continuous Fermi level throughout each superlattice, which in turn leads to appreciable band bending. It is also observed that the carriers are confined to the GaAs layer and form pseudo-two dimensional electron gas (2DEG).

The dominant carrier scattering mechanisms in uniformly doped semiconductors are phonons and impurities; from which the phonon process dominates at high temperatures and that of impurity scattering dominates at low temperature.

Dingle et al. [7] reported temperature dependent mobilities of differently doped GaAs based materials as shown in Fig. 2.12. In the plot, modulation doped (MD) GaAs/GaAs-$Al_xGa_{1-x}As$ superlattice with n ≈ 5 × 10^{16} cm^{-3}, uniformly doped (UD) structures with a range of concentration data, and that of MBE-grown GaAs samples are represented. At a temperature range of < 100 K, the mobility of GaAs and UD samples is mainly influenced by ionized impurity scattering [73]. The UD samples and the MBE grown GaAs do show a $T^{3/2}$ scattering behavior, although a good quantitative fit to the appropriate expression using reasonable parameters is only possible for the bulk samples. In contrast, modulation doped samples show a strong reduction of impurity scattering and improved mobility. In MD structures, the coulomb interaction with ionized impurities responsible for the $T^{3/2}$ scattering is greatly reduces by the separation of carriers and impurities. This exhibits more metal-like behavior, the mobility showing a smooth increase with decreasing temperature.

In summary, the conventional modulation doping mechanism can alleviate the carrier mobility restriction in highly doped semiconductors, although it cannot overcome the carrier density limit imposed by formation of compensating defects. This restriction is caused by the general use of two materials of similar chemical and lattice structure, GaAs and GaAs-$Al_xGa_{1-x}As$, for the formation of the doped interface.

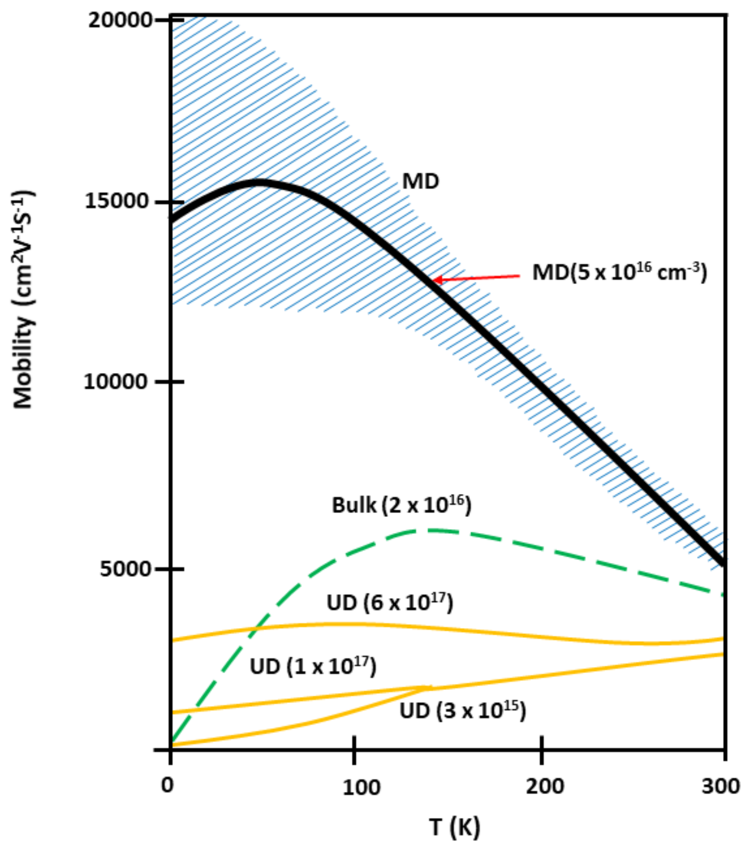

Figure 2.12: *Electron mobility versus temperature for bulk GaAs, several uniformly doped (UD) and modulation doped (MD) superlattices. The crosshatched region includes most of the MD data. (Redrawn from [7]).*

2.4.2 Modulation Doping and TCO Materials

The carrier transport in transparent conducting oxides (ITO, SnO_2, and ZnO) can be limited by several scattering mechanisms, as discussed earlier in subsubsection 2.1.1.2. In case of heavily doped TCOs, ionized impurity scattering or/and impurity clustering is/are the main reason for universal limitation of carrier transport. Thus, new doping principles are needed to surmount this limit. In this section, various strategies employed by different researchers over the years to overcome this universal limitation will be reviewed.

Traditionally, the mobility of TCO thin films has been enhanced by improving the crystalline structure by such a means of heat treatment, choice of deposition technique as well as choice of substrate, as efforts have been reviewed by Calnan et al. [74] and Exarhos et al. [75].

TCO thin films prepared without intentional substrate heating or with low process temperature exhibit low electron mobility due to scattering by grain boundaries and/or point defects. Post annealing treatment in different ambient conditions reduces point and/or dislocation defects in the amorphous or poorly crystallised TCO films by increasing the grain size and improving the overall crystal structure, which in turn enhance electron mobility [76].

The choice of deposition methods also has an influence on the mobility of TCO thin films. According to Ellmer [77], films produced by RF sputtering show higher mobility than those prepared by DC sputtering. This is by the discharge voltage in RF sputtering, which is lower resulting a better crystalline structure than for DC sputtering.

Controlling the crystal growth by using highly oriented substrates is also another way of enhancing the mobility by improving crystallinity. ITO films grown on Yttria-stabilized zirconia with (100) orientation show higher conductivity than the same films prepared on glass substrate [34]. Similarly, highly conductive ZnO:Al with $\mu \sim 70\ \mathrm{cm^2V^{-1}s^{-1}}$ have been reported for film grown on c-plane sapphire [78]. The relatively high cost and limited suitability of these highly oriented substrates on large areas precludes the use of epitaxially grown TCO in a wide range of applications, especially displays and solar cells.

In addition to the approaches discussed above, researchers proposed further more strategies to obtain higher mobilities in TCO materials. Hydrogen incorporation during or after film growth tends to improve mobility [79]. It has been observed that the choice of appropriate dopants also can improve mobilities. Some works have reported on implementation of modulation doping concept on TCO materials. Other than GaAs/GaAs-$Al_xGa_{1-x}As$ [7], modulation doping was highly implemented in Si/SiGe [80], and GaN/AlGaN [81] hetrostructures. Some of reported works by different groups on both experimental as well modeling predictions of modulation doping on TCO materials will be discussed below.

Ellmer [82, 83], tested the modulation doping concept on heavily doped epitaxial ZnO/ZnO:Al and ZnO/$Zn_{1-x}Mg_xO$:Al multilayer films, to overcome the inherent mobility limitation of ZnO due to ionized impurity scattering. The multilayers were prepared by radio frequency magnetron sputtering on a-, c-, and r- plane sapphire substrates. The total superlattice thickness was kept at 550 nm, while the single layer thickness [3] was varied down to 3 nm.

[3] thickness of ZnO, ZnO:Al, and $Zn_{1-x}Mg_xO$:Al single layers

The variation of electrical properties was reported as a function of single layer thickness and substrate type, which the results are shown in Fig. 2.13. As can be seen in Fig. 2.13(b), the carrier concentration (n) of the multilayer decreased significantly with decreasing single layer thickness, which was ascribed to a high oxidation sensitivity of very thin films, which passivated the donors and reduced the carrier density. While, Hall mobility (μ) did not change much, see Fig. 2.13(a).

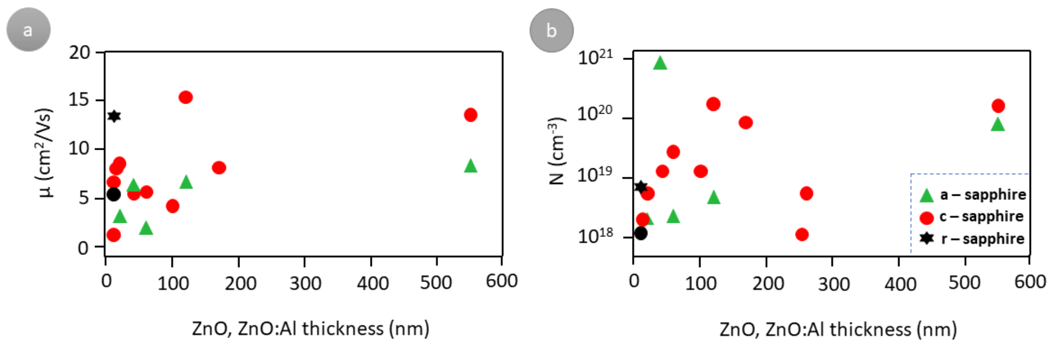

Figure 2.13: *Hall mobility and charge carrier density of ZnO/ZnO:Al multilayers in dependence of the single layer thickness is shown. The total thickness was kept constant at about 550 nm, while the single layer thickness (ZnO and ZnO:Al) was varied down to 3 nm.* $ZnO/Zn_{1-x}Mg_xO : Al$ *films also shown in a black notations. The legends in the figure describes the different substrates used. (Reprinted from [83], Copyright 2006, with permission from Elsevier).*

Ellmer et al. [83] also mentioned the resistivities of these multilayers were scattered up to 3 orders of magnitude compared to single layers, which was also assigned to higher oxidation sensitivity of thin films. Even though, the approach did not show promising results, the authours [83] remarked that adjusting the deposition conditions of multilayer could lead to the promised modulation doping.

Rauf [84] reported very high mobilities in ITO films, which he claimed to be due to modulation doping effect. However, in this case, the highly and lowly doped regions were laterally arranged in the films and not vertically, as in true superlattice structures. This lateral arrangement was achieved by a zonal confining process [85], in which films are crystallized under a local temperature gradient. During film growth, the impurities tend to accumulate in the colder areas of the substrate surface. The impurity movement and temperature gradient are mutually parallel and are perpendicular to the growth direction. In the zone-confined specimens, electrons travel at least twice the average size of the grains, in which high mobilities are achieved.

Cohena and Barnet [86] predicted electrical properties of modulation doped (MD) ZnO-based TCOs. The prediction considered the effect of layer thicknesses, donor

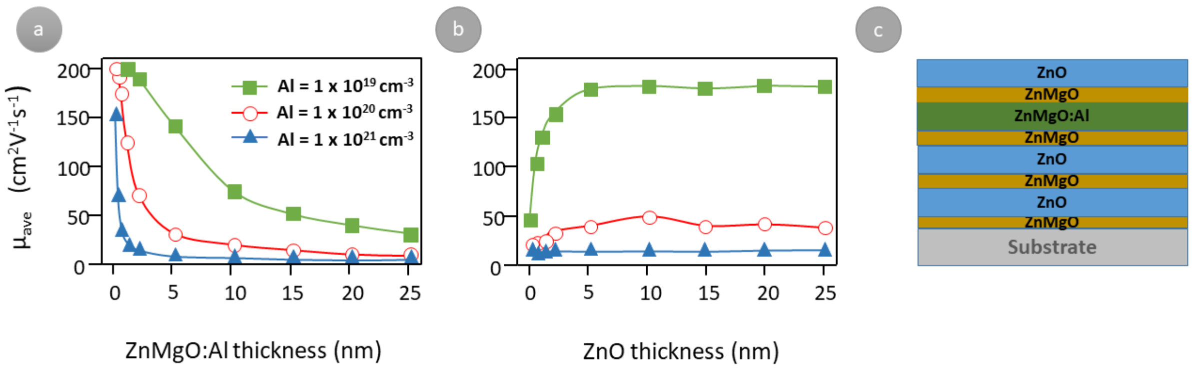

Figure 2.14: *The predicted average mobility of MD ZnO/ZnMgO multilayer structures: (a) the effect of doped layer thickness and donor concentration on the average multilayer mobility, (b) the effect of ZnO layer thickness and donor concentration on the average multilayer mobility, and (c) schematic diagram of two periods of the simulated modulation-doped multilayer structure. (Redrawn from [86]).*

concentration, and band-gap offset on the electrical properties of MD ZnO/ZnMgO multilayer structures. The effect of ZnMgO:Al and ZnO layers thicknesses and different dopant concentrations on predicted average mobility (μ_{ave}) is shown in Fig. 2.14. In addition, schematic structure of multilayer used in their prediction is also depicted in Fig. 2.14(c), in which a pure ZnMgO spacer layer with a thickness of $\sim$ 1.5 nm was used in order to minimize the impact of remote ionized impurity scattering on mobility.

Figure 2.14(a), shows the effect of ZnMgO:Al dopant layer thickness and dopant concentration on predicted μ_{ave}. According to the calculation, μ_{ave} is independent on ZnO layer thickness for a thickness $>$ 5 nm. For a dopant layer thickness of 5 nm , μ_{ave} decreases from $\sim$150 cm^2/Vs to $\sim$10 cm^2/Vs with a change of Al doping level from 10^{19} cm^{-3} to 10^{21} cm^{-3}. The higher mobility at the lower Al content reflects an efficient electron transfer to the high-mobility ZnO layer, whereas the higher electron density is mostly retained in the low mobility. In general, as the ZnMgO:Al dopant layer thickness decreases, the average multilayer mobility increased and it was possible to transfer a greater fraction of electrons. Typically an average multilayer mobility of $\sim$150 cm^2/Vs was achieved for an electron transfer of $\geq$ 88 %, which occurred for electron sheet densities of $\leq 10^{13}$ cm^{-2}.

Cohen and Barnet [86] also considered the effect of ZnO layer thickness on the average mobility, see Fig. 2.14(b). In this case the thickness of ZnMgO:Al was kept at 5 nm and that of ZnMgO at 1.5 nm. Higher mobilities were achieved only for lower Al concentrations and due to ineffective electron transfer with higher Al concentrations, lower μ_{ave} was obtained. According to the calculation, the multilayer mobility was almost independent of ZnO layer thickness, for thicknesses $>$ 5 nm. Whereas, for ZnO thicknesses < 5 nm, μ_{ave} decreased. They explained this phenomenon by a rapid decrease of the number of confined electron states with decreasing ZnO thickness, which limit the density of electrons that could be transferred to ZnO, thereby limits the mobility.

In summary, for ZnO based modulation doped structures, mobility as high as 145 cm^2/Vs have been predicted for a structure with an average carrier density of 3.8×10^{18} cm^{-3} and a resistivity of 1×10^{-2} Ωcm. In monolithic ZnO for a comparable resistivity, the mobility would be as low as $\sim$30 cm^2/Vs [86].

Simulation by Robbins and Wolden [87] on multi-layered films composed of $InGaO_3$ (relatively large electron affinity and low carrier density) alternately stacked with ZnO:Al layers (low electron affinity and high carrier density) have predicted that high conductivity $> 4.2 \times 10^4$ Scm^{-1} and carrier densities $\sim 10^{20}$ cm^{-3} are possible. The authors proposed that high mobilities derived from modulation doping would require individual layers of $<$5 nm thickness and high crystal quality materials with close lattice matching in order to avoid interface defects, which would be challenging to achieve in practice.

H-A Chin et al. [88] also reported an improved electrical conductivity of rf-sputtered polycrystalline MgZnO/ZnO hetrostructure, which they claim is due to modulation doping. Polarization effect at the MgZnO/ZnO interface and carrier transfer from the modulation doping layer contribute to the improvement of electrical conductivity of the heterostructure. Even though, the carrier concentration of heterostructures was increased, there was slight decrease in mobility, which was attributed to impurity and alloy scattering from the modulation doping layer.

In summary, as it has been reviewed above most of the reports on modulation-doped TCO materials are only based on ZnO heterostructures. Experimental results of these reports did not demonstrate the desired improved electrical properties. Since, both doped and undoped layers used for modulation doping originate from the same material with similar chemical and lattice structure, there is high chance of recombination and self compensation, which in turn limits the expected improvements in carrier density and mobility. Thus, a better strategy is needed to implement the concept of modulation doping into TCO materials.

2.4.3 Defect Related Modulation Doping for TCOs

In the previous section, it is clearly shown that conventional modulation doping is not suitable for TCO materials due to intrinsic defect formation, which determine the maximum possible carrier concentration. Therefore, a novel strategy for modulation doping, which relies on defect related Fermi level pinning in insulators as dopant phase namely " *defect modulation doping*" will be discussed in this section.

The defect modulation doping approach uses two chemically and structurally dissimilar materials to circumvent the alignment of doping limits [8]. This was not the case for classical modulation doping, in which the resulting doping limits are typically aligned for similar materials [89, 90]. The use of dissimilar materials, which do not have to be conducting on their own, remove the constraint of aligned doping limits. By aligning two dissimilar materials, it is therefore, in principle, possible to obtain Fermi levels outside the doping limits of the host material. This is possible by a careful control of the interface properties used to induce previously unattainable charge carrier densities in one of them. Such a situation can, from a thermodynamic point of view, only be achieved if defects in the host material cannot form spontaneously when the Fermi energy is raised during deposition of a modulation layer [8].

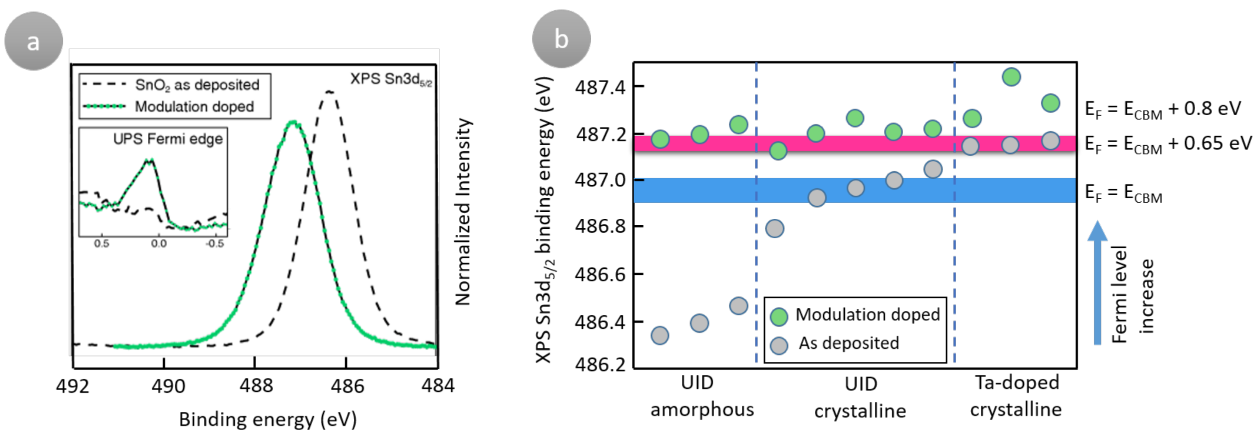

Figure 2.15: *Comparison of SnO_2 (Unintentionally doped (UID) amorphous, crystalline, and Ta- doped crystalline SnO_2) photoemission data before and after deposition of an Al_2O_3 modulation layer. (a), the defect modulation doping results in an increased Fermi level position, reflected by a Sn3d5/2 emission line shift, as well as the filling of conduction band states (insert); (b) comparison of Sn3d5/2 binding energy values before (gray) and after (green) modulation doping. The blue bar indicates typical values of UID samples. The red bar indicates the highest binding energies achieved by conventional doping, which is surpassed by most modulation-doped samples. The increased Sn3d5/2 binding energy is caused by a Fermi Level shift, but the correlation is not linear [8, 9, 91].*

Weidner [9] successfully implemented this "*modulation doping*" concept during his PhD work by depositing a defective and amorphous insulator material (Al_2O_3) on sputtered SnO_2 films, in order to induce conduction electrons in the interface-near region of the latter. The modulation doping effect in SnO_2 substrate was not achieved by the introduction of substitutional dopants in the alumina layer, but instead by pinning of the Fermi level in the defective Al_2O_3, deposited at low process temperature, and at its interface to SnO_2 [8].

A significant rise of the Fermi level position and an increase of conductivity of SnO_2 films by several orders of magnitude has been observed after ALD-Al_2O_3 deposition on top of it. In the experiments, differently prepared (unintentionally doped (UID) amorphous, UID crystalline, and Ta-doped crystalline) SnO_2 films have been used. In situ X-ray photoelectron spectroscopy (XPS), comparing the spectra of Sn3d5/2 emissions before and after deposition of alumina modulation layer are also shown in Fig. 2.15(a). Al_2O_3 deposition resulted a binding energy shift from 486.33 eV to 487.17 eV. This shift is accompanied by peak broadening. He attributed these two effects to an increased Fermi level position in the sampled SnO_2 volume [8]. The increased Fermi level position is furthermore verified by ultraviolet photoelectron spectroscopy (UPS), in which visualization of the filling of conduction band states upon modulation doping was possible [92], see the insert of Fig. 2.15(a). The influence of $\sim$ 1 nm ALD-Al_2O_3 coating on photoemission binding energy of Sn3d5/2 spectra of differently prepared SnO_2 samples is shown in Fig. 2.15(b). Sn3d5/2 binding energy values of 486.9 - 487.0 eV correlate with a Fermi level position close to the conduction band minimum, typically found in unintentionally doped crystalline samples. For substitutionally doped SnO_2, Sn3d5/2 binding energy observed is 487.20 $\pm$ 0.05 eV, which corresponds to a Fermi level position at 0.65 eV above E_{CBM} [93]. After alumina deposition, Sn3d5/2 binding energy increased for all samples, indicating that the Fermi level position can be pushed up to 0.8 eV or even higher into the conduction band.

In order to prove an actual modulation-doping effect, Weinder [9] performed electrical measurements to observe changes in SnO_2 film conductivity after deposition of an Al_2O_3 doping layer. In-situ conductance measurements showed an increase in sample current of up to 6 orders of magnitude after alumina deposition. Ex-situ Hall effect measurements also showed an increase in carrier concentration up to 6 orders of magnitude and carrier mobility by factor of 8 upon alumina deposition. This indicates that, the accumulation layer at the interface does not only increase charge carrier density but also increase intragrain transport, in which the charge carrier mobility can increases [8].

The defect modulation doping approach makes use of the Fermi level pinning on the Al_2O_3 side of the interface, which was found to be located around 4.5 eV above the valence band maximum (VBM), regardless of the employed substrate [38, 94, 95]. This is in good agreement with DFT calculations by Weber et al. [96], in which the formation energy of native defects in k-Al_2O_3 as a function of Fermi level was presented[4]. According to Weber et al. [96], the charge neutrality level of cation Frenkel pair (Al_i^{+3} - V_{Al}^{-3}) defects in Al - rich condition is $\sim$5 eV. The doping level obtained for SnO_2/Al_2O_3

[4]The defect structure of Al_2O_3 is discussed in detail in Chapter 3.3.3

interface is above the substitutional doping limit and is in a good agreement with an Al_2O_3 Fermi level pinning at 4.5 eV. The defects are responsible for a Fermi level pinning in the alumina film. This allows to give a general picture of the applicability of defect modulation doping, which is based on the energy band alignment between materials. In principle, defect modulation doping can be transferred to other materials with known energy band positions [97]. In order to illustrate a number of materials suitable for defect modulation doping using ALD-Al_2O_3, the band alignment of different oxides is shown in Fig. 2.16. The energy band positions have been derived from a large number of interface studies [98]. Most of the materials listed in Fig. 2.16 (except that of Cu_2O and r-TiO_2) have similar valence band maximum energies (E_{VBM}), that is only small valence band discontinuities at the interfaces of each combination of them are expected. As these studies include Al_2O_3, the limit of Fermi energy, which can be reached, is shown by the dashed red line. According to this scheme, defect modulation doping should be a viable approach for many oxides. However, one must keep in mind that defect modulation doping can only overcome the doping limit by self-compensation, if the formation of compensating defects can be avoided [8].

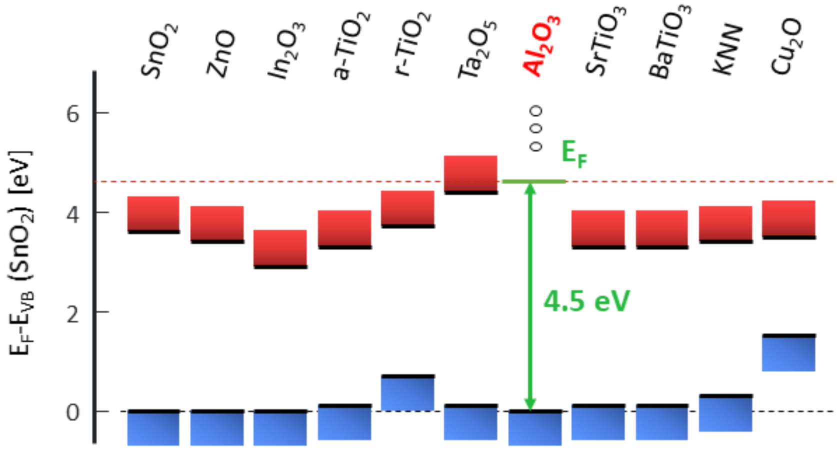

Figure 2.16: *Energy band alignment at contacts of a series of oxides determined from interface experiments using XPS [8]. Details of the measurements and explanation of the origin of band alignment is given elsewhere [98]. The valence band maximum energy (E_{VBM}) of SnO_2 is represented by the black dashed line and is set as a reference of the energy scale as a guide to the eye. The Fermi level position which can be reached by defect modulation doping using low-pressure ALD grown Al_2O_3 is indicated by the red dash-dotted line at* 4.5 *eV above E_{VBM} by taking the value from [38]. The high Fermi energies can only be reached if formation of compensating defects valence changes of the cations can be avoided.*

Short Framework and Depiction of the Thesis

The successful demonstration of the modulation doping concept for SnO_2/ Al_2O_3 films by Weidner [9] was the pivotal point for beginning this project. In this work, the viability of the defect modulation concept for sputtered undoped and Sn-doped In_2O_3 films using ALD - Al_2O_3 and sputtered SiO_{2-x} as dopant insulator will be tested. In addition, the versatility of the approach will be assessed by production of composite materials of nominally undoped TCO hosts embedded with dopant nanoparticles. The thesis is separated in two two parts based on the experimental strategies followed during this work.

Part I "Physical Approach" will focus on sputtered TCO thin films with coating of different dopant insulators in the top. *Chapter 5*, Sn-doped In_2O_3 sputtered in different condition used as TCO host and 5-cycles of ALD-Al_2O_3 used as a dopant. In *chapter 6*, undoped but dopable In_2O_3 sputtered films used as TCO host and different cycles of ALD-Al_2O_3 as dopant. While, in *chapter 7* viability of using different wide band gap material SiO_2 as potential dopant will be examined. For this purpose different $SiO_{2-\mathrm{x}}$ layers were sputtered from Si target on the top of In_2O_3 substrates. The results will be discussed with interfacial and electrical study.

Part II "Chemical Approach" will focus on testing defect modulation doping on nanocomposite materials prepared by ultrasonic spray deposition. Nominally undoped SnO_2 used as as TCO host and the sub-part is divided into three chapters based on type of dopnat used. In *chapter 8*, TiO_2 nanoparticles(NPs) used as a potential dopant and bid to embed them into SnO_2 host matrix. The case for two demixed composite films of SnO_2 (TCO host)/ Al_2O_3 (dopant) from $SnCl_4.5H_2O$/Al(acac)$_3$ precursors respectively, will be covered in *chapter 9*. Finally, *Chapter 10* discuss the approach followed to embed dopant Al_2O_3 NPs into SnO_2 host for realization of defect modulation doping. At the end, the key points in this thesis have been selected and addresses in conclusion, as well as future perspectives.

Chapter 3

Materials

3.1 Indium Oxide

As transparent conducting oxide (TCO), indium oxide is a semiconducting material. It is the most widely used TCO material, which is commonly used for transparent electrodes in optoelectronics, e.g., solar cells, display devices, light-emitting diodes, as well in gas sensing technology. Especially, tin-doped In_2O_3 exhibits a unique combination of optical and electrical transport properties by retaining high optical transparency in the visible range and low electrical resistivity.

In this section the fundamental properties of indium oxide, its crystal structure, electronic structure, defect chemistry and doping, which must considered to call In_2O_3 as TCO material, will be discussed.

3.1.1 Crystal structure

Indium oxide crystallizes in the cubic bixbyite crystal structure, which is also called C type rare earth sesquioxide and belongs to the space group Ia3, number 206 [99]. The bixbyite unit cell contains 16 formula units, which correspond to 80 atoms. The cubic lattice parameter is 10.117Å[100]. The 32 cations in the unit cell occupy two different sites, the Wyckoff positions 8*b* and 24*d* [30] referred as *b* and *d* positions in short.

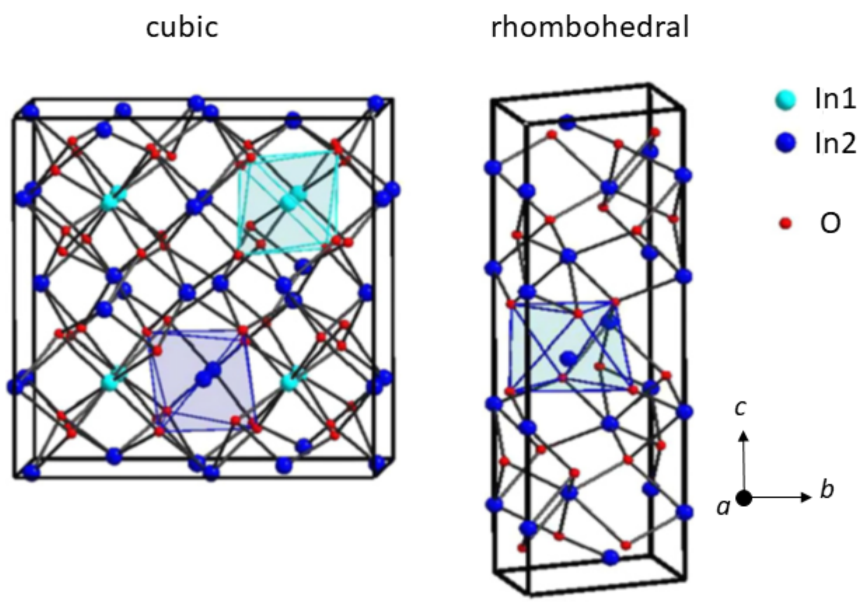

Figure 3.1: *Illustration of crystal structure of the stable cubic bixbyite (left) and metastable rhombohedral (right) polymorph of* In_2O_3. *Different coordinations of In are marked by different colors (Reprinted figures from [101], Copyright 2007 American Physical Society).*

Figure 3.1 (left) shows the bixbyite crystal structure of In_2O_3, in which cations are present in the center of distorted cubes. The six corners of the cube are occupied by oxygen anions and the remaining two corners are empty. The two empty corners located at 16c positions are the sites for interstitial oxygen ions and are important for the defect structures of ITO. In 8*b* cation position, the two oxygen interstitial positions are positioned along a body diagonal of the cube and the six oxygen anions are coordinated at symmetrical distance of 2.18 Å. For the 24*d* cations, the two oxygen interstitial sites are along a face diagonal of the cube and the six oxygen anions are coordinated with less symmetry along with three different distances (2.13, 2.19, and 2.23 Å).

Indium oxide can also adopt another metastable phase of rhombohedral corundum structure [102], with space group R3c and cell parameters a= 5.487 Å and c = 14.510 Å, see Fig. 3.1 (right). This is the high pressure polymorph of In_2O_3 [103, 104, 105], in which the cations are at the center of regular octahedra. The structural transition from bixbyite to corundum can be considered as a distorted ccp to hcp transition. Since the corundum structure of In_2O_3 is metastable at ambient conditons, it transforms irreversibly into the cubic bixbyite-type In_2O_3 upon heating at temperature from 700 to 900 °C [106].

In case of indium tin oxide, which is obtained by doping cubic In_2O_3 with tin, the dopant tin cations prefer to be located at the higher symmetry 8b sites [107]. When the concentration of tin increases, the first oxygen polyhedron around indium becomes more and more disordered and change its symmetry from cubic to a hexagonal [107].

3.1.2 Electronic structure

To consider In_2O_3 as a TCO candidate, it should have a transparency in the visible wavelength range, with the band structure having energy band gap (E_G) of at least 3 eV. At the same time the free charge carriers should be available to ensure electrical conductivity.

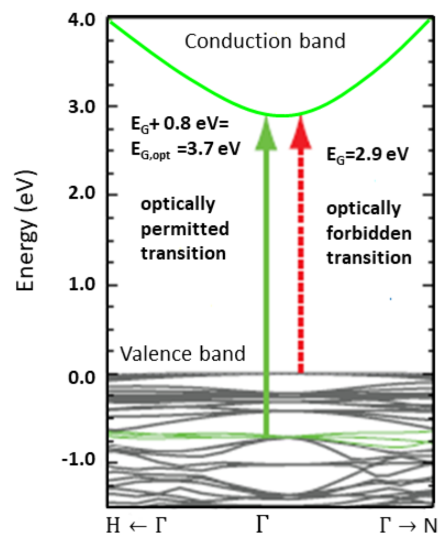

Figure 3.2: *Calculated band structure of In_2O_3 (Reprinted figure with permission from [108], Copyright 2008 by the American Physical Society). Optically forbidden fundamental interband transition (right, red arrow) causing only weak optical absorption and permitted energy transitions (left, green arrow) to lower lying valence band resulting in strong absorption are shown.*

Even though it has been widely used, the band gap of In_2O_3 remained controversial until $\sim$ 2008. The optical measurements of thin films showed band gaps of 3.75 eV [109] (erroneously, this value has been widely quoted as the fundamental band gap of In_2O_3). Recent X- ray photoelectron spectroscopy (XPS) experiments challenged the widely quoted band gap (based on optical absorption in thin films) of $\approx$ 3.7 eV and corrected its value to 2.7 - 2.9 eV [35, 110]. Angular-resolved photo-electron spectroscopy (ARPES), ultimately proved a band gap of $\approx$ 2.7 eV located at the Γ point of the Brillouin zone [111]. The better understanding of the band structure of In_2O_3

comes from density functional theory (DFT) calculations. Generally, the band gap of materials is underestimated by DFT calculation, as can be seen from Mryasov et al. [112] calculation; they reported the band gap of In_2O_3 as $\approx$ 1 eV and it is direct. There are some DFT calculations, which support the presence of indirect band gap at lower energy: A presumption of that In_2O_3 possibly could have an indirect band gap at a lower energy [109, 113] than the direct band gap was not demonstrated by DFT calculations. First Principle DFT calculations by Fuchs et al. [114] and Walsh et al. [108] showed that In_2O_3 has a direct band gap of $\approx$ 2.9 eV.

Optically permissible energy transition of In_2O_3 at 3.7 eV and that of optically forbidden energy transition at 2.9 eV are shown in Fig. 3.2. In the depicted figure, the top of the valence band is flat, indicating lower mobility of holes, while the conduction band is highly dispersed. For optically permissible transitions, electrons must be excited from energy bands about 0.8 eV below the maximum of the valence band at Γ. This explains why the observed band gap of these films is usually of the order of 3.75 eV, which means the optical band gap is 0.8 eV larger than fundamental electronic gap.

In summary, according to the current understanding there is a direct gap of 2.9 eV and also there is indirect band which is smaller than direct band gap.

3.1.3 Defect Structure

Indium oxide have unusual high conductivity due to high concentrations of free electrons. Regardless of higher conductivity, their are uncertainties on the fundamental questions of defect mechanism which leads to high conductivity. In the last few decades several theoretical and experimental works have been done to well understand the defect chemistry. De Wit et al. [115, 116, 117] and Weiher [118] indirectly deducts the defect structure of pure In_2O_3 from electrical measurements with the observation of *-1/6* dependence of carrier concentration log (n) as a function of partial pressure of oxygen (P_{O2}).

The two possible non-stoichiometric intrinsic and oxygen partial pressure control defect reactions, in which either oxygen vacancies $V_O^{\bullet\bullet}$ or indium interstitial $In_{In}^{\bullet\bullet\bullet}$ can be formulated, as demonstrated below [116, 117]:

$$2In_{In}^X + 3O_O^X \Longleftrightarrow 2In_{In}^X + 3V_O^{\bullet\bullet} + 6e' + \frac{3}{2}O_2 \tag{3.1}$$

$$2In_{In}^{X} + 3O_{O}^{X} \Longleftrightarrow 2In_{i}^{\bullet\bullet\bullet} + 6e' + \frac{3}{2}O_2 \tag{3.2}$$

The corresponding equilibrium constant for oxygen vacancies is obtained as:

$$K_{V_O^{\bullet\bullet}} = \frac{[In_{In}^{X}]^2[V_O^{\bullet\bullet}]^3[e']^6 PO_2^{\frac{3}{2}}}{[In_{In}^{X}]^2[O_O^{X}]^3} \approx [V_O^{\bullet\bullet}]^3[e']^6 PO_2^{\frac{3}{2}} \tag{3.3}$$

Charge neutrality condition: Where, [2V$_O^{\bullet\bullet}$]=[e']

$$K_{V_O^{\bullet\bullet}} = \frac{1}{2}[e']^9 PO_2^{\frac{3}{2}} \tag{3.4}$$

For indium interstitials the equilibrium constants are as follow:

$$K_{In_i^X} = \frac{[In_i^{\bullet\bullet\bullet}]^2[e']^6 PO_2^{\frac{3}{2}}}{[In_{In}^{X}]^2[O_O^{X}]^3} \approx [In_i^{\bullet\bullet\bullet}]^2[e']^6 PO_2^{\frac{3}{2}} \tag{3.5}$$

Charge neutrality condition: Where, 3[$In_i^{\bullet\bullet\bullet}$]= [$e$']

$$K_{In_i^X} = \frac{1}{3}[e']^8 PO_2^{\frac{3}{2}} \tag{3.6}$$

The correlation between charge carrier concentration (n = [e']) and oxygen partial pressure of P$_{O_2}$ is then

$$n \propto P_{O_2}^{\frac{-1}{6}}\ for\ [V_O^{\bullet\bullet}] \tag{3.7}$$

$$n \propto P_{O_2}^{\frac{-3}{16}}\ for\ [In_i^{\bullet\bullet}] \tag{3.8}$$

Therefore, the observed exponential slopes -1/6 =0.16667 and -3/16 =0.1875 indicated that undoped In_2O_3 exhibits n-type conductivity due to the presence of interstitial indium and/or oxygen vacancies under reducing conditions. The formation of oxygen vacancies is related to removal of lattice anions located at the e sites and which leads to introduction of non-stoichiometry in the sample to obtain In_2O_{3-x}, where x depends on the oxidizing conditions of the material, but it is usually less than 0.01 [119]. Due to the small population of oxygen vacancies that is predicted in pure indium oxide less than 0.33 % of the lattice oxygen site, no X-ray or neutron diffraction experiments have been able so far to confirm their existence [120].

Several theoretical models have been developed in the last few years to obtain information about dominant defect mechanism. In the reports there is an agrement that the enthalpy of defect formation for interstitial indium ($In_{In}^{\bullet\bullet\bullet}$) is significantly higher than that of oxygen vacancies ($V_O^{\bullet\bullet}$). However, the results are contradictory in terms of information on the defect formation energies and position of doping levels, especially with oxygen vacancies. Lany and Zunger [28] argued that the formation energy of oxygen vacancies are low and these authors demonstrated that these defects are the dominant defect causing n-type conductivity in pure indium oxide.

The carrier concentration of In_2O_3 can be limited by self-compensation, which trace back dependence of defect formation energies on Fermi level position. Detail defect calculations of In_2O_3 were performed by Ágoston et al. [27, 121, 122].

The formation energy of examined point defects depends on Fermi level positions as shown in Fig. 3.3. In the same plot, separate indium and oxygen-rich conditions are represented. In indium rich conditions, oxygen vacancy($V_O^{\bullet\bullet}$) is the defect with the lowest formation energy for all reasonable values of Fermi energy. While, under oxygen reach conditions mostly oxygen interstitials ($O_i^{\bullet\bullet}$) are expected to be present. Indium vacancies ($V_{In}^{\bullet\bullet\bullet}$) have lowest formation energies only for Fermi levels well above the band gap. Under indium rich conditions, oxygen interstitials ($O_i^{\bullet\bullet}$) become the compensating defect and for very high Fermi level ($V_{In}^{\bullet\bullet\bullet}$) will become the compensating defect. While, under oxidizing conditions oxygen vacancy ($V_O^{\bullet\bullet}$) become compensating defect.

3.1.4 Sn - Doping

Indium-tin oxide (ITO) is obtained by doping of In_2O_3 with tin. In the process Sn^{4+} ions are substitutionally built into the lattice on indium sites [124]. For low dopant concentrations, ideally all Sn atoms are ionized and located on In lattice site and each Sn atom considered as an available electron for conduction mechanism as shown in

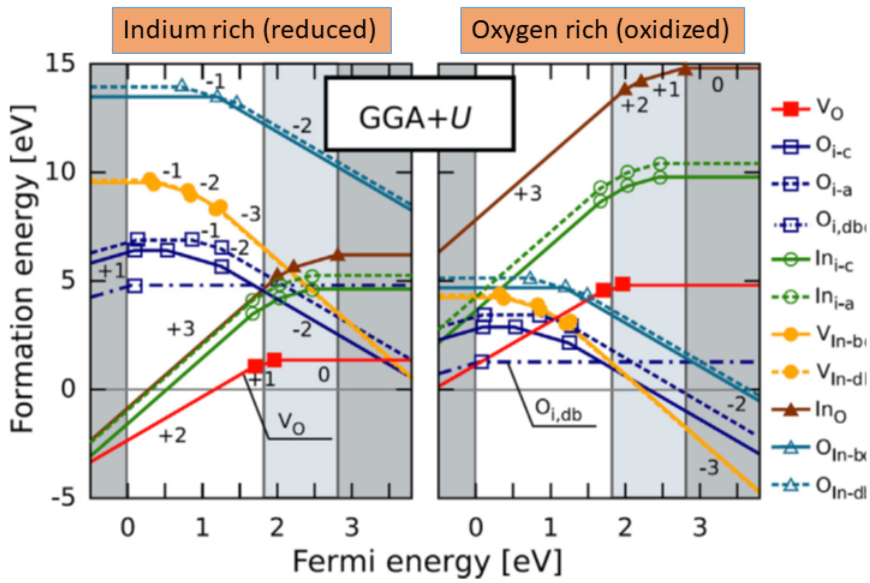

Figure 3.3: *Formation energies of intrinsic defect in In_2O_3 calculated using density function theory within the GGA + U approximation [123]. Valence and conduction bands are indicated by gray shaded areas. The valence band maximum position is at $E_F = 0\ eV$. The calculated energy gap is 1.81 eV, the deviation from experimental band gap is also indicated by light gray area. In the left is indium rich condition and in right oxygen rich condition as indicated at the top.*

Eq. 3.9. By tin doping, the charge carrier concentration can increase up to 10^{21} cm^{-3} and conductivity of more than 5000 S/cm.

$$In_{In}^{X} + Sn \Longleftrightarrow Sn_{In}^{\bullet} + e^{'} + In \tag{3.9}$$

Frank and Köstlin [125] pioneered the study of defect models for ITO. The model was developed based on measurements of carrier concentration and structural investigations of differently doped ITO layers after heating at different oxygen partial pressures. They proposed different clusters of defects to fit the observed electrical properties. For dopant concentrations of more than 1 cation % of Sn, they observed that the charge carrier concentration was no longer linear with the dopant concentration but is partially compensated. The compensation of Sn occurs by interaction of ionized tin ($\mathrm{Sn}_{In}^{\bullet}$) donors with interstitial oxygen($\mathrm{O}_i^{''}$) and forming neutral defect complexes $(2\mathrm{Sn}_{In}^{\bullet}\mathrm{O}_i^{''})_X$. The neutral defect equation is shown as follow:

$$\frac{1}{2}O_2 + 2Sn_{In}^{\bullet} + 2e^{'} \Longleftrightarrow (2Sn_{In}^{\bullet}O_i^{''})_X \tag{3.10}$$

According to the model, the two tin ions are not the nearest neighbors and if the partial pressure of oxygen is decreased, it is possible to reduce the cluster as shown in reversible neutral defect equation of Eq. 3.10:

The equilibrium constant of the reaction is given as:

$$K_{(2Sn^{\bullet}_{In}O''_i)^X} = \frac{[Sn^{\bullet}_{In}]^2[e']^2 P_{O_2}^{\frac{1}{2}}}{(2Sn^{\bullet}_{In}O''_i)^X} \tag{3.11}$$

Conservation of mass:

$$[Sn_{total}] = [Sn^{\bullet}_{In}] + 2[(2Sn^{\bullet}_{In}O''_i)^X] \tag{3.12}$$

Assuming that oxygen vacancies ($V_O^{\bullet\bullet}$) are minority species, the electron concentration is equal to concentration of ionized tin ($Sn^{\bullet}_{In}$)

Charge neutrality condition:

$$[e'] = [Sn^{\bullet}_{In}] + 2[V_O^{\bullet\bullet}] \approx [Sn^{\bullet}_{In}] \tag{3.13}$$

In the regime of high oxygen partial pressures and high Sn concentrations the contribution of oxygen vacancies to charge carries concentration can be neglected according to Eq. 3.13 and more tin neutral complex $[(2Sn^{\bullet}_{In}O''_i)^X] >> [Sn^{\bullet}_{In}]$ are then formed. By combining the equations of (3.11, 3.12, and 3.13) and under the conditions mentioned above, the dependency of carrier concentration on partial pressure of oxygen is shown as follow:

$$n \propto PO_2^{\frac{-1}{8}} \tag{3.14}$$

A calculated Brouwer diagram is used to illustrate the defect chemistry that depend on partial pressure of oxygen. Based on the defect equilibria postulated by Frank and Köstlin for ITO, Hwang et al. [126] derived at Brouwer diagram for ITO with 1 cation % Sn dopant at 500 °C, shown in Fig. 3.4. In the figure, charge carrier concentration versus oxygen partial pressure are shown and only dominant defects are considered in the calculation. The defect model presented in Fig. 3.4, indicates three prevailing defect regimes.

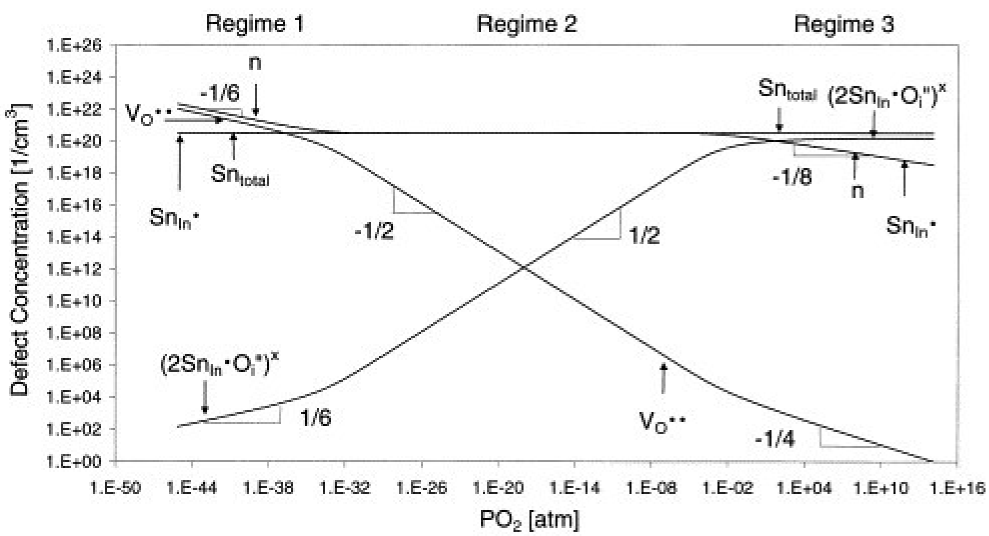

Figure 3.4: *Calculated Brouwer diagram, shows the defect concentration for different defects of ITO as a function of oxygen partial pressure. The values are calculated for ITO with 1 cat % Sn at* $500\,^\circ C$. *(Reprinted from [126], Copyright 2000, with permission from Elsevier).*

Regime I: It is a regime with an extremely low partial pressure of oxygen (pO_2). The electron concentration (n) is given by the concentration of oxygen vacancies ($V_O^{\bullet\bullet}$)

$$n = 2[V_O^{\bullet\bullet}] \propto pO_2^{\frac{-1}{6}}$$

Regime II : At intermediate oxygen pressures practically none of the tin dopants are compensated and n follows the same curve as the amount of tin at indium sites,(Sn $^{\bullet}_{In}$)·

$$n = [Sn_{In}^{\bullet}] \propto pO_2^0 = [Sn_{In}^{\bullet}]$$

Regime III: high (pO_2) and high Sn contents; as the oxygen partial pressure is increased, more $[(2Sn_{In}^{\bullet}O_i^{''})^X]$ clusters appears and at some point the amount of electrons are reduced by compensation of the tin donors. In this regime the amount of free electrons is proportional to $pO_2^{\frac{-1}{8}}$

$$n = [Sn_{In}^{\bullet}] \propto pO_2^{\frac{-1}{8}}$$

In summary, the doping in ITO stems from two sources; four - valent tin substituting three - valent indium in the crystal and the creation of doubly charged oxygen vacancies. Even below the solubility limit, tin is not fully activated in indium oxide lattice. This is due to an oxygen dependent relation between substitutional Sn and Sn in the form of neutral oxide complex that does not contribute for charge carriers.

3.2 Tin Oxide

Tin oxide (SnO_2) is an important and widely used wide band-gap semiconductor and is part of a family of binary transparent conducting oxides (TCO), such as ZnO, In_2O_3 and CdO. Since tin is less scarce and expensive compared to indium, SnO_2 is an attractive material in transparent conductor industry. It has been extensively used for semiconductor based gas sensors, microelectronics, solar cells, and low emissivity window coatings. The fundamental properties of SnO_2 will be discussed in this section.

3.2.1 Crystal structure

Tin oxide (SnO_2) occurs in nature as the mineral Cassiterite. At an ambient pressure it crystallizes in the rutile structure, that has tetragonal symmetry with ($P4_2/mnm$) space group [128]. A unit cell contains two tin and four oxygen atoms with lattice constants of a = 4.7374 Å and c = 3.1864 Å. Each oxygen octahedra is connected to two adjacent octahedra through edge sharing along the c-axis and connected to other octahedra through corner sharing. Many other metal dioxides like TiO_2, PbO_2, TaO_2, TeO_2, and RuO_2 share the same rutile crystal structure as that of SnO_2 [128, 129]. The bulk structure of this system and other high pressure polymorphs of SnO_2 are depicted in Fig. 3.5.

The discovery of rutile type structure from impact craters has led to several experimental investigations on the pressure and temperature stability relationship of these phases [130]. Thus, analysis on pressure- induced phase transitions in SnO_2 have been enabled by advancements on techniques of crystallography that are carried out in-situ under high-pressure conditions. Starting from the rutile-type structure, there could be six phase transitions that can be found under high-pressure conditions as shown in Fig. 3.5. The sequence of pressure driven transition of crystal structures goes like; rutile-type

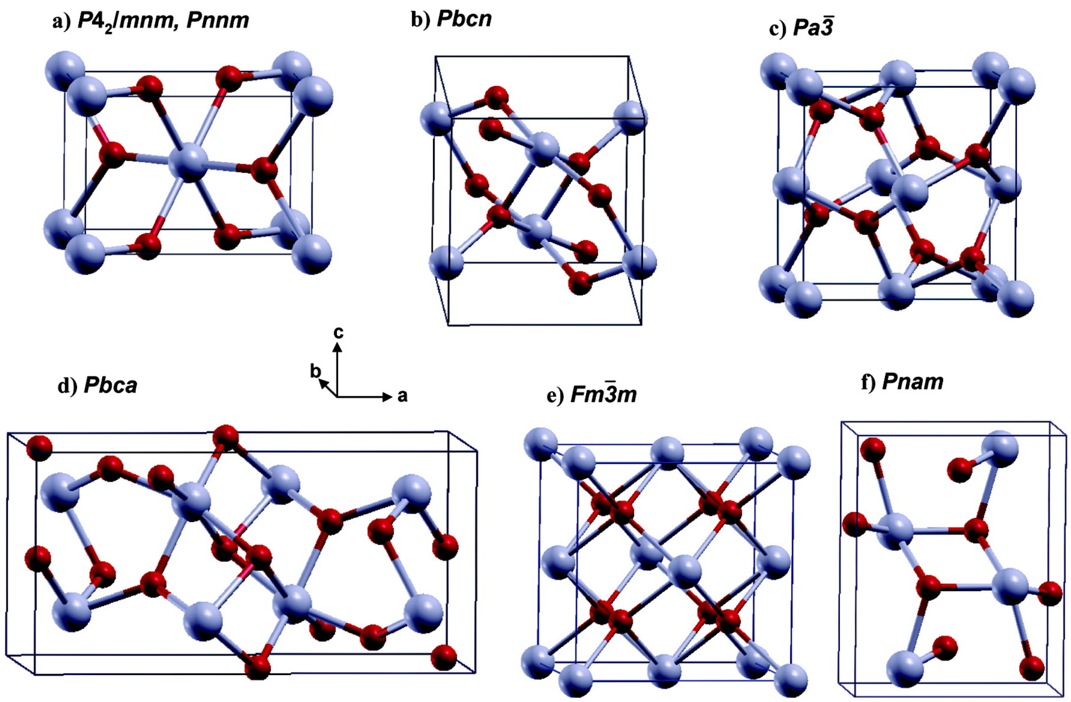

Figure 3.5: Bulk structures of the SnO_2 polymorphs (gray and red colors represent Sn and O atoms, respectively). (a) Rutile (P42/mnm) and $CaCl_2$ type (Pnnm), (b) α-PbO_2-type (Pbcn), (c) pyrite-type (Pa$\bar{3}$), (d) ZrO_2-type (Pbca), (e) fluorite-type (Fm$\bar{3}$m), and (f) cotunnite-type (Pnam) (Reprinted with permission from [127], Copyright 2007 American Chemical Society).

$\rightarrow$ $CaCl_2$-type $\rightarrow$ α-PbO_2-type $\rightarrow$ pyrite-type $\rightarrow$ ZrO_2-type orthorhombic phase I $\rightarrow$ fluorite-type cotunnite-type orthorhombic phase II. These phase transition sequences are consistent with an increase of the coordination number of tin ions, from 6 in the first three phases to 6 + 2 in the pyrite phase, 7 in the ZrO_2-type orthorhombic phase I, 8 in fluorite phase, and 9 in cotunnite orthorhombic phase II [127, 131].

3.2.2 Electronic Structure

Most of band structure studies of SnO_2, both theoretical and experimental are done only on rutile structure and the band gap is ≈ 3.57 eV [131, 132, 133, 134, 135].

The calculated band structure of pure tin oxide using HSE03+G_0W_0 approach is shown in Fig. 3.6. The conduction band exhibits significant free-electron-like character in the $\triangle$ direction ($\Gamma - X$ direction) or $\wedge$ direction ($\Gamma - M$ direction). The minimum

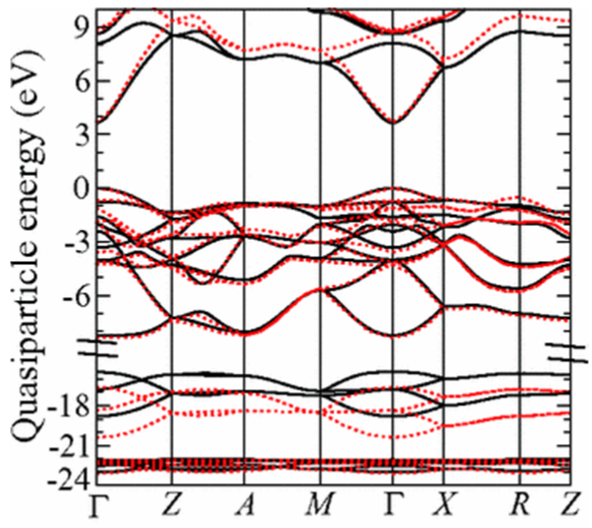

Figure 3.6: *Quasiparticle band structure of undoped rutile SnO_2 HSE03+G_0W_0 (dotted red lines) and LDA+U+△ (solid black lines). The valence-band maximum has been chosen as the common zero of energy (Reprinted with permission from [132], Copy right 2011 by the American Physical Society).*

gap is observed at the Γ point, which is direct gap of 3.65 eV, and the results do not indicate the presence of any lower indirect gap [132]. The optical transition across the fundamental gap are also dipole forbidden [132]. The band gap of tin oxide has also been investigated experimentally by a number of workers, and the value varies from 2.25 to 4.3 eV, which is possibly due to variations in the purity of samples. Fröhlich et al. [133] measured a band gap of 3.56 eV in two-photon absorption experiments, which is now widely accepted as the band gap of SnO_2. Nagata et al. reported a band gap of ~3.6 eV using XPS [1] experiments [134]. Barbarat et al.[136] determine the direct band gap from first principle calculation as 3.6 eV; While, Mishra et al. [137] calculated as 3.7 eV.

3.2.3 Defect Structure

Tin oxide is an n-type conductor, in which wide band-gap and high conductivity coexist. As in the case of other binary metal oxides (e.g. ZnO, In_2O_3), it was believed that oxygen vacancies ($V_O^{\bullet\bullet}$) are responsible for conduction electron-carrier generation in

[1]X-ray photoelectron spectroscopy

SnO_2 [138, 139]. Recent study by Ágoston et al. [122] reveal that, in contrast to In_2O_3, the vacancy of oxygen ($V_O^{\bullet\bullet}$) is a deeper defect in SnO_2. It can therefore not cause high electron concentration at room temperature.

Samson and Fonstand [140] studied the defect chemistry of SnO_2 by measuring the conductivity of stannic oxide crystals as a function of oxygen partial pressure at elevated temperatures. They observed approximately a $-1/6$ slope in a log (conductivity) as a function of log (pO_2), similar to the behavior observed for pure In_2O_3. Thus, they concluded that the major defect species in SnO_2 consists of oxygen vacancies ($V_O^{\bullet\bullet}$). The non-stoichiometric decomposition and its corresponding equilibrium constant can be written as follows:

The equilibrium constant of the reaction is given by:

$$Sn_{Sn}^{x} + 2O_O^{x} \Longleftrightarrow Sn_{Sn}^{x} + 2V_O^{\bullet\bullet} + 4e^{'} + O_2 \tag{3.15}$$

$$K_{vac} = [V_O^{\bullet\bullet}]^2 n^4 PO_2 \tag{3.16}$$

The electroneutrality condition is n= [$2V_O^{\bullet\bullet}$] results in:

$$n \propto PO_2^{\frac{-1}{6}} \tag{3.17}$$

Therefore, the observed exponential slope $-1/6 = 0.16667$ indicated SnO_{2-x} have n- type conductivity due to presence of oxygen vacancies. The material can then be expressed as SnO_{2-x}, where x depends on the oxidation state. As in the case of In_2O_3, the hypothesized population of oxygen vacancies responsible for n-type conductivity is relatively small, so it is not possible to detect it using XRD, neutron diffraction or XRF techniques.

3.3 Aluminium oxide

3.3.1 Crystal structure

Polycrystalline Al_2O_3 is a widely used ceramic material. It can exist in different crystalline phases depending on its purity, mechanical, and other physical properties. Alpha phase, α - Al_2O_3, is the thermodynamically stable phase (corundum form) and it is stable at high temperature up to its melting temperature of 2015 °C .

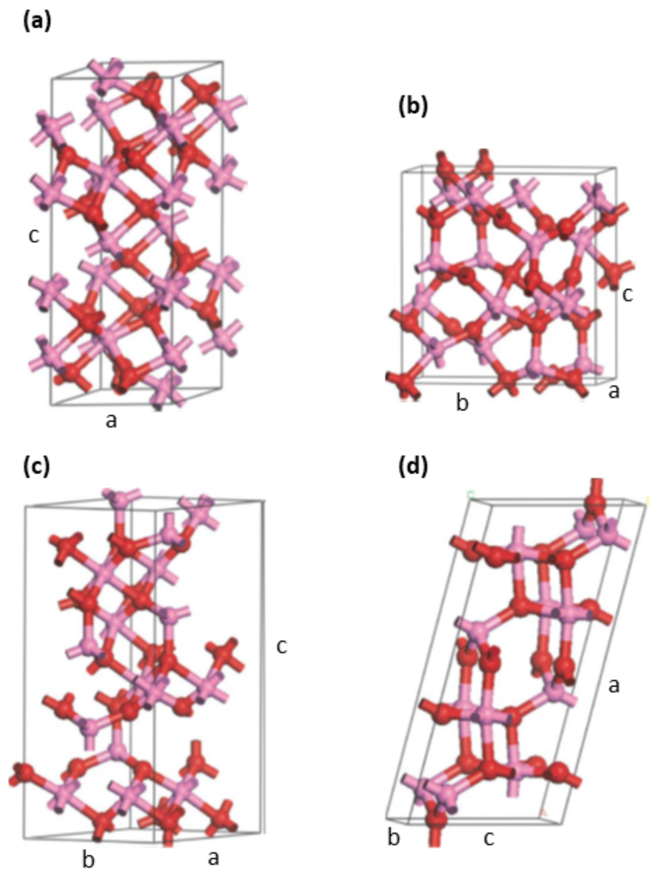

Figure 3.7: *Different polymorphs of Al_2O_3: (a), α-Al_2O_3 (hexagonal) (b), κ-Al_2O_3 (orthorhombic) (c), γ-Al_2O_3 (triclinic), and (d), θ-Al_2O_3 (monoclinic). The light and dark (red and purple in color) spheres indicate oxygen and aluminum atoms, respectively (Reprinted with permission from [141], Copy right 2007 by the American Physical Society).*

Al_2O_3 have also other metastable polymorphs than the stable α- phase. These metastable polymorphs can be divided into two broad catagories: a face-centered cubic (fcc) or hexagonal close-packed (hcp) arrangement of oxygen anions. These different polymorphs are the result from different distribution of cations within each subgroup [142]. The polymorphs based on fcc packing of oxygen include γ, η (cubic), θ (monoclinic), and δ (tetragonal or orthorhombic). Polymorphs based on hcp packing are represented by α (tetragonal), κ (orthorhombic), and χ (hexagonal) phases. The crystal structure of some of the polymorphs (α, κ, γ, and θ) are depicted in Fig. 3.7.

The α-phase has hexagonal close packed (hcp) crystalline structure [143, 144] as shown in Fig. 3.7. It has a trigonal symmetry with a rhombohedral Bravais lattice centering (space group R-3c, (No. 167) and has 10 atoms in the unit cell. The structure of α-alumina can be considered as hcp sublattice of oxygen anions, with 2/3 of the octahedral interstices filled with aluminum cations in an ordered array. The oxygen anions in the α-phase occupy 18c Wyckoff positions (in the hexagonal description) with coordinates x, 0, 1/4 (x= 0.306), where the aluminium cations are located at 12c positions with coordinates $0, 0, z (z = 0.347)$. Both the x and z values deviate from the ideal value of 1/3, which would correspond to the atomic positions in the ideal close-packed structure. The aluminum cations are displaced along the [0001] direction toward the neighboring empty octahedral sites, resulting in a "puckering" of the cation layers. The cation displacements are accompanied by distortion of the oxygen sublattice. The hexagonal parameters for α-phase are c = 1.297 nm and a = 0.475 nm with c/a = 2.73, and corresponds to six oxygen layers along the c-axis of the unit cell [145].

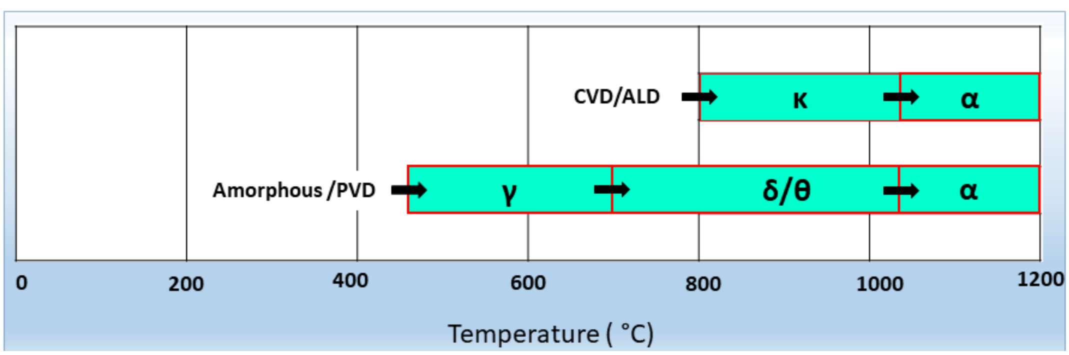

Figure 3.8: *Crystalline temperature of different metastable phases of alumina (i.e. γ, κ, θ, and $\delta-$ phases) and their transformation temperature to stable $\alpha-$phase is shown [146].*

Since the α-phase is the only stable phase at higher temperature, other metastable polymorphs can transform to the α-phase upon heating: The transformation temperature of these different metastable polymorphs is summarized in Fig. 3.8. The $\gamma-$ phase is unstable and it can transform to another unstable phase of θ-Al_2O_3 at a temperature of $\approx$ 700 - 800 °C. While, this θ-phase can further transform to the stable α-phase at a temperature of about 1050 °C.

3.3.2 Electronic Structure

The calculated band structure of α - Al_2 O_3 is shown in Fig. 3.9. It has a minimum at the Γ - point with a very large band gap. The DFT calculations were generated by Liu et al. [147] using hybrid functions, which reproduce the band gap better and is in good agreement with experimentally determined value of E_g= 8.8 eV by French [148], who obtained the gap by a measurement of UV reflection in vacuum.

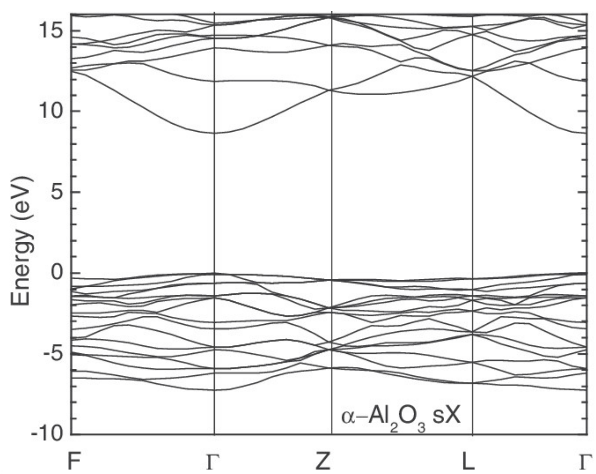

Figure 3.9: *DFT calculation of the band structure of* $\alpha - Al_2O_3$ (Reprinted from [147], with the permission of AIP Publishing).

Lee et al. [141] also investigated the variations in electronic structures of different alumina polymorphs using DFT calculation. For the study, stable α - Al_2O_3 and metastable polymorphs of κ, θ, and δ - Al_2O_3 were considered. The computed energy gaps of these polymorphs are α - phase = 6.72 eV, κ- phase = 5.49 eV, θ - phase = 5.04 eV , and κ - phase = 4.4 eV. The calcuated band gaps of all Al_2O_3 polymorphs are smaller than the experimental values; this is due to LDA approximation. However, relative reduction in band gap of polymorphs shown correctly as $\alpha > \kappa > \theta > \delta$, which is associated with the decrease of the mean coordination number of Al ions [149].

Filatova et al. [150] reported the band gaps of 7.0 $\pm$ 0.1 for amorphous and 7.6 $\pm$ 0.1 eV for γ-Al_2O_3, which were determined using high-resolution near -edge X-ray absorption fine structure and soft X-ray photoelectron spectroscopy. Similarly, other research groups also reported experimental band gap value for α-Al_2O_3 is 8.8 eV [148], for γ-Al_2O_3 7.0-8.7 eV [151] and for amorphous phase from 5.1 to 7.1 eV [151]. It is noteworthy that the band gap value depends on the method of synthesis. For instance, the method of atomic layer deposition (ALD) allows to synthesize the amorphous films with band gap of 6.2 eV [152], while the amorphous-Al_2O_3 film, grown by spray pyrolysis has a band gap 5.6 eV [153].

3.3.3 Defect Structure

The defect structure of κ - Al_2O_3 was calculated by Weber et al. [96] using DFT calculations to examine the formation energy of native defects as a function of Fermi level E_F in order to assess their behavior under different doping or band bending conditions. The defect structure of Al_2O_3 in reducing (Al-rich) and oxidizing (O-rich) conditions are shown in Fig. 3.10.

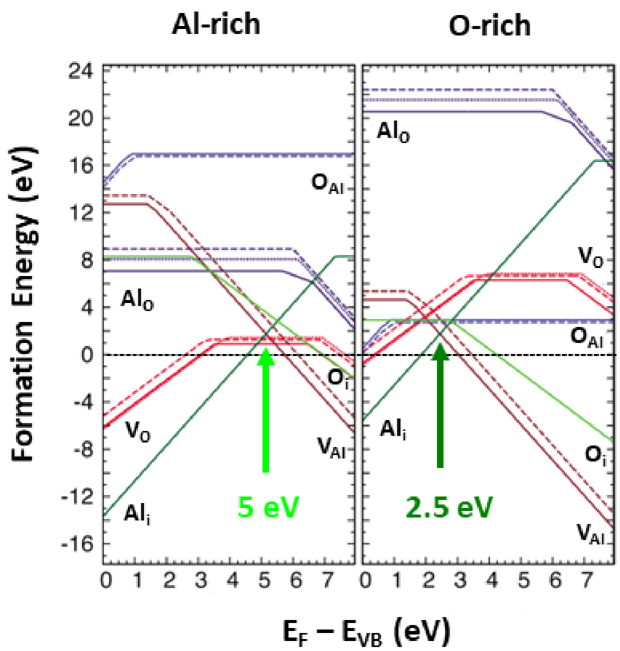

Figure 3.10: *Formation energy for native point defects in $\kappa - Al_2O_3$ as a function of Fermi level (Reprinted from [96], with the permission of AIP Publishing). For each defect, only the lowest energy charge state is shown for a given value of Fermi level. $Al - rich$ limit is shown in the left side of the plot, while $O - rich$ limit is shown in the right side. The Fermi level position of charge neutrality level for the cation Frenkel pair (Al_i^{+3} - V_{Al}^{-3}) in both Al-rich and O-rich conditions are indicated by green arrows (light green for Al-rich condition with $E_F \approx 5$ eV and dark green for O-rich condition with $E_F \approx 2.5$ eV).*

Aluminum interstitial Al_i^{+3} and Al vacancy V_{Al}^{-3} are the lowest energy charged defects over the entire range of Fermi level in both Al-rich and O-rich limits. The other native defects have significantly higher formation energies and thus will occur in much lower concentrations. Highly negative values for formation energies of point defects indicate major instabilities of the material. In addition, extreme Al-rich or O-rich conditions are not achievable.

Charge neutral combination of cation Frenkel pair (Al_i^{+3} - V_{Al}^{-3}) defects are also shown in Fig. 3.10 and are indicated by green arrows for both Al- rich and O-rich conditions. In Al-rich condition, the charge neutrality is obtained for $E_{\mathrm{F}} \approx 5$ eV, while for O-rich condition it is found in much lower Fermi level position of $\approx$ 2.5 eV. Thus, Fermi level position is limited to 2.5-5 eV, although under realistic production conditions neither of the two stability limits might be reached.

Chapter 4

Preparation and Characterizations

4.1 Film production

In this chapter, the fundamentals of experimental techniques employed during the present study for synthesis and characterizations of thin films will be outlined. Undoped - In_2O_3, Sn-doped In_2O_3, and SiO_{2-X} were prepared using magnetron sputtering technique at TU Darmstadt, Germany. In addition, ultrathin coating of Al_2O_3 layers were also prepared by atomic layer deposition technique in the same laboratory. While, SnO_2 based composite films of SnO_2 - Al_2O_{3-x} from $Al(acac)_3$[1] dopant precursor, SnO_2 - Al_2O_{3-x} from Al_2O_{3-x} NPs [2] precursors and SnO_2 - TiO_2 NPs were synthesized using a chemical approach by ultrasonic spray pyrolysis technique, at LMGP, Grenoble INP, France.

The prepared thin films were then characterized (structural, optical, and electrical) by implementing different characterization techniques. The working principles and features

[1] Aluminium acetylacetonate

[2] Nanoparticles

of these instruments used for characterizations will also be discussed.

4.1.1 Radio Frequency Magnetron Sputtering

Sputter deposition is a thin film deposition technique belonging to the group of physical vapor deposition (PVD) methods. Sputtering is a phenomenon, which consists of bombarding a solid target surface by energetic accelerating ions, in which surface atoms of the target scatter back and deposit on the surface of substrate and grow a layer by physisorption. It is used for the deposition of thin films. Most of the information on this section are adapted from books of Wasa [154] and Ohring [155].

There are several sputtering systems proposed for the purpose of thin film deposition, which includes ion beam sputtering, DC diode, RF diode, and magnetron sputtering. Among them, direct current (DC) sputtering is the simplest model, in which direct current is used to create the necessary electric field. High sputtering rates at relatively low power are achieved due to the acceleration of the argon ions towards the cathode surface. However, only conductive materials can be sputtered by this technique. If insulating materials are sputtered using DC sputtering, surface charge will build up on the target surface and terminate the glow discharge. Therefore, in order to deposit semiconducting and insulator materials, it is necessary to use alternating current (AC) at higher frequency. In this way the positive charges accumulated during one half-cycle can be neutralized by electron bombardment during the next cycle and it's possible to sustain the glow discharge. Generally the frequencies used for these alternating voltages are typically in the radiofrequency (RF) range (1 kHz–103 MHz), with a most common value of 13.56 MHz[3] in order to avoid interfering with other RF devices.

Magnetron sputtering has emerged to complement other vacuum coating techniques by offering advantages including high deposition rate, ease of sputtering any metal, alloy, or compound, high purity of films, extreme high adhesion of films, and excellent coverage of steps and small features. In a magnetron sputtering system, the magnetic field increases the plasma density, which leads to increase of the current density at the cathode target and an increase in sputter rate. Historically, magnetron sputtering was first proposed by Penning [156] in 1936. A prototype of the planar magnetron was invented by Wasa [157] in 1967, and a practical planar magnetron system was proposed by Chapin [158] in 1974.

In magnetron sputtering, the movement of emitted particles from the target is controlled

[3] 13.56 MHz has been reserved for plasma applications by the US Federal Communication Commission

by a magnetic field. Magnetrons are commonly classified as balanced or unbalanced based on their magnetic field configuration. In balanced magnetrons, the magnetic field lines are well confined around the target racetrack with low release of plasma to the substrate. In this configuration, energetic electrons escape from the primary magnetic trap near the cathode surface and go to anode. In unbalanced magnetrons, the excess magnetic field lines trap the escaping energetic electrons and electrons make ionizing collisions. The secondary plasma is generated near the substrate and boost the sputtering yield. Conventional magnetrons are usually of the balanced type.

Compared to other thin film deposition techniques, radio-frequency magnetron sputtering (RF-MS) is widely used in industry for its capability of fast and reliable deposition on large areas. Due to the gases low working pressure, the sputtered particles traverse the discharge space without collisions, which results in a high deposition rate. The schematic representation of balanced planar magnetron cathode is shown in Fig. 4.1.

As can be seen in Fig. 4.1, the target material is placed in the cathode position; permanent magnets are also embedded along with the cathode target for having strong resultant magnetic field for enhancing cathode sputtering. In this study, 2″ pellets of ceramic targets of In_2O_3 and ITO, and Si were used. Since the targets are exposed to ion bombardment during operation, the magnetron were cooled by water cooling system.

Magnetron Sputtered Samples

All the samples produced at TU Darmstadt (undoped - In_2O_3, Sn-doped In_2O_3, and SiO_2) were prepared in custom made RF - magnetron sputtering chambers, which are part of the Integrated system for MATerial research (DAISY-MAT) and are connected via UHV transfer system as shown in Fig. 4.2.

The schematic representation of sputtering chamber with top down sputtering source is shown in Fig. 4.3. The base pressure of the chamber was in the upper 10^{-8} mbar range. The pressure was monitored by capacitive gauge for $> 10^{-4}$ mbar and cold-cathode ionization gauge for lower values. The sputtering gas was introduced to the system through the mass flow controllers at the top of the source. While, reactive gases can be introduced together with sputtered gas or separately in the side of the chamber. Process gases of 100% argon, argon with up to 10% O_2 from inlet of 90% Ar + 10 % O_2, and argon and oxygen from two different gas sources were used.

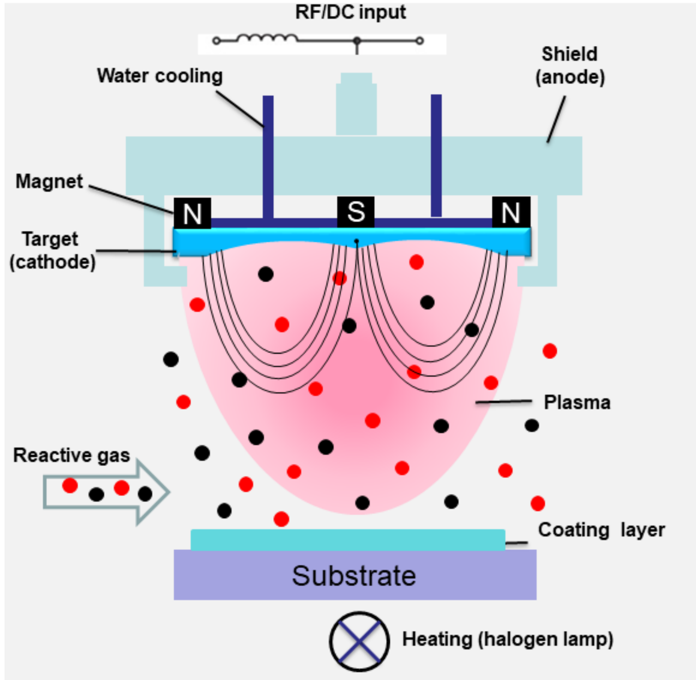

Figure 4.1: *Schematic diagram of magnetron cathode with magnetic field lines and the cycloidal trajectory at the target surface.*

Experimental procedure

Substrates of 10 x 10 x 0.5 mm quartz glass and 10 x 10 x 1 mm corning glasses were used. The substrates were cleaned in ultrasonic bath prior to usage. The cleaned substrates then had an electrical contact in the edge. For the deposition of electrical contacts, the commercial sputter coater Q300T D of the company Quorum was used. Thin platinum films were deposited as a contact by direct current sputtering up to a thickness of 100 nm. Shadow masks were used for patterning the edge contacts.

Substrates with edge contacts were then placed on the sample holder with 10 x 10 mm mask. A Halogen light bulb was installed below the substrate holder was used for sample heating. After introduction of the sample into the chamber, it was brought to height of deposition. Pre-sputtering was then done to clean the target surface. The deposition parameters of sputtered films are summarized in Tab. 4.1.

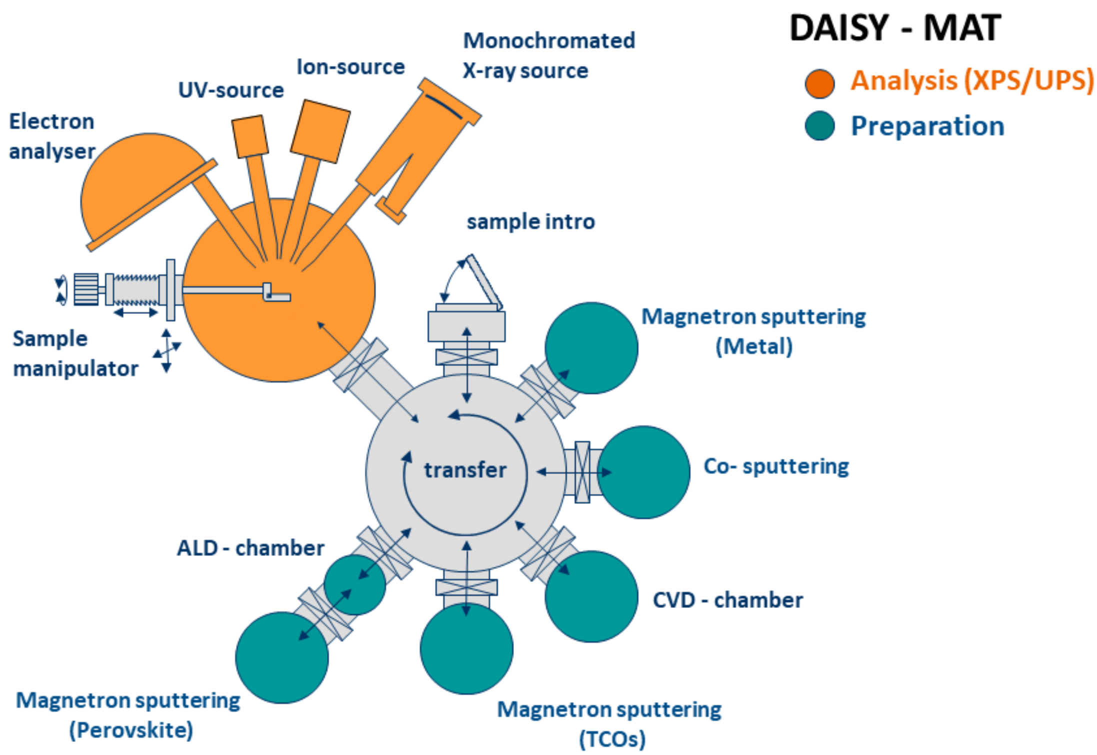

Figure 4.2: *Schematic diagram of the DArmstadt Integrated System for MATerial Research (DAISY-MAT). The deposition chambers and the photoelectron spectrometer (Physical Electronics PHI 5700) are connected via UHV transfer system; so both sample preparation and analysis are performed without breaking the vacuum [12].*

4.1.2 Atomic Layer Deposition (ALD)

Basics of Atomic Layer Deposition

ALD is a thin film deposition method, which belongs to the methods of chemical vapor deposition (CVD). In CVD, inorganic thin films are produced by chemical reactions of partly organic volatile reagents (precursors) with other gases. The reaction usually takes place between an organometallic precursor and an oxidizing reagent. ALD is different from conventional CVD due to self-limiting nature of the reaction, which contribute to the layer formation [160].

In ALD, the chemical reaction does not occur simultaneously between two or several gaseous species, but alternately between only one gaseous species and the solid surface.

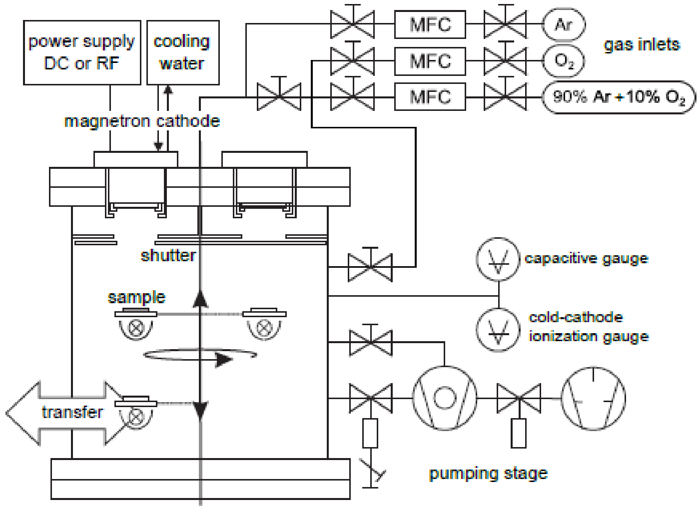

Figure 4.3: *Schematic diagram of sputtering chamber at DAISY-MAT [13, 159].*

Once this reaction is over, the layer growth stops automatically. By alternating self terminating reactions, it is possible for layer by layer growth and this is called Atomic layer deposition (ALD). The sum of two alternating steps is called ALD cycle [160].

The temperature window available for the ALD reaction is schematically illustrated in Fig. 4.4. Initially, at lower temperature, it is limited by the activation enthalpy required for the two surface reactions and yield either condensation of precursors on substrate surface or incomplete reaction. While, the upper limit is decided by thermal decomposition temperatures of the precursors and the sublimation or melting temperatures of the deposited materials (the latter are usually much higher than the former). This temperature window makes it possible to use and combine the precursor materials. Sufficient vapor pressure at moderate temperatures and the self-limiting nature of precursor-surface reactions are further criteria for suitability of precursor material to be used in ALD process [160].

The amount of material adsorbed in gas–solid reactions can depend on time in various ways, as schematically illustrated in Fig. 4.5. Both reversible and irreversible adsorption can be saturated in nature. For the adsorption to be self-terminating as in case of ALD, the adsorbed material should not be desorbed from the surface during the purge or evacuation. Thus, the monolayer of precursor saturated in an irreversible (irreversible in the time scale of the experiment) way by forming strong chemical bonds (chemisorption) as shown in Fig. 4.5(a). In case of reversible saturation only physisorption (weak bonds like van der waals) formed and once the precursor flux is stopped, surface species will be

Table 4.1: Deposition parameters for RF-magnetron sputtered films

Material	ITO	In_2O_3	SiO_{2-x}
Target	10 % Sn-doped In_2O_3	In_2O_3	Si
Target purity %	99.9	99.9	99.9
Supplier	-	-	-
Temperature (°C)	RT - 400	200 - 600	RT - 400
RF power (W)	25	25	40
Pressure ($\times 10^{-3}$ mbar)	5	5	5
Process gas (O_2 %)	0 - 0.5	0 - 0.5	0 - 5
Target - substrate (cm)	10	10	7
Deposition rate (nm/min)	4 - 4.6	4 - 4.6	2
Layer thickness (nm)	8 - 200	20 - 200	1 - 10

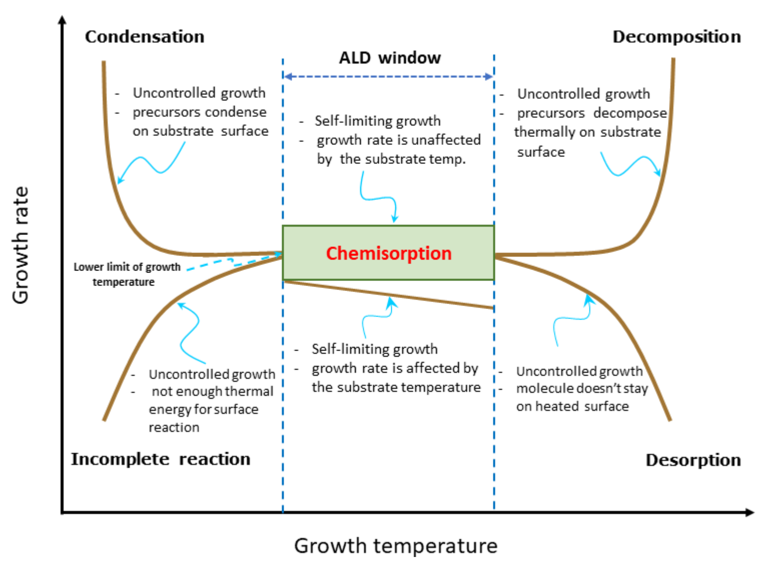

Figure 4.4: *Schematic representation of the ALD process with temperature (Redrawn from [161]).*

desorbed, see Fig. 4.5(b). This kind of saturation does not contribute to ALD growth. Irreversible adsorption could also be continuous and non-saturating. In this case the process is in CVD regime. The more precursors are pulsed, the thicker film will be deposited continuously, as can be seen in Fig. 4.5(c) [160].

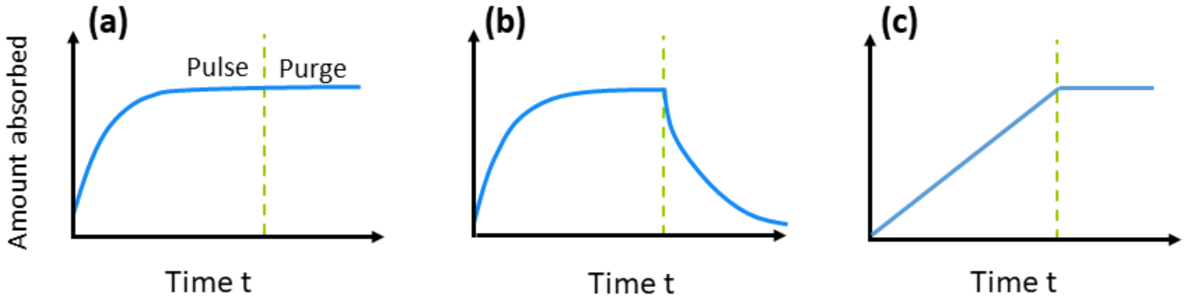

Figure 4.5: *Schematic representation of amount of materials adsorbed with time. (a) Irreversible saturating adsorption-ALD mode, (b) reversible saturating adsorption, (c) Irreversible non saturating adsorption- CVD mode. The vertical green dashed line marks the end of the reactant supply and the beginning of a purge or evacuation (Redrawn from [160]) .*

The practical implementation of ALD process is described below on the basis of the data used in this work and synthesis of Al_2O_3 (which is well known from many years of research as a model system) from Trimethylaluminium (TMA) precursor and water. Figure 4.6, describes an ALD cycle of the TMA/water process. The substrate whose surface is to be coated, must be first brought to the required processing temperature under vacuum or inert gas conditions. In addition, the substrate surface should ideally be prepared for the TMA/water cycle before deposition as TMA requires hydroxyl groups for reaction in the first step.

In the first step of an ALD cycle, a controlled quantity of TMA precursor is introduced into the deposition chamber, which then reacts with the surface of substrate. This primarily reaction is schematically represented in Fig. 4.6 (A1) and is given by Eq. 4.1. In the equation the surface of substrate is represented by (‖) symbol:

$$\| - O - H + Al(CH_3)_3 \rightarrow \| - O - Al(CH_3)_2 + CH_4 \uparrow \tag{4.1}$$

This is referred as the 1st half reaction of the ALD cycle. In the reaction, the amount of adsorbed TMA molecules depends on the available hydroxyl groups on the surface. Once the adsorption is irreversibly saturated, no further reaction will occur and is called self - terminated reaction. This is followed by the second step of ALD cycle, in which the remaining precursor material as well as methane by-product are removed from the chamber by purging with an inert gas (usually nitrogen) [162] or evacuation of the chamber [38], as shown in Fig. 4.6 (A2).

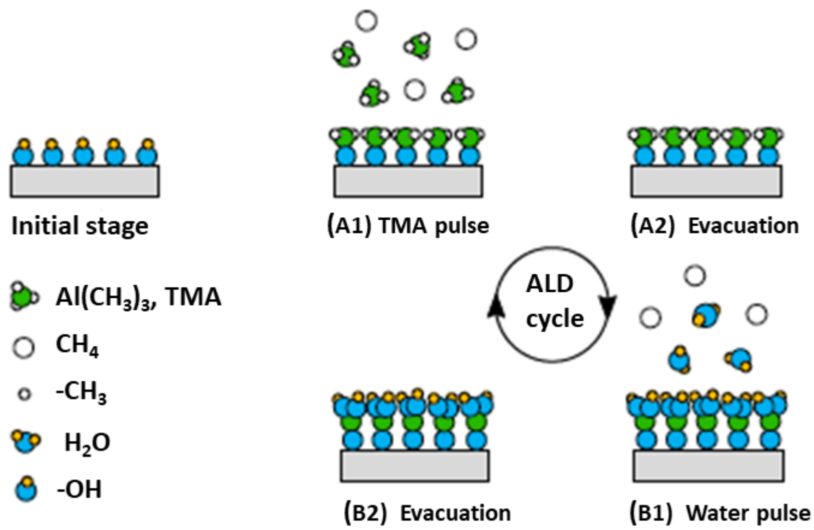

Figure 4.6: *Schematic representation of the ALD process of Al_2O_3 production. (A) represents the first half-cycle and (B) the second half cycle. The legends in the figure describes the chemical species involved. The figure is taken from a PhD thesis of J. Deuermeier, from Technische Universität Darmstadt, Germany [13].*

In the third step, the second precursor (water) is introduced into the processing chamber, which will then react with oxidizable species on the surface to form hydroxyl groups. The reaction is represented by Eq. 4.2 and shown in step (B1) of Fig. 4.6 (2nd half reaction):

$$\| - O - Al(CH_3)_2 + H_2O \rightarrow \| - O - Al(OH)_2 + 2CH_4 \uparrow \tag{4.2}$$

Educts and excess gaseous precursors are removed in the fourth step by purging the chamber again, see Fig. 4.6 (B2). After completion of these four steps, ideally the full ALD cycle will result in a monolayer of Al_2O_3. However, the availability of surface sites is limited by steric hindrance of the involved molecules. Consequently, during one ALD cycle typically less than one monolayer is deposited [160]. The pulse and purging times should be calibrated carefully. During pulsing, there should be a complete surface coverage without too much excess precursors, while during pumping, all excess precursors should be removed before the subsequent pulse [38].

The degree of substrate coverage achieved after a complete ALD cycle can be obtained using the Growth Per Cycle (GPC). This means the incremental layer thickness added after an ALD cycle. The average GPC of ALD Al_2O_3 using TMA/water precursors is ≈

0.08 - 0.1 nm/ cycle [160, 162, 163].

Experimental conditions of ALD on this work

In this work, ultra thin layers of ALD Al_2O_3 were used as a dopant material for TCOs and were coated on undoped and Sn-doped In_2O_3 substrates. The ALD chamber used in this work is part of the DAISY-MAT system at TU Darmstadt as shown in Fig. 4.2. Since the ALD chamber is part of integrated UHV[4] system, the excess precursors were evacuated via a turbo molecular pump. The base pressure of the deposition chamber was kept at 10 $^{-8}$ mbar. The substrates were heated to 200 ^{o}C by radiative heating prior to deposition.

Table 4.2: Overview on deposition condition of ALD - Al_2O_3

TMA pulse time(ms)	80
Evacuation (min)	5
H_2O pulse time (ms)	150
Base pressure (mbar)	10^{-8}
Pressure between pulses (mbar)	10^{-6}
Substrate temperature (°C)	200
ALD cycle	1 - 20

The amount of TMA and water was controlled by setting the pulse length of two individual ALD 3 series valves by Swagelok. Electronic grade TMA was purchased from SAFC Hitech. To achieve highest purities of the water precursor, Millipore water was evaporated and condensed several times in alternate arms of a double arm glass vessel. A hot air gun and dry ice was used for this procedure. The pulse length for TMA was set to 80 ms and for water to 150 ms, the evacuation time between pulses was set to 5 min, which reduced the pressure down to 10^{-6} mbar [38]. The deposition parameters used during deposition are summarized in Tab. 4.2.

[4]ultra high vacuum

4.1.3 Ultrasonic Spray Pyrolysis

4.1.3.1 Deposition Principle of Aerosol Pyrolysis

Spray pyrolysis is a chemical deposition process, which is based on thermal decomposition of the initial material. The decomposed material will oxidize on the substrate and form the desired layer material. To ensure the deposition of the desired material, pyrolysis should take place only at the surface of substrate and it is also necessary to keep the temperature of the initial material below the decomposition temperature. This can be achieved by dissolving the initial material (precursor) in a solvent through precursor solution, atomizing it into fine droplets (aerosol) and carrying these droplets to the hot substrate with a carrier gas.

The pyrolysis process can take place in different ways depending on various factors including: substrate temperature, temperature gradient at substrate surface, nature of solution species, and size and speed of the aerosol droplets. The influences of substrate temperature and initial droplet size on deposition processes is schematically represented in Fig. 4.7. For clarity, four potential paths of the droplet towards the substrate labeled as A - D are represented with the influence of change in substrate temperature Fig. 4.7 (a), and change in starting droplet size Fig. 4.7 (b).

Figure 4.7 (a) shows the influence of change in substrate temperature on transformation of precursor solution droplet to its final state, while keeping the initial droplet size the same [164].

- At low temperature in process A, the droplet splashes on the substrate in liquid form. The solvent vaporizes and leaves a dry precursor precipitate in which decomposition under solid form occurs.
- At moderate temperature in process B, the solvent evaporates before the droplet reaches the substrate surface and the precursor reaches the substrate surface in solid form and the precipitate impinges upon the surface.
- For an average temperature in process C, the solvent vaporizes as the droplet approaches the substrate, then the solid melts and vaporizes (or sublimes) and the vapor diffuses to the substrate to undergoes a heterogeneous reaction there. In this case, we are in chemical deposition mode in vapor phase and is labeled as a true chemical vapor depostion (CVD) process.

- At high temperature in process D, the metallic compound vaporizes before it reaches the substrate surface and the chemical reaction takes place in the vapor phase and form particles.

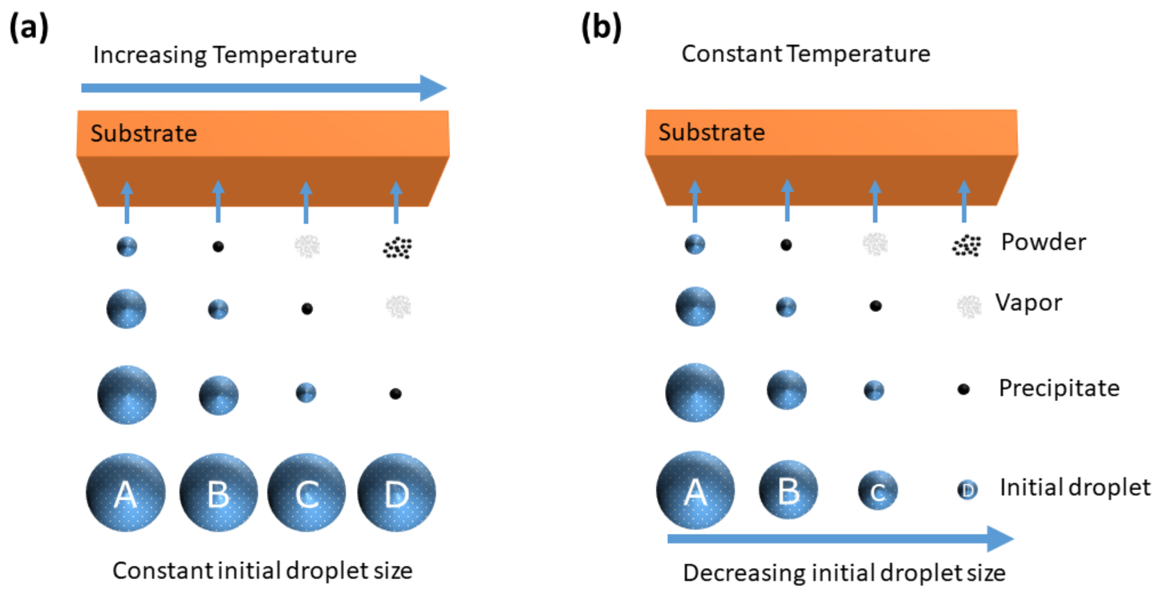

Figure 4.7: *Schematic representation of modifications on spray pyrolysis droplets as they are transported from the atomizing nozzle to the substrate. There are four potential paths which the droplet can take as it moves towards the substrate and are labeled as A-D in the figure. The two main factors,(a) the influence of change in substrate temperature and (b) change in initial droplet size are represented. Inspired by the works of Vigui and Spitz [164] and Siefert [165]*

.

The ideal transportation of droplets to the substrate would be when the droplet approaches the substrate surface just as the solvent and then vaporized entirely. However, since in the generation of droplets obtaining a uniform droplet size is strenuous and the thermal behavior of the droplets depends on their masses, different deposition processes are possible depending on the size of the droplets. Figure 4.7 (b) show various deposition processes that occur above the required decomposition temperature depending on the droplet size [165] .

- In a process A, the droplet is so large that the heat absorbed from the surroundings will not be sufficient to vaporize entirely the solvent on the way to the substrate. The droplet hits the substrate, where the solvent is entirely vaporized leaving a dry precipitate; the temperature has now increased above the boiling point of the solvent and decomposition occurs. Because the vaporization of the solvent locally removes a lot of heat, the substrate temperature decreases at this point. This affects adversely the kinetics of the reaction, i.e. equalization of the particle concentrations does not occur. The surface becomes rough and the specular transmission decreases markedly.

- Process B is distinguishable in that the droplet dries up entirely before reaching the substrate and then hits the surface in a statistical distribution. Some of the particles evaporate and condense in the gaps between the particles where the surface reaction starts. In this process also, the vaporization of the particle locally removes a lot of heat, but not to the same extent as in process A.

- Process C includes the classical chemical vapour deposition process leading to the optimum film properties. In this process, the solvent is entirely vaporized short of the substrate. Before the particle reaches the substrate, there is sufficient time for it to warm up to ambient temperature. The particle then melts and vaporizes and undergoes a heterogeneous reaction. This reaction is divided into the following steps: (i) diffusion of the reactant molecules to the surface; (ii) adsorption of one or several reactant molecules at the surface; (iii) surface diffusion, chemical reaction, incorporation into the lattice; (iv) desorption of product molecules from the surface; (v) diffusion of product molecules away from the surface into the vapor space.

- The behavior of the smallest droplets is shown in process D. In this process the solvent is already completely vaporized far away from the substrate. The particle melts and vaporizes and a chemical reaction will occur in the vapor phase. This is a homogeneous reaction, because all reactant molecules and product molecules are in the vapor phase. The molecules condense as microcrystallites, which form a powdery precipitate on the substrate. This powder disturbs the formation of the layer and leads to a reduction in transmission. In addition the homogeneous reaction diminishes the deposition efficiency of this procedure.

As highlighted in the description above, the size of the droplets affects the morphology and adhesion of the layer on the substrate surface. Therefore, care must be taken during aerosol generation. Aerosols are generated from the precursor solution and commonly three main techniques are used to generate them: pneumatic spraying, electronic spraying and ultrasonic spraying (used during this work).

Pneumatic-based spraying systems use a stream of pressurized air or gas (e.g. nitrogen or argon) that breaks up the precursor solution into droplets at the narrow nozzle jet [166]. In electrostatic spraying, electrostatic field is used to atomize the precursor solution and the chemicals will undergo a controlled chemical reaction and deposited on a substrate [167].

Ultrasonic spraying gives full control over the most important process parameters, such as ultrasonic amplitude, precursor solution, precursor composition/viscosity, flow rate, and deposition temperature [168]. Moreover, this method allows to obtain a well defined and monodispersed drop diameter, which ensures an identical deposition mechanism for each droplet.

The working principle of ultrasonic spraying is described as follows: ultrasound is generated from mutifrequency disc shaped piezoceramic transducers in the precursor solution. These produce oscillations of the free surface of the solution, called capillary waves. These capillary waves have chessboard like pattern as shown in Fig. 4.8 (a). This phenomenon occurs when the vibration amplitude A exceeds a threshold value. On further increase of the amplitude, breakup of a drop from precursor solution follows and droplets are hurled from the crests of capillary waves [169]. In this way production of liquid fogs of droplets is possible.

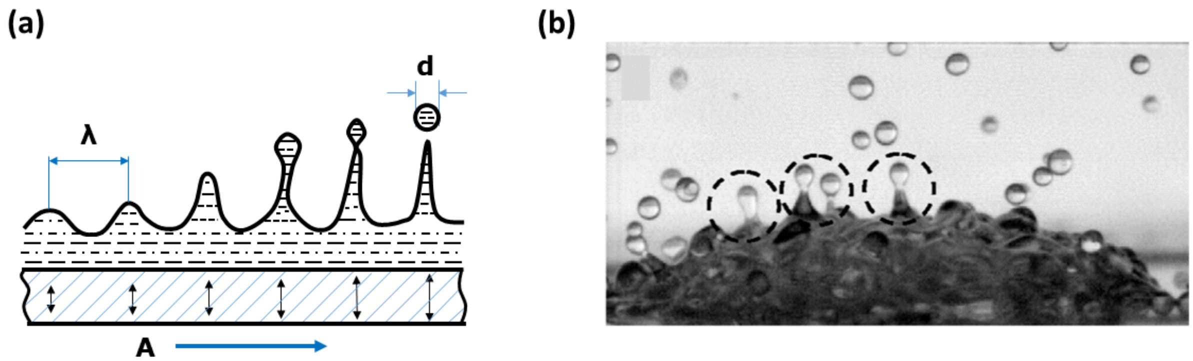

Figure 4.8: *Illustration for atomizations of precursor solution. (a) Schematic illustration of capillary wave atomization, where d is the diameter of the drop, λ the wavelength of the capillary wave, and A the amplitude of the vibrational frequency (Redrawn from [168]); (b) Photograph of capillary wave instability during droplet formation (Reprinted from[170], with the permission fo AIP Publishing).*

The droplet size is governed by ultrasonic parameters of transducers, including: transducer frequency, transducer amplitude, physical properties of precursor solution, and by the viscosity of the solution. The average droplet diameter d is then proportional to the wavelength λ of the capillarity wave. This relation has been experimentally established by Lang [171] and is represented by the following equation:

$$d = 0.34\lambda = 0.34\left(\frac{8\pi T}{\rho f^2}\right)^{\frac{1}{3}} \tag{4.3}$$

Where, λ is the wavelength of capillary wave, T is the liquid surface tension, ρ is the liquid density, and f is the excitation sound frequency in cps. Spraying takes place above a vibration threshold amplitude of the piezoelectric transducer, and this depends on f, λ and the viscosity of the solution.

4.1.3.2 Precursor Solution Preparation

Different SnO_2 based composite films were produced using ultrasonic spray pyrolysis technique. Demixed composite films of SnO_2 - Al_2O_3, composite films of SnO_2-Al_2O_3 using nanoparticles of Al_2O_3, and composite films of SnO_2-TiO_2, using nanoparticles of TiO_2 as a dopant were produced using this technique. For demixed composite films, precursor solutions were prepared by dissolving $SnCl_4.5(H_2O)$ and $Al(acac)_3$ precursors in methanol by keeping the total concentration at 0.1 M. For the other two types of composite films, $Al(acac)_3$ was replaced by the dispersion of Al_2O_3 and TiO_2 nanoparticles. The deposition conditions followed during production of these films are summarized in Tab. 4.3.

Table 4.3: Deposition parameters used for synthesis of SnO_2 based composite films

Material	[1]SnO_2-Al_2O_3	[2]SnO_2-Al_2O_3NPs	[3]SnO_2- TiO_2 NPs
Precursor(TCO)	$SnCl_4.5(H_2O)$	$SnCl_4.5(H_2O)$	$SnCl_4.5(H_2O)$
Precursor(dopant)	$Al(acac)_3$	Al_2O_3-NPs	TiO_2-NPs
Suppliers (TCO)	sigma-aldrich	sigma-aldrich	sigma-aldrich
Suppliers (dopant)	sigma-aldrich	US Res. Nanomat.	Lotus Synthesis
Solvent	Methanol	Methanol	Ethanol
Conc. of solution ($mol.l^{-1}$)	0.1	0.1	0.1
molar ratio (Al_2O_3/SnO_2) in soln.	0 - 0.15	0 - 1	0 - 0.1
Substrate temperature (°C)	420	420	420

[1] SnO_2-Al_2O_3 $\longrightarrow$ demixed composite films using $Al(acac)_3$ dopant

[2] SnO_2-Al_2O_3 $\longrightarrow$ composite films using Al_2O_3 NPs as dopant

[3] SnO_2- TiO_2NPs $\longrightarrow$ composite films using TiO_2 NPs as dopant

4.1.3.3 Description of the Reactor

The schematic representation of ultrasonic spray pyrolysis reactor used during this study is shown in Fig. 4.9. It consists two distinct parts: the spray zone and the pyrolysis

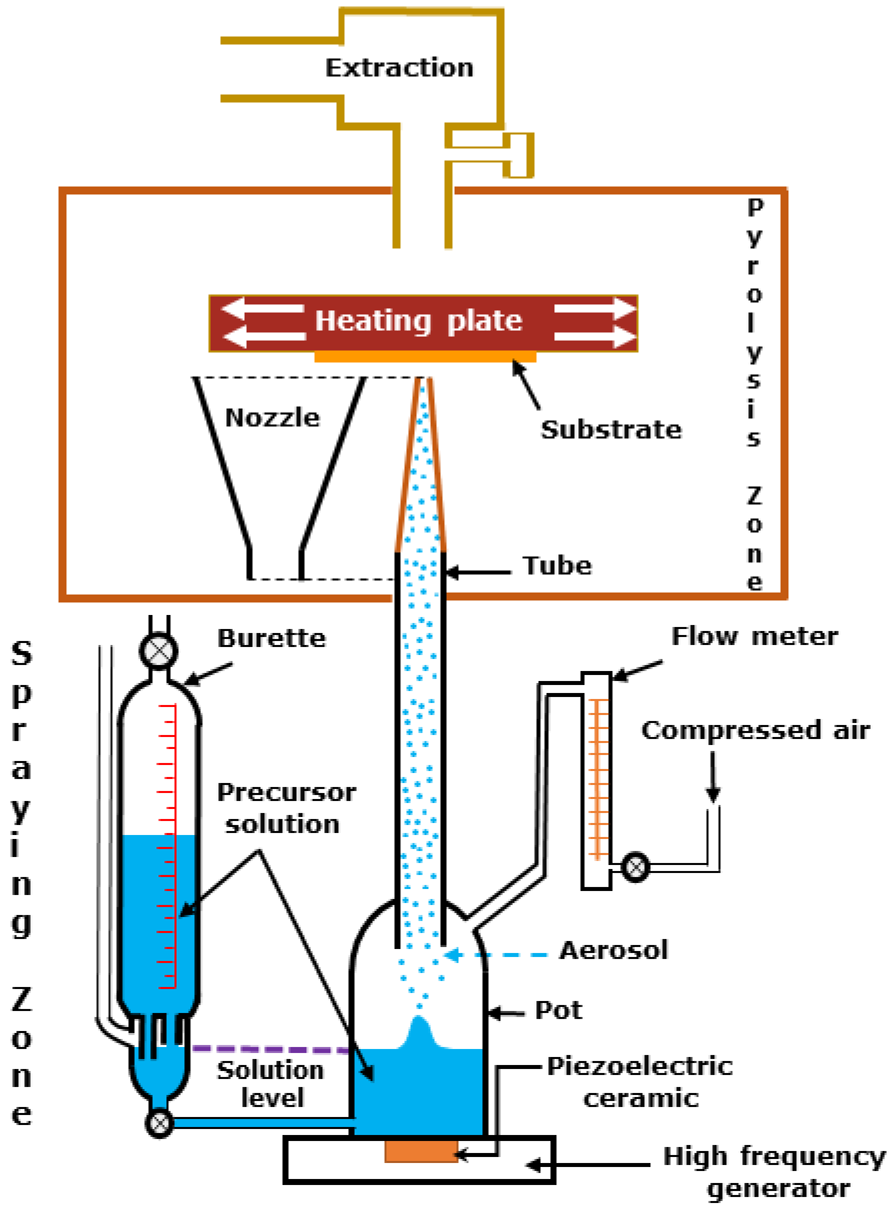

Figure 4.9: *Schematic representation of ultrasonic spray pyrolysis setup in LMGP, Grenoble INP.*

zone. Primarily, in the spray zone, precursor solutions are filled into the burrete and transferred into spray pot upto halfway. When the pot is half filled the leveling between two solutions will occur, as can be seen in the schematic diagram. The pot has two inlets, one at the bottom to fill the solution and one at the top to inject a carrier gas, which transport the aerosol from spray to pyrolysis area. A piezoelectric ceramic is placed at the bottom of the pot. It was used as a transducer to generate ultrasound in solution. A high frequency generator allows to adjust both the voltage and frequency of signal sent to the ceramic. To obtain an optimal spraying, the frequency of the excitation must be tuned to the resonance frequency of the solution. To ensure a controlled spray rate, the solution level must be kept constant. To satisfy this condition, a continuous transfer of solution from the burette to the pot was needed.

Once the aerosol was produced, it was transported to the pyrolysis zone through a glass tube. In the top end of the tube, a rectangular nozzle (4.7 x 125 mm^2) was installed, which was located 15 mm under a hot plate, in which sample substrates were mounted. The hot plate was movable with speed of 2.14 cm/s and covering the distance of 15 cm, which allow to produce homogeneous films throughout the substrate surface. The resistive heating allows to heat the substrate up to 520 °C.

4.2 Materials Characterizations

4.2.1 Structural characterizations

4.2.1.1 Photoelectron Spectroscopy (PES)

Photoelectron spectroscopy (PES) is one of the most widely used techniques for surface analysis. It is based on the photoelectric effect, where the incident light of sufficient energy causes the emission of electrons from the sample. This photoelectric effect was first observed by Hertz [173] in 1887 and later described by Einstein [174] in 1905. The spectroscopic use of the photoelectric effect was first developed by Kai Siegbahn and his team in Sweden [175]. PES can supply information on the elemental composition, electronic structure, and oxidation states of samples with high precision. Most of the informations in this section are adapted from the following books [172, 176, 177, 178].

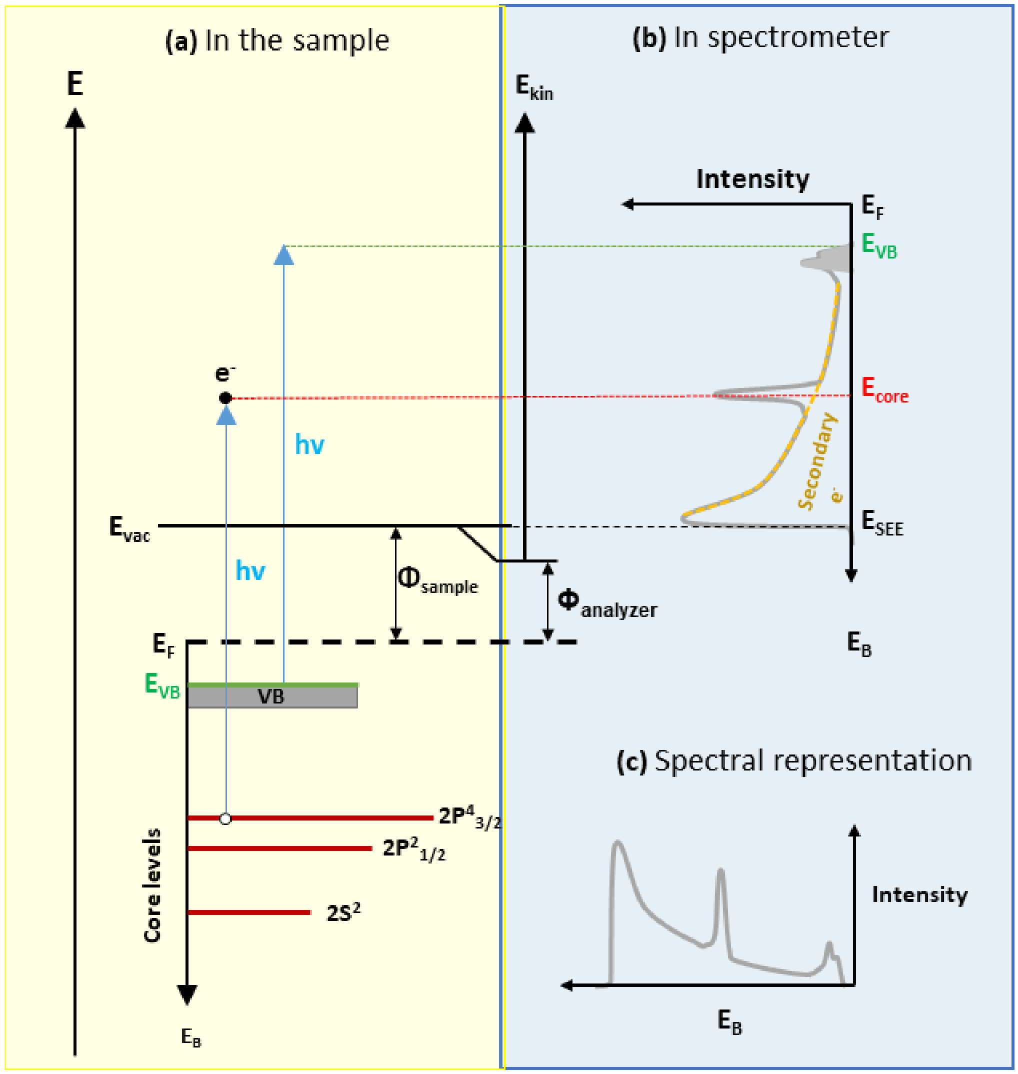

Figure 4.10: *Schematic illustration of photoelectric effect and the resulting PES spectrum. An electron from occupied energy level can be excited to an energy state exceeding the vacuum level, so leaving the sample. (a) Energy levels in a material give rise to a kinetic energy of photoelectrons, (b) Translation of the kinetic energy into an intensity with respect to the electron binding energy and (c) Typical data representation from PES. Core level measurements and the secondary electron edges are shown in the same representation, though such datas are typically obtained using different excitation energies (XPS and UPS , respectively). Inspired by [172].*

Operating Principle

The operating principle of photoelectron spectroscopy (PES) is explained with supporting schematic representaion of Fig. 4.10. The measuring principle of PES is based on the external photoelectric effect, according to which photoelectrons can be released from a sample by illumination with electromagnetic radiation. Depending on the energy range of monochromatic light $E_\lambda = hv = hc/\lambda$, PES is often known as X-ray photoelectron spectroscopy (XPS) for $E_\lambda \approx 10^3$ eV or as ultraviolet photoelectron spectroscopy (UPS) for $E_\lambda \approx 10^1$ eV. The relationship between the kinetic energy (E_{kin}) of the photoelectrons and the irradiated energy (hv) was first described by Einstein [174] as shown in Eq. 4.4.

$$E_{kin} = hv - E_B - \Phi_{sample} \tag{4.4}$$

The kinetic energy of the photoelectrons is modified by the potential difference between the analyzer and the sample. A contact potential ($\Phi_{sample} - \Phi_{analyzer}$) exists between the sample surface and analyzer once they are connected electrically. Thus, the kinetic energy of the photoelectrons when entering the analyzer is :

$$\begin{aligned} E_{kin} &= hv - E_B - \Phi_{sample} + (\Phi_{sample} - \Phi_{analyzer}) \qquad (4.5) \\ &= hv - E_B - \Phi_{analyzer} \end{aligned}$$

Since the energy is measured inside the analyzer, see Fig. 4.10(b) the binding energy is related to $\Phi_{analyzer}$ not Φ_{sample} according to Eq. 4.5.

The electrons from a core level with a sharp emission line associated to characteristic binding energy is shown as a red line, see Fig. 4.10(b). The electron intensity continuously increased towards higher binding energy (lower kinetic energy) due to the emission of secondary electrons, that is inelastically scattered electrons. They are represented in dashed yellow line in Fig. 4.10 (b) and their contribution to the total intensity is referred to as the background of photoelectron spectrum. At the point $E_{kin}= \Phi_{analyzer} - \Phi_{sample}$, the photoelectrons will not have sufficient kinetic energy to leave the sample surface. Thus, the intensity drops sharply at binding energy E_{SEE}, known as secondary electron edge. The work function of the sample (Φ_{sample}) can be determined from E_{SEE} according to the Eq. 4.6

$$\Phi_{sample} = hv - E_{SEE} \tag{4.6}$$

The inelastic mean free path of the electrons in solids is very small down to atomic level, as can be seen in Fig. 4.11. Only those electrons that originate within a few nanometers below the sample surface can escape from the sample surface and be detected by analyzer; that is why XPS is highly surface sensitive measurement. In addition,

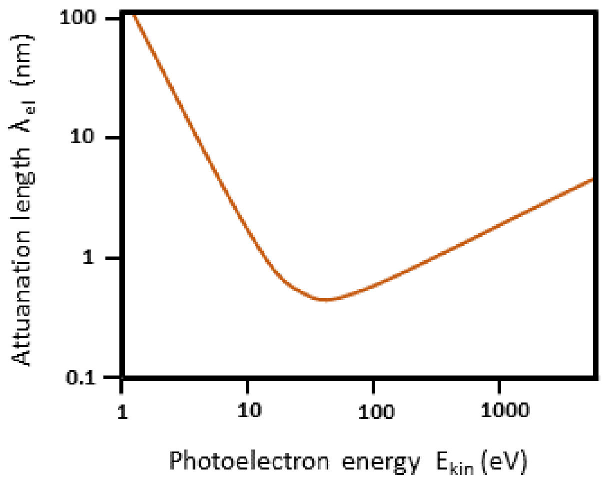

Figure 4.11: *Schematic illustration of Inelastic mean free path dependence on the photoelectron kinetic energy (Redrawn from [179]).*

XPS measurements should be performed in ultrahigh vacuum system to minimize the scattering of electrons and to keep the surfaces clean.

Experimental Conditions During This Work

XPS measurements have been carried out with a Physical Electronics PHI 5700 multi-technique surface analysis unit, using monochromatic Al Kα radiation with an energy of 1486.7 eV, an emission angle of 45° and a pass energy of 5.85 eV, resulting in an overall energy resolution of better than 0.4 eV. X-ray gun and detector have an angle of 90°; the geometry is an important information, e.g. for the use of atomic sensitivity factors for quantitative analysis of the surface composition. Binding energies are reported with respect to the Fermi energy, which was calibrated by measuring a metallic silver sample after cleaning typically for 5 - 10 min with an argon sputter gun. This standard sample is stored in vacuum at 10^{-9} mbar.

The surface analysis unit is the part of the cluster tool in DArmstadt Integrated SYstem for MATerial research (DAISY-MAT) [12] as shown in Fig. 4.2. DAISY-MAT provides a central distribution chamber, which connects the Physical Electronics PHI 5700 multi-technique surface analysis unit to the sample preparation chambers. The base pressure of the distribution chamber was 10^{-9} mbar, which allows for rapid transfer of samples between preparation and analysis chambers without breaking UHV conditions.

In-situ XPS measurements allow to study the electronic structure of films without any contamination by air.

The analysis system offers different measurement modes. These will shortly be explained in the following

- **Survey mode**: it provides a fast scan over a broad range of binding energies. It allows a qualitative overview of the elemental composition of the sample surface. As example, Fig. 4.12 shows a survey measurement of ITO coated with Al_2O_3 with all core level assigned. The region around 75 eV in the insert shows the Al2p core level. In addition, the survey measurements also helps to identify contamination of the sample.

- **High-resolution (HRES)**: it offers a detailed scan with a high resolution of any region wanted. The results can be used to determine binding energies and the area below the emissions from one measurement. It can be used for a quantitative determination of the surface composition and chemical bonding.

- **Utility mode (UTIL)**: it offers a fast scan over dedicated regions with a higher sensitivity of trace elements than the HRES mode due to a higher pass energy. On the other hand, it does not have such a good energy resolution. The customary settings for these different measurement modes of analysis system are summarized in Tab. 4.4.

Table 4.4: Settings for different measurement modes of analysis system

Modes	**Range**	**pass energy**	**eV/step**	**time/step**
Survey mode	-1 eV to 1400 eV	187.75 eV	0.8 eV	100 ms
High-resolution(HRES)	variable	5.85 eV	0.05 eV	100 ms
Utility mode (UTIL)	variable	57.7 eV	0.25	50 ms

In addition, UPS measurements of the valence band region have been carried out using the same chamber and same detector. For this measurement, a bias of -4 V was applied to the sample. The bias is used to accelerate low kinetic energy electrons (as low as $E_{kin} = 0$ eV at the surface) into the detector. Additionally, the sample is tilted in order to have an angle of 90° towards the detector, which is important to have homogeneous electric field distribution.

The measurement is usually performed with HeI-radiation (hv =21.22 eV) from a helium-discharge lamp. HeII-radiation at a higher photon energy (hv =40.8 eV) would be available as well. It can offer a different insight into the electronic structure of oxide materials due to different cross-sections of the elements. The detector settings for an UPS measurements are the following:

- Mode: Survey or HRES
- Range: variable, usually -2 eV to 21 eV (after bias subtraction)
- pass energy: 57.7 eV
- eV/step: 0.25 eV
- time/step: 50 ms

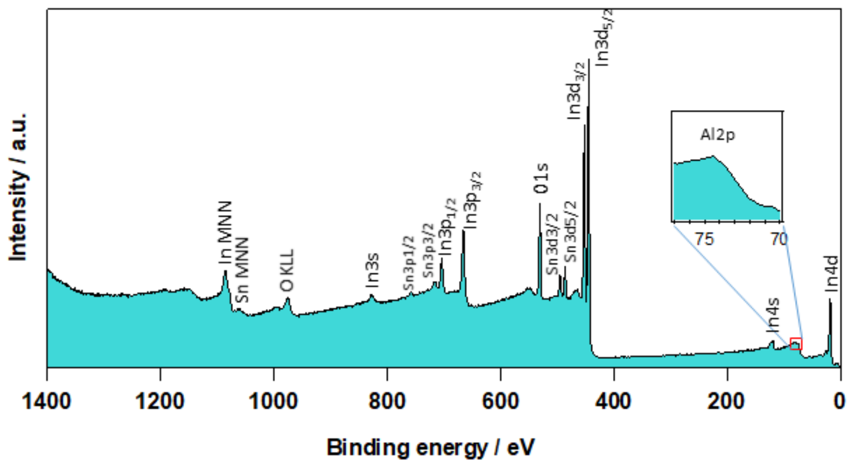

Figure 4.12: *Example for survey measurement of ITO coated with ultrathin ALD-Al_2O_3, all observable core level emissions are labeled. In addition, magnified spectra of Al2p peak is also shown in the insert.*

.

4.2.1.2 X-ray Diffraction and GIXRD

X-ray diffraction (XRD) is a versatile technique that provides information about the crystal structure of materials [180]. All crystalline materials have one thing in common: their components (atoms, ions or molecules) are arranged in a regular manner. This is a necessary requirement for XRD measurements as diffraction can only occur, if X-rays are scattered by a periodic array of particles with long-range order. X-rays are photons with energy $\sim$ 125 eV – 125 keV (wavelength $\lambda \sim 0.01$ – 10 nm). They were first discovered by W. Röntgen in 1895, who was awarded the first Nobel prize in physics (1901) for this achievement [181].

XRD is sensitive to crystalline phases down to 0.1 - 1 % by weight [180]. Conventional XRD instruments use monochromatic X-ray radiation from Cu, Cr, Mo or Ag sources. Cu, in particular with K -α line (which is the specific electronic transition in Cu used to generate a wavelength 0.15418 nm, energy 8.05 KeV), is the mostly used radiation in laboratories [182]. Cr is normally used for applications involving Fe and steel materials, and Mo and Ag are used for applications where deeper X-ray penetration is required. During XRD analysis, typical probed volume in a sample depends on the X-ray penetration depth, which is a function of X-ray energy, sample material and angle of incidence of the primary X-ray beam relative to the surface. When Cu radiation is used, the penetration depth in most of the materials would be up to several tens of microns [180].

The information on the working principles of XRD measurements is adopted from books of Guinier [181] and Mauro [180]. The incident beam arrives at an angle θ with respect to the surface of the sample, it interacts with the electrons and scattered out. These scattered X-ray photons are collected in the detector without any energy loss and phase change in specific condition known as Bragg condition. The detector is positioned at an angle 2θ with respect to the incident beam. The Bragg condition is expressed by a simple equation, known as Bragg equation as expressed below in Eq. 4.7.

$$2d_{hkl} sin\theta = n\lambda \tag{4.7}$$

Where, d_{hkl}, is the interplanar distance (or d-spacing) of a specific plane identified by its Miller indices (hkl) inside a crystalline solid, θ is the incident angle defined as the angle between incident X-ray and probed (hkl) plane, also called Bragg angle, n is the diffraction order, and λ is the X-ray wavelength.

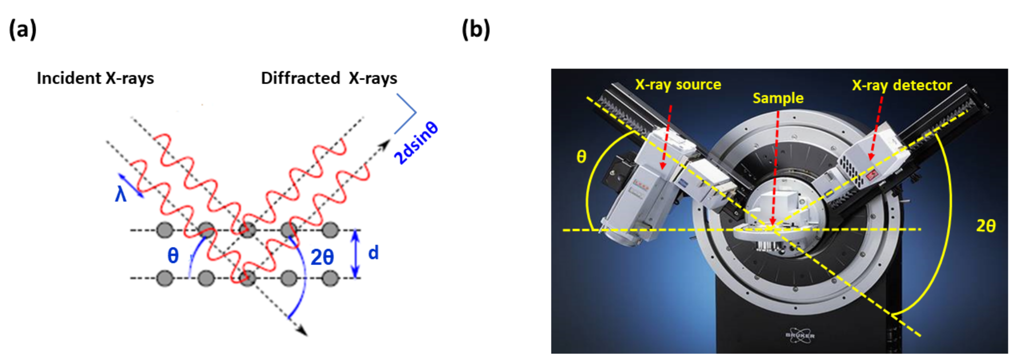

Figure 4.13: *(a) Schematic representation of Bragg condition, where constructive interference of two beams occurs if the path difference ($2dsin\theta$) is integer multiple of the incident X-ray wavelength: (b) Photograph of a Bruker AXS D8 Advance Diffractometer with sample on it (Photograph from Bruker).*

The XRD measurements during this thesis work were performed using Bruker AXS D8 Advance diffractometer in a Bragg-Brentano $\theta/2\theta$ configuration. Schematic representation of Bragg condition and the photograph of Bruker AXS D8 Advance diffractometer are shown in Fig. 4.13 (a) and (b), respectively.

Grazing Incidence X-ray Diffraction (GIXRD)

For ultra thin films, Bragg-Brentano ($\theta - 2\theta$) scan configuration is not convenient. Since the incident angle (θ) is so high, the X-ray often penetrates through the film and the substrate with a penetration depth much larger compared to the thickness of measured thin films. As a result, the diffraction pattern contains very weak signal of the film and strong signal from the substrate. To improve the signal from the film, a different approach, namely grazing incidence configuration, can be used. In grazing incidence XRD, a very small incidence angle called (ω) is chosen in order to reduce the penetration depth of the incoming beams. The X-ray and sample are fixed to ensure a small incident angle ($\omega \approx 0.1 - 5°$), while the detector moves at 2θ angle to collect diffraction signals.

As explained above, the angle of incidence relative to the sample surface is one of the main factors which determines the penetration depth of X-ray in a material. X-ray penetration depth varies over several orders of magnitude for most of materials over ω angle below 1°, as a function of angle of incidence [180]. By properly choosing the angle of incidence, a specific sample depth can be probed. Measurements at various ω angles, therefore results in lead probing different sample depths, which can then be used to "depth profile" materials properties such as phase variations, strain variations and defect formations [183].

Texture Analysis

For polycrystalline thin films, the diffractogram show several peaks, which correspond to the diffraction of the incident beam by crystals having different orientations. The position of the peaks determine the crystal phase of the material and any deformations. The existence of a preferential crystallographic orientation of the crystallites is associated with a texture. This can be estimated by Harris's method [184], by comparing the different intensity of the diffraction peaks associated with the sample studied with that of a powder of the same phase. It is considered that in a powder, the orientation of the crystallites is totally random and there is no preferential orientation. The texture coefficient (C_{hkl}) can then represent the preferred occurrence of particular planes (hkl), whose deviation from the standard sample implies the preferred growth and it can be calculated using the following formula:

$$C_{hkl} = \frac{\dfrac{I_{hkl}}{I_{o,hkl}}}{\frac{1}{N}\sum_{h'k'l'}\dfrac{I_{h'k'l'}}{I_{o,h'k'l'}}} \tag{4.8}$$

Where; I_{hkl} is the intensity of reflection of studied samples, $I_{h'k'l'}$ is the intensity of corresponding plane in PDF data according to standard X-ray diffraction powder patterns [185], and N represent number of reflections.

4.2.1.3 Scanning Electron Microscopy(SEM)

A scanning electron microscope (SEM) is a type of electron microscope that uses a focused electron beam, which scans the sample surface and analyzes emitted electrons to yield information about topography, morphology, composition, and crystallographic information of probed samples.

Electron beams used in SEM are generated from thermionic, Schottky or field-emission cathodes; and are accelerated by voltage difference between cathode and anode that can be as low as 0.1 keV or as high as 50 keV [186]. The generated incident primary electrons (PE) interact with sample within interaction volume and from which signals of secondary electrons (SE) and back scattered electrons (BSE) can be detected. The most important interaction processes and their information volumes are schematically depicted in Fig. 4.14.

Secondary electrons (SE) are the most important image mode of SEM. They have an energy, which is typically about 1000 smaller than the primary electrons. This implies they are emitted only from a region of a few Ångstroms from the surface of the sample, as can be seen in Fig. 4.14. This low exit depth allows a resolution of the order of 1 - 10 nm to be reached [186]. Secondary electrons provide a topographical contrast of the sample.

When the primary electron beam strikes the sample, some of the electrons will interact with the nucleus. The negatively-charged electron will be attracted by the positive nucleus, but, if the angle is just right instead of being captured by the “gravitational pull” of the nucleus, it will circle the nucleus and return back out of the sample without

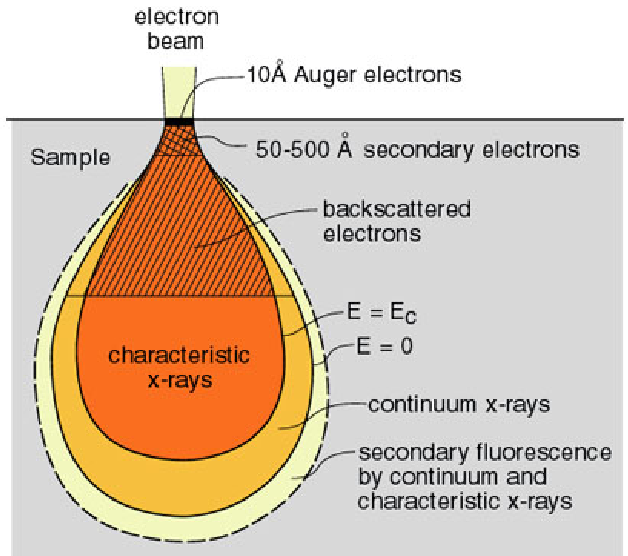

Figure 4.14: *Schematic representation of interaction volume for various electron-specimen interactions in SEM. Different depth lengths produce different signals.*

.

loosing energy. These electrons are called backscattered electrons (BSE). In order to form an image with BSE, a detector is placed in their path. BSE have a kinetic energy similar to the primary electrons and are obtained up to a depth of a few tenths of a micrometer from the sample surface [186]. The most important contrast mechanism of BSE is the dependence of the backscattering coefficient on the mean atomic number $\bar{Z}$, which allows phases with different values of atomic number to be recognized. Thus, imaging with elemental contrast is possible.

Backscattered electron images in SEM exhibit compositional contrast that results from different atomic number elements and their distribution. Identification of those particular elements and their relative proportions (e.g atomic %) is possible by using Energy Dispersive Spectroscopy (EDS) [186].

In this work, an FEI Quanta 250 FEG Scanning Electron Microscope with Schottky field emission gun (FEG) was used to examine topological images and elemental analysis of the samples.

4.2.1.4 Raman Spectroscopy

Raman spectroscopy is based on the Raman effect, which is a change in photon energy upon inelastic scattering on molecules or solids. The effect was discovered by Sir C.V. Raman, who was awarded a Nobel prize in physics (1928) for this achievement [187]. It is a complementary technique to Fourier transform infrared spectroscopy (FTIR).

In Raman spectroscopy, a sample's reflectance under illumination with monochromatic light, usually from a laser in the visible range, is measured. When the incident photons collide molecules, three different kinds of reflection are possible, mentioned in the order of their cross section: elastic or Rayleigh scattering ($E'_\lambda = E_\lambda$), inelastic Stokes-Raman scattering with phonon creation ($E'_\lambda < E_\lambda$), or inelastic anti Stokes-Raman scattering under phonon absorption ($E'_\lambda > E_\lambda$). A typical Raman spectrum of the scattered light is generally given by the photon intensity over the photon energy loss E_λ, the Raman shift Δv. The raman shift Δv defined as the difference between the scattered radiation emitted by the sample and that emitted by the source, a parameter therefore independent of the wavelength of the laser.

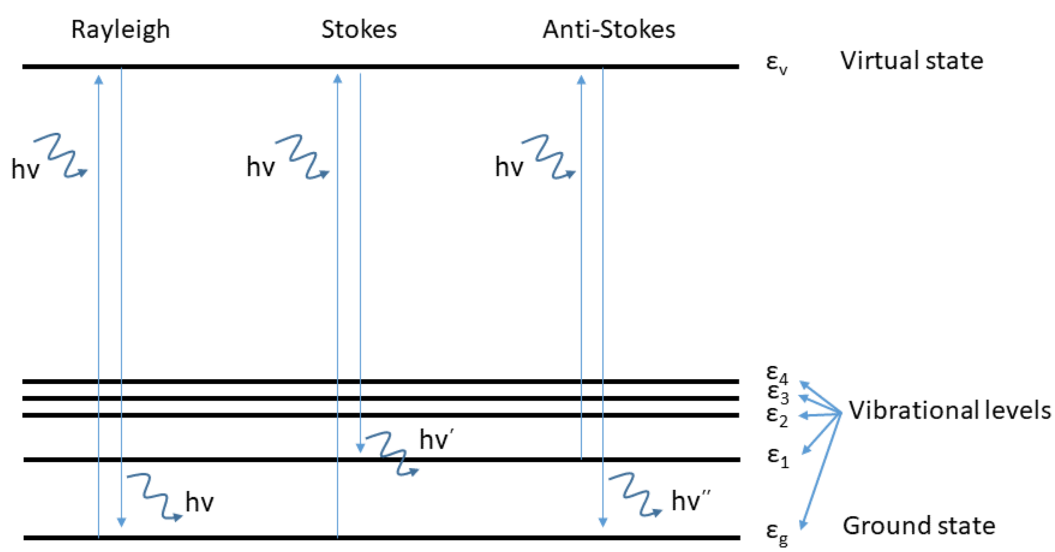

Figure 4.15: *Schematic representation of Rayleigh scattering and Raman (stokes and anti-stokes) scattering: Inspired by [188].*

.

If the molecule absorbs part of the photon energy to transform to an excited state the photon will reflect with less energy and form the so-called Stokes lines of the Raman spectrum. Thus, the Stokes-Raman scattered photons give rise to peak structure at Δv > 0. While in anti Stockes- Raman, the molecule is already in excited state and can transfer energy to the incident photon, so the reflected photon will have higher energy and form anti-Stokes lines. When the collisions between molecules and photons happen with no energy loss, this is called elastic or Rayleigh scattering [188]. These three possible reflections are schematically represented in Fig. 4.15

In this study Raman spectra were recorded for SnO_2 based demixed composite films using a Jobin Yvon/Horiba Labram spectrometer equipped with a liquid nitrogen cooled charge-coupled device (CCD) detector. The measurements were conducted at room temperature in the micro-Raman mode in a backscattering geometry. A green Ar^+ laser (514.5 nm) was focused ($\times 100$ objective) to a 1 μm^2 spot on the sample surface. The laser power on the sample surface was close to 2 mW. For easy calibration of Raman spectra with standard Si spectrum samples prepared on Si wafer were used. A crossed polarizer and analyser (VH) was used to minimize the background signals originating from the Si substrate.

4.2.1.5 UIV-Vis-NIR Spectrophotometer

The optical studies were performed using a Perkin Elmer Lambda 950 spectrophotometer, which allows the measurement of transmittance and reflectance of thin films. The spectrophotometer is equipped with two light sources, a deuterium arc lamp for ultraviolet (UV) light and a tungsten-halogen lamp for visible and infrared (IR) light; as a result it was possible to have wavelength range that can span from 250 - 2500 nm. Therefore, the measurements of ultraviolet region (10 - 400 nm), visible spectrum (400 - 700 nm), and near infrared region (800 - 2500 nm) of the electromagnetic spectrum was possible.

During the measurement, the incident light is directed to the sample with the help of different optical elements and gets transmitted, reflected or absorbed. The two detectors equipped in the spectrophotometer, a photomultiplier (PM) for UV and Visible regions of the spectrum and an InGaAs sensor responsible for the near infrared range, can then collect the transmitted (T) and reflected (R) light. Due to conservation of energy, both can be related via

$$T + R + A = 1 \tag{4.9}$$

where, A is the absorbance.

UV-Vis-NIR spectrum can be used to determine the band gap (E_{BG}) and absorption coefficient (α) of semiconducting samples. In the absence of reflectance, transmission through a sample of thickness (Δd) follows the Lambert-Beer law:

$$I = I_o \cdot exp(-\alpha \Delta d) \tag{4.10}$$

Where, I_o is the light intensity before, and I is the intensity after sample transmission. α is the absorption coefficient and is measured in cm^{-1}.

Tauc Plots are obtained by plotting the quantity $(\alpha \cdot E_\lambda)^{\frac{1}{n}}$ over E_λ. Where, E_λ is the photon energy and the value of n has to be chosen based on the nature of observed electron transition: $n = 1/2$ for direct allowed, $n = 3/2$ for direct forbidden, $n = 2$ for indirect allowed, and $n = 3$ for indirect forbidden transition.

4.2.2 Electrical Characterizations

4.2.2.1 Hall Effect Measurement

Basics of Hall Effect

The carrier transport properties of TCO materials can be determined using a variety of magneto-optical and standard transport measurements. The most common measurements are based on the Hall effect. Since the discovery of the Hall effect by Edwin Hall in 1879 [189], it has became an important characterization method for semiconductors. This is not only possible to determine the dominant charge carrier type (electrons or holes), but also its concentration and charge carrier mobility can be obtained.

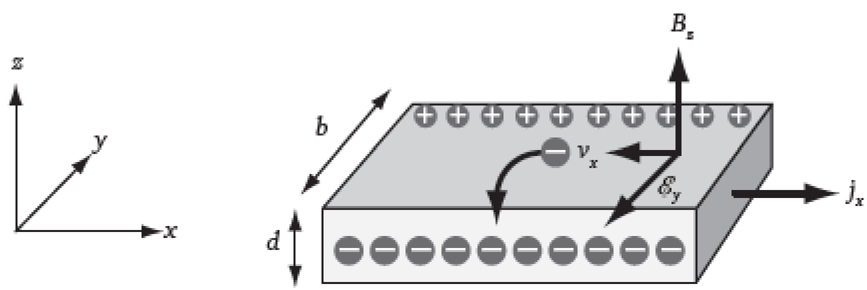

Figure 4.16: *Schematic representation of the Hall effect geometry, adapted for n type semiconductors. Current flowing in the x - direction with the current density j_x; the coordinate system (x, y, z) ; magnetic field in Z direction B_Z and charge carriers are moving with the drift velocity $v_{d,x}$, which will be deflected by Lorentz force $\vec{F}$ in y - direction, are given [193].*

The information on working principle of Hall effect measurements is adapted from books of Marius Grundmann [190] and Donald Neamen [191]. Schematic representation of the Hall effect geometry, adapted for n type semiconductors, is shown in Fig. 4.16. The semiconductor has charge carrier of charge q, charge carrier density n, and charge carrier drift velocity $v_{d,x}$. A current I_x flow due to an applied voltage in x-direction. The drift velocity is an average velocity of the charge carriers over the volume of the semiconductor. Each charge carrier may move in a seemingly random way within the conductor, but under the influence of applied fields there will be a net transport of carriers along the length of semiconductor. The current I_x is the current density J_x times the cross-sectional area (bd) of semiconductor. The current density J_x is charge density nq times the drift velocity $v_{d,x}$. In other words

$$J_x = I_x/bd = nqv_{d,x} \tag{4.11}$$

Where, b and d are the width and thickness of the sample, respectively.

When a perpendicular magnetic field $\vec{B}$ is applied to a semiconductor, the charge carriers will experience a Lorenz force $\vec{F} = \text{q}\vec{v}\vec{B}$ that will deflect them towards one side of the conductor. This deflection will cause an accumulation of charges along one side and create a transverse electric field E_y, which counteracts the force of the magnetic field. When steady state is reached, there will be no net flow of charge in the y direction, since the electrical and magnetic forces on the charge carriers in that direction must be balanced. Assuming these conditions, it is easy to show that:

$$\vec{F} = q\vec{E} + q(\vec{v} \times \vec{B}) = qE_y + qv_{d,x}B_z = 0 \tag{4.12}$$

In Fig. 4.16, E_y points in negative y-direction and is therefore negative. By considering the semiconductor is n - type with electrons e as charge carriers and taking into account equation Eq. 4.11 of current density, Eq. 4.12 can be rewritten as:

$$E_y = v_{d,x}B_z = -\frac{B_z j_x}{ne} = -\left(\frac{1}{ne}\right)B_z j_x = R_H B_z j_x \tag{4.13}$$

The term in parenthesis is known as Hall coefficient and the charge carrier concentration n can thus be calculated directly from R_H

$$R_H = -\frac{1}{ne} \tag{4.14}$$

In an experiment, the potential difference across the sample namely the Hall voltage V_H, is measured. The Hall voltage is related to the electric field by:

$$V_H = -\int_0^d E_y d_y = -E_y d \tag{4.15}$$

Thus, from equations 4.11, 4.13, and 4.15, it is possible to obtain:

$$V_H = -\frac{B_z I_x}{ned} \tag{4.16}$$

If the electrical conductivity σ is also measured, the charge carrier mobility μ can be calculated from measured conductivity (σ) using the relationship σ = enμ.

This simplified approach assumes the same mobility for charge carriers moving along x due to the electric field as for carriers moving along y due to the magnetic field in z. This means the mobility is proportional to a uniform, average scattering time τ. However, this is only true at very large magnetic fields, which are typically not encountered in laboratory-based Hall effect equipment. In order to understand some of the ideas involved in theory of the Hall effect in real materials, it is instructive to construct a more careful model for electric currents under electric and magnetic fields from a classical point of view. The charge carriers move in a medium associated to a given resistivity. The resistance could be due to scattering between the carriers and impurities in the material and between the carriers and vibrations of the material's atoms. Thus, the relaxation time τ depends on dominant scattering mechanism. This results in a more general expression for previously derived Hall coefficient R_H by supplementing the Hall scattering factor r_H

$$R_H = -\frac{r_H}{ne} \tag{4.17}$$

The knowledge of r_H allow to distinguish between Hall carrier mobility μ_H and actual drift mobility μ_d of the charge carriers.

$$\mu_H = r_H \mu_d \tag{4.18}$$

Description of the Equipment

The custom made Hall effect system at TU Darmstadt is described in a publication [192]. The experimental set-up was build during preparation of the PhD theses of Mareike Frischbier and André Wachau [193]. The schematic representation of the setup is shown in Fig. 4.17.

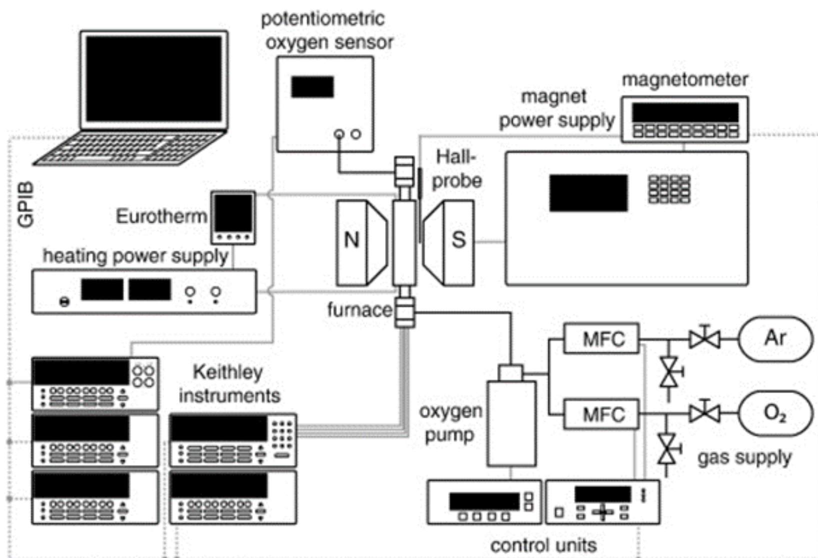

Figure 4.17: *Schematic representation of the Hall effect set-up at TU Darmstadt: Hall effect and relaxation conductivity measurements are performed as a function of temperature and for different atmospheres [192].*

The sample in van der Pauw geometry [194] is installed inside a quartz tube, which may be evacuated through a turbo molecular pump down to a pressure of 10^{-8} mbar. Alternatively, a gas flow at atmospheric pressure of an argon oxygen mix may be chosen by separate mass flow controllers and an optional oxygen pump. The gas mixture at the outlet is monitored by a potentiometric oxygen sensor. The quartz tube is fit into a furnace, which allows for measurement at temperatures up to 700 °C. The furnace with quartz tube carrying the sample is then placed between the pole shoes of a electromagnet (Type EM4-HVA, Lake Shore Cryotronics), capable of a maximum magnetic field of 1 T. A Hall probe serves to monitor the actual magnetic field in the vicinity of the sample. Several Keithley instruments are responsible for supplying the measurement current, measuring the Hall voltage and performing the permutation among the four contacts of the sample in van der Pauw geometry. A buffer amplifier is included in order to measure high impedance samples. A LabView routine controls the Keithley instruments and the magnet power supply to perform conductivity and Hall effect measurement.

Part II

Results, Discussion and Considerations

Subpart II-A

Physical Approach

Defect Modulation Doping for Indium Oxide Based Thin Films

The defect modulation doping approach uses two dissimilar materials to circumvent the alignment of doping limits. The use of dissimilar materials removes the constraint of aligned doping limits. By aligning two dissimilar materials it is therefore, in principle, possible to obtain Fermi levels outside the doping limits in the host material. Such a situation can, from a thermodynamic point of view, only be achieved if defects in the host material cannot form spontaneously when the Fermi energy is raised during deposition of a modulation layer. The detail concept of defect modulation doping are described in subsection 2.4.3.

In this part of the project ultra thin defective and amorphous insulators (Al_2O_3 and SiO_{2-x}) are used as a potential dopant and deposited at the surface of TCO (In_2O_3, Sn-doped In_2O_3, and SnO_2). As a result it is expected for them to induce conduction electrons at the near interface region on TCO and allows to realize defect modulation doping. The energy band diagram of the hetrostructure is schematically illustrated in Fig. 4.18. In which, the Fermi level of TCO is forced into the conduction band at the interface and resulting surface band bending-Φ_{bb}. Thus, the Fermi level is expected to be well above the classical doping limit of these TCOs and evident modulation doping effect.

In the following chapters, experimental approach and results of different dissimilar materials will be presented with discussions in the context of defect modulation model. *Chapter 5* will focus on the effect of Al_2O_3 deposition by ALD on interfacial and electrical properties of Sn-doped In_2O_3 (ITO) thin films in order to observe the modulation doping effect. In *Chapter 6* the case for undoped In_2O_3 with the effect of changing the thickness of dopant Al_2 O_3 layer will be discussed. Finally, in *Chapter 7* different dopant namely SiO_{2-x} will be used with undoped In_2O_3 as a TCO host .

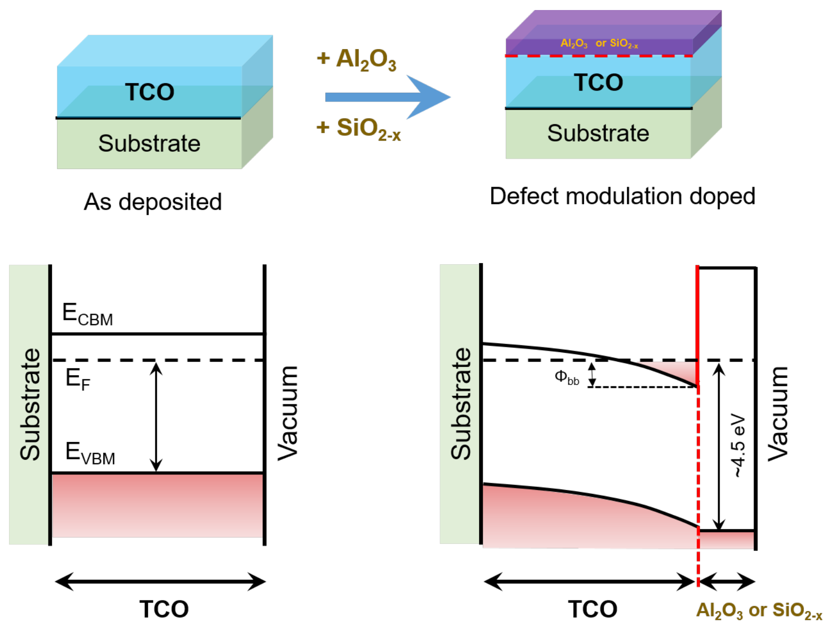

Figure 4.18: *Schematic illustration for energy band diagram of TCO (In_2O_3, Sn-doped In_2O_3, and SnO_2) thin films before (left) and after (right) deposition of ultra thin potential dopants ($Al_2\ O_3$ and SiO_{2-x}) modulation layers. The Fermi level of TCO forced into the conduction band at the doped interface, but it remains low near the interface to the substrate. At the position of maximum surface band bending (Φ_{bb}), the Fermi level is expected to be positioned well above the classical doping limit of these TCOs and demonstrate the success of defect modulation doping effect.*

Chapter 5

Surface Modification of Sputtered ITO by ALD-Al_2O_3

5.1 Introduction

As it has been discussed earlier in subsection 2.4.3, the deposition of an ultra thin defective and amorphous insulator material on the surface of a TCO (In_2O_3, Sn-doped In_2O_3, and SnO_2) should induce conduction electrons in the interface near region of TCOs, which is called defect modulation doping. This chapter is designed to assess the viability of defect modulation doping by ultra thin ALD-Al_2O_3 coated ITO thin films. For this purpose, different ITO thin film samples were prepared with and without ALD-Al_2O_3 coating. The prepared samples were examined using in-situ photoelectron spectroscopy for near surface properties as well as using ex-situ electrical conductivity measurements. The chapter is divided in the following sections.

Section 5.2, shortly describes the experimental procedures followed during thin film preparation and characterization. The photoelectron spectra of uncoated and ALD-

Al_2O_3 coated ITO films will be addressed briefly in section 5.3. Since defect modulation doping utilizes Fermi level manipulation in heterostructure contacts to achieve higher carrier concentrations and mobilities in thin films, the Fermi energies will be discussed in relation to macroscopic electrical sample properties. Furthermore, photoemission of the important core levels will also be addressed in this section.

In order to answer whether coating of ultra thin ALD-Al_2O_3 would enhance the electrical properties of ITO and ensure the presence of modulation doping effect, the electrical study of uncoated and Al_2O_3 coated ITO thin films was performed, which will be discussed in section 5.4. The influences of ITO substrate deposition temperature, ALD-Al_2O_3 coating, temperature exposure during ALD process, and further post deposition treatment (thermal annealing) on electrical properties of ITO thin films will be discussed separately. Finally, in section 5.5, the main findings of this chapter will be summarized and concluded. Furthermore, the future perspective for defect modulation doping will also be outlined.

Part of the results of this chapter have been published in the journal of *Materials* [195].

5.2 Sample preparation

ITO films were deposited in oxide II of DAISY-MAT [12] on platinum coated quartz glass substrates by magnetron sputtering with radio-frequency (RF) excitation. The background pressure of the deposition chamber was 10^{-6} Pa. A ceramic 2 inch ITO target with 10wt % SnO_2 doping, a RF power of 25W, a process pressure of 0.5 Pa, an Ar flux of 6.6 sccm or 9.5 sccm of Ar and 0.5 sccm O_2 and a target-to-substrate distance of 10 cm were used for deposition. The film thickness of ITO was varied from 8–200 nm and the substrate temperature during deposition from room temperature to 400 °C. Two different targets having the same composition were used for preparation of the films and discriminated as "*old*" and "*new*" target, respectively.

ITO thin films prepared from the old target are prepared either in pure Ar or with addition of 0.5 % O_2 in the processing gas. All RT films, as well as 200 nm thick films deposited at 200 °C and 400 °C, are prepared in pure Ar environment with a gas flux of 6.6 sccm. As the XPS of these films revealed a chemical reduction [1], the next batches of 10, 20, and 50 nm thick films deposited at 200 °C and 400 °C were deposited with

[1] we suspected that the target surface was highly reduced due to repeatedly sputtered in pure Ar environment. The XPS spectra of these films with chemical reduction phenomenon will be discussed in

0.5 % O_2 in the processing gas using fluxes of 9.5 sccm Ar and 0.5 sccm O_2. Thin films prepared from the new target are exclusively deposited in pure Ar environment with a gas flux of 6.6 sccm. Thus, the results and discussion of this chapter will be described by distinguishing thin films prepared from the two targets as samples from the old target and samples from the new target.

Ultra thin ALD-Al_2O_3 coatings were deposited using a low-pressure process in a separate vacuum chamber with a background pressure of 10^{-6} Pa. The description of the setup and deposition conditions can be found in subsection 4.1.2. 2 and 5 ALD cycles of Al_2O_3 were used on different ITO substrates, with corresponding thicknesses of$\approx$ 0.2 and $\approx$0.5 nm, respectively. The deposition conditions are summarized in Tab. 5.1.

Table 5.1: Summary of deposition parameters for ITO and ITO/ALD-Al_2O_3 thin films

Sn-doped In_2O_3 /ALD- Al_2O_3 thin films							
Sample	ITO				ALD-Al_2O_3		
	Target	Process gas	Temp. (°C)	Thickness (nm)	Precursor	ALD-cycle	Temp. (°C)
ITO	10% Sn-doped In_2O_3	Ar and 99.5% Ar/0.5 % O_2	RT-400	8-200	-	-	-
ITO/ALD-Al_2O_3	10% Sn-doped In_2O_3	Ar and 99.5% Ar/0.5 % O_2	RT-400	8-200	TMA and H_2O	2-5	200

5.3 Photoemission

A typical XPS survey spectrum of a tin-doped indium oxide (ITO) thin film deposited by rf-magnetron sputtering from the old target before and after 5-cycle of ALD-Al_2O_3 coating is shown in Fig. 5.1. Survey spectra are measured with comparatively low energy resolution, enabling a quick scan of the entire binding energy range accessible with the respective excitation energy. As photoemission lines are characteristic of the specific elements, the resulting spectrum is mainly used to check whether the detected elements are in general agreement with the expected qualitative atomic composition of the sample. In addition, surface contamination by carbohydrates can also be examined from existence or non-existence of the carbon C1s emission peak found around 285 eV

section 5.3.

binding energy. Due to the in-situ processing and analysis, no such contamination is present in the spectrum.

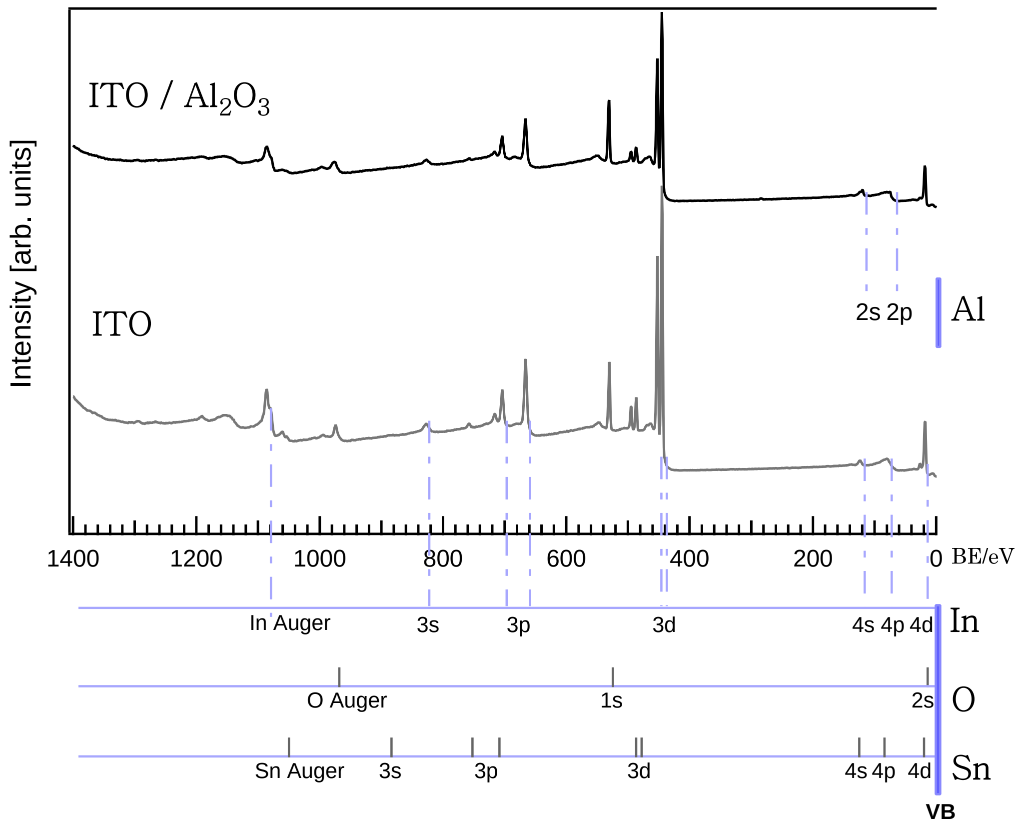

Figure 5.1: *XP (AlKα) survey spectrum of Sn-doped In_2O_3 before and after ALD-Al_2O_3 coating, annotated with the binding energy (BE) of In, O, Sn and Al.*

For further sample characterization, selected areas of the photoemission spectra are routinely measured at high energy resolution and at elevated counting times to achieve reasonable signal-to-noise ratios according to the user's needs. In the case of uncoated and ALD-Al_2O_3 coated ITO, the detailed measurement contain at least one core-level emission for each of the elements contained in the sample and the valence band (VB) region. Compared to core levels, valence band emissions generally have poor intensity in XPS measurements. Consequently extended counting times are needed in order to obtain satisfactory signal-to-noise ratios [176]. In uncoated Sn-doped In_2O_3 excited by Al Kα radiation, In3$d_{5/2}$, Sn3$d_{5/2}$, O1s, and VB are the emissions. For ALD-Al_2O_3 coated samples, Al2p and Al2s emissions are also included.

Core level spectra of the O1s, Sn3$d_{5/2}$, In3$d_{5/2}$, Al2p, and VB regions recorded from a 20 nm thick ITO films deposited from the old target are displayed in Fig. 5.2. The thin films were deposited at the substrate temperatures of RT-400 °C, and coated with 5 cycles of ALD-Al_2O_3. For comparison, spectra from a 20 nm ITO thin film deposited at RT without Al_2O_3 coating are also presented in the figure. The displayed spectra were selected since they are representative for showing different changes in shape and binding energies of the core levels and VB.

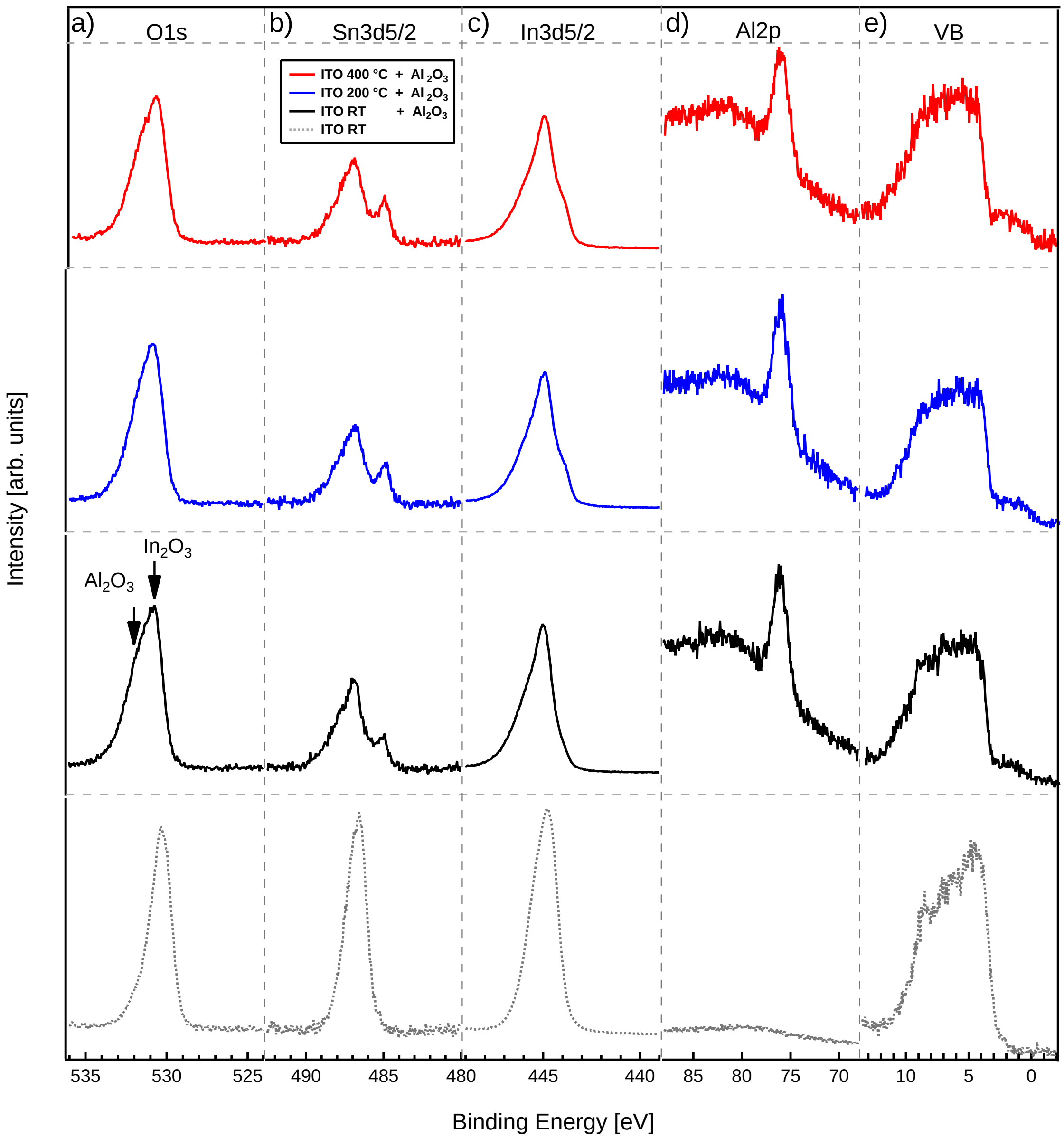

Figure 5.2: *XP (AlKα) detail spectra of the O1s (a), Sn3d$_{5/2}$(b), In3d$_{5/2}$ (c), Al2p (d), and VB (e) regions for 20 nm thick ITO films deposited at substrate temperatures of RT, 200 °C and 400 °C and coated with 5 ALD cycles of Al_2O_3. For the room temperature (RT) films both before and after spectra are represented for comparison.*

The O1s, $Sn3d_{5/2}$, and $In3d_{5/2}$ core level spectra of uncoated films show a clear asymmetry, which is caused by excitation of plasmons in the free electron gas of the highly doped material [35, 196]. The high doping level of the substrate is further evident from the high binding energy of the valence-band maximum (VBM) of E_F–E_{VB} = 3.0 ± 0.1 eV (at least for the films prepared at elevated temperatures of 200 °C and 400 °C, RT films show lower Fermi energy values), which is comparable or a slightly larger than the band gap and hence above the conduction band edge, which is at 2.6-2.9 eV above the VBM [108]. For more information about the band gap of In_2O_3 see also section 3.1.

By deposition of Al_2O_3, the intensity of Sn3d and In3d core levels are attenuated due to the coverage of substrate with Al_2O_3, while the O1s intensity remains approximately constant due to the increase of the Al_2O_3-related emission at higher binding energy of ∼532 eV. For 5 cycles of ALD-Al_2O_3 coverage, the chemical components of ITO- and Al_2O_3-related O1s emissions are overlapping in the spectra due to comparable binding energies of the O1s in ITO and Al_2O_3. An interface experiment of these two materials revealed the appearance of an additional O1s peak at ∼532 eV for ALD cycles of ≥ 10 [38]. The binding energy of Al2p emission corresponds well with the value expected for Al_2O_3 [197].

With Al_2O_3 coating, the binding energy of the core levels and valence levels shift considerably to the higher binding energy. This corresponds to an increase of the carrier concentration near the surface, which is also indicated by the change of the Sn3d and the In3d line shapes. After alumina coating both core levels exhibit a further increase of asymmetry, indicating the presence of a high electron concentration [35, 196, 198, 199, 200, 201].

Figure 5.3 presents a comparison of $Sn3d_{5/2}$ and $In3d_{5/2}$ core levels and VB photoelectron spectra for 20 nm ITO films with and without Al_2O_3 deposition. Al_2O_3 deposition resulting reduction of the ITO, which is evident from the appearance of additional metallic Sn and In peaks at their respective lower binding energies. These features appear for all probed ITO substrates prepared from both targets and for all deposition conditions. The intensity of valence band is also attenuated after Al_2O_3 deposition.

The characteristic shape of the valence band of Sn-doped In_2O_3 is characterized by O2p states close to the VBM[2], but has also some mixing of other orbital character away from the VBM [202]. These consisted of In4d-O2p, Sn5p-O2p, and hybridization between these states. For comparison, the valence band of uncoated and Al_2O_3 coated ITO films is displayed in Fig. 5.3(c). The changes and appearance of new features are briefly described in the following:

- (1) represents the shift of Fermi energy to a higher binding energy upon Al_2O_3

[2]valence band maximum

deposition. This indicates the presence of surface electron accumulation. Such accumulation layer have been frequently reported to be present at the In_2O_3 surfaces [202, 203, 204, 205]. This accumulation layer is not observed in as deposited surfaces, as the samples have not been exposed to air before XPS measurement.

- (2) indicates an increase of the band gap emission for Al_2O_3 coated films. These features are usually observed for strongly reduced films and is generally accepted that this emission is caused by Sn5s electrons of Sn^{2+} cations [206]. These cations are preferentially present at low-symmetry lattice sites, especially at the surfaces and grain boundaries [207]. Here, it is also due to the presence of metallic Sn and In.

- (3) the shape of valence band changed from the characteristic shape of ITO towards the one observed for Al_2O_3 [38, 196, 208].

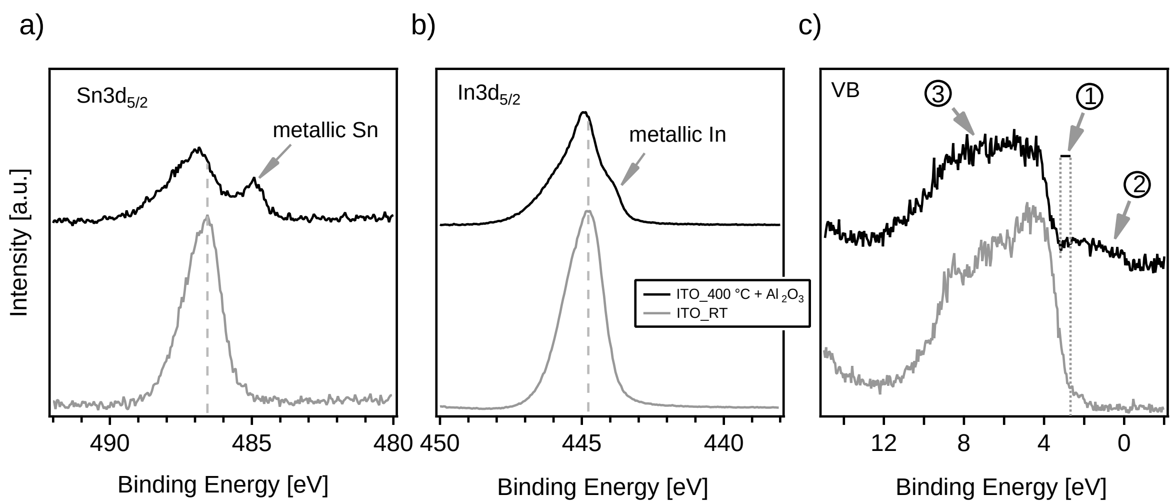

Figure 5.3: *Comparison for XP (AlKα) detail spectra of $Sn3d_{5/2}$(a), $In3d_{5/2}$ (b), and VB (c), regions for 20 nm thick ITO film deposited at RT and for the film with the same thickness but deposited at 400 °C and with Al_2O_3 coating.*

The Fermi level at the surface

Photoemission is a highly surface sensitive technique [209]. Therefore, the binding energies obtained from photoemission reflect the Fermi level position at the surface of the film. The absolute position of the Fermi level with respect to the band edges can be directly determined from the valence band maxima, since the binding energies are calibrated such that zero binding energy corresponds to the Fermi level position. The Fermi level position (E_F-E_{VB}) of ITO films with different thickness deposited at the substrate temperature of RT, 200 °C, and 400 °C with and without Al_2O_3 coating are displayed in Fig. 5.4.

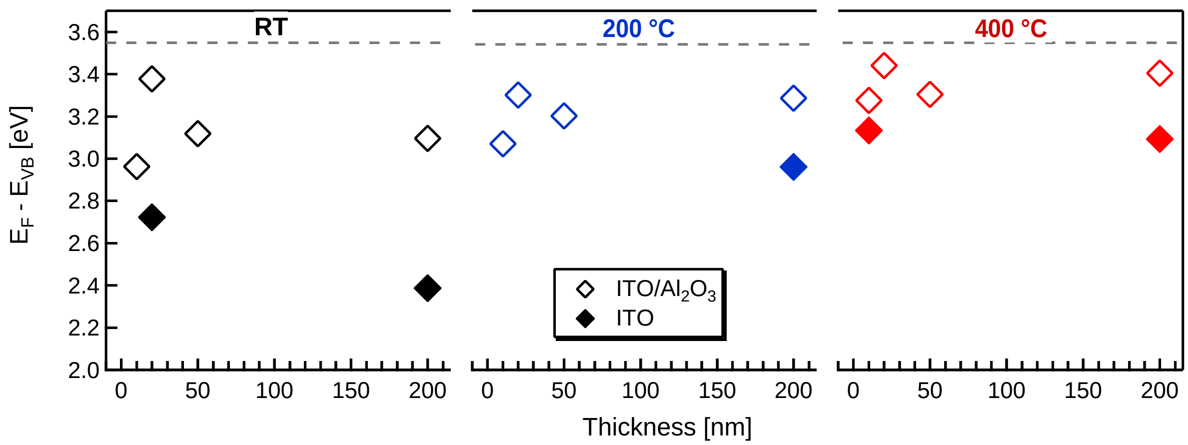

Figure 5.4: *Surface Fermi level position of ITO films anticipated to different thickness, different substrate temperature and with and without 5 ALD cycles of Al_2O_3 coating. Each E_F-E_{VB} data points are extracted from different samples.*

For uncoated room temperature ITO films, the Fermi energy of 20 nm thick film is higher than that of 200 nm thick film. This corresponds well with the higher carrier concentration of thinner films than thicker ones, as shown in subsection 5.4.1. For the films deposited at 400 °C, the Fermi energy does not change with film thickness. This also corresponds well with the carrier concentrations of films deposited at elevated temperature (see also Fig. 5.7(c)). In all cases, an upward shift of the Fermi energy is observed after Al_2O_3 deposition. This upward shift indicates, on one hand, the presence of surface electron accumulation and, on the other hand, it can partially be assigned to a chemical reduction of ITO substrate as it has been discussed above, see also Fig. 5.3. The Fermi energy in the Al_2O_3 films deposited by the low-pressure process in DAISY-MAT is reproducibly found at 4.5 eV above the valence band maximum, independent on substrate [8, 38, 94, 95]. Moreover, a very small valence band offset between ITO and Al_2O_3 [98] is expected in the absence of pinning [38]. Therefore, it can be expected that the Fermi energy in the ITO also raises to E_F - E_{VB} $\geq$4 eV after Al_2O_3 deposition. This is clearly not the case as the binding energies of the ITO films correspond to only to E_F - $E_{VB} \approx 3.2 \pm 0.2$ eV. The discrepancy between the expected and the measured Fermi energies might be explained by the formation of a very narrow space charge region at the surface of the highly doped ITO, which is schematically represented in Fig. 5.5(b). If this is narrower than the depth probed by XPS, the Fermi level directly at the interface cannot be observed. This is equivalent to an effective modification of the band alignment [12, 38, 210, 211].

For semiconductors, a Fermi level position, which is different at the surface and bulk, can be explained by the presence of charged surface states and development of a space charge layer [212]. The density of surface states (D_{ss}) and their energetic position leads to surface Fermi level modification. The width of space charge layer (δ), which compensates the negative surface charge, depends on the doping of the material. For undoped semiconductor, it is expected to have larger width of space charge region, see (δ_1) of Fig. 5.5. However, degenerate semiconductors such as ITO should develop very thin space charge layer and also required a very high density of surface states, which give rise to the Fermi edge emissions observed for highly doped semiconductors like ITO [35]. Even with a sufficiently high density of surface states one has to expect a rather thin space charge layer of the order of 1 nm [213]. Since ITO contains mobile donors, which is indicated by Sn segregation during deposition at elevated temperatures of $\geq$ 300 °C or post annealing at higher temperature [21], an even thinner space charge layer would result due to pile up of donors near the surface [214].

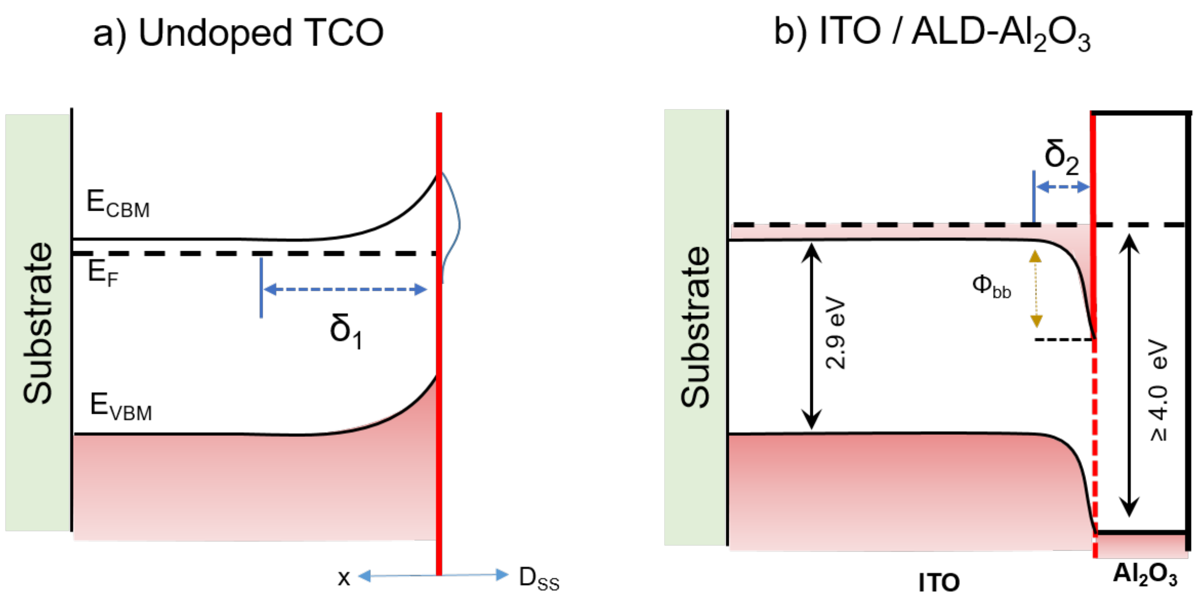

Figure 5.5: *Schematic representation for electronic structures of surfaces of undoped TCO (a) and ITO / ALD-Al_2O_3 system. The density of surface states (D_{ss}) and their energetic position leads to surface Fermi level modification. The width of space charge layer (δ), which compensates the negative surface charge, depends on the doping of the material. Undoped TCO have larger width of space charge layer (δ_1) compared to ITO/ ALD-Al_2O_3 system (δ_2), which could be as thin as $\approx$ 1nm.*

5.4 Electrical studies

In this section, the electrical properties of ITO thin films deposited at different substrate temperatures with different film thickness will be presented. The influence of ALD-Al_2O_3 coating on the bulk conductivity and Hall effect will also be presented with the aim of demonstrating a potential defect modulation doping effect. The influence of different temperature treatments together with change of annealing environment on the electrical properties of ITO thin films will also be presented.

5.4.1 Uncoated ITO

5.4.1.1 The effect of substrate temperature and film thickness

As a first step, the influence of substrate temperature on the electrical properties of ITO thin films with different thickness is presented in this section. Films deposited at elevated substrate temperature are expected to be crystalline, while films grown at room temperature might be amorphous [215, 216, 217, 218]. To verify this, X-ray diffraction patterns recorded in grazing incidence of the films deposited at room temperature are shown in Fig. 5.6.

The thinnest film does not show any reflections. This is not due to the low film thickness as clear reflections are observed after annealing the same film (see the insert of Fig. 5.6). The diffraction peaks associated to In_2O_3 are increased with increasing film thicknesses. Hence, only the thinnest film is completely amorphous after deposition. The increasing crystallinity with film thickness has been observed previously and can be attributed, on the one hand, to the energy of the impinging particles [219] and, on the other hand, to an increase of substrate temperature induced by the heat of condensation of the film [215, 218]. Nevertheless, despite the observation of crystalline structure, it is expected that the crystallite size of the films grown at room temperature is substantially smaller than that of films grown at higher temperature. The films may also still contain some amorphous regions. The microstructure will be important for understanding the dependence of electrical properties on film thickness and annealing, which will be discussed below.

The conductivities, carrier mobilities and concentrations of films with thickness ranging

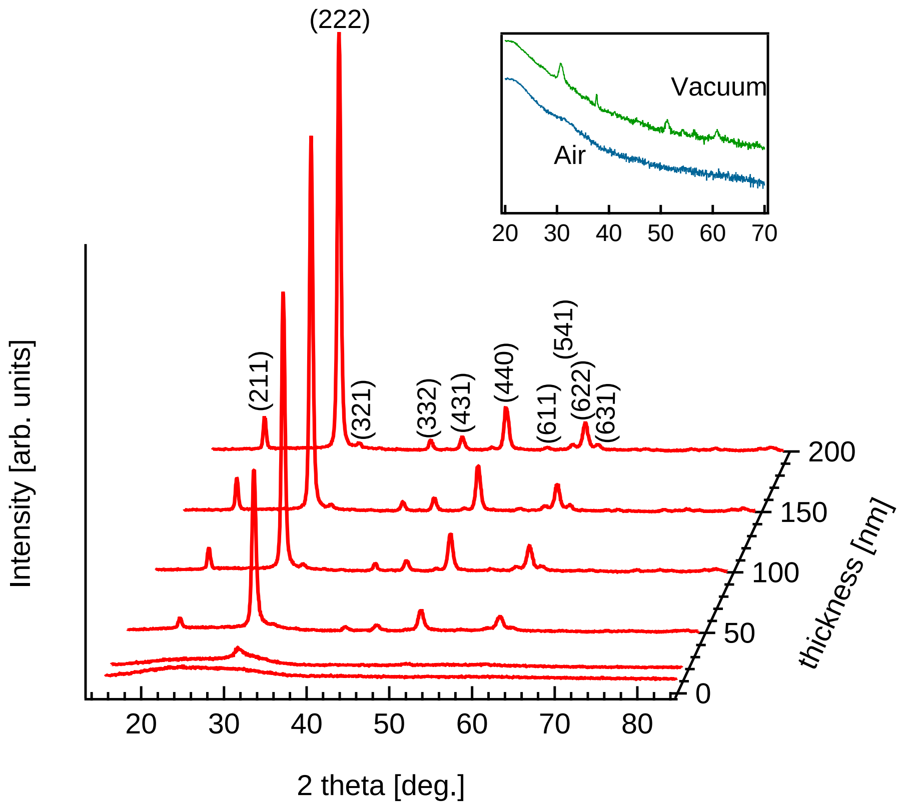

Figure 5.6: *Grazing Incidence XRD patterns of ITO films with different film thickness deposited at room temperature.The indexed lattice planes corresponds to those of cubic In_2O_3 (PDF card 00-006-0416-High-bcc). The insert shows grazing incidence diffraction patterns of two 10 nm thick films annealed at 200 °C in air (blue) or vacuum (green).*

from 10-200 nm deposited at room temperature, 200 °C and 400 °C, respectively, are shown in Fig. 5.7. It is apparent that the conductivity of the films generally increases with deposition temperature, whereby Hall effect measurements demonstrate that this is mostly due to an increase of carrier concentration. The dependence of carrier concentration on temperature can at least partially be attributed to different concentrations of oxygen interstitials. It is reasonable to state that less oxygen is incorporated in the films at higher deposition temperature, due to a lower residence time of oxygen on the growing film's surface.

The carrier mobilities, see Fig. 5.7(b), are rather independent on film thickness and substrate temperature with value ∼40 cm^2/Vs. This is not surprising for the films deposited at 200 °C and 400 °C, which have carrier concentrations near 10^{21} cm^{-3}. At such high carrier concentrations, grain boundary scattering, which is reducing the

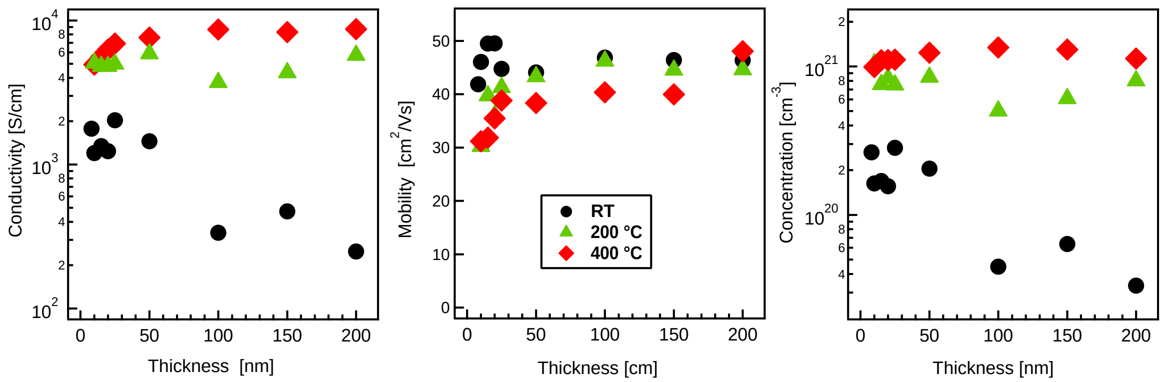

Figure 5.7: *Conductivity (a), carrier mobility (b), and carrier concentration (c) of ITO films deposited at room temperature, 200 °C, and 400 °C as a function of film thickness.*

mobility at carrier concentrations below ~10^{20} cm^{-3} [21, 40, 220, 221], is screened by the electron gas. The electron mobility is given by ionized impurity scattering, resulting in a carrier mobility of ~40 cm^2/Vs [58].

For the films deposited at room temperature, the situation is more complex. The carrier mobility of the thinnest films, which are amorphous, correspond well with those of amorphous ITO films reported in literature [222, 223, 217]. However, with increasing film thickness, the carrier concentration is reduced to values as low as $\sim 4 \times 10^{19}$ cm^{-3}. Given the polycrystalline nature of the thicker films deposited at room temperature, a lower carrier mobility is expected due to grain boundary scattering. The mobility of crystalline films with carrier concentrations $< 10^{20}$ cm^{-3} deposited at room temperature might be explained by a small grain size of the room temperature films. If the grains are very small, the depletion regions induced by the potential barriers at adjacent grain boundaries overlap. Thereby, the bending of the energy bands will be reduced. The potential barrier for grain boundary scattering is then reduced according to the Seto model, which assumes the potential barrier to correspond to the band bending [40, 220].

The conductivities of films deposited at different substrate temperature exhibit a different dependence on film thickness. For films deposited at 400 °C, the conductivity increases with film thickness. This can be explained by a thickness dependent change in grain size, which is common in film growth. In the presence of potential barriers at the grain boundaries, which are the origin of grain boundary scattering, the average carrier concentration decreases when the grains become very small as in the initial stage of growth. An opposite behavior with a conductivity decreasing with film thickness would be observed if the grain boundaries are more conductive than the grains, as it is the case for p-type Cu_2O [224].

The films deposited at room temperature exhibit a decrease of conductivity with increasing film thickness. This is due to the carrier concentration, which decreases by about one order of magnitude from 10 nm to 200 nm. On the one hand, the carrier concentration in the thinner (amorphous) films is determined by the coordination of the cations with oxygen, while the Sn-dopants remain ineffective. One might therefore expect that the carrier concentration increases once the films crystallize with increasing film thickness and thereby activate the Sn donors. However, for a very small grain size of the thicker (crystalline) films grown at room temperature, the depletion regions of adjacent grain boundaries overlap. This does not only decrease the band bending, which affects the carrier mobility, but also decreases the average carrier concentration. While this is suggested to be the main reason for the lower carrier concentration of the thicker (crystalline) films deposited at room temperature, a higher oxygen incorporation may also contribute to this observation.

5.4.1.2 Post Annealing Treatments

In the previous section it has been suggested that the low electrical conductivity of films deposited at room temperature is mostly determined by their microstructure, which is characterized by a very small grain size. In order to confirm this hypothesis, in-operando Hall effect measurements have been conducted during annealing of films deposited at room temperature. In order to follow the changes in conductivity, carrier concentration and mobility, samples were heated in vacuum (10^{-5} Pa) or in air with a rate of 0.5 K/min up to 200 °C and hold at that temperature for 1 hour. The results obtained for ITO films of 10 and 200 nm thickness are shown in Fig. 5.8.

The changes in conductivities, carrier mobilities, and carrier concentrations during heat treatment in vacuum or air are almost identical for the 200 nm thick films. The starting conductivity of the two samples is different by about a factor of 2. This is mainly due to the difference in carrier concentration as demonstrated by Hall effect (see Fig. 5.8). Meanwhile, in the beginning of the heat treatment, the two samples have the same mobility. During heat treatment, the conductivity first decreased by a factor of 2 and then increased by factor of $\sim$3 for both samples. The carrier concentration increases by about a factor of 2 and the carrier mobilities decrease first by a factor of 2 before they increase again slightly. Both carrier concentration and mobility saturate after 1 hour at 200 °C.

The comparable behavior upon annealing in vacuum and air indicates that the changes in carrier concentration are not related to a change in oxygen content, as the latter should depend on the annealing atmosphere. The fact that the oxygen content of the 200 nm films is not changing upon annealing is consistent with DFT calculations of oxygen diffusion [225] and with in-operando Hall effect measurements of crystalline ITO

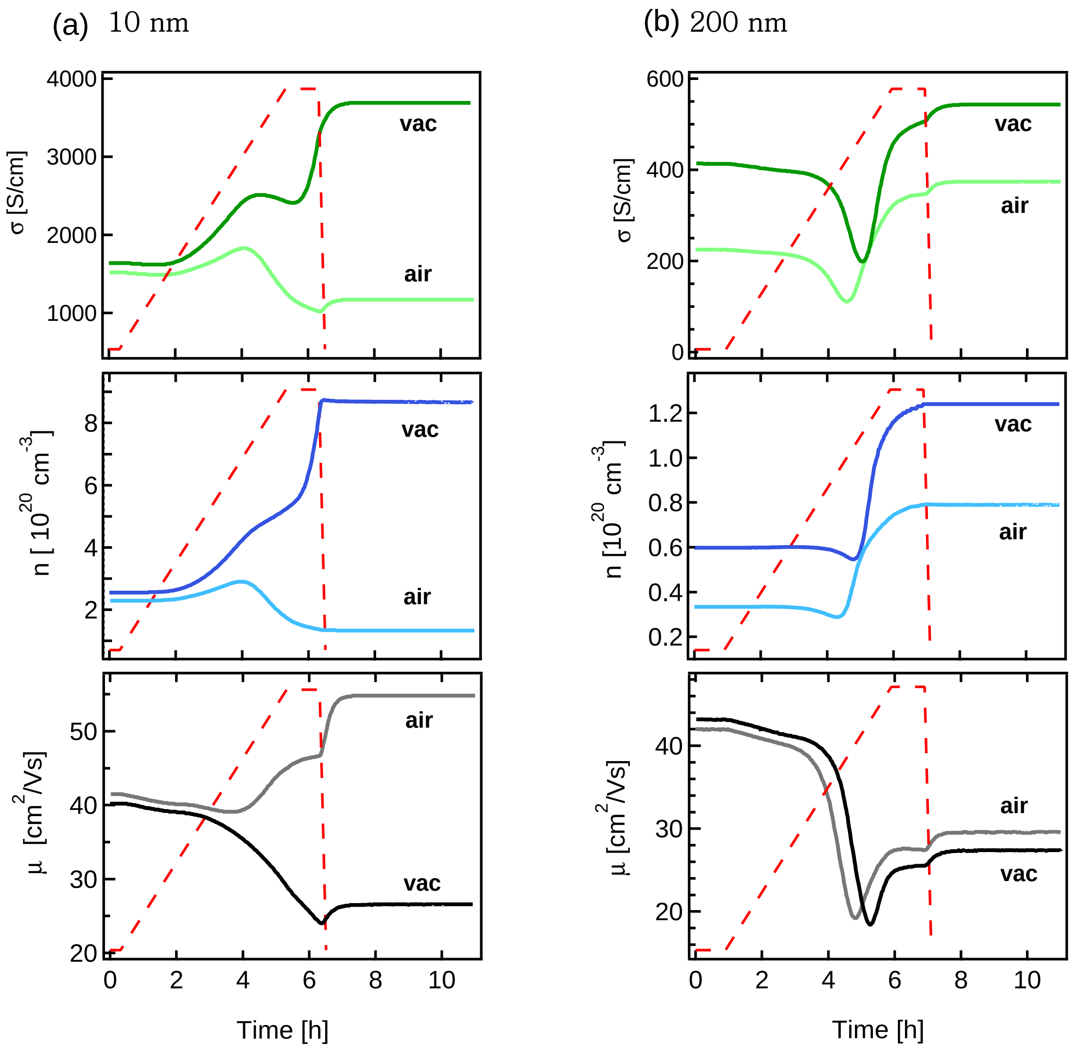

Figure 5.8: *Conductivity, carrier concentration, and carrier mobility measurements during annealing of 10 and 200 nm thick ITO films deposited at room temperature in vacuum or in air. The red dashed lines show the programmed temperature with a controlled heating ramp from 25 °C-200 °C and a holding time of 1 hour at 200 °C.*

films [192], which indicate that oxygen diffusion at 200 °C is not fast enough.

Crystallization and grain growth can explain the increase of carrier concentration and the decrease of mobility upon heat treatment of the 200 nm thick films. Crystallization of amorphous regions, which might still be present in the 200 nm thick films deposited at room temperature, would activate the Sn donors [216, 222] and thereby increase the carrier concentration. An increased carrier concentration will narrow the space charge regions at grain boundaries. The overlap between space charge regions of neighboring grain boundaries will therefore be reduced and the band bending within the grain will be increased. This results in an increase of the average carrier concentration and an increase of the band bending between grain boundaries as illustrated in Fig. 5.9. The latter explains the decrease of carrier mobility. Grain growth will also have a similar effect.

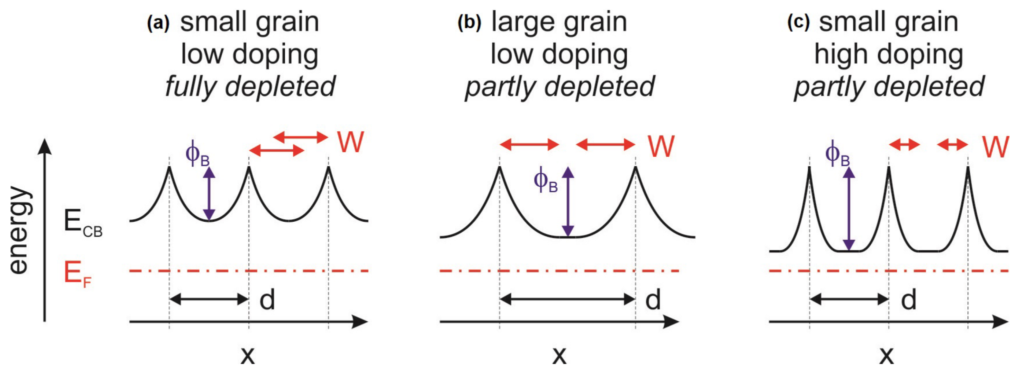

Figure 5.9: *Energy band diagram of n-type polycrystalline semiconductor with depleted electron concentrations in the space charge layers at grain boundaries. The positions of grain boundaries are indicated by dashed vertical lines. For small grains (a), when the width of the space charge region (W) exceeds half of the distance between the neighboring grain boundaries ($d < 2W$), the potential profiles of neighboring grain boundaries overlap as indicated by the red arrows. The width of space charge region is ∼5 nm for a doping concentration of 10^{20} cm^{-3}. The potential barrier at the grain boundary (Φ_B), which corresponds to the band bending , increases with grain size (b) or doping concentration (c). Smaller grains can therefore exhibit lower effective carrier concentrations and higher carrier mobility.*

In contrast to the 200 nm thick film, the annealing behavior of the 10 nm thick films is drastically different for annealing in vacuum and air. Annealing in vacuum results in a behavior, which is similar to that of the 200 nm thick films. The conductivity of the vacuum annealed sample increases with heat treatment, while for air annealed sample the conductivity decreased after initial increase during heating. Hall effect measurements show that this is mostly due to the carrier concentrations. For vacuum annealed sample, the carrier concentration increased by about a factor of 3 upon annealing treatment. Meanwhile, after an initial increase during heating, the carrier concentration of 10 nm thick sample decreases during annealing in air. Hall effect measurements also reveal that, in contrast to thicker films, for vacuum annealed samples both the carrier concentration and the mobility do not saturate after 1 hour at 200 °C. The different carrier concentration after annealing in vacuum and in air indicates that the effective doping concentration in the films increases during annealing in vacuum. This is consistent with the much higher increase of carrier concentration of the 10 nm vacuum annealed film compared to that of the 200 nm thick films. Not only the increase is much higher, also the starting level is much higher.

The annealing atmosphere has also an effect on the crystallization behavior, which is illustrated in the insert of Fig. 5.6. Grazing incidence X-ray diffraction only shows lattice reflections after annealing in vacuum. The film annealed in air remains amorphous, for reasons which remain unclear. The different crystallinity is also reflected by the change of carrier mobility during cooling of the samples at the end of the annealing process (see Fig. 5.8). The air annealed (amorphous) film shows a much higher increase of mobility with decreasing temperature, as expected due to the ionized impurity scattering. A lower or even inverted, temperature dependence indicates the presence of grain boundary scattering [21]. Grain boundary scattering should thus not contribute to the temperature dependence of the air annealed 10 nm film, which is consistent with the amorphous structure.

The decrease of carrier concentration and increase of mobility during air annealing of the 10 nm thick film can both be explained by incorporation of oxygen. Medvedeva and coworkers have clearly demonstrated that the carrier concentration in amorphous doped In_2O_3 films is determined by the oxygen stoichiometry [222]. Addition of oxygen will therefore reduce the carrier concentration and by the concomitant reduction of ionized impurities, also raise the mobility.

Two effects can contribute to the increase of doping concentration during vacuum annealing of the 10 nm thick film: i) the activation of the Sn dopants due to crystallization and ii) the extraction of oxygen. It has been argued above that the latter is not important for the 200 nm thick films. However, the time τ required to establish equilibrium by bulk diffusion (of oxygen) depends on the square of the film thickness L and is given by Eq. 5.1 [226]:

$$\tau = \frac{L^2}{\pi^2 D} \tag{5.1}$$

where, D is the diffusion coefficient. It is therefore not unlikely that oxygen diffusion can be important for very thin films, but not for thicker ones, at 200 °C .

To further check whether the removal of oxygen contributes to the strong increase of carrier concentration of the 10 nm film during vacuum annealing, an extended annealing experiment has been carried out. The measurement is shown in Fig. 5.10.

In contrast to the behavior shown in Fig. 5.8, there is a clear saturation of carrier concentration and mobility after $\sim$ 15 hours annealing at 200 °C. The carrier concentration saturated with a values n $\approx 1.05 \times 10^{21}$ cm^{-3}, which is higher than those observed for deposition at 200 °C, see Fig. 5.7. After cooling down to room temperature, a conductivity of 4520 S/cm is reached. This is the same magnitude as those obtained with films of the same thickness at higher deposition temperatures. Vacuum annealing is therefore

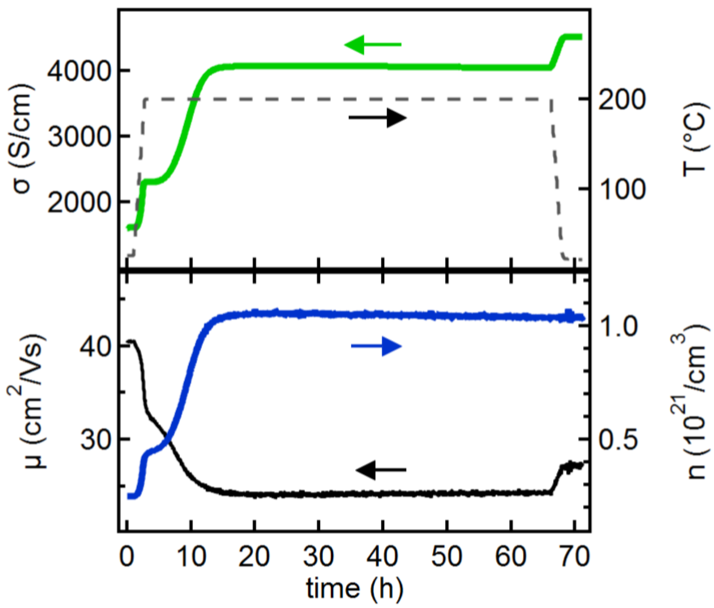

Figure 5.10: *Conductivity and Hall effect measurements during extended annealing of a 10 nm thick ITO film deposited at room temperature in vacuum. The black dashed lines show the programmed temperature with a controlled heating ramp from 25 °C to 200 °C and a holding time of ∼67 hours at 200 °C.*

suitable to obtain highest conductivities with very thin films. However, the required annealing times are rather long, as shown by the presented in-operando Hall effect study. The in-operando measurements demonstrate that annealing experiments with fixed (shorter) annealing times and post-anneal analysis can only provide a snapshot of the effects of annealing. This makes an analysis of the origin of the changes of electrical properties by fixed time annealing experiments very difficult.

The very high carrier concentrations reached after long vacuum annealing of the 10 nm film can only be reached if oxygen is extracted from the films during annealing. This can be concluded by comparison with ITO films grown under identical process conditions at room temperature but on Fe_2O_3 seed layers [223]. The Fe_2O_3 seed layers strongly enhance crystallization at room temperature, which results in a substantial increase of carrier concentration and conductivity due to donor activation and increased grain size. The carrier concentrations reached with Fe_2O_3 seed layers are, however, lower than 6.5 $\times$ 10^{20} cm^{-3}. Donor activation by crystallization is therefore not sufficient to explain carrier concentrations higher than 10^{21} cm^{-3} reached by vacuum annealing. The effect of annealing in dependence on film thickness and atmosphere is summarized in Fig. 5.11.

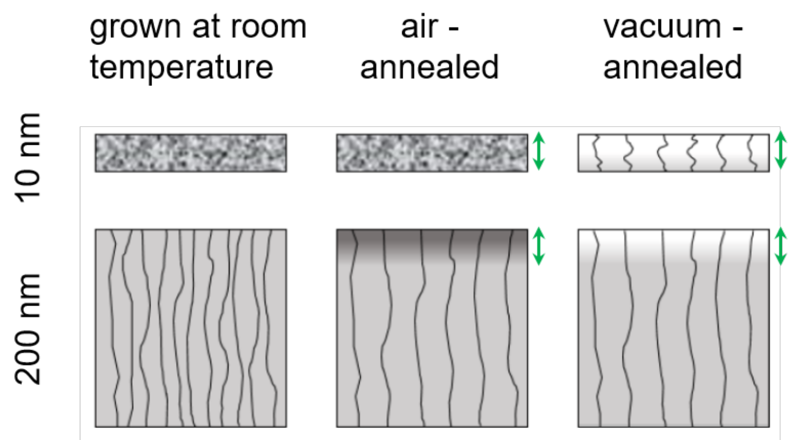

Figure 5.11: *Effect of annealing of 10 and 200 nm thick ITO films deposited at room temperature. The annealing was performed with a heating rate of 0.5 K/min up to 200 °C and a holding time of 1 h either in vacuum or in air. Curved lines indicate grain boundaries and fill color the oxygen concentration. The filling style of the as-grown 10 nm thick sample indicates an amorphous structure.*

5.4.2 The effect of ALD-Al_2O_3 coating

RT ITO / ALD-Al_2O_3

Conductivity and Hall effect measurements performed on ITO films deposited at room temperature are shown in Fig. 5.12 together with those obtained after Al_2O_3 deposition. Data for uncoated samples are the same as those in Fig. 5.7. After Al_2O_3 deposition, the conductivity of the films is lower / higher than without Al_2O_3 for films thinner / thicker than ∼15 nm. This behaviour is contradictory to defect modulation doping, which has been shown to increase the conductivity for 10 nm thick SnO_2 films [8]. Modulation doping should affect only the near interface region. No substantial change of electrical properties is therefore expected for thicker films.

The carrier concentration is increased by Al_2O_3 deposition, independent on film thickness, in accordance with the raise of the Fermi level, see Fig. 5.4. The highest carrier concentrations of $n \approx 8 \times 10^{20}$ cm^{-3} are obtained for 20 and 25 nm thick films. It is the increase of carrier concentration, which explains the increase of conductivity by Al_2O_3 deposition for films thicker than 15 nm. For films thinner than 15 nm, the reduction of conductivity by Al_2O_3 deposition is caused by a significant lowering of the mobility.

The Al_2O_3 deposition is performed in a vacuum chamber at 200 °C and involves heating of the samples in vacuum before and during exposure to the process gas. The heating process in vacuum strongly affects the electrical properties as demonstrated in section 5.4.1.2. To discriminate between the effects of annealing and Al_2O_3 deposition, additional samples were annealed in the ALD chamber under the conditions present during the ALD process, just without exposure to TMA and H_2O. This annealing referred to as ALD-anneal here, is shorter than the one performed in the Hall effect setup, which has been discussed in section 5.4.1.2. Conductivity and Hall effect measurements performed after the ALD-anneal are also shown in the Fig. 5.12.

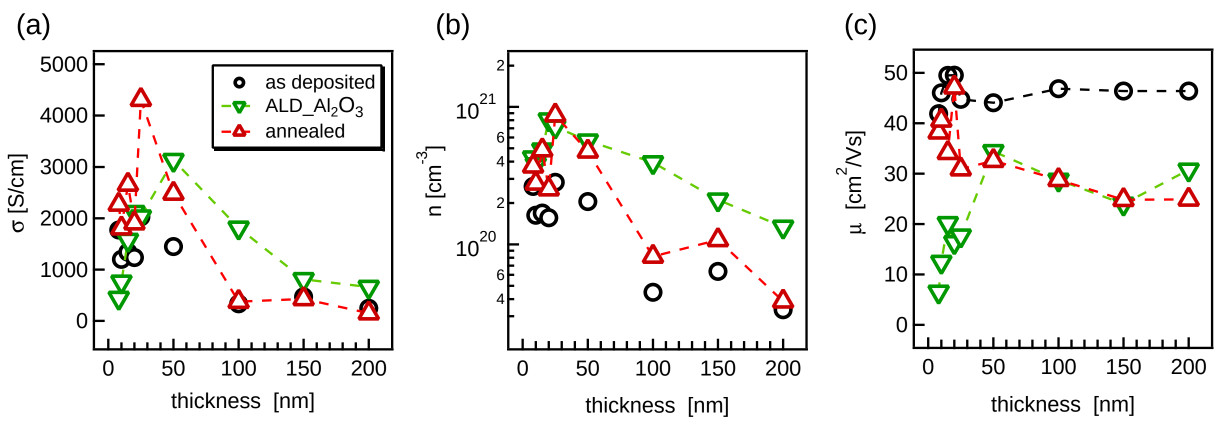

Figure 5.12: *Conductivity (a), Carrier concentration (b), carrier mobility (c); as a function of film thickness of ITO films deposited at room temperature (black circles), ITO films deposited at room temperature after ALD- Al_2O_3 deposition (green inverted triangles), and ITO films deposited at room temperature after annealing in the ALD chamber (ALD-anneal) in vacuum at 200 °C (red triangles). The data of the room temperature films are the same as those in Fig. 5.7. The dashed line are guide for the eyes.*

The dependence of carrier concentration on film thickness after the ALD anneal is comparable to the behaviour described in section 5.4.1.2. Except for the 200 nm thick film, the carrier concentrations of thicker films are 10^{20} cm^{-3}. For thinner films values of up to 8×10^{20} cm^{-3} are reached. This behavior has been explained in section 5.4.1.2 by grain growth and, for the thinner films, by donor activation and oxygen extraction. Up to an ITO thickness of 50 nm, the carrier concentrations of the ALD-annealed samples and of those coated with Al_2O_3 are the same within the experimental uncertainty. This again rules out the presence of modulation doping. For films thicker than 50 nm, the Al_2O_3-coated films exhibit higher carrier concentrations than the ALD-annealed ones. Apparently, the exposure to Al_2O_3 is more reducing than vacuum annealing alone, in agreement with the partial reduction of the films observed by XPS.

Al_2O_3 deposition results in a strong reduction of mobility for samples with thickness < 50 nm. This reduction is not related to the high temperature but must be caused by the ALD process. It is probably related to the chemical reduction of the film, which is indicated by $Sn3d_{5/2}$ and $In3d_{5/2}$ core levels in Fig. 5.3. The strong reduction of the film might increase grain boundary potential barriers, which have been related to reduction of Sn to Sn^{2+} at the grain boundaries [21]. Extraction of oxygen from grain boundaries would then increase the density of trapping centers and increase the potential barrier height. As the effect will be restricted to the surface region due to the limited diffusivity of oxygen at 200 °C, the observed increase of mobility of the Al_2O_3 coated films with ITO thickness is reasonable.

In summary, the results show that deposition of 5-cycles of ALD-Al_2O_3 on RT ITO films does not result in a modulation doping. This is most likely related to the high mobility of defect species. The annealing experiments discussed in section 5.4.1.2 clearly demonstrate that oxygen defects are sufficiently mobile to diffuse several nanometers during processing at the Al_2O_3 deposition temperature of 200 °C. The compensating oxygen interstitial defects will then diffuse towards the interface to screen the potential difference induced by the high Fermi energy at the interface [227]. The condition required to enable defect modulation doping, which is the kinetic suppression of equilibrium concentrations, is not fullfield with ITO at 200 °C. Lower processing temperatures for ALD deposition, which has been demonstrated in literature [228, 229], would be required.

High temperature ITO / ALD-Al_2O_3

Another batches of ITO thin films were prepared at elevated temperatures of 200 and 400 °C from the old target with film thicknesses of 10, 20, 50, and 200 nm. For both deposition temperatures, films with thickness range of 10-50 nm were prepared using 0.5% O_2 and 99.5 % Ar as a processing gas, while 200 nm thick films were deposited in pure Ar environment. The conductivity and Hall effect measurements of these films together with those obtained after Al_2O_3 deposition are displayed in Fig. 5.13. In general, by comparing the films with the same deposition temperature and film thickness, uncoated ITO films prepared from the old target exhibit inferior electrical properties than those prepared from the new target (see also Fig. 5.7 and Fig. 5.13 for comparison).

The conductivity of ITO films deposited at 200 °C from the old target decreases with film thickness for the first three films in the series (10-50 nm). Meanwhile, 200 nm thick film showed higher conductivity. Hall effect measurements revealed that this is mainly due to carrier concentration, in which the concentration decreased from $\sim 2.5 \times 10^{20}$ cm^{-3} for 10 nm to $\sim 9 \times 10^{19}$ cm^{-3} for 50 nm, and finally it increased to $\sim 3.5 \times 10^{20}$ cm^{-3} for 200 nm thick film. The decrease of carrier concentration with the

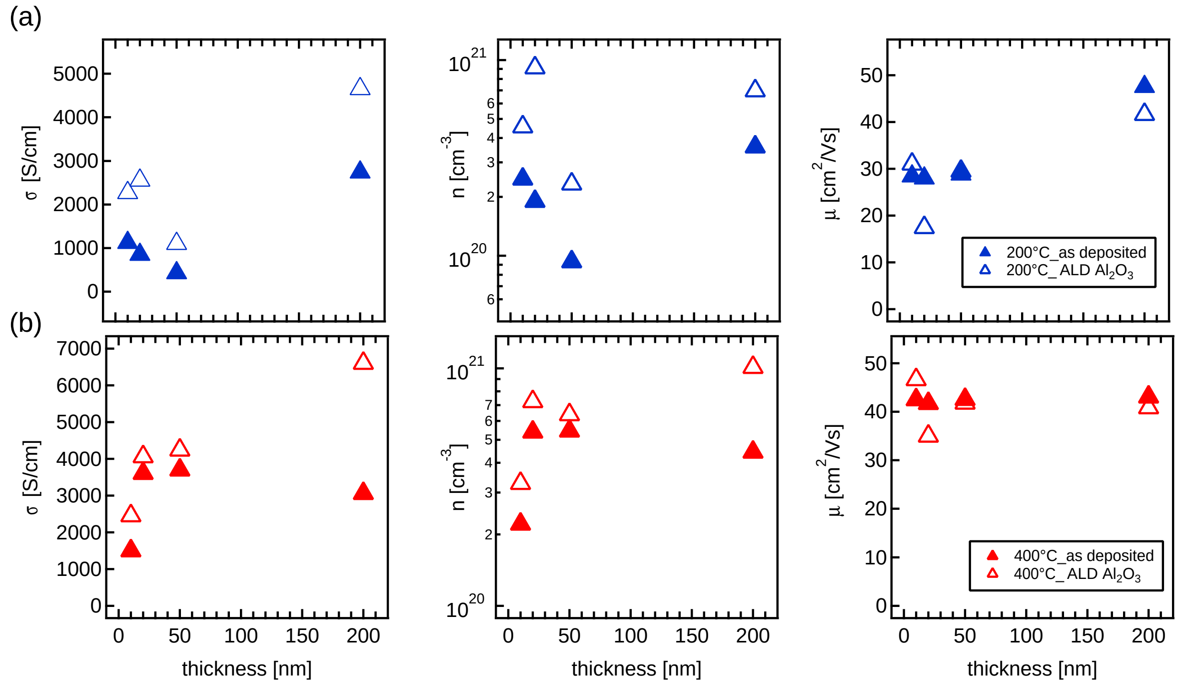

Figure 5.13: *Conductivity (a), carrier concentration (b), and carrier mobility (c) as a function of film thickness of ITO films deposited at 200 °C (blue triangles) and 400 °C (red triangles) with (empty triangles) and without (filled triangles) 5-cycle ALD Al_2O_3 coating. Note: all Hall effect data presented here are from the samples prepared from old target.*

film thickness of the first three films can be explained by higher oxygen incorporation during deposition, as the samples are prepared in oxidized environment. In addition, the grain size of these films is expected to be small. For small grains, the depletion regions of adjacent grain boundaries overlap leading to a decrease of an effective carrier concentration the material (see also Fig. 5.9(a)). On the other hand, the higher carrier concentration of 200 nm film is explained by the formation of bigger grain size and by the deposition process, which takes place in reducing condition. The carrier mobilities of these films do not change for thinner films, 10-50 nm ($\approx$ 28 cm^2/Vs) and increased to $\approx$ 48 cm^2/Vs for 200 nm thick film. In contrast, ITO films prepared from the new target (with comparison of the same thickness and deposition temperature) have a carrier concentration of $\geq 8 \times 10^{20}$ cm^{-3} and mobility of ∼40 cm^2/Vs.

The scenario is different for the films deposited at 400 °C. For these films, the conductivity and carrier concentrations increased with increasing the film thickness. The thinner films exhibited lower carrier concentration compared to the thicker ones. This can be explained by the thickness dependent change in the grain size. In the presence of potential barriers at the grain boundaries, the average carrier concentration ($\bar{n}$), is determined by the integral of the local carrier concentration according to the expressions in Eq. 5.2:

$$\bar{n} = \frac{1}{d}\int_0^d n(x)d(x) = \frac{1}{d}\int_0^d \int_{E_{CB}(x)}^{\infty} N_C(E)\frac{1}{1+\exp^{(E-E_\mathrm{F}/K_BT)}}dEdx \tag{5.2}$$

where, $N_C(E)$ is the density of states in the conduction band.

According to Eq. 5.2, the average carrier concentration is therefore decreased for very small grains, as this is the case for thinner films. Even though, the trend of increasing conductivity as a function of film thickness is the same for the films prepared from both targets, films from the new target exhibit higher conductivity with values about a factor of 2 and that of carrier concentrations of $\approx 1 \times 10^{21}$ cm^{-3}, which indeed is higher than what is measured for old target.

In contrast to the films prepared at 200 °C, the carrier mobilities of 400 °C films are independent of film thickness with values ∼42 cm^2/Vs. The fact that, the reduction of the potential barriers at the grain boundaries and narrowing enough for tunneling of highly doped semiconductors with carrier concentrations of $\sim 10^{21}$ cm^{-3}, is valid here. In this case, the carrier mobility is then no longer reduced by the grain boundary potential barriers, but solely determined by ionized impurity scattering. This scenario explains that the carrier mobility of the films deposited at 400 °C which have a carrier concentrations of $\geq 2 \times 10^{21}$ cm^{-3}, is largely independent of film thickness. Similar observations are reported in [21, 58]. As it is described above, the films from the new target exhibit much higher conductivity as high as a factor of 13 compared to those prepared from the old target, see Fig. 5.7. The origin of different electrical properties of films grown from the two targets, which have the same nominal composition and deposition conditions, remains unclear.

5-cycle of ALD-Al_2O_3 deposition on ITO substrates results in enhanced electrical conductivity, independent of film thickness or deposition temperatures. This is caused by an increase of carrier concentration in accordance with the upward shift of Fermi energies, see Fig. 5.4. Meanwhile, the carrier mobilities seem not much sensitive to alumina coating. The changes in μ showed similar trends for both temperatures. For 10 nm films, μ increased slightly, while it decreased for 20 nm and 200 nm films. No changes are observed for 50 nm sample.

In summary, compared to RT films, ITO films deposited at elevated temperatures of 200 °C and 400 °C exhibited an enhanced electrical properties. This is due to crystallization, grain growth, and activation of Sn-donors for the films grown at the higher temperature. Al_2O_3 coating of these films resulted in a slight increase of conductivity. This is mainly due to an increase of carrier concentrations, as mobilities seem insensitive to alumina coating. The conductivity values obtained after alumina coating are still lower than that of uncoated ITOs from the new target Fig. 5.7. Even though an increase of conductivity and carrier concentration is observed for these films, we can not conclude the modulation effect is demonstrated. In comparison to what is reported for SnO_2 [8] the changes of σ and n are moderate. The chemical reduction of ITO substrates also rule out the modulation doping.

5.4.2.1 Post annealing treatments

In order to assess the incorporation / extraction of oxygen on ITO films and to further investigate the effect of 0.5 nm ALD-Al_2O_3 coating on oxygen exchange, in-operando conductivity measurements have been conducted during thermal treatments of ITO films together with those of ALD-Al_2O_3 coated samples. ITO films were deposited at different substrate temperature of from RT to 400 °C from the old target while the film thickness was varied between 10 nm and 200 nm. In order to follow the change in conductivity, the samples were heated in Ar gas[3] with a rate of 100 K/h up to 500 °C and hold at that temperature for 5 minutes and finally cooled down with the same rate. The resulting conductivity measuements are presented in Fig. 5.14, together with the temperature profile, which are shown in red dashed line. According to Friscbbier [193], the actual temperature in the probed samples can deviate up to 20 °C for such high annealing temperature.

Table 5.2: Purity of Ar gas used as annealing environment

Designation	**purity / foreign gasses**
Ar	99.999 %
	O_2 < 2 parts per million (ppm)-mol
	H_2O < 2 ppm-mol
	N_2 < 5 ppm-mol
	CO_2 < 0.2 ppm-mol
	Hydrocarbons < 0.2 ppm-mol

An annealing temperature of 500 °C was chosen because oxygen is mobile enough in ITO and oxygen exchange between the surfaces of ITO layer and the environment would be possible at this temperature. This was already demonstrated to occur at lower

[3] the purity/quality of Ar gas used during annealing is summarized in Tab. 5.2

temperature of 300 °C [192, 225] . Post annealing treatments of the ITO samples up to 500 °C are expected to result in the following changes depending on initial deposition conditions: complete crystallization of the films; increase of grain size; activation of tin donors; and segregation of Sn in grain boundaries. In addition, depending on the annealing environment, possible gas exchange is expected between ITO surface and the surrounding.

ITO films deposited at room temperature with different film thicknesses show a similar trend of changes in electrical conductivity upon heat treatment Fig. 5.14(a). The conductivity of 10 nm film showed an initial sharp decrease by about a factor of 3 during heating step at ≈300 °C, then a steep increase about a factor of 7.5 exhibited at 500 °C. The conductivity then decreased during cooling to almost the value at the start of annealing treatment. These conductivity changes can be explained by: microstructural change (as the film becomes crystalline during heating), activation of Sn donors, donor migration to the surface, and possible oxygen exchange with the environment (see also the discussion in section 5.4.1.2). During heating step, crystallization and activation of Sn, are the upside for an increase of carrier concentration (n) and thereby conductivity. Meanwhile, at an elevated temperature of 500 °C, segregation Sn to the grain boundaries is inevitable for degenerately doped TCOs like ITO [21, 35, 192], which would reduce donor concentration in the grain. Segregation of Sn to the grain boundaries is indicated by Hall effect measurement at ∼ 500 °C [192] and the reversible Sn segregation also observed at temperature as low as 300 °C in high -temperature near -ambient-pressure XPS measurements [35]. The enhanced influence of grain boundaries on electron transport in highly Sn-doped In_2O_3 is therefore associated with segregation of Sn to the grain boundaries. Sn impurities can be present in a +4 or/and +2 oxidation state. Under reducing condition (high temperature annealing), segregation of Sn to the grain boundaries may particularly occur as Sn^{2+} state. Sn^{2+} constitute acceptor states, which are responsible for electron trapping at grain boundaries Sn^{2+} state.

Surface oxygen exchange is also expected to be occur during the heat treatment. The sharp decrease of conductivity at ≈ 300 °C can be explained by an incorporation of oxygen, which reduces the carrier concentration. Originally the sample has been prepared under effectively reducing conditions. It can be expected that oxygen concentration is far from equilibrium. Once exposed to the gas atmosphere[4] at temperatures where diffusion is fast enough, an equilibrium oxygen concentration can be established. Further increasing of the heating temperature to 500 °C results in an increase of conductivity as oxygen species are extracted from the surface of the film, which could be attributed to the temperature dependence of oxygen chemical potential (as higher temperature corresponds to a more reducing atmosphere at the same oxygen partial pressure). Similar observations have been reported by Frischbier et al. [192]. Finally, during cooling step, oxygen reincorporated at the surface of ITO, which results in a decrease of conductivity

[4]N.B, the percentage of oxygen is very low in the annealing gas

together with the other influencing factors described above.

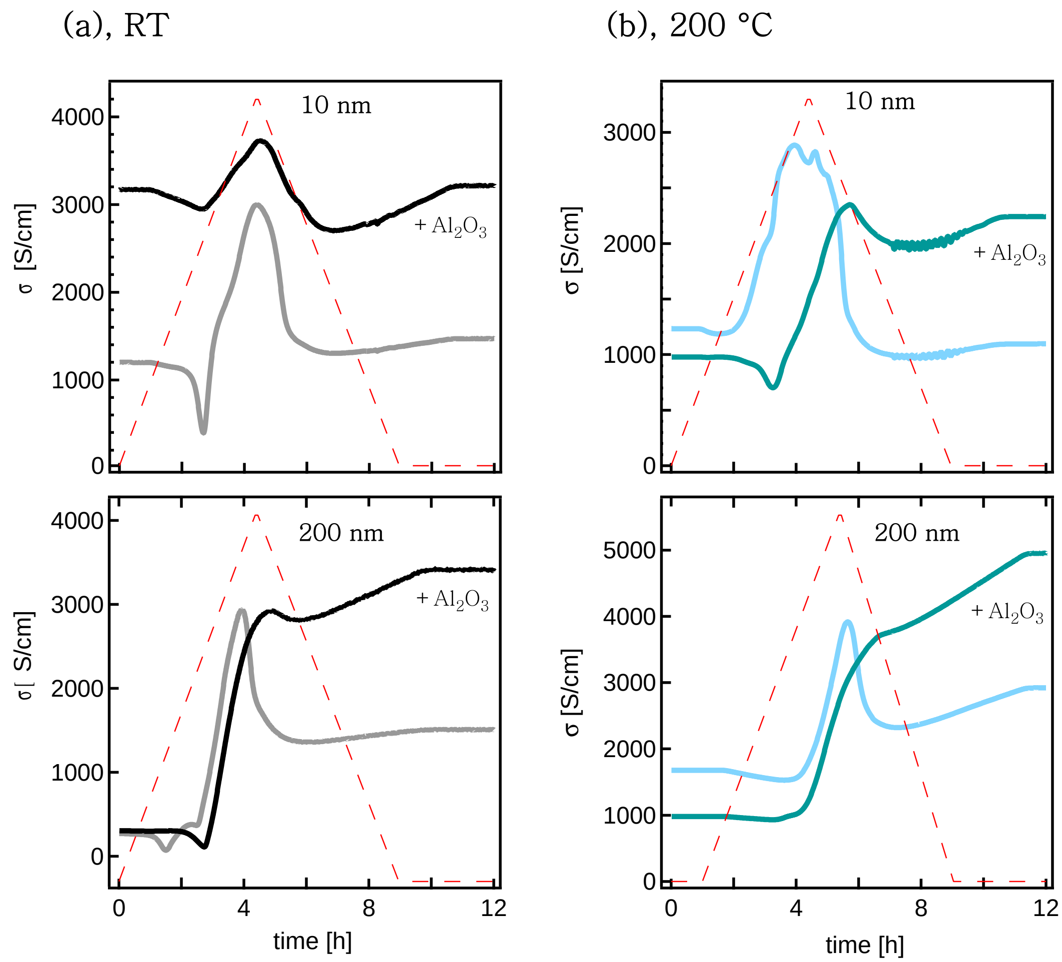

Figure 5.14: *Conductivity relaxation measurements during annealing of uncoated and AlD-Al_2O_3 coated ITO films prepared in different conditions. ITO films were deposited at substrate temperature of RT (a) and 200 °C (b) with thickness in the range of 10-200 nm. Annealing was performed using Ar gas. The green dashed lines show the programmed temperature with a controlled heating ramp from 25 °C-500 °C and holding time of 5 minutes at 500 °C. Note that additional conductivity relaxation measurements are performed on RT (20 nm and 50 nm) and 400 °C (10 nm and 200 nm) films in the same annealing conditions. Although the images are not displayed in this figure, the observed conductivity changes are discussed in the text of section 5.4.2.1.*

The other RT ITO films (20, 50, and 200 nm) also show a similar trend of changes of conductivities during heat treatment (see Fig. 5.14(a)[5]). Here as well, crystallization, grain growth (for thicker films), Sn donor activation, dopant segregation at the

[5]Here, conductivity relaxation measurements of only 10 nm and 200 nm are presented.

grain boundaries, and surface oxygen exchange contributed to the changes of electrical properties. An initial a step decrease at ≈300 °C during heating, a sharp increase until 500 °C, and steep decrease during cooling step are observed. However, the extent of the valley at ≈300 °C decreased with increasing film thickness and almost disappeared for 200 nm film. In addition, the conductivity of heat treated samples did not return to the values at the beginning of the treatment, specially for 200 nm thick film the σ increased by a factor of ∼5.5 after the heat treatment. This phenomenon could also be explained by the dependence of (oxygen) bulk diffusion on the square of film thickness according to Eq. 5.1. Thus, during the cooling step, the kinetics of oxygen exchange is much slower for 200 nm film than that of thinner films, especially for 10 nm (more detailed description of this phenomenon can be found section 5.4.1.2).

Interestingly, Al_2O_3 coating resulted in different conductivity behavior upon heat treatments. During heating step both alumina coated and uncoated films exhibit a similar trend of change in conductivity. Meanwhile, during cooling step, alumina coated samples showed different conductivity behavior. For 200 nm sample, in contrast to the uncoated film, the conductivity increased for alumina coated film during the cooling step (see the bottom image of Fig. 5.14 (a)). This can be attributed to the fact that alumina coating passivate ITO surface and blocks oxygen incorporation on to the surfaces of the film. Similar behavior have been observed for the thinner 20 and 50 nm Al_2O_3 coated samples. However, this effect is not observed for 10 nm sample.

ITO films deposited at 200 °C are expected to be crystalline and have an enhanced carrier concentration due to Sn donor activation. Post annealing treatment of these films at 500 °C will then result in a complete crystallization, grain growth (for thicker films), Sn segregation, and oxygen exchange at the surface; which in turn have an effect on the electrical properties. At the beginning of the measurement, ITO films deposited at 200 °C exhibit room temperature conductivities shown in Fig. 5.14(b), which are in a good agreement with the results presented in Fig. 5.13. 10 nm samples show a steep increase of conductivity during heating after very slight decrease at ≈ 300 °C and reached an increase of σ by about a factor of 2 at 500 °C. The conductivity then decreased during the whole cooling step and have a final RT conductivity slightly lower than the value recorded at the beginning of the heat treatment. 200 nm ITO sample also have a similar trend of changes in conductivity as that of 10 nm sample. Meanwhile, unlike 10 nm sample the decrease of conductivity during cooling step is not drastic. Comparing the RT value at the start of the annealing, the conductivity value increased by about a factor of ∼2 after the heat treatment. As in the case of RT ITO films, these different conductivity behavior during cooling step is related to the kinetics of interstitial oxygen diffusion between ITO layer and the surrounding as a function of square of film thickness.

As in the case of RT films, here as well, ALD-Al_2O_3 coated samples behave differently, see Fig. 5.14(b). At the beginning of the heating step both 10 and 200 nm films exhibited a conductivity values much lower than the values recorded during RT Hall effect measurements Fig. 5.13 [6]. Similar to other probed samples, the conductivity σ increased during heating step and in contrary to uncoated ITO, the conductivity of these samples did not decrease during cooling step rather kept unchanged for 10 nm and further increased for 200 nm Al_2O_3 coated ITO films. The argument that Al_2O_3 coating acts as a passivation layer and blocks oxygen incorporation during cooling step of the heat treatment is valid here as well.

Similarly, different uncoated and Al_2O_3 coated ITO films deposited at 400 °C with thickness of 10 nm and 200 nm are examined during heat treatment. Due to the issue with contact electrode, conductivity relaxation was recorded only for alumina coated 10 nm ITO sample. For other samples only the values before or/and after the annealing process are recorded. The 10 nm alumina coated sample showed slight increase in σ during ramping step and a decrease of almost half during cooling step. This is in contrary to the results obtained for other alumina coated samples as oxygen is incorporated during the cooling step of heat treatment, which resulted in a decrease of conductivity. Uncoated 200 nm thick ITO film showed a decrease of σ by about half during heat treatment. While, for alumina coated 200 nm film, heat treatment does not change σ atleast as the results before and after annealing treatment are very comparable.

In summary, indeed annealing of the probed samples to 500 °C resulted in several structural and electrical conductivity changes on uncoated and ALD-Al_2O_3 coated ITO films. During heat treatment the following main phenomena are expected to be occur on the probed films.

- Change in microstructure: complete crystallization of films deposited at room temperature and 200 °C. But, for the films prepared at 400 °C it is expected for them to be crystalline during deposition. Along with crystallization of the films the possible grain growth is expected during heat treatment.

- Activation of Sn donors, which results in an increase of carrier concentration and that of conductivity. This effect is more pronounced for the films deposited at lower temperatures (RT and 200 °C). For the films deposited at 400 °C, Sn donors are already activated during deposition and post annealing of these films may not lead to further activation.

- Segregation of Sn to the grain boundaries: Sn impurities can be present in a

[6] the two measurements were preformed in few weeks difference and the samples were placed in dry and clean sample boxes. Hence, it is not expected for the sample to loss its electrical property during storage/aging

+4 or/and +2 oxidation state. Under reducing condition (the annealing process followed), segregation of Sn to the grain boundaries may particularly occur as Sn^{2+} state. Sn^{2+} constitutes acceptor states, which are responsible for electron trapping at grain boundaries.

- Even though, the the heat treatment was performed in pure Ar environment, there was some ppm[7] impurity gases including oxygen[8]. Hence, it is expected to have oxygen exchange during heat treatment. During heating step, initially slight decrease of conductivity exhibited for most of studied films at around 300 °C and this can attributed to the possible oxygen incorporation into ITO films. Further increase of annealing temperature resulted an extraction of oxygen from the layers of samples and increases of conductivity. Finally, oxygen reincorporated during cooling step. In contrast, this is not the case for Al_2O_3 coated films, unlike uncoated films, alumina coated films does not show a decrease of conductivity (for most of the probed samples) during cooling step and this could attributed to passivation of ITO layer and blocking the oxygen diffusion into the surface of ITO by alumina coating. These influences of oxygen exchange on the conductivity of the probed samples is summarized in Fig. 5.15.

	Step I Heating (25 °C – 500 °C)								**Step II Cooling (500 °C – 25 °C)**			
	200 °C – 300 °C				**300 °C – 500 °C**				**500 °C – 25 °C**			
	ITO		ITO + Al_2O_3		ITO		ITO + Al_2O_3		ITO		ITO + Al_2O_3	
	10 nm	200 nm	10 nm	200 nm	10 nm	200 nm	10 nm	200 nm	10 nm	200 nm	10 nm	200 nm
σ	↘↘ O_2 incorporation	↘ O_2 incorporation	↘ O_2 incorporation	↘ O_2 incorporation	↗ O_2 extraction	↗↗ O_2 extraction	↗ O_2 extraction	↗↗ O_2 extraction	↘↘ O_2 reincorporation	↘ O_2 reincorporation	↗→ passivation	↗↗ passivation

Figure 5.15: *Summary of explanations for the changes in conductivity (σ) of different uncoated and ALD-Al_2O_3 coated ITO films. The summary only considered the effect of oxygen exchange, other effects like crystallization, grain growth, Sn segregation, and donor activation are not included for the sake of simplicity. In addition, only the thinnest (10 nm) and thickest (200 nm) films are reported.*

[7] parts per million

[8] see Tab. 5.2

5.5 Summary and Conclusion

In this chapter, the effect of Al_2O_3 deposition by ALD on interfacial and electrical properties Sn-doped In_2O_3 (ITO) thin films has been described. The study developed by correlating the microstructural, interfacial and electrical study of ITO films prepared in different deposition conditions with and without Al_2O_3 deposition. Several post deposition treatments were then followed to discriminate different effects, which govern the changes of carrier concentrations and mobility. The finding of this chapter emphasizes on the following points:

- GIXRD revealed only the thinnest ITO films deposited at room temperature are completely amorphous. The intensity of diffraction peaks increases with increasing film thickness. This is due to ion bombardment effect and gradual increase of substrate temperature with deposition time through heat of convection.

- Films deposited at room temperature exhibit significantly lower conductivities compared to films deposited at 200 °C and 400 °C. The differences are caused by different carrier concentrations, while the mobilities are rather insensitive on deposition temperature and film thickness.

- The carrier concentration of room temperature deposited films decreases with film thickness. As the carrier mobility is not affected by the reduced carrier concentration, which would be expected for grain boundary scattering, the reduction of n has been assigned to the formation of very small grains with overlapping space charge regions.

- Room temperature deposited amorphous 10 nm thick and crystalline 200 nm thick films have been annealed either in vacuum or in air at 200 °C. Conductivity and Hall effect measurements were recorded during the complete annealing cycles. The thicker films exhibit a slight increase in carrier concentration and reduction of mobility during annealing, regardless of the annealing atmosphere. The changes can be explained by grain growth. A change of effective doping concentration by variation of the oxygen content is not indicated for the thicker films.

- In contrast to the 200 nm thick films, the evolution of electrical properties of the 10 nm thick films inevitably involves a change of oxygen concentration, indicating that oxygen diffusivity (and surface exchange) is fast enough for 10 nm thick films. Extraction of oxygen during annealing in vacuum therefore results in a substantial increase of carrier concentration by almost an order of magnitude up to $n > 10^{21}$ cm^{-3}, while incorporation of oxygen during annealing in air results in a decrease of carrier concentration. It is noted that, in contrast to annealing in vacuum, annealing in air does not lead to crystallization of the 10 nm thick films. The differences might be related to the different changes of oxygen content in dependence on annealing atmosphere.

- Different influencing factors, which contribute to the change in electrical properties of RT ITO films during annealing at 200 °C in different environment are summarized in Fig. 5.16.

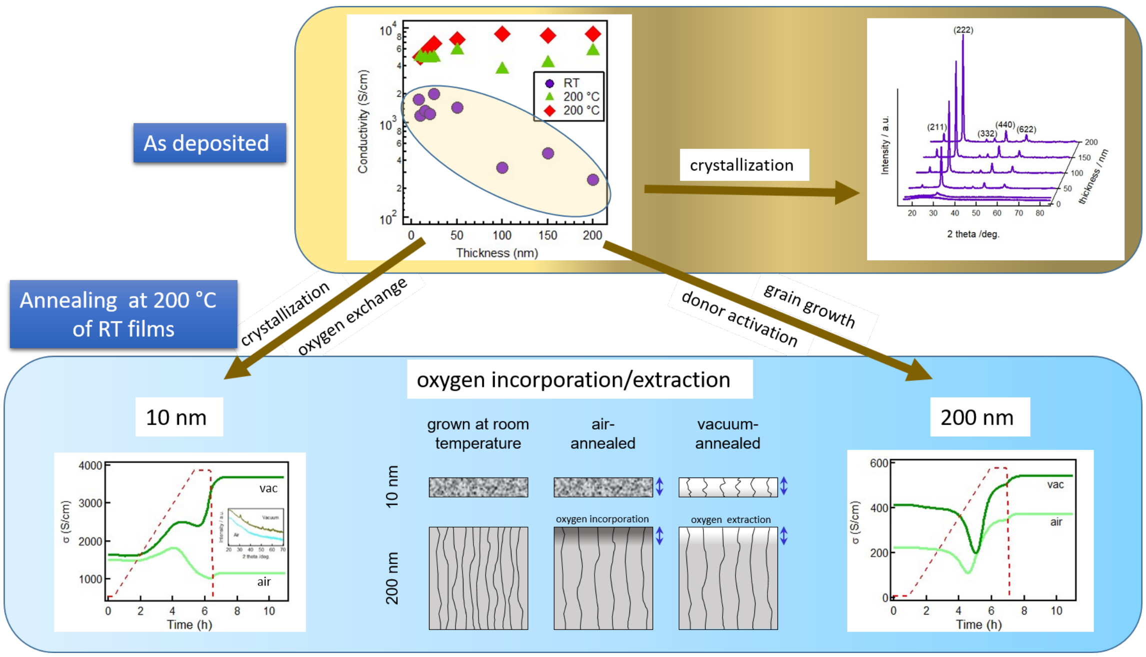

Figure 5.16: *Summary for different effects, which contribute to the change in electrical properties of RT ITO during annealing at 200 °C either in vacuum of air. For simplicity only the thinnest (10 nm) and thickest (200nm) are represented.*

- During annealing at 200 °C, diffusion of oxygen does therefore only affect a very thin region near the surface of thicker films. Manipulation of the carrier concentration in thicker films is therefore not possible at this temperature. However, the remaining diffusivity of compensating oxygen defects at 200 °C is sufficient to screen the high Fermi level induced by deposition of Al_2O_3 using atomic layer deposition thereby preventing defect modulation doping.

- The XPS measurements revealed the upward shift of Fermi energy of ITO films after Al_2O_3 deposition. This upward shift indicates the presence of surface electron accumulation. But, Al_2O_3 deposition also resulted in the chemical reduction of ITO substrates, which also contributes to the rise of Fermi energy.

- Additional annealing experiments were conducted at 500 °C on both Al_2O_3 coated and uncoated ITO films in Ar gas with few ppm oxygen impurity. After the heat treatment, alumina coated films exhibit higher conductivity than uncoated ITO. This is due to the fact that Al_2O_3 was acted as a passivation layer and blocks oxygen reincorporation during cooling step of heat treatments.

- Additional ITO films were prepared at 200 °C and 400 °C with Al_2O_3 deposition. The carrier concentrations were increased following Al_2O_3 deposition. Eventhough, the slight increase of n was an upside for these films, the chemical reduction of ITO substrates rule out modulation doping.

- In a nutshell, this work provides a more detailed understanding of the processes, which determine the carrier concentrations of ITO films processed at substrate temperatures where oxygen diffusion is strongly but not completely suppressed.

In conclusion, it was found that realization of defect modulation doping is not possible on ITO films under the current deposition conditions of Al_2O_3, as diffusion of oxygen interstitials, which are counter acting high Fermi energies, were not kinetically suppressed during Al_2O_3 deposition. To overcome this problem, low temperature deposition processes with a very low oxygen activity could be an option. If low temperature deposition is applied for ITO, the inherently small grain size of low-temperature grown films has to be overcome, as this clearly limits the carrier concentration. The use of seed layers, such as the recently demonstrated Fe_2O_3 [223], might be a solution for this. On the other hand, performing ALD deposition at lower temperature is also still possible. Here, it must be noted that ALD must be done at a temperature within the "ALD of Al_2O_3 window" to avoid condensation and incomplete reactions.

Chapter 6

Defect Modulation Doping for Sputtered In_2O_3 by ALD-Al_2O_3

6.1 Introduction

This chapter will focus on testing *defect modulation doping (DMD)* by using undoped TCO, namely In_2O_3[1] as a host material and coverage of ultra thin ALD-Al_2O_3 as a potential dopant with the aim of inducing conduction electrons in the interface near region of In_2O_3. For this purpose different In_2O_3 thin film samples were prepared with and without ALD-Al_2O_3 coating. The prepared samples were examined using in-situ photoelectron spectroscopy for near surface properties as well as using ex-situ electrical conductivity measurements. The chapter is divided in the following sections.

Section 6.2, shortly describes the experimental procedures followed during thin film preparation. The thin films were prepared with different deposition conditions; In_2O_3

[1] The test of DMD on Sn-doped In_2O_3 thin films can be found in Chapter 5

was deposited with different film thickness, substrate temperature, and processing gas. Similarly, the dopant Al_2O_3 layers were prepared with different numbers of ALD cycles. In order to discriminate the influence's of these different deposition conditions on the near surface and bulk properties, in-situ photoelectron spectroscopy, conductivity and Hall effect measurements were performed. The photoemission results will be presented in section 6.3. Photoemission comparisons for the important core levels and the Fermi energies in relation to macroscopic electrical properties will also be addressed in this section. Conductivity and Hall effect results of the studied samples will be presented in section 6.4. Finally, the main points of the chapter will be summarized and concluded in section 6.5.

6.2 Sample preparation

In_2O_3 films were deposited in oxide II of DAISY MAT [12] on quartz glass substrates by magnetron sputtering with radio-frequency (RF) excitation. The background pressure of the deposition chamber was 10^{-6} Pa. A ceramic 2 inch In_2O_3 target, a RF power of 25W, a process pressure of 0.5 Pa, a processing gas flux of 6.6 sccm Ar as well as fluxes of Ar/O_2 (99.5%/0.5%) and a target-to-substrate distance of 10 cm were used for deposition. The film thickness of In_2O_3 was varied from 20–200 nm and the substrate temperature during deposition from 200 to 600 °C. Films deposited at 200 and 400 °C were grown with fluxes of Ar/O_2 (99.5%/0.5%). Additional samples were prepared at deposition temperatures of 400-600 °C in a pure argon environment.

Table 6.1: Deposition parameters of In_2O_3 and In_2O_3 /ALD-Al_2O_3 thin films

In_2O_3/ALD-Al_2O_3 thin films							
Sample	In_2O_3				ALD-Al_2O_3		
	Target	Pprocess gas	Temp. (°C)	Thickness (nm)	Precursor	ALD-cycle	Temp. (°C)
In_2O_3	In_2O_3	Ar and 99.5% Ar/0.5 % O_2	200-600	8-200	-	-	-
In_2O_3/ALD-Al_2O_3	In_2O_3	Ar and 99.5% Ar/0.5 % O_2	200-600	8-200	TMA and H_2O	1-20	200

Ultra thin ALD-Al_2O_3 coatings were deposited using a low-pressure process in a separate vacuum chamber with a background pressure of 10^{-6} Pa. The description of the setup and the deposition conditions can be found in subsection 4.1.2. 1 to 20-cycles of Al_2O_3

were deposited on different In_2O_3 samples, with corresponding thicknesses of $\approx$ 0.1 to 2 nm, respectively. The deposition conditions are summarized in Tab. 6.1.

6.3 Photoemission

Core level spectra of the O1s, In3d$_{5/2}$, Al2p and XPS valence band regions recorded for 20 nm In_2O_3 thin films deposited at substrate temperature of 200-600 °C using processing gases of either pure argon or an Ar/O_2 (99.5%/0.5%) gas mixture and coated with 5-cycles of ALD-Al_2O_3 are shown in Fig. 6.1. The spectra of uncoated In_2O_3 deposited at 200 °C in Ar/O_2 (99.5%/0.5%) gas mixture is also presented for comparison.

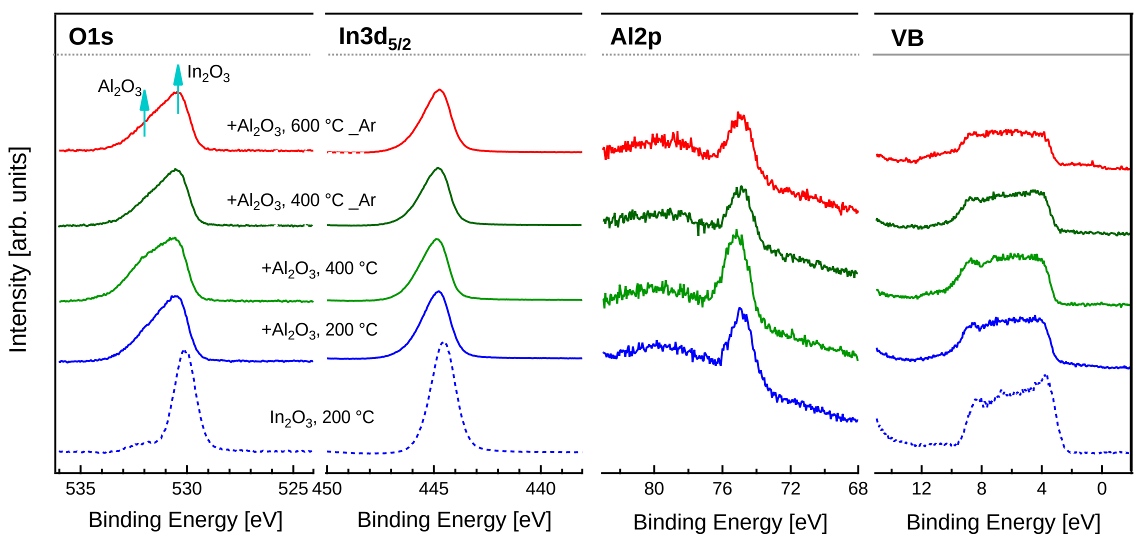

Figure 6.1: *XP (AlKα) detail spectra of O1s, In3d$_{5/2}$, and VB regions for 20 nm thick In_2O_3 films deposited at the substrate temperatures of 200-600 °C with processing gas of either pure Ar or Ar mixed with 0.5 % of O_2 and coated with 5-cycles of ALD-Al_2O_3. For the films deposited at 200 °C the spectra from both with and without ALD-Al_2O_3 coating are represented for comparison.*

The O 1s level of the uncoated In_2O_3 show a pronounced second emission at a binding energy of $\sim$ 532.5 eV, which is associated with adsorbed species as the sample is prepared in with oxygen in the sputter gas. Similar shoulders have been reported on the spectra of bulk and thin film In_2O_3 either prepared with oxygen in the sputter gas or heat tretaed in the oxidized conditions [213]. Exposing *in situ* prepared films to air can also lead to an increase in intensity at the higher binding energies in the O1s peak.

By deposition of Al_2O_3, the intensities of In3d core level emissions are attenuated due to the coverage of the substrate with Al_2O_3, while the O 1s intensity remains approximately constant due to the increase of Al_2O_3-related emission at the higher binding energy of $\sim$ 532 eV. The clear peak of Al_2O_3-related emission can be seen for 10-cycles of ALD-Al_2O_3 deposition [38].

After Al_2O_3 deposition, the $In3d_{5/2}$ core level spectra of the studied samples show a clear asymmetry towards the higher binding energies. These changes in line shape are accompanied by small binding enegry shifts, which are in the same direction and are thus attributed to the changes of Fermi level position at the surface. The changes in line shape can be interpreted by the interaction of photoemisson core holes with the conduction electrons [35, 196, 198, 199, 200, 201]. In particular the asymmetry is the result of inelastic scattering process of the photoelectrons due to excitation of plasmons. The plasmon energy depends on the electron concentration and is typically 0.5 - 1 eV in highly Sn-doped In_2O_3 films [61, 200]. The binding energy of Al2p emissions corresponds well with the value expected for Al_2O_3 [197]. The shape of valence band changed from the characteristic shape of In_2O_3 towards observed for Al_2O_3 [38, 95, 213].

In order to study the influences of Al_2O_3 layer thickness on the near surface and bulk properties of In_2O_3, additional samples were prepared using different number of ALD-cycles (1, 5, 10, and 20) during Al_2O_3 deposition, which were coated on the top of 20 nm In_2O_3 prepared at 400 °C in Ar/O_2 (99.5%/0.5 %) gas mixture. The core level spectra of O1s, $In3d_{5/2}$, Al2p, and XPS valence band regions of the studied samples are displayed in Fig. 6.2. The O1s level of the uncoated In_2O_3 shows a slight secondary emission at a binding energy of $\sim$ 532.5 eV, which is associated with the adsorbed species. However, the intensity of this peak is smaller compared to the sample prepared in the same condition, but at 200 °C (see Fig. 6.1).

By deposition of Al_2O_3, the O1s level shows a comparable difference in line shape and shifting of binding energies as a function of increasing the number of ALD-cycles. When the number of ALD-cycles increased from 1 to 20 cycles, the O1s peak associated to In_2O_3 is attenuated, and a new peak associated with Al_2O_3 appears at higher binding energy. The growth of Al_2O_3 layer is indicated by the steady increase of the Al2p intensity. In return, the intensity of the In3d core level is attenuated. The shape of valence band changes from the characteristic shape of In_2O_3 [213] towards the one observed for films covered with Al_2O_3 [38, 95].

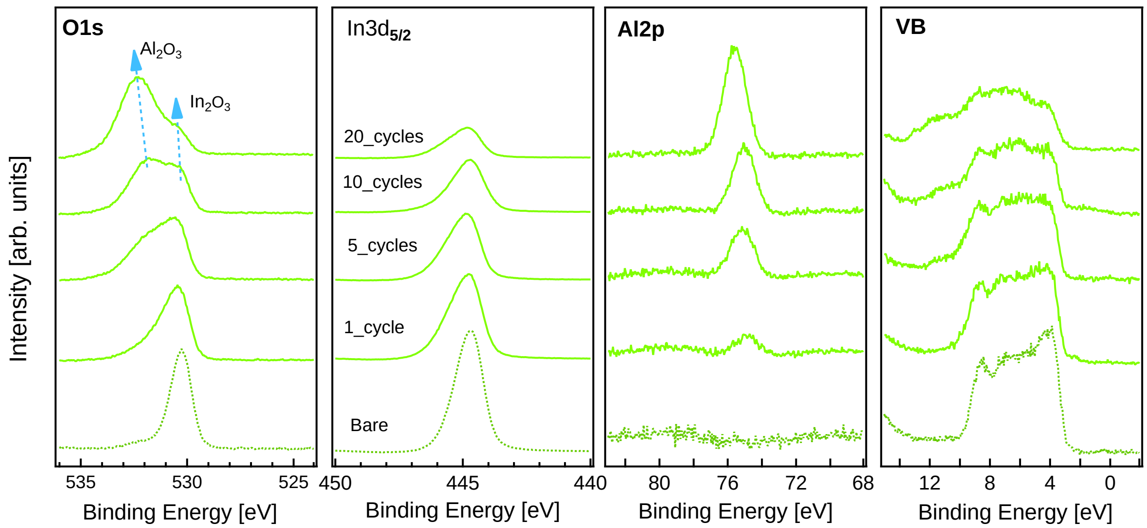

Figure 6.2: *XP (AlKα) detail spectra of O1s, In3d$_{5/2}$, and VB regions for 20 nm thick In_2O_3 films deposited at 400 °C with processing gas of 99.5 % Ar and 0.5 % of O_2 and coated with 1-20 cycles of ALD-Al_2O_3. The spectra of uncoated sample is also represented for comparison.*

The Fermi level at the surface

The Fermi level position strongly varies at In_2O_3 and Sn-doped In_2O_3 surfaces and can have values E_F-E_{VB} = 2.2 - 3.5 eV depending on the preparation conditions [35, 38]. The absolute position of the Fermi level with respect to the band edges of the studied films are directly determined from the valence band maxima, as the binding energies are calibrated such that zero binding energy corresponds to the Fermi level position. Additional values are extracted from the core levels by using core level to valence band maximum energy differences of 71 eV (Al2p), 441.8 eV (In3d), and 527.39 eV (O1s). The determined surface Fermi level position (E_F-E_{VB}) of In_2O_3 thin films deposited at 200 and 400 °C in Ar/O_2 (99.5%/0.5 %) gas mixture, with a film thickness of 20-200 nm together with the one covered with 5-cycles of ALD-Al_2O_3 are displayed in Fig. 6.3 (a). To study the influence of Al_2O_3 layer thickness, additional 20 nm In_2O_3 films were deposited at 400 °C and covered with different cycles [2] of ALD-Al_2O_3 layers. The Fermi energies of these films are also presented in the same figure. Additional samples of 20 nm In_2O_3 deposited at 400-600 °C in a pure Ar gas together with 5 and 10-cycles of ALD-Al_2O_3 are presented in Fig. 6.3 (b).

For uncoated In_2O_3 films deposited at 200 °C, the Fermi energy of 20 nm sample is lower

[2] 1-20 ALD-cycles corresponds to the thickness of 0.1-2 nm of Al_2O_3 coverage

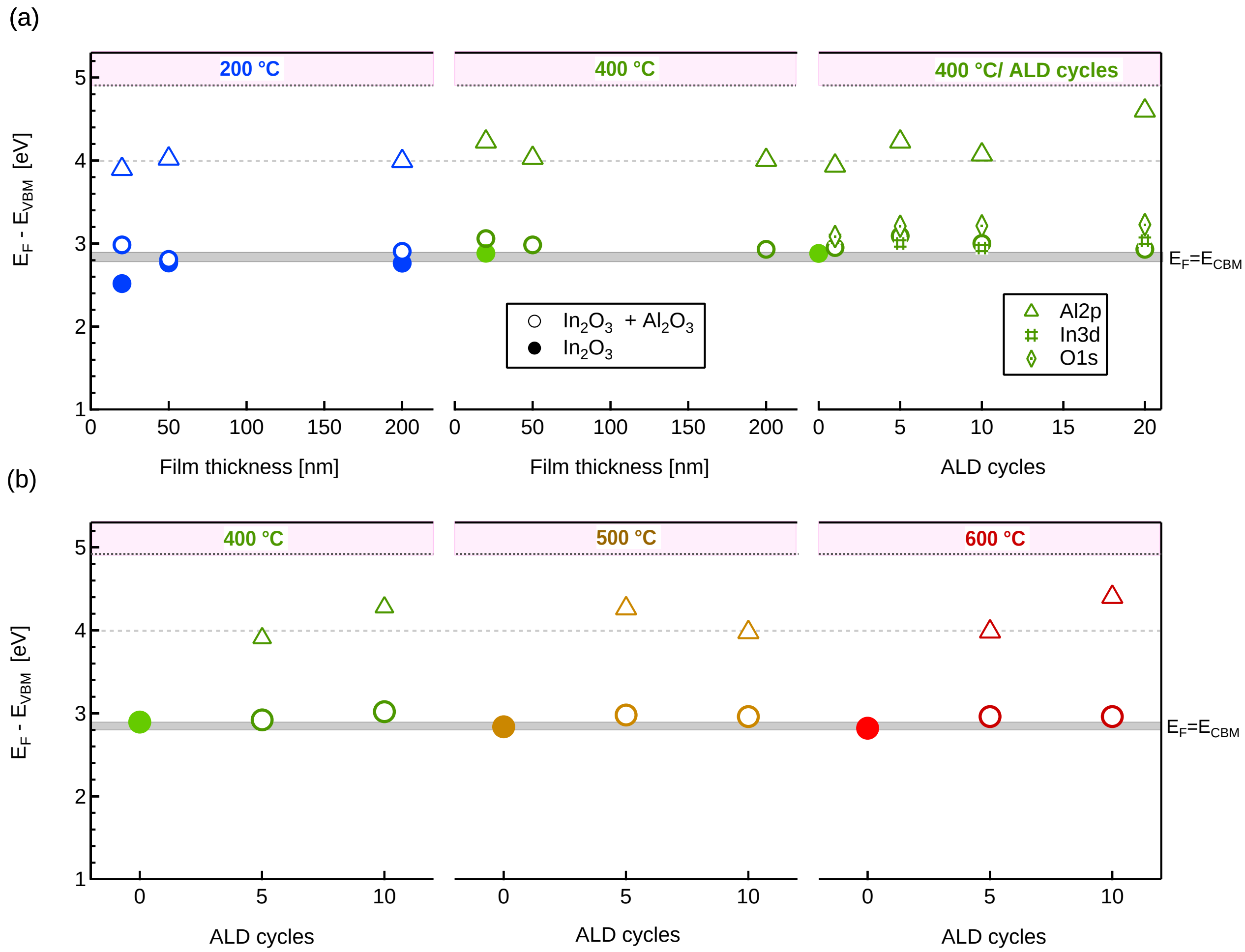

Figure 6.3: *XP (AlK_α) induced photoelectron spectra of surface Fermi level position determined either directly from valence band maxima or by using core level to valence band maxima energy difference of 71 eV (Al2p), 441.8 eV (In3d), and 527.39 eV (O1s) for (a), In_2O_3 thin films deposited at 200 °C and 400 °C, with a film thickness of 20, 50, and 200 nm using Ar/O_2 (99.5 %/O_2 %) gas mixture in the processing gas and with 5-cycles of ALD-Al_2O_3. For 20 nm In_2O_3 films deposited at 400 °C, the influence of the number of ALD cycles also reported for 1-20 cycles: (b), 20 nm In_2O_3 thin films deposited at 400-600 °C in pure Ar together with 5 and 10-cycles of ALD-Al_2O_3. The gray bar indicate the E_F=E_{CBM} value of 2.8-2.9 eV according to [108]. Additional gray dashed line at 4 eV is used to indicate the extracted Fermi energies in Al_2O_3. Each data points represent different samples.*

than that of 50 nm and 200 nm thick films. This corresponds with the higher electron concentration of thicker films compared to the thinner ones. For the films deposited at 400 °C, the Fermi energy does not change with film thickness, as both 20 and 200 nm samples exhibit E_F-E_{VB} of ≈ 2.9 eV. Similarly, for the 20 nm In_2O_3 films deposited at elevated temperatures of 400 - 600 °C in a pure Ar gas, the Fermi energy does not change with increasing deposition temperature and exhibit a value of 2.8-2.9 eV.

Al_2O_3 deposition resulted an upward shift of the Fermi energy in all studied samples. This upward shift indicates the presence of surface electron accumulation. By taking into account the higher Fermi energy of ALD-Al_2O_3 films deposited in DALSY-MAT of ≈ 4-4.5 eV [8, 38, 94, 95] (this is true for the studied films, as the Fermi energies in Al_2O_3 lies between 3.9 eV and 4.6 eV, see Fig. 6.3) and the expected very small valence band offset between In_2O_3 and Al_2O_3 [98], the Fermi energy in In_2O_3 is regarded as likely to raise to E_F-E_{VB} of ≥ 4 eV after Al_2O_3 deposition. However, this is not the case as the binding energies of the In_2O_3 corresponds only to E_F-E_{VB} ≈ 2.9 ± 0.1 eV.

In order to study the influence of Al_2O_3 layer thickness, different In_2O_3/ALD-Al_2O_3 thin films were prepared by varying the number of ALD-cycles. For In_2O_3 films deposited at 400 °C in Ar/O_2 (99.5%/0.5%) gas mixture, 1, 5, 10, and 20-cycles of Al_2O_3 were deposited. The Fermi energies of these films is presented in the right graph of Fig. 6.3 (a). The Fermi energies are extracted both directly from the valence band maxima and from In3d and O1s (corresponding to In_2O_3) core levels, which have values of 2.9-3.1 eV. Thus, there is no trend of change in Fermi level position of In_2O_3 in accordance with change in the number of ALD cycles. However, this is not the case for the Fermi energies in Al_2O_3, as it changed from 3.95 eV for 1-cycle to 4.6 eV for 20-cycles of Al_2O_3. Similarly, The Fermi energies of In_2O_3 films deposited in pure argon at 400 °C, 500 °C, and 600 °C and coated with 5 and 10 cycles of ALD-Al_2O_3 are shown in Fig. 6.3(b). The Fermi energies in In_2O_3 lies between 2.9 eV and 3.0 eV after both 5 and 10 cycles of Al_2O_3 deposition. However, the Fermi energies in Al_2O_3 increase from 3.9 to 4.3 eV for 400 °C, decreased from 4.3 to 4 eV for 500 °C, and increased from 4 to 4.4 eV for 600 °C films by changing the Al_2O_3 layer thickness from ≈ 0.5 nm (5-cycles) to ≈ 1 nm (10-cycles) respectively.

As it was the case in ITO/ALD-Al_2O_3 system (see also section 5.3), the discrepancy between the expected and the measured Fermi energies of Al_2O_3 covered In_2O_3 films might be explained by the formation of a very narrow space charge region (δ) at the surface of In_2O_3. Because of the high doping level of the In_2O_3, the depletion layer (δ) should be confined to a few Ångstroms from the surface [110]. This is narrower than the depth probed by XPS as a result, the Fermi level directly at the surface can not be observed. Therefore, by taking the recently determined band gap of In_2O_3 E_g = 2.8 - 2.9 [108], the determined surface Fermi energies are found in ± 0.1 eV of conduction band minimum. This is represented by the energy scheme in Fig. 6.4.

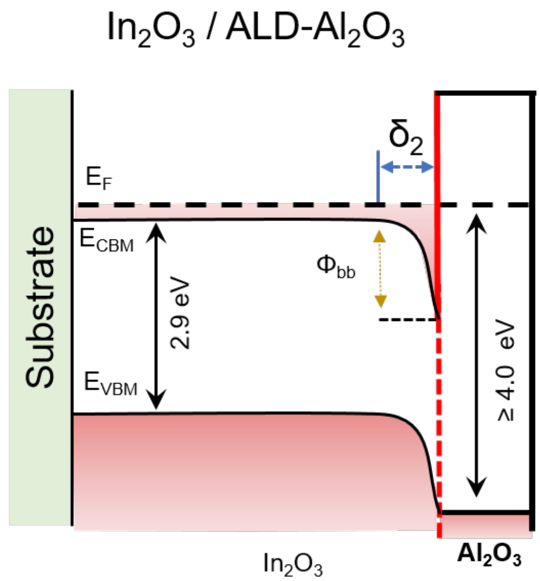

Figure 6.4: *Electronic structure of the surface of undoped In_2O_3/ALD-Al_2O_3 system. The width of space charge layer (δ), which depends on the doping of the material can be as narrow as $\approx$ 1nm for high doping level of In_2O_3.*

6.4 Electrical study

It is well known that nominally undoped bulk crystal and thin films of In_2O_3 exhibit a high level of n-type conductivity [116] with a carrier concentrations in the range of 10^{18} - 10^{20} cm^{-3}. Like other binary oxides such as ZnO, unintentional n-type conductivity in In_2O_3 has been attributed to the presence of native defects such as O vacancies and In interstitials[3] [27, 123]. All intrinsic point defects in indium oxide, including vacancies, interstitals and antisites have shallow states and are capable of producing free electrons in the conduction band. Ágoston et al. [225] calculated V_O to be indeed a shallow donor using hybrid-functional method within DFT, and showed that its diffusivity is high enough to provide the necessary oxygen exchange with the ambient at elevated temperatures. From the experimental point of view, both the non-stoichiometry and n-type conductivity have been assigned to doubly charged oxygen vacancies $V_\mathrm{O}^{\bullet\bullet}$ [117]. This is indicated by the characteristic oxygen partial pressure dependence ($\sigma \sim p_{\mathrm{O}_2}^{-1/6}$) of free electron concentration.

[3]More detailed information on the defect structure of In_2O_3 could be found in subsection 3.1.3

6.4.1 Moderate Temperature Deposited Films

The conductivities of undoped In_2O_3 films prepared at substrate temperatures of 200 and 400 °C in Ar/O_2 (99.5%/0.5 %) gas mixture with a film thicknesses of 20, 50, and 200 nm together with those covered with 5-cycles of ALD-Al_2O_3 are displayed in Fig. 6.5. In addition, the conductivities of 20 nm In_2O_3 films deposited at 400 °C and covered with different cycles of ALD-Al_2O_3 are also presented in the same figure. For these films only the conductivity data is available, as Hall effect measurements were not performed.

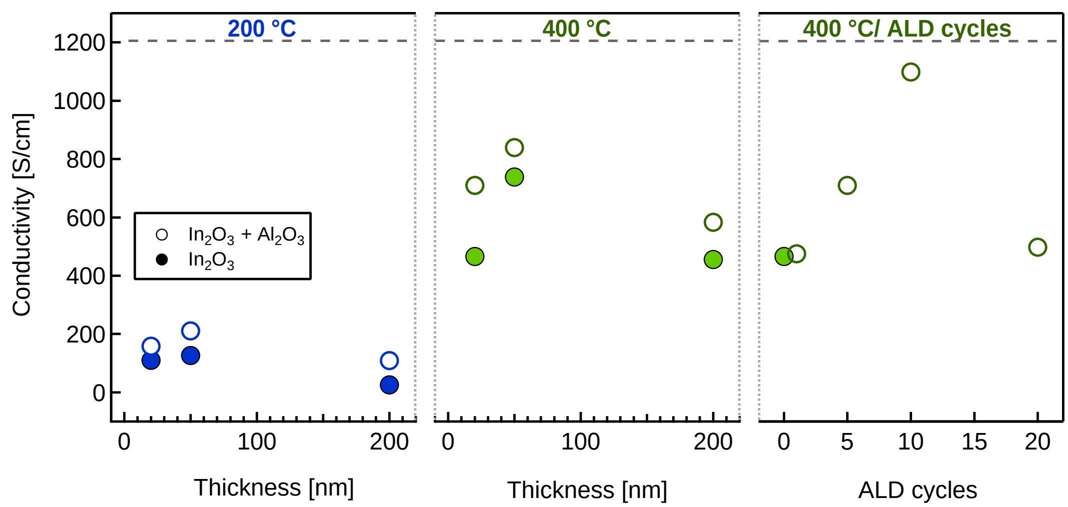

Figure 6.5: *The conductivities of undoped In_2O_3 films deposited at the substrate temperatures of 200 and 400 °C using Ar/O_2 (99.5%/0.5 %) gas mixture with film thickness of 20, 50, and 200 nm are presented together with those covered with 5-cycles of ALD-Al_2O_3. In addition, to study the influence of Al_2O_3 layer thickness, the conductivity of 20 nm In_2O_3 deposited at 400 °C and then covered with different cycles (1-20) of ALD-Al_2O_3 reported.*

Effect of Film Thickness and Deposition Temperature

For the films deposited at 200 °C, the conductivity of undoped In_2O_3 decreased from ≈120 S/cm for thinner 20 and 50 nm films to ≈25 S/cm for 200 nm sample. Similarly, thin films prepared using the same deposition conditions, but at the higher deposition temperature of 400 °C exhibit an increase of conductivity from 466 S/cm for 20 nm to 739 S/cm for 50 nm and finally decreased to the value of 456 S/cm for 200 nm sample. For these films Hall effect measurements and mircostructural studies were not performed, the following discussions are on the basis of reasonable speculations.

As it is evident from Fig. 6.5, the conductivity of the films generally increases with deposition temperature. This is mostly due to an increase of carrier concentration in accordance with the upward shift of Fermi energies, see Fig. 6.3(a). Since oxygen exchange in In_2O_3 is possible at the moderate temperature of 300 °C [225] and by taking into account the samples are prepared in the same oxygen partial pressure, the films deposited at 400 °C are expected to have more ionized doubly charged oxygen vacancies $V_{\mathrm{O}}^{\bullet\bullet}$ and thereby higher carrier concentration and of course higher conductivity.

The films microstructure is also important to understand the dependence of electrical properties on the film thickness and deposition temperature. Buchholz, D. Bruce, et al. [230, 231] reported amorphous-to-crystalline transition temperature of In_2O_3 thin films grown by PLD[4] with deposition temperatures varies from −100 to 600 °C. The X-ray diffraction (GIXRD) analyses revealed that the films grown at the lower temperature of −100 to 0 °C are completely amorphous. The films grown at RT show first signs of crystallinity but the amorphous phase still dominates for the films grown up to 100 °C. For the films grown between 100 and 400 °C, the crystalline phase dominates and the high temperature films (400 - 600 °C) are highly crystalline [231]. Sn-doped In_2O_3 thin films deposited at room temperature in DAISY-MAT also show In_2O_3 related crystalline behavior depending of the thickness of the film (see section 5.4.1.1). Therefore, the In_2O_3 films deposited in the same deposition chamber at 200 °C are expected to be mostly crystalline but could still contain some amorphous regions.

Given the polycrystalline nature of the films grown at 200 °C, the lower conductivities of these films compared to films grown at higher temperatures can be explained by the presence of smaller grains even in thicker films and possible oxygen incorporation. If the grains are very small, the depletion regions induced by the potential barriers at the grain boundaries overlap (see Fig. 5.9 (a)). Thereby, the bending of the energy bands will reduced. The potential barrier for grain boundary scattering is then reduced and increases the carrier mobility. However, the average carrier concentration decreases due to the high number of grain boundaries according to Eq. 5.2. This is expected to be the dominant factor for lower conductivity. Higher oxygen incorporation during longer sputtering time of thicker films, which would decrease the donor defect concentration or increases the acceptor defect concentration, *i.e.*, the concentration of $\mathrm{V}_{O}^{\bullet\bullet}$ and O_i'', respectively [27], may also contribute to this observation.

The undoped In_2O_3 films deposited at 400 °C are expected to be completely crystalline and thickness dependent grain growth is expected for these films, which is common in film growth. These films have higher conductivity values compared to those deposited at 200 °C. Thinner films (20 and 50 nm) have higher conductivity compared to thicker 200

[4] pulsed laser deposition

nm sample. The lower conductivity of thicker sample may be related to higher oxygen incorporation during longer sputtering time of thicker films, which would decrease the concentration of ionized oxygen vacancies. On the other hand, the sample is expected to have bigger grain and lower carrier concentration, thus, having higher barrier height and lower carrier mobility.

Effect of Al_2O_3 Deposition and Change in Al_2O_3 Layer Thickness

Al_2O_3 deposition is performed in vacuum chamber at 200 °C and involves heating of the samples in vacuum before and during exposure to the process gas. The heating process is not expected to change the microstructure of the films as all the studied films are deposited at 200 °C or higher deposition temperature.

Deposition of Al_2O_3 resulted an increase of conductivities in all studied samples, independent of film thickness and deposition temperature (see Fig. 6.5). This is due to an increase of carrier concentration in accordance with the raise of the Fermi level, see Fig. 6.3. As the variation in the surface Fermi energy directly corresponds to a change in electrical conductivity for thin films [35, 213]. For the films deposited at 200 °C, the coverage of 5-cycles of ALD-Al_2O_3 resulted a very slight increase in conductivity for thinner films and an increase by about a factor of 4 for 200 nm thick film. This higher increase of conductivity for thicker 200 nm sample can be explained, on one hand, by an increase of surface Fermi level position, which will induce conduction electrons on the surface of In_2O_3. On the other hand, the possible change in Fermi energy in the bulk, this could be due to the chemical reduction of the film. However, the XPS In3d core level emission of the same sample do not show the presence of metallic In at the lower binding energy of ≈ 443.96 eV[5]. In addition, the deposition of ALD-Al_2O_3 at 200 °C is not expected to change the microstructure of In_2O_3 as they are also deposited at the same temperature of 200 °C. Thus, the reduction of the film is not expected.

Similarly, the films deposited at 400 °C also exhibited a moderate increase of σ after Al_2O_3 deposition. This is also due to an increase of carrier concentration in accordance with the upward shift of surface Fermi level position Fig. 6.3. 20 nm thick sample show an increase of conductivity about a factor of 2.

In order to study the influence of Al_2O_3 layer thickness, different In_2O_3/ALD-Al_2O_3 thin films were prepared by varying the number of ALD-cycles. For In_2O_3 films deposited at 400 °C in Ar/O_2 (99.5%/0.5%) gas mixture, 1, 5, 10, and 20-cycles of Al_2O_3 were deposited. The change in electrical conductivity of these films is presented in the right graph of Fig. 6.5. The conductivity increases with increasing the number of ALD cycles

[5] clear metallic In shoulder was observed for chemically reduced ITO films after Al_2O_3 deposition, see section 5.3

until 10 cycles, in which the value increased by a factor of ≈2.5 compared to undoped and uncoated In_2O_3. For 20 cycles of Al_2O_3 deposition, the conductivity almost returned to the value of uncoated In_2O_3, in accordance with the change in surface Fermi energy, see Fig. 6.3. However, there is no Hall effect results in order to quantify the change in carrier concentration. Therefore, according to the conductivity data the In_2O_3 film coated with 10-cycles of ALD-Al_2O_3 is resulted the highest conductivity values. Similarly, deposition of 10-cycles of ALD-Al_2O_3 on ITO films resulted the highest surface Fermi energy of ≈3.5 eV in ITO films [38].

6.4.2 High Temperature Deposited Films

Another batch of In_2O_3 thin films are prepared in pure Ar gas with film thickness of 20 nm at substrate temperatures of 400 °C, 500 °C, and 600 °C together with those coated with 5 and 10- cycles of ALD-Al_2O_3. These films[6] are expected to be completely crystalline and having bigger grain size for thicker films [230, 231]. Al_2O_3 deposition is performed in vacuum chamber at 200 °C and involves heating of the samples in vacuum before and during exposure to the process gas. However, the heating process is not expected to change the microstructure of these films as the studied films are deposited at elevated temperatures of 400-600 °C. The conductivties and Hall effect results of these films are presented in Fig. 6.6.

The films deposited at 400 °C with and without 5-cycles of ALD-Al_2O_3 exhibited conductivity values, which are in a good agreement with the values of the films deposited in Ar/O_2 (99.5%/0.5 %) gas mixture having the same film thickness and temperature, see Fig. 6.5. This indicates addition of 0.5 % O_2 in the processing gas do not change the electrical properties of thin (20 nm) In_2O_3 films deposited at 400 °C, at least in our case. Al_2O_3 deposition resulted an increase of σ by about a factor of 2, which is mostly due to an increase of carrier concentration in accordance with the upward shift of Fermi energies, see Fig. 6.3 (b). In contrast, the coverage of 10-cycles of Al_2O_3 resulted a slight reduction of conductivity, but still higher than uncoated sample. This is mostly due to the carrier mobility as it slightly reduces from 54 cm^2/Vs for 5-cycles to 44 cm^2/Vs for 10-cycles of ALD. However, the carrier concentration remains unchanged with increasing ALD-cycles.

Compared to the samples deposited at 400 °C, In_2O_3 films deposited at 500 °C have slightly higher of conductivities. Here as well, the conductivity increased with alumina coating and alumina layer thickness. The Hall effect measurement revealed that this is

[6]deposited at elevated temperatures of 400-600 °C

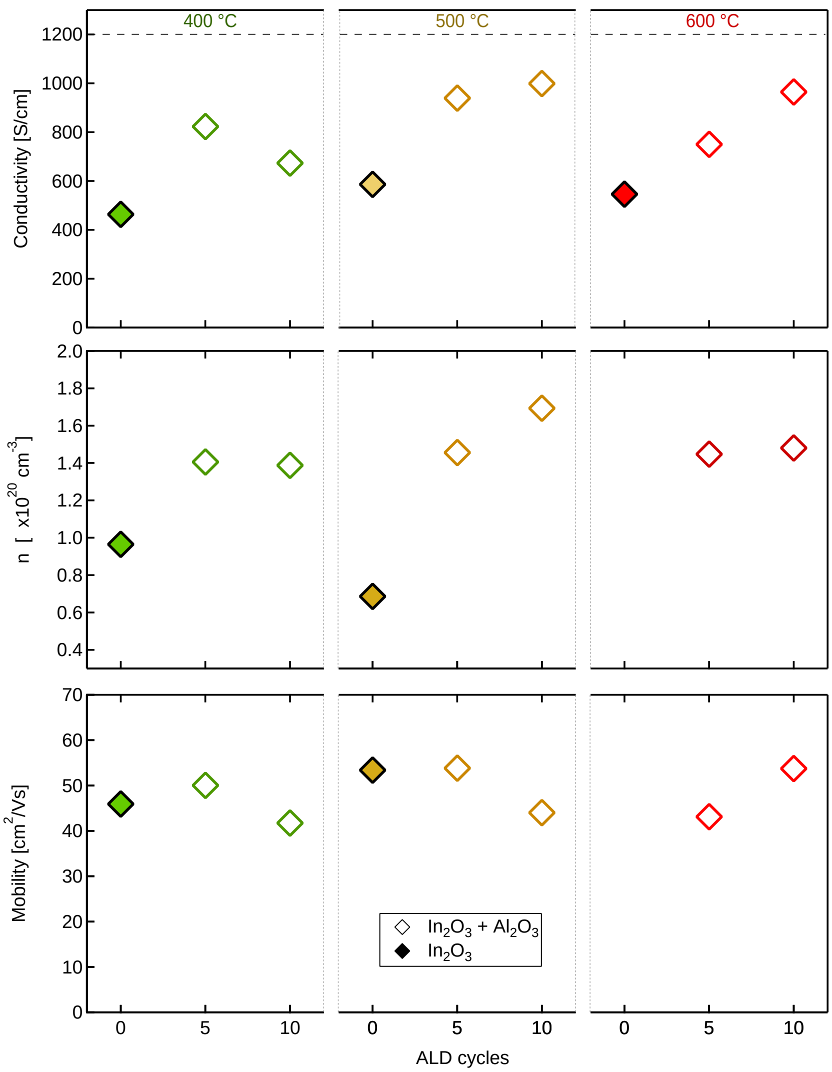

Figure 6.6: *Conductivity and Hall effect of uncoated and 5- and 10-cycle ALD-Al_2O_3 coated In_2O_3 films deposited at 400 °C, 500 °C and 600 °C as a function of ALD-cycles. Due to sample failure, Hall effect measurement was not possible for uncoated In_2O_3 deposited at 600 °C .*

due to an increase of the carrier concentration, which increases from 6.8×10^{19} cm^{-3} of uncoated to 1.42×10^{20} cm^{-3} for 5-cycles, and to 1.6×10^{20} cm^{-3} for 10-cycles of alumina coating, which is indeed an increase of up to one magnitude unit. This is also supported by the XPS VB measurements, as the Fermi energies increased slightly increased after Al_2O_3 deposition. Therefore, it is reasonable to argue that alumina deposition induced conduction electrons in the interface near region of In_2O_3. Meanwhile, the mobility slightly decreased with increasing ALD cycles.

Similarly, undoped In_2O_3 grown at 600 °C exhibit a conductivity value comparable to the films deposited at 400 and 500 °C. Furthermore, alumina deposition resulted an increase of conductivity and it further increased with increasing the number of ALD cycles from 5 to 10. Hall effect measurements revealed that these increases of conductivity is mostly due to an increase of mobility. This is in contrary to the films deposited at 400 and 500 °C, as the μ of these films decreased with increasing ALD cycles. The carrier concentration is unchanged for both ALD cycles with a value of $\approx 1.4 \times 10^{20}$ cm^{-3}. Due to the contact electrode failure, the Hall effect measurement was not possible for the uncoated sample.

Undoped 20nm In_2O_3 deposited at higher substrate temperatures of 400-600 °C shows very comparable conductivity values. Deposition of 5 and 10-cycles of ALD-Al_2O_3 resulted an increase of conductivities for all studied films. This is mostly due to an increase of carrier concentration in accordance with the upward shift of surface Fermi level positions. For the samples deposited at 500 °C, Al_2O_3 deposition results an increase of carrier concentration upto a factor of two.

A model for defect modulation doped layer of In_2O_3 thin films

The defectively modulation doped surface layer and its coverage on thin films having different film thicknesses are schematically represented in Fig. 6.7.

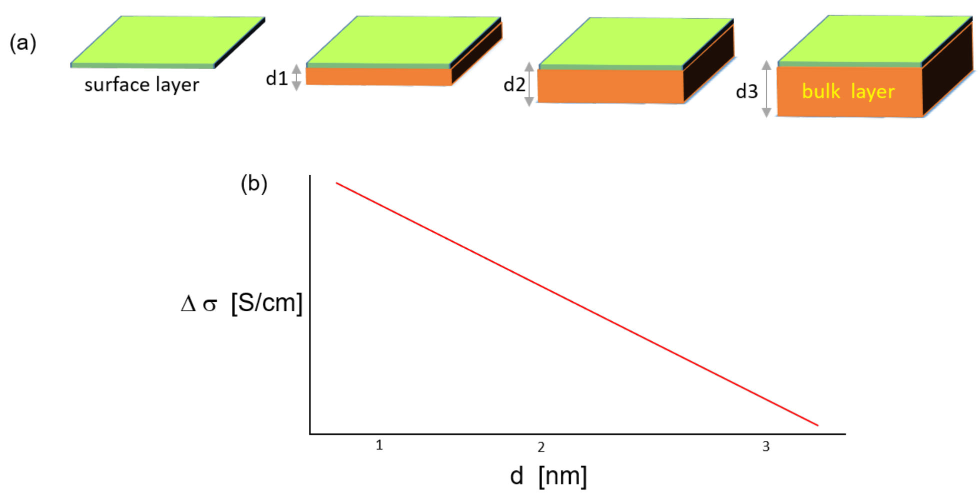

Figure 6.7: *Schematic illustration for defect modulation doped surface layer and its effect on the bulk conductivity of thin films having different films thickness. The change in conductivity ($\Delta\sigma$) after the coverage of dopant surface layer is plotted as a function of change in film thicknesses. d1, d2 and d3 represents the total film thicknesses of individual films.*

Since defect modulation doping is near surface phenomenon, the change in bulk conductivity ($\Delta\sigma$) is more pronounced for thinner films, which as well is schematically represented in Fig. 6.7(b). In the graph, d1, d2 and d3 represents the total film thickness (surface and bulk layers). The thinner film (d1) shows the most pronounced change in the conductivity after the dopant layer coverage.

In order to study the influence of defective modulation doped surface layer on the bulk electrical properties of the studied films, the conductivity of surface layer is estimated. The estimation is done by considering constant electron mobility in the surface layer with a values of 40 cm^2/Vs [7] and taking different carrier concentration values of 5 $\times 10^{20}$, 1×10^{21} and 2×10^{21} cm $^{-3}$, which results the conductivity of surface layers to be ≈3204 S/cm, ≈6410 S/cm, and ≈12800 S/cm, respectively. These surface conductivities are up to a factor of 12 higher than the bulk experimental values. The carrier concentration values are chosen as an experimental values for the bulk films is $\sim 1\times10^{21}$ cm $^{-3}$ (see Fig. 6.6) and higher carrier concentration is expected at the modulation doped surface layer. The resistances of surface layers (Rs) are then calculated by taking different layer thicknesses of 1 nm, 2 nm and 5 nm.

The calculated modulation doped surface layer resistances (Rs) are then summed up to the experimental values (Ru) obtained for uncoated In_2O_3 thin films prepared at the substrate temperature of 400 °C in Ar/O_2 (99.5%/0.5 %) gas mixture with a film thicknesses of 20, 50, and 200 nm, see Fig. 6.5. The total resistance (Rt) of the film can then obtained by adding the two parallel resistances. In order to asses the reasonable estimation modulation doped surface layer thickness and carrier concentration, the calculated total resistance (Rt) are compared with the experimental values of the 5-cycles of ALD-Al_2O_3 coated In_2O_3 thin films.

The comparison for the resistance of experimental uncoated In_2O_3, ALD-Al_2O_3 coated and calculated total resistance (Rt) are plotted as a function of the film thicknesses as shown in Fig. 6.8. Different total resistance (Rt=Ru + Rs) were calculated for each carrier concentration by changing the surface layer thicknesses from 1 to 5 nm. For n= 5×10^{20} cm $^{-3}$, Rt is fitted well with the experimental values of coated films for 1nm and 2 nm layer thicknesses. For n= 1×10^{21} cm $^{-3}$ only 1 nm is fitting to the experimental curve. Finally, for n= 2×10^{20} cm $^{-3}$ no fitting is observed.

These results suggested that the modulation doped surface layers can have the carrier concentrations in the range of 5×10^{20} cm $^{-3}$ to 1×10^{21} cm $^{-3}$ and a layer thicknesses of upto 2 nm. By taking the experimental value of n=1×10^{20} cm $^{-3}$, there can be an increase of carrier concentrations upto a factor of 10. However, this is rough estimation; in order to have more precise estimation proper calculation and experimental works needed.

More precise estimation of modulation doped surface layer electron density distribution

[7] this mobility value is comparable to the experimental results for the bulk In_2O_3 films

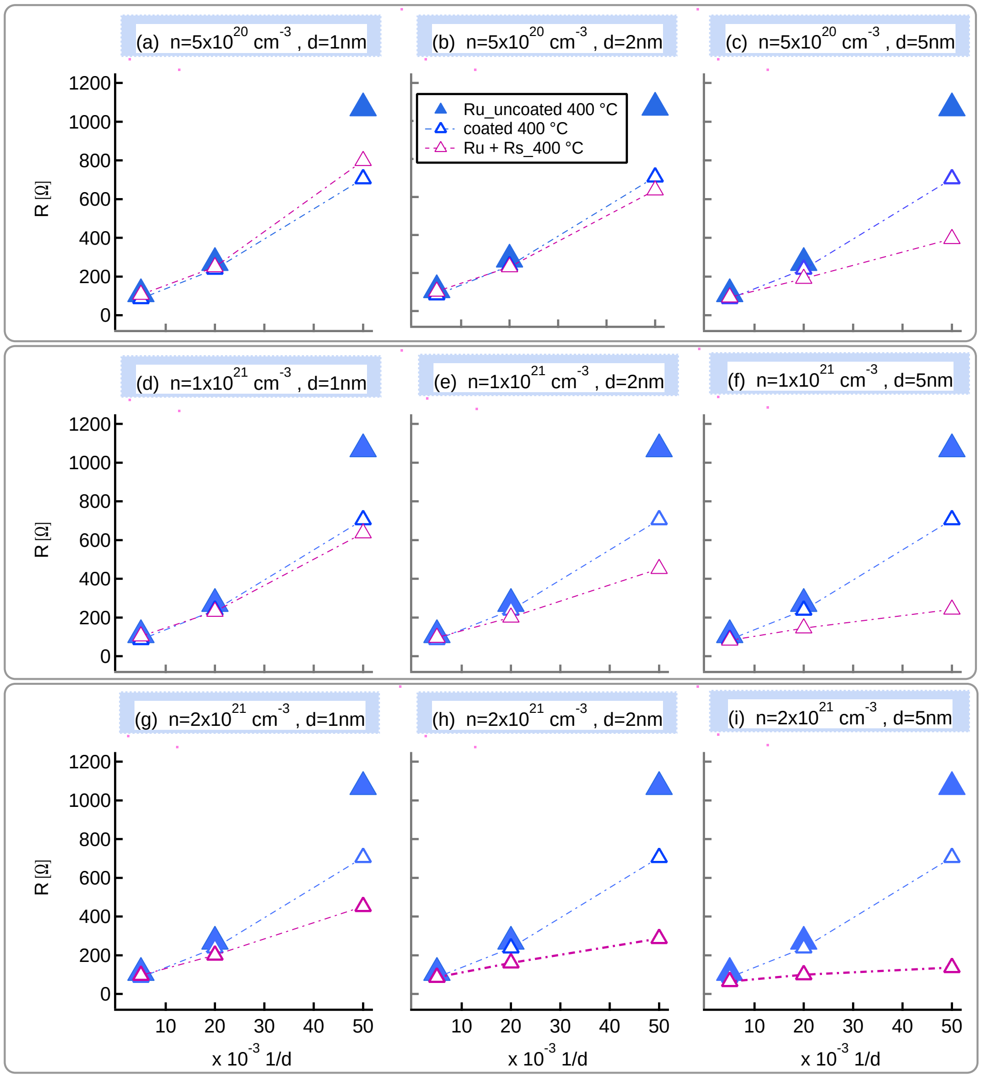

Figure 6.8: *The resistance of undoped In_2O_3 (Rs)(solid blue triangles) thin films prepared at 400 °C in Ar/O_2 (99.5%/0.5 %) gas mixture with the film thicknesses of 20, 50, and 200 nm together with those covered with 5-cycles of ALD-Al_2O_3 (open blue triangles). The pink triangles represent the total resistance, which is obtained by adding the resistance of uncoated In_2O_3 (Ru) and calculated modulation doped surface layer (Rs). The surface layer was calculated by taking the surface carrier concentration (n)and surface layer thickness (d) variables, as "n" varies from 5×10^{20} to 2×10^{21} and "d" from 1 to 5 nm.*

and the corresponding CBM/VBM[8] profiles can be obtained by using self-consistent Schrödinger-Poisson calculations [202, 203, 205]. For the calculations experimental bulk electron concentration and band bending values are used as an input parameter for

[8]conduction band minimum/valence band maximum

simulations. Besides, the presented conductivity and Hall effect results of uncoated and Al_2O_3 coated films were obtained from two different samples. This could cause uncertainty for comparing the before and after coating results, as there is reproducibilty issue in the produced In_2O_3 films. In order to avoid this uncertainty, the electrical study should be done on the individual sample before and after Al_2O_3 coverage. This will require the Hall measurement to be performed immediately after deposition without breaking the vacuum. If the sample is taken out of vacuum chamber it will accumulate surface electrons due to its exposure to air and the electrical properties will change [202, 203, 204, 205]. Therefore, care must be given during preparation of samples.

6.5 Summary and Conclusion

In this chapter, the effect of ALD-Al_2O_3 deposition on interfacial and electrical properties of undoped In_2O_3 films prepared in different conditions have been described. The finding of this chapter emphasizes on the following points:

- Undoped uncoated In_2O_3 thin films deposited at 400 °C in Ar/O_2 (99.5%/0.5 %) gas mixture exhibit higher conductivites compared to the films deposited at 200 °C. This is mostly due to an increase of carrier concentration, which is assigned to the creation of doubly charges oxygen vacancies $V_{\mathrm{O}}^{\bullet\bullet}$. In addition, films deposited at 400 °C either in a pure Ar or in (99.5%/0.5 %) gas mixture shows comparable conductivity values. The uncoated thin films deposited at the substrate temperatures of 400-600 °C in a pure Ar gas do not show an appreciable difference in conductivity.

- Al_2O_3 deposition does not bring the Fermi energies of In_2O_3 the expected value of E_{F}-$E_{\mathrm{V}B}$ of ≥ 4 eV but is limited to E_{F}-$E_{\mathrm{V}B}$ of $\approx 2.9 \pm 0.1$ eV. The discrepancy between the expected and measured Fermi energies is explained by the formation of a very narrow space charge region at the surface of In_2O_3.

- Deposition of Al_2O_3 resulted an increase of conductivities for all studied samples, independent of film thickness and deposition temperatures.

In conclusion, conductivity and Hall effect measurements revealed Al_2O_3 deposition results an increase of conductivity of In_2O_3 thin films. This was mostly due to an increase of carrier concentration. The systemic study on the influence of Al_2O_3 layer thickness on the near surface and bulk properties of In_2O_3 revealed that an enhancement of electrical properties occurs up to 10-cycles of ALD. For 10-cycles of Al_2O_3 deposition, the carrier concentration increased up to a factor of 2.5. In a nutshell, In_2O_3/ALD-Al_2O_3 thin films indicate that defect modulation doping occurs and results in a moderate enhancement of electrical properties. However, in order to improve the interface properties and firmly prove the modulation doping effect, more detailed studied are required on the doped interface.

Chapter 7

Defect Modulation Doping for Sputtered In_2O_3 by Sputtered SiO_{2-x}

This chapter is concerned with using a different ultra thin defective and amorphous insulator material, namely silicon dioxide (SiO_2), on the surface of undoped In_2O_3 with the aim to induce conduction electrons in the interface near region of TCO and then satisfying the required conditions of defect modulation doping. SiO_2 layers are reactively sputtered from a Si target, which results partially reduced silicon dioxide, represented as SiO_{2-x}. The reduction of SiO_{2-x} can come from either vacancies of oxygen or silicon interstitials. These defects should generate a Fermi level pinning in the upper half of the band gap ($\geq$ 4.5 eV)[1], as for Al_2O_3 [96]. Combining In_2O_3 with very thin layer of reduced SiO_{2-x} can then result in a very high Fermi level position at the interface, even higher than the doping limit. For this purpose, different In_2O_3 thin film substrates were prepared with and without deposition of reactively sputtered SiO_{2-x} layers. The prepared samples were examined using in-situ photoelectron spectroscopy for near surface properties as well as ex-situ electrical conductivity measurements. The chapter is divided in the following sections.

[1] The band gap of SiO_2 is $\sim$ 9 eV.

In section 7.1, the structural and other physical properties of the potential dopant material silicon dioxide will be briefly reviewed. Section 7.2 shortly describes the experimental conditions followed during the thin film preparations. The photoelectron spectra of uncoated and SiO_{2-x} coated In_2O_3 thin films will be addressed in section 7.3. The effect of oxygen concentration and substrate temperature during deposition of SiO_{2-x} will be addressed. In order to answer whether addition of ∼2 nm SiO_{2-x} enhances the electrical properties of In_2O_3 films, conductivity and Hall effect measurements were performed on the studied samples. The results of these measurements will be presented in relation to the photoemission data with further discussion in section 7.4. Finally, the main points of the chapter will be summarized and concluded in section 7.5.

7.1 Introduction

7.1.1 Silicon Dioxide

Silicon dioxide and its suboxides with specific electrical, optical, and mechanical properties play a central role in most of contemporary electronics and photonics technologies. Indeed, its amorphous form (a-SiO_2) [232, 233] is present in the cores and claddings of fiber optics for communications [234] and medical applications, comprises the gate and passivation oxide layers in 90% of all metal-oxide-semiconductor (MOS) devices (e.g., computer chips) [235]. It is used to fabricate windows, photomasks, and transmissive optics for excimer-Iaser microchip lithography, and is commonly one of the components of the multi-layer coatings used to produce highly reflective mirrors or highly transmissive lenses for laser optics [236]. The crystalline α-quartz form of silicon dioxide is fabricated into frequency standards (e.g., for digital watches) and accelerometers [232, 237, 238].

7.1.1.1 Structure of pure silicon dioxide

Silicon dioxide can have amorphous form (as opal, hyalite, sintered pearl, lechateierite and natural silica glass) or crystalline form (as quartz, cristobalite, coesite, keatite, stishovite, chalcedon, agate, moganite and others). The basic structural unit of vitreous SiO_2 and silicate glasses is the SiO_4 tetrahedron [239, 240]. A tetrahedron is a polyhedron composed of four triangular faces, three of which meet at each vertex. A regular tetrahedron is one in which the four triangles are regular or equilateral, and is one of the platonic solids (convex polyhedron). There are four oxygen atoms, one located at each apex of a regular tetrahedron and a single silicon atom is located at the center of the tetrahedron, see Fig. 7.1. This silicon atom has a valence charge of 4 in sp^3 orbitals, meaning that it is looking to acquire four electrons through sharing with other atoms to complete its outermost energy shell, known as the valence shell. An oxygen atom has two electrons in its outermost shell that are available to bond with the silicon atom. If four oxygen atoms surround one silicon atom, where each oxygen atom offers one electron, then the silicon atom's outermost shell will be complete and stable. The resulting arrangement comprises a silicate molecule. One electron remains, allowing those oxygen atoms to search for another silicon atom to share an electron and form another tetrahedron. Tetrahedrons are linked together through oxygen bonds and the arrangement of these links between the basic tetrahedral units determines the classification of the silicate [241]. When the tetrahedra are not linked together, as each exists in isolation, the material is classified as a Nesosilicate. If groups of two tetrahedra are linked together, the material is then classified as a Sorosilicate. If all of the tetrahedra link back onto each other to form a closed ring, then the material becomes a Cyclosilicate [241].

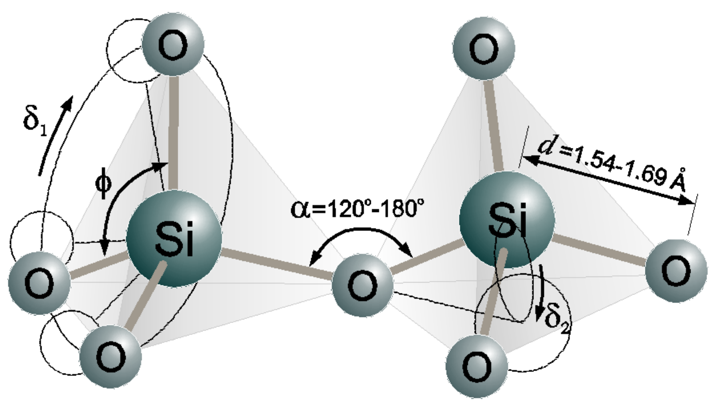

Figure 7.1: *Three-dimensional schematic of a pure fragment of the regular silica structure. The structure is defined by several parameters; the Si-O bond length (d), the tetrahedral angle (φ), the inter-tetrahedral bond angle (α), and the bond torsion angles ($\delta 1, \delta 2$) [241].*

The bonding in silicon dioxide is complex. The Si-O bond energy is very high (4.5 eV) compared to the Si-Si bond (2.3 eV) and has an approximately 50:50 ionic:covalent [242]. The covalency favors tetrahedral coordination of Si by O and maintains the O-Si-O bond angle (φ) very close to the tetrahedral angle 109.5°. Some of the literature indicates that the Si-O bond length d in various modifications of silicates may vary in the range of 0.154 nm to 0.169 nm [243], while the mean value specified for d is 0.162 ± 0.005 nm. In most cases one can treat the SiO_4 tetrahedra as rigid units, which can be linked together by their corners to form pairs, rings, chains, sheets, or frameworks. In this case the inter-tetrahedral Si-O-Si bond angle (α) can be defined. Measurements have been shown that the angle (α) varies with the different tetrahedra of the polyhedron, according to respective form of silicas (for vitreous SiO_2 from 120° to 180° and for quartz between 146° and 155° [241, 242].

The parameters, such as the inter-tetrahedral bond angle (α) and the bond torsion angles ($\delta 1, \delta 2$), that define the way in which individual tetrahedra are linked together are highly variable. This variation in parameters distinguishes a glass from its corresponding crystalline analogue. As a result of the alternative possibilities of structural arrangement, there exist a number of modifications of crystalline silica [241].

7.1.1.2 Intrinsic defects in silicon dioxide

The presence of defects in the silica matrix can dramatically change its structural, electrical, and optical properties. Many parameters, such as manufacturing process, irradiation, mechanical stress, change of temperature, and the presence of impurities may cause the formation of defects and/or lead to the transformation of the existing defects to other type of defect. A variety of defect structures are known to exist in silica materials and were one of the major subjects of extensive experimental and theoretical studies. Many aspects regarding the nature of the defects and their correlated properties are still controversial and not yet completely understood. Quite a lot of defect types have been discussed in the literature and many reproduction models have been proposed for each one [241, 244].

Intrinsic point defects involve atoms of the host matrix only, i.e. vacancies (the host atoms are missing, Schottky defects or Frenkel pairs) and self-interstitials (additional host atoms at an interstitial position). Defects in a perfect silica glass could include oxygen or silicon vacancies and their interstitials, Si-Si or O-O homobonds or under-coordinated silicons or oxygens [241]. Some of them are described briefly below:

- **Silicon dangling bond or the "generic" E'-center**- probably the best known paramagnetic defect in all forms of SiO_2 is the E'-center, which was first detected in the late fifties using electron paramagnetic resonance (EPR) spectroscopy [245]. E'-centers are present on surfaces of SiO_2 and their properties are well understood. From studies of the hyperfine structure in the EPR spectrum it is known that E'-center can comprise an unpaired electron in a dangling tetrahedral (sp^3) orbital of a single silicon atom, which is bonded to just three oxygens in the glass network. This generic E'-center is often denoted by ≡Si•, where the three parallel lines represent three oxygen separate bonds to one silicon atom and the dot denotes the unpaired electron. Since the original discovery [245], many (>10) different variants of E'-centers have been found [246]. There are several distinguishable variants of the E'-center in terms of their g-matrix orientation values but in common all have the structure of ≡Si•.

- **Interstitial Oxygen**- mostly all variants of manufactured high-purity dry SiO_2 contain natural interstitial oxygen atoms and an additional amount can be generated by ejecting oxygen atoms from their normal sites in the SiO_2 network during the irradiation. O, O_2, and O_3 are most studied forms of interstitial oxygen in silica. *Interstitial oxygen molecules (O_2)* can principally be formed in irradiation processes from the already present oxygen atoms [246]. They are introduced in concentrations $> 10^{17}$ cm^{-3} in some types of "oxygen rich" silica during synthesis. They can diffuse in stoichiometric silica from gas phase thanks to thermal treatment, and they are created in concentrations up to 10^{16} cm^{-3} by high-dose ionizing or particle irradiation in any silica sample [246]. In concentrations above 5 $\times 10^{17}$ cm^{-3} they can be detected by Raman or IR spectroscopy. *Interstitial oxygen or peroxy linkage (POL) ≡Si-O-O-Si≡*; theoretical studies unanimously predict that interstitial oxygen atoms associate with the bridging oxygen in α-quartz lattice or silica network, forming POL ≡Si-O-O-Si≡. On the other hand *Interstitial ozone molecules (O_3)* can be present in irradiated oxygen-rich silica. Similarly to free O_3 molecules, it has an absorption band peak at 4.8 eV, and is easily photolysed by photons with an energy larger than 4 eV. Although the amount of interstitial (O, O_2 and O_3) can be negligible in comparison with the whole oxygen content in a silica network, the presence of these interstitial atoms or fragments has to be considered when analyzing a large amount of accumulated defects in the silica matrix [241].

- **Oxygen-deficiency center (ODC)**- this defect center is entitled simply by a neutral oxygen vacancy which is often denoted ODC and indicated generally as ≡Si-Si ≡. It is diamagnetic and can be directly investigated. The literature mostly describes two models for the ODCs: neutral oxygen vacancy ODC(I) and the twofolds coordinated silicon ODC(II) denoted as ≡Si••. The ODC(I) represents one of the essential defects in all silicon dioxide modifications in a form of simple oxygen vacancies; here two Si atoms could relax and make a silicon silicon bonding relaxed oxygen vacancy (≡Si-Si≡) or stay in unstable interaction and form an unrelaxed oxygen vacancy (≡Si$\cdots$Si≡), which each one of them could be a precursor for the other under some undeclared circumstances and both are considered to play a key role in many defect-type generations and transformations in the silica matrix [247].

7.1.1.3 Band structure

The band structures of different amorphous and crystalline polymorphs of silicon dioxide have been extensively investigated both theoretically and experimentally by several groups. In general, comparing the reported literature there is a serious discrepancy among the different band calculations using different methods. The DFT calculations of α-quartz, β-quartz, and β-tridymite reported by Li and Ching [248] are shown in Fig. 7.2. In their calculations [248], α-quartz has an indirect band gap of $\approx$8.8 eV from $\kappa \longrightarrow \Gamma$, which is close to the experimental value of 8.9 eV. Calabrese and Fowler [249] reported a lower direct band gap of 6.3 eV at Γ. Chelikowsky and Schlüter[250] used self-consistent pseudopotential method and reported that α-quartz have indirect band gap of 9.2 eV from $M \longrightarrow \Gamma$. In addition, Li and Ching [248] reported β-quartz having 8.82 eV $A \longrightarrow \Gamma$, and β-tridymite 11.15 eV $\Gamma \rightarrow \Gamma$, see Fig. 7.2(b) and (c).

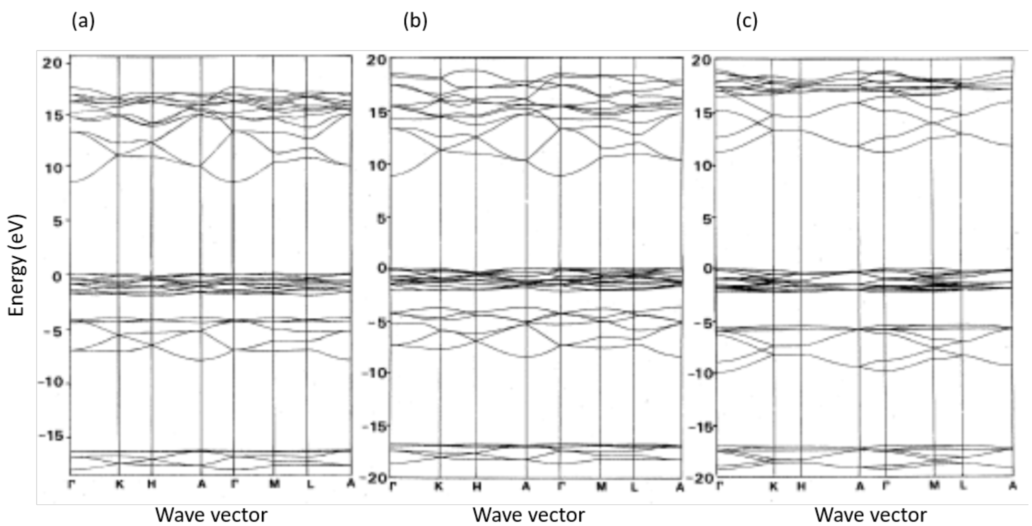

Figure 7.2: *Band structure of (a) α-quartz, (b) β-quartz, and (c) β-tridymite. (Reprinted with permission from [248], .*

In addition, Li and Ching [248] reported β-quartz have 8.82 eV $A \longrightarrow \Gamma$, and β-tridymite 11.15 eV $\Gamma \rightarrow \Gamma$. The DFT calculations have demonstrated stishovite is a direct band gap insulator with the top of valence band and bottom of conduction band in the center of Brillouin zone, at the τ point. The calculated band gap of stishovite is 4.7 eV [251].

Van de Walle [252, 253] reported the band alignment for selected semiconductors and oxides including SiO_2 and In_2O_3, see Fig. 7.3. In the Fig. 7.3, the band structures of the materials on the left-hand side of the diagram, upto SiO_2 (green background) is based on explicit first-principles DFT-LDA calculations [252]. Meanwhile, the alignment for the other materials (including In_2O_3) are based on experimental electron affinities to position the conduction band minimum with respect to the vacuum level (orange background) [254] and are included to illustrate the type of predictions and insights that can be obtained from the alignment model. The position of the charge transfer $\varepsilon(+/-)$ level for SiO_2 is to be ∼4.5 eV in the middle of band gap. The calculation shows that the valence band of SiO_2 is very deep. According to the band alignment model, there is a valence band discontinuity of ∼ 1 eV between SiO_2 and In_2O_3 and the Fermi level of In_2O_3 is found at the conduction band minimum. Therefore, in this condition SiO_2 does not bring higher Fermi level in In_2O_3 and can not be used as a potential dopant to demonstrate defect modulation doping. However, in the model (Fig. 7.3), Van de Walle [253] consider the band gap of In_2O_3 to be 3.6 eV[2]. This value is not valid anymore, as the DFT calculations by Fuchs et al. [114] and Walsh et al. [108] showed that In_2O_3 has a direct band gap of ≈ 2.9 eV. By considering the band gap of In_2O_3 as 2.9 eV, the Fermi energy at the interface of In_2O_3/SiO_2 is expected to be high and SiO_2 can be considered as a potential dopant to demonstrate defect modulation doping.

7.2 Sample preparation

In_2O_3 thin films were deposited on quartz glass substrates by magnetron sputtering with radio-frequency (RF) excitation. The background pressure of the deposition chamber was 10^{-6} Pa. A ceramic 2 inch In_2O_3 target, a RF power of 25W, a process pressure of 0.5 Pa, an Ar flux of 6.6 sccm and a target-to-substrate distance of 10 cm were used for deposition. Since defect modulation doping is a near surface related phenomenon, the film thickness of In_2O_3 was kept constant at 20 nm and the substrate temperature during deposition at 400 °C for all prepared samples.

Ultra thin layers of SiO_{2-x} were deposited on the top surfaces of In_2O_3 substrates from a Si target, with a RF power of 40 W, a process pressure of 0.5 Pa and a target-to-substrate distance of 7 cm. The SiO_{2-x} layer thickness was kept at ∼ 2 nm for each deposition. The substrate temperatures during SiO_{2-x} deposition was kept at RT or 400 °C and the oxygen was varied from 0.65 % to 5 %. The deposition conditions are summarized in Tab. 7.1. The two different deposition temperatures required different oxygen concentrations in the processing gas to produce the desired near stoichiometric SiO_2 layers, see Tab. 7.1.

[2] Van de Walle [253] published his article in 2006 and for afterward it was believed that the band gap of In_2O_3 was 3.6 eV

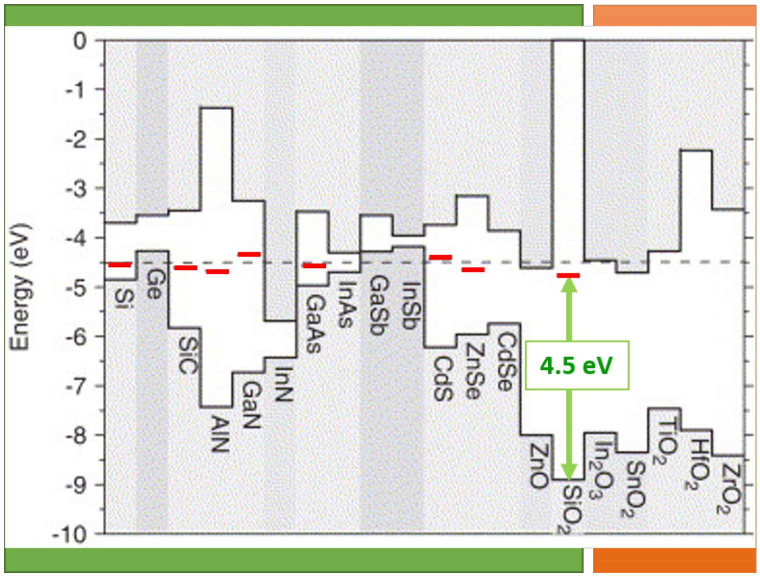

Figure 7.3: *Band alignments and position of the hydrogen transition level ε(+ / -) for selected semiconductors and insulators (Reprinted from [253], Copyright (2006), with permission from Elsevier). For each semiconductor, the lower line indicates the position of the VBM, the upper line the position of the CBM, and the thick red line the position of the charge transfer ε(+ / -) level with respect to the VBM. The band offsets have error bars of ± 0.2 eV. For SiO_2, ε(+ / -) was taken from[255]. The dashed line at -4.5 eV indicates the universal alignment level. The alignment of the band structures of the materials on left hand side of the diagram (up to SiO_2) is based on explicit first-principles DFT calculations (green background), while the alignments for the other material are based on electron affinities(red background) [254]. The valence band maximum of SiO_2 is ∼ 1eV lower than that of In_2O_3.*

Table 7.1: Deposition parameters of In_2O_3 and In_2O_3/sputtered SiO_{2-x} thin films

In_2O_3 /Sputtered SiO_{2-x} thin films								
Sample	In_2O_3				Sputtered SiO_{2-x}			
	Target	Process gas	Temp. (°C)	Thick. (nm)	Target	Process gas	Temp. (°C)	Thick. (nm)
In_2O_3	In_2O_3	Ar	400	20	-	-	-	-
In_2O_3/SiO_{2-x}	In_2O_3	Ar	400	20	Si	Ar/O_2 97.5-99.4 %/0.6-2.5 %	RT	∼2
In_2O_3/SiO_{2-x}	In_2O_3	Ar	400	20	Si	Ar/O_2 95-98 %/2-5 %	400	∼2

7.3 Photoemission

Figure 7.4 presents the detail core level photoelectron spectra of O1s, $In3d_{5/2}$, Si2p, and XPS valence band regions recorded for nominally undoped 20 nm In_2O_3 thin films deposited at 400 °C with and without coverage of silicon dioxide (SiO_{2-x}). SiO_{2-x} layers are deposited from a Si target either at room temperature with oxygen concentration of 0.6%-2.5 % in the sputter gas (the spectra displayed in Fig. 7.4 (a)) or at 400 °C with oxygen concentration of 2%-5 % (the spectra displayed in Fig. 7.4 (b)) and having a thickness of $\sim$ 2nm in both cases.

The room temperature SiO_{2-x} deposition resulted in an attenuation of In3d core level emissions, see Fig. 7.4 (a). In addition, it results in a slight shifting of the same core level emissions depending on the oxygen concentration in the sputter gas. For lower oxygen concentrations of 0.6 - 1.3 %, the emissions are shifted to lower binding energies. With the intermediate oxygen contents of 1.35 - 1.5 %, the binding energies of the emissions are almost unchanged and at the higher oxygen concentrations of 1.6-2.5 %, the emissions are shifted to the higher binding energies.

By the coverage of room temperature deposited SiO_{2-x}, the intensities of In_2O_3-related O1s core level emissions are reduced. Besides, additional peaks related to SiO_2 emission appear at higher binding energy of $\sim$533.5 eV. The binding energies of SiO_2 related O1s emissions correspond well with the values reported in literature [197]. Here as well, the shift of the peak position to higher binding energies is observed for the layers prepared in oxygen concentrations of 0.6 % to 1.7 %. The peak positions are nearly unchanged for the higher oxygen content (1.75 - 2.5 %) samples. This can be clearly observed in the top image of Fig. 7.5 (a). In the figure, the binding energies of O1s peaks determined from the maxima of each emissions corresponding to both In_2O_3 and SiO_2 are plotted as a function of oxygen concentrations in sputtering gas. The binding energy shifts are very little in the In_2O_3 related emissions. However, this is not the case for SiO_2 related emissions, as a shift of more than 1 eV is observed when the of oxygen content is changed in the films from 0.6% to 2.5%.

Deposition of SiO_{2-x} resulted in an appearance of Si2p peaks at the binding energies of $\sim$99 eV for elemental silicon (Si^0) and higher binding energies for different oxidation states (Si^{1+}, Si^{2+}, Si^{3+} and Si^{4+}) of SiO_2 compound [233, 256], see Fig. 7.4(a). The binding energies are determined from the curve fitting of the Si2p core level emissions. Si^0 peak has closely spaced spin-orbit components (Δ=0.63eV) and the doublet consists of $Si2p_{3/2}$ and $Si2p_{1/2}$. Normally, the splitting is only observed for elemental Si^0 and not for silicon compounds [257]. At the lower oxygen concentrations, the Si2p emissions corresponding to elemental silicon Si^0 (attributed to Si-Si bonds) are more intense than

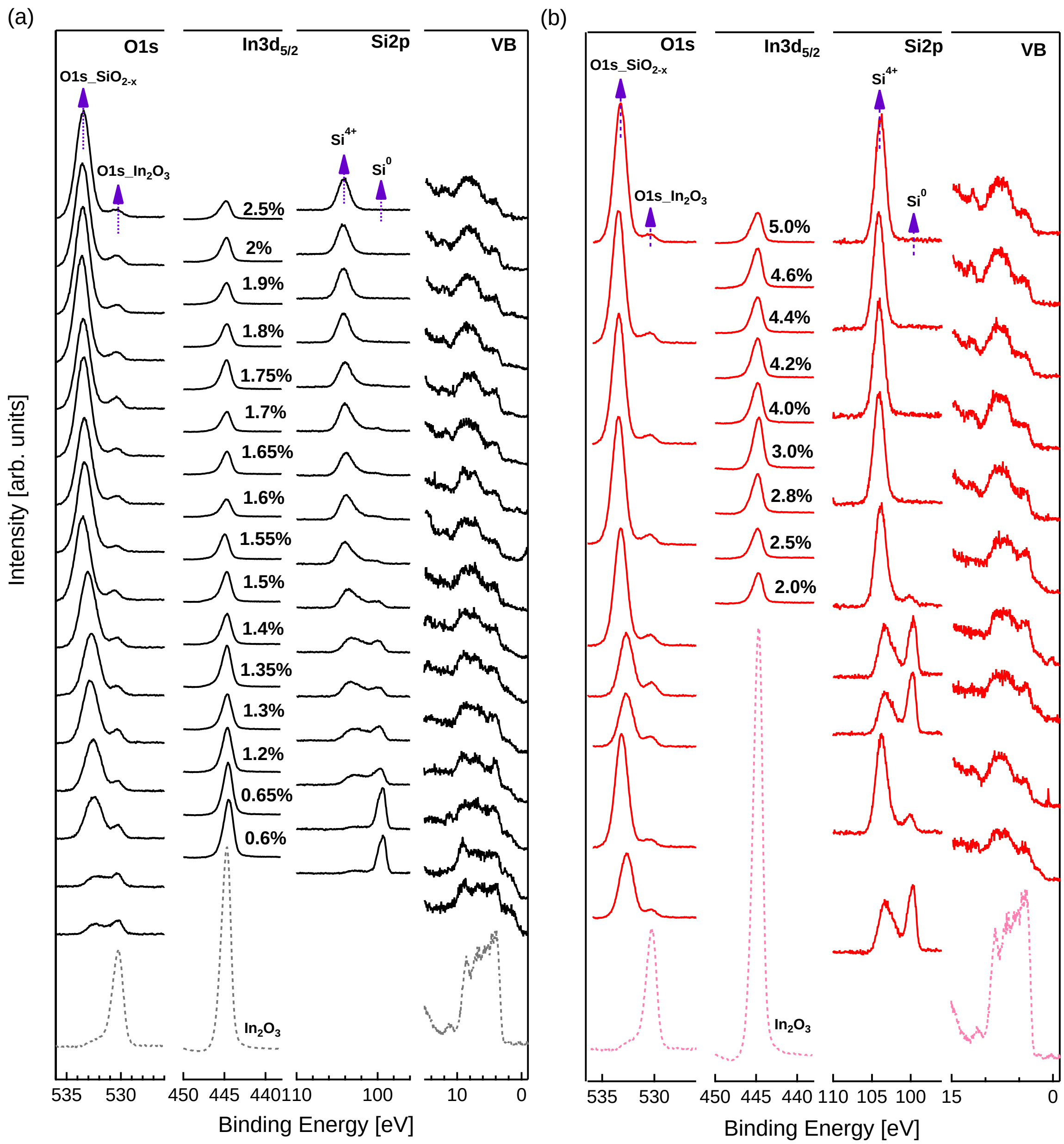

Figure 7.4: *XP (AlK_α) detail core level spectra of the O1s, $In3d_{5/2}$, Si2p, and valence band regions for nominally undoped 20 nm In_2O_3 films deposited at a substrate temperature of 400 $^\circ C$ with and without SiO_{2-x} coating. SiO_{2-x} layers are sputtered from Si target in different deposition conditions: (a), substrate temperature of RT and 0.6-2.5 % of oxygen content in sputter gas; (b), substrate temperature of 400 $^\circ C$ and oxygen content in sputter gas of 2-5 %.*

the oxidized states. With increasing oxygen concentration, the Si2p peak corresponding to Si^{4+} (attributed to Si-O bonds) intensifies and that of Si^0 attenuates. For oxygen concentrations $\geq$1.7%, the emission corresponding only to Si^{4+} state are present. This

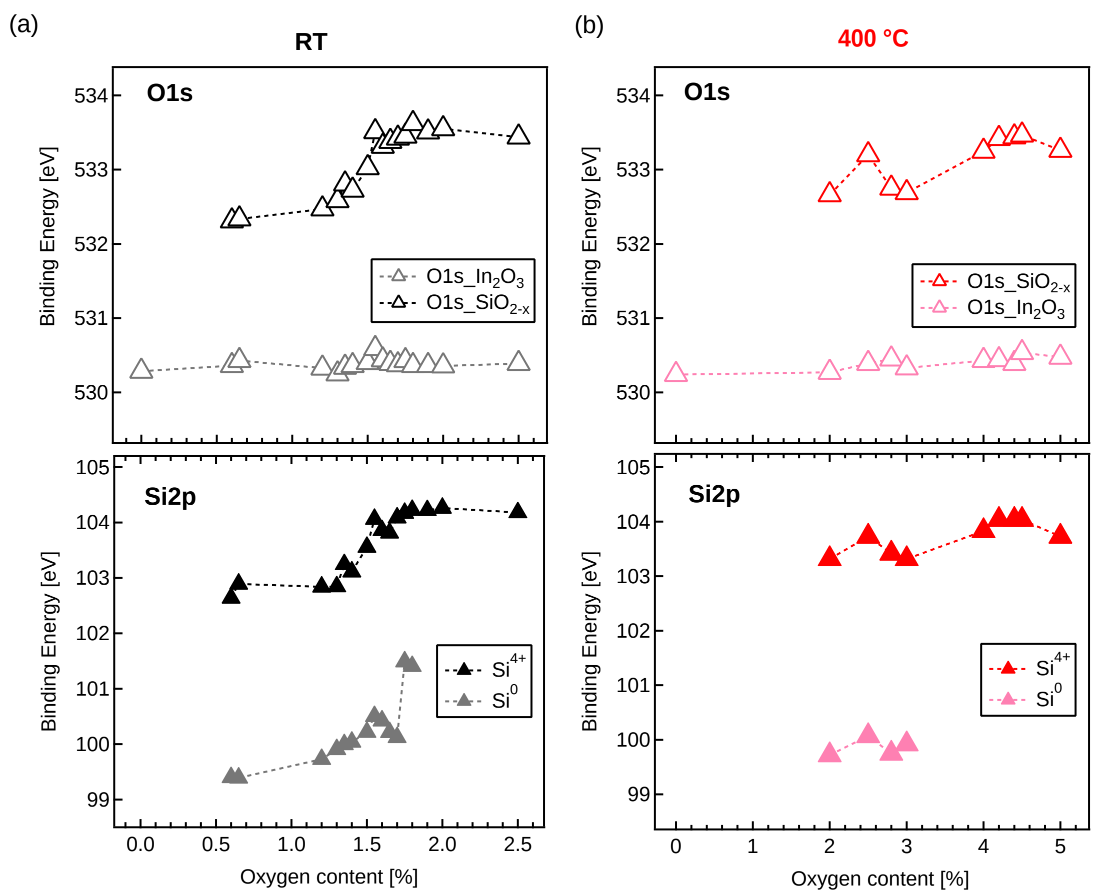

Figure 7.5: *The evolution of O1s and Si2p core level binding energies, which are determined by curve fitting from the maxima of individual emission's , as a function of increasing oxygen content during SiO_{2-x} deposition of films at (a) room temperature and (b) at 400 °C.*

indicates that at these oxygen concentrations near stoichiometric SiO_2 layers are formed. It is important to note that other oxidation states of SiO_2 can be present in the spectra of Fig. 7.4. However, Si^0 and Si^{4+} states are the only dominant emissions. The binding energies of Si^0 and Si^{4+} oxidation states as a function of increasing oxygen concentration in the sputter gas are displayed in the bottom graph of Fig. 7.5(a). The binding energies of the Si^0 state increases with oxygen concentration. For samples with oxygen concentrations of 1.75% and 1.8 %, an emission with binding energy of ≈101.5 eV is observed. This higher binding energy can be attributed to the transition of Si^0 to Si^{1+} states or to the formation of mixed states [233].

The deposition of ∼2 nm SiO_{2-x} onto In_2O_3 at an elevated temperature of 400 °C causes similar changes of the core levels as that of room temperature deposited films (see Fig. 7.4(b)). The In3d core level emissions are attenuated and show slight shifts to higher binding energies for all studied samples. Similarly, the intensity of the O1s peak related to In_2O_3 is reduced and an additional peak corresponding to SiO_2 appears at higher binding energies. Here as well, the binding energies of the SiO_2 related O1s peak increases with increasing oxygen concentration in the processing gas. Near stoichiometric SiO_2 layers are obtained for high oxygen content samples, as can be seen in the top graph of Fig. 7.5(b).

Additionally, the Si2p core levels of elemental silicon Si^0 and different oxidation states (mostly Si^{4+}) appear after SiO_{2-x} coverage. For oxygen concentrations between 2% to 3 %, the Si^0 peak is intensified compared to the oxidized Si. For higher oxygen concentrations, the Si^{4+} state becomes more intense and the Si^0 is reduced. Here, it must be noted that during room temperature deposition, the complete oxidization of silicon and formation of near stoichiometric SiO_2 was possible at lower oxygen concentrations of $\approx$ 1.7 %. Meanwhile, for the layers deposited at 400 °C, higher oxygen concentrations are required in the processing gas to see completely oxidized Si^{4+}, with corresponding oxygen concentration of $\sim$ 4%.

The valence band maximum energies can be derived directly from the valence band emission but also from the core level binding energies by subtracting their energy differences to the valence band maximum. The binding energy shifts for $In3d_{5/2}$ and O1s core levels corresponding to In_2O_3 as a function of change in oxygen concentration in the processing gas during SiO_2 deposition are summarized in Fig. 7.6. For the films covered with room temperature SiO_{2-x} (Fig. 7.6(a)), the binding energies of the In3d core level emissions decreases for the lower oxygen concentrations of 0.6 - 1.3%. This corresponds to a lowering of the surface Fermi level position. At the higher oxygen content (1.35 - 2.5%), the binding energies are either unchanged or slightly increased. Similarly, the O1s core level binding energy is unchanged or slightly increased with increasing oxygen content.

For the films covered with 400 °C deposited SiO_{2-x} (Fig. 7.6(b)), In3d core level emissions show a very slight increase of the binding energies with increasing oxygen content in the sputtering gas. This corresponds to the slight increase of near surface electron concentration. In addition, the O1s core level emissions show an increase of binding energies with oxygen concentration. The increase in the O1s binding energy is more pronounced than that of the In3d core levels.

The Fermi energy of In_2O_3 is expected to move upward by deposition of partial reduced SiO_{2-x} layers, at least for the films deposited at an oxygen content just below fully oxidized samples. This is due to the presence of oxygen vacancies or silicon interstitials intrinsic defects, which are responsible for pinning the Fermi energy above the mid gap in silicon dioxide. However, this is not the case for the studied samples. According to the results described above, it is reasonable to argue that SiO_{2-x} deposition does not induce the desired increase of Fermi energy (conduction electrons) at the surfaces of In_2O_3.

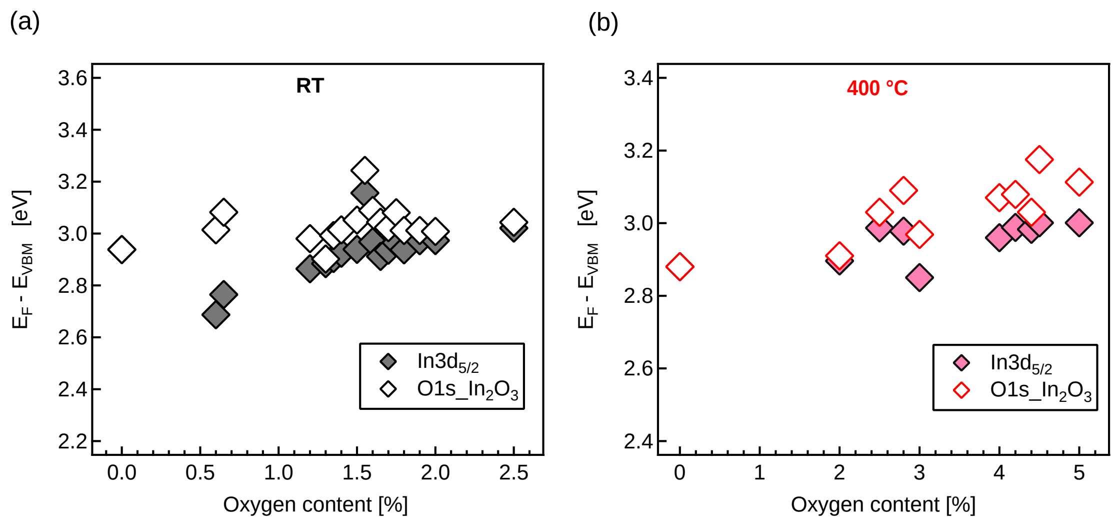

Figure 7.6: *The evolution of core level binding energies with increasing O_2 content in the sputtering gas during deposition of SiO_{2-x} from Si target at a substrate temperature of RT (a) and 400 °C (b). The core level to valence band maximum binding energies, as determined from In_2O_3 substrate have been subtracted in order to follow the evolution of the valence band maximum binding energies.*

7.3.1 In_2O_3/SiO_2 Interface

In order to determine changes in the Fermi energy at the interface, core levels of both In_2O_3 (substrate) and SiO_2 (deposited layer) are measured after step wise deposition. The obtained O1s, In3d, Si2p and XPS valence band regions are presented in Fig. 7.7(a).

In_2O_3 substrate was deposited at 400 °C from In_2O_3 target in a pure Ar gas with a thickness of 100 nm. The SiO_2 layer was sputtered from Si target by adding 4.5 % O_2 in the processing gas with substrate temperatures of 400 °C. SiO_2 layer was deposited in the following steps with corresponding thicknesses: 15 sec (∼1 nm), 30 sec (∼2 nm), 60 sec(∼4 nm), 120 sec(∼8 nm), and 150 sec(∼10 nm). As it is expected, the intensity decrease of substrate emission lines and the increase of film emissions with sputter time is observed. Furthermore, significant binding energy shifts occur as more and more SiO_2 is deposited.

The In 3d core level attenuated due to the coverage of the substrate and after 120 seconds of SiO_2 deposition the In3d peak disappears. With increasing the film thickness, the O1s peak associated to In_2O_3 is continuously decreased and a new peak associated to SiO_2 appears at the higher binding energy. The growth of SiO_2 layer is indicated by

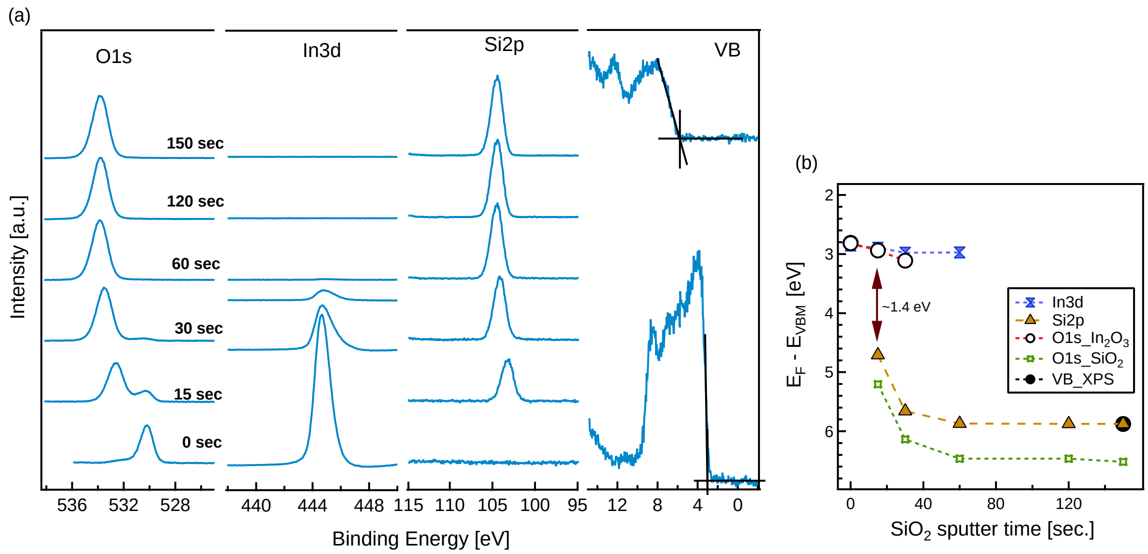

Figure 7.7: *(a) X-ray photoelectron data of core level lines O1s, In3d, and Si2p and the valence band region recorded during step-wise growth of SiO_2 on In_2O_3 substrate at 400 °C. In_2O_3 is sputtered at 400 °C with a thickness of 100 nm. SiO_2 were deposited from Si target using 4.5 % O_2 in the sputter gas. The deposition time of SiO_2 layer are indicated in O1s peak: (b) Valence band maximum energies of the In_2O_3 substrate and SiO_2 layer in dependence with sputtering time of SiO_2 layer.*

a steady increase of the Si2p (Si^{4+} oxidation state) intensity.

The energy band alignment is directed derived from the binding energy plot shown in Fig. 7.7(b) where the positions of the valence band band maxima are plotted in dependence of layer deposition time (layer thickness), following the standard procedure described in the literature [258]. Monitoring the difference in valence band maxima in dependence of film thickness eliminates artifacts which may occur at low film thickness [259]. The valence band maximum energies can be derived directly from the valence band emission but also from the core level binding energies by subtracting their energy differences to the valence band maximum, which are material constants. A valence band discontinuity for the In_2O_3/SiO_2 interface of $\triangle E_{VB} = \sim 1.4$ eV is extracted from the data plotted in Fig. 7.7(b). This value could be lower to $\triangle E_{VB} = \sim 1 \pm 0.1$ eV if more step-wise depositions were performed at the lower thickness in the beginning of the interface experiment, only few steps are performed in the current experiment. The energy band alignment at the In_2O_3/SiO_2 interface is then characterized by large band discontinuity, where the valence band maximum of SiO_2 is ~ 1.4 eV lower than that of In_2O_3. The band alignment is shown in Fig. 7.8. The difference in band gap of the two materials is accompanied by a large conduction-band discontinuity. As can be seen in

Fig. 7.7(b), the Fermi level position in SiO_2 is pinned at ∼5.8 eV by some defect. The type of defect is not yet clear.

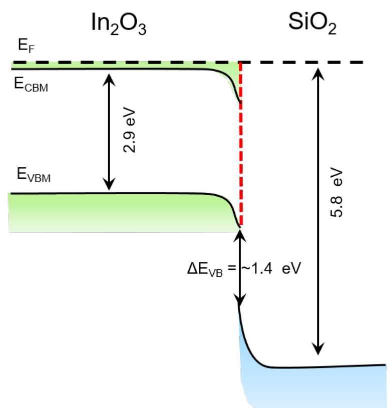

Figure 7.8: *The energy band alignment in In_2O_3/SiO_2 interface. The Fermi level position are taken directly from the experiment. The band gap is taken from [108, 114].*

7.4 Electrical Study

The conductivity and Hall effect measurements of undoped 20 nm In_2O_3 films deposited at 400 °C in a pure Ar gas together with those coated with ∼ 2nm SiO_{2-x} are presented in Fig. 7.9. SiO_{2-x} were deposited from Si target using different oxygen concentrations in sputter gas and deposition temperatures of either room temperature or at 400 °C. The undoped and uncoated In_2O_3 samples show a conductivity of 956.6 S/cm, a carrier concentration of 1.04×10^{20} cm^{-3} and a mobility 57.5 cm^2/Vs. This conductivity is slightly higher than those [3] reported in section 6.4. The Hall effect measurements show that SiO_{2-x} deposition induces a moderate changes in carrier concentration and mobility.

The room temperature deposition of SiO_{2-x} changes the conductivites of the In_2O_3 thin films by up to ± 200 S/cm. Eventually, the conductivity is increased only for films deposited with higher oxygen concentration of 1.7 and 1.8 %. The Hall effect measurements revealed that it is mostly due to the carrier concentrations as it slightly increased for the last three films in the series from 1×10^{20} cm^{-3} to 1.4×10^{20} cm^{-3}. On the other hand, the carrier mobility showed a slight reduction with increasing oxygen concentration, having the lowest mobility of 39.5 cm^2/Vs for the sample with oxygen

[3] for the films deposited in the same deposition conditions and having the same film thickness

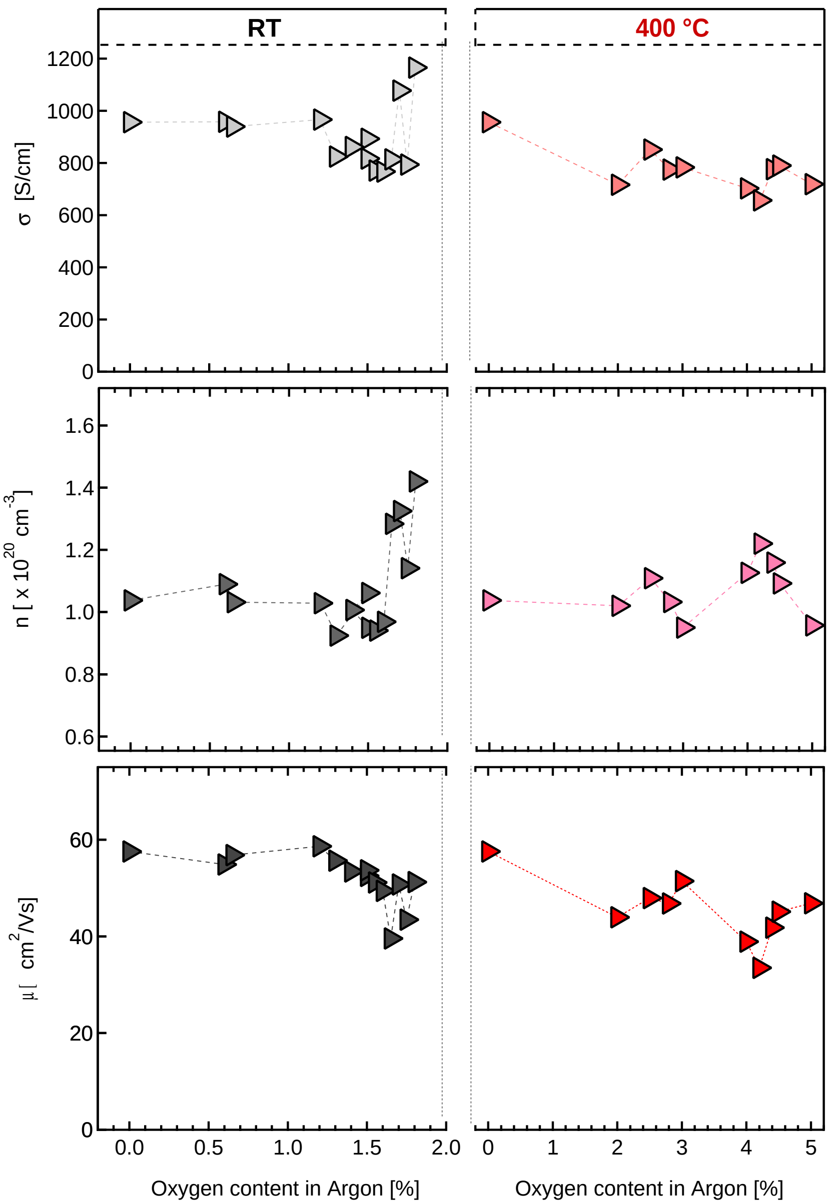

Figure 7.9: *Conductivity and Hall effect characteristics of uncoated 20 nm thick In_2O_3 deposited at 400 °C using pure Ar as a sputtering gas and those coated with sputtered SiO_{2-x} layers from Si target at different oxygen concentration with a sputtering temperature of RT(black diamond) and 400 °C (red diamond) as a function of oxygen content in the processing gas during SiO_{2-x} deposition.*

concentration of 1.65 % sample, see Fig. 7.9. These variations could also be observed from the In_2O_3 thin films themselves, as the conductivity of In_2O_3 deposited in the same deposition conditions can vary up to a factor of two (see section 6.4).

SiO_{2-x} deposition at 400 °C causes a slight reduction of the conductivity of the In_2O_3 films with increasing oxygen content in the processing gas, see Fig. 7.9. The Hall effect measurements revealed that this is mostly due to a reduction of the carrier mobility, which slightly decreases with oxygen concentration and having the lowest mobility of 33.5 cm^2/Vs for 4.2 % sample. On the other hand, the carrier concentrations do not show a noticeable change upon SiO_{2-x} coating with values between $\approx 9.5 \times 10^{19}$ cm^{-3} to 1.22×10^{20} cm^{-3}.

In_2O_3 thin films have sufficiently fast oxygen exchange with the ambient at a temperature of 300 °C [225]. Thereby, it is expected for oxygen to incorporate into the surfaces of In_2O_3 during the coverage of SiO_{2-x} layers at 400 °C. Partially similar situaltion is expected for RT SiO_{2-x} depositions, as the In_2O_3 thickness is only 20 nm. The impact of oxygen is expected for higher oxygen concentrations in the sputter gas and might result in a reduction of the carrier concentration in accordance with oxygen partial pressure ($\sigma \sim p_{O_2}^{-1/6}$) dependence of free electrons in In_2O_3 [116, 117]. This is evidently not the case for the studied films, as the carrier concentration does not decrease with increasing oxygen content, see Fig. 7.9.

The conductivity and Hall effect results indicate that, under the current deposition conditions, the addition of SiO_{2-x} layer on 20 nm In_2O_3 thin films does not induce the desired defect modulation doping. This could be related, on the one hand, to the impinging of oxygen particles on the indium oxide surface, which reduce the carrier concentration. On the other hand, the absence of defect modulation doping might be related to the intrinsic point defect properties of SiO_2. Richard and coworkers [260] performed a first principle study of neutral and charged intrinsic-defects in amorphous SiO_2. The defect configurations were generated by adding an atom to the silica model cell (for the interstitials) or removing one from it (for vacancies). The calculations have been performed for all the possible point defect sites in the cell, that are oxygen vacancy (V_O), oxygen interstitial (I_O), silicon vacancy (V_{Si}), and silicon interstitials (I_{Si}). Richard et al. [260], found that oxygen interstitials (I_O) are the dominant defect throughout the whole Fermi level range. The variation of formation energies as a function of the Fermi level at 300 K for the important point defects of SiO_2 reported by Richard et al. [260] is shown in Fig. 7.10. According to the calculation the Fermi level position of SiO_2 is only 1.25 eV, which is far low than the mid gap of SiO_2 and the band gap is much lower than that of SiO_2[4]. Hence, the data can only be used qualitatively. In addition the, figure does not include the defects at the higher Fermi energies. At the higher Fermi energy the silicon interstitial-Si_i can be a donor with a low formation energy and can pin the Fermi energy above the mid gap.

Therefore, the formation of interstitial oxygen during deposition of SiO_{2-x} would reduce the Fermi energy of the layers. This will lead to lowering of the In_2O_3/SiO_2 interface

[4]The band gap of SiO_2 is $\sim$ 9 eV.

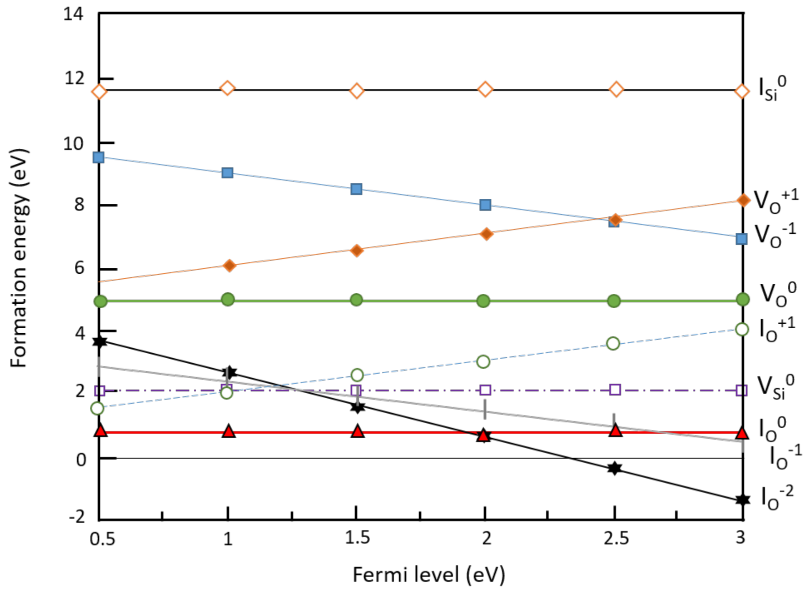

Figure 7.10: *Boltzman average of the formation energies (E_F) of each studied self-defect in function of the Fermi level at 300 K. (Redrawn from [260]).*

Fermi energy. In order to realize the prospect of SiO_2 dopant layer in modulation doping, further optimization of deposition conditions are required. Furthermore, during deposition, the interstitial oxygen should be kinetically suppressed.

7.5 Summary and conclusion

This chapter provided insight into using a different defective amorphous insulator material, namely reactively sputtered silicon dioxide (SiO_2), on the surface of undoped In_2O_3 in order to induce conduction electrons in the interface near region and perceive defect modulation doping.

- For this study the deposition conditions of In_2O_3 TCO host were kept constant with a film thickness of 20 nm (since defect modulation is near surface related phenomenon a lower thickness of 20 nm is chosen) and substrate temperature of 400 °C. SiO_{2-x} with an average thickness of ≈ 2 nm were deposited on top of the In_2O_3 substrates from a Si target at different substrate temperatures (RT and 400 °C) and different oxygen concentrations in the processing gas (0.6-5 %).

- The XPS analysis revealed the complete oxidation of sputtered silicon and formation of near stoichiometric SiO_2 requires different oxygen concentration for the layers prepared in different substrate temperature. For the layers deposited at 400 °C, complete oxidation of silicon is observed at ∼ 4 % O_2 content. Meanwhile, for RT depositions only ∼ 1.7 % of oxygen is required to produce near stoichiometric SiO_2 layers.

- The coverage of ultra thin SiO_{2-x} layers both at RT and 400 °C does not result in an accumulation of electrons in a near surface region of In_2O_3 thin films. Photoemission experiments suggest the surface Fermi energies do not shift upward after SiO_{2-x} coverage.

- The energy band alignment at the In_2O_3/SiO_2 interface is characterized by a rather large valence band discontinuity, where the valence band maximum of SiO_2 ∼ 1.4 eV lower than that of In_2O_3. In addition, the interface interface experiment revealed that the Fermi level position of SiO_2 is pinned at ≈5.8 eV. The type of defect responsible for the pinning is not clear.

- The bulk conductivity and Hall effect measurements revealed indeed that the coating of ≈2 nm SiO_{2-x} does not bring the desired improved electrical properties on In_2O_3 thin films. This is true for silicon dioxide coating prepared at both temperatures and for most oxygen concentrations. This can explained by, on one hand, by impinging of oxygen species on the surface of In_2O_3 during SiO_{2-x} deposition. This can cause a reduction of vacancy of oxygen V_O or introduce O_i and therefore reduce the conductivity. This is valid for SiO_{2-x} depositions at both temperatures. On the other hand, the intrinsic point defect present in

SiO_2 (oxygen interstitial (O_i)), which is dominant defect with the lowest formation energy though the whole Fermi level range, can result in a Fermi level value of only ≈2.25 eV. Therefore, the Fermi level at the interface of In_2O_3/SiO_2 will be low.

In conclusion, reactively sputtered partially reduced SiO_{2-x} was used as a potential dopant for 20 nm In_2O_3 thin films to demonstrate defect modulation doping. The reduction of SiO_{2-x} can come from vacancies of oxygen or silicon interstitials. These defects should generate a Fermi level pinning in the upper half of the band gap (≥4.5 eV), as for Al_2O_3 [96]. However, this does not happen to the deposited SiO_{2-x} layers, as in-situ XPS analysis does not show suitable Fermi level pinning by the V_O or Si_i defects. In addition, ex-situ Hall effect measurements do not show enhanced electrical properties of In_2O_3 after SiO_{2-x} deposition. Therefore, defect modulation doping is not observed on the studied films.

Subpart II-B

Chemical Approach

Defect Modulation Doping For Tin Oxide Based Composite Films

This part of the thesis will focus on testing defect modulation doping on composite films prepared by ultrasonic spray pyrolysis technique. Based on this motive, two models were proposed for the production of composite structures as shown in Fig. 7.11 and different composite thin films were prepared.

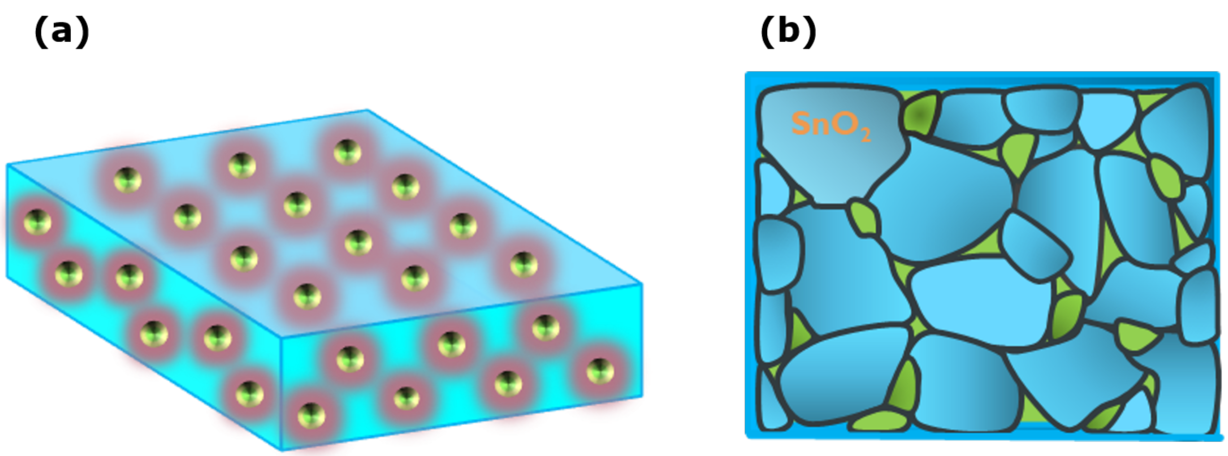

Figure 7.11: *Schematic illustrations of models proposed for production of tin oxide based composite thin films to test defect modulation doping effect. (a), tin oxide based nanocomposite films obtained by incorporation of nanoparticles (NPs) into the matrix structure. Here, the light blue color represent the matrix phase of tin oxide structure and the green circles are the dopant nanoarticles (NPs) with dopant effect of individual nanoparticles expected to extend until red circles: (b), In this case, composite films are prepared by forming two demixed crystalline phases. The big grains (colored in blue) represent the matrix tin oxide phase, while the small grains (colored in green) represent the demixed dopant phase.*

The first strategy is focused on synthesis of nanocomposite thin films prepared by incorporation of different nanoparticles (NPs) which could be used as a potential dopant, see schematic illustration in Fig. 7.11 (a). In the model, the light blue color represent the matrix phase of tin oxide structure and green circles are the dopant nanoarticles (NPs) with dopant effect of individual nanoparticles expected to extend until red circles. According to the model, if enough nanoparticles are incorporated into nanocomposite structure, the host tin oxide electrical properties will be highly improved.

While, the second strategy relies on production of composite thin films from two demixed crystalline phase of materials. Tin oxide is used as a TCO host phase and the dopant will serve as a second phase. This model is schematically illustrated in Fig. 7.11. In the model, big grains (colored in light blue) represent tin oxide matrix phase, while the small grains (colored in grain) represent the dopant materials. Thus, for enough dopant phase in the composite structure, the electrical properties of host tin oxide will be improved.

The work is divided into three chapters. *Chapter 8* will focus on incorporation of nanoparticles into tin oxide matrix structure in the framework of proposed model in Fig. 7.11 (a). TiO_2 NPS are chosen as a potential dopant for this purpose. While in *Chapter 9*, modulation doping is tested on tin oxide based demixed composite thin films, see the model in Fig. 7.11 (b). Al_2O_3 from $Al(acac)_3$ precursor used as a dopant phase here. Finally in *Chapter 10*, Al_2O_3 NPs will be incorporated into tin oxide matrix to test the modulation effect of produced nanocomposite films.

Chapter 8

TiO_2 NPs-SnO_2 Nanocomposite Thin Films

In this chapter, the concept of defect modulation doping is tested on nanocomposite films produced by ultrasonic spray pyrolysis technique. Titanium dioxide nanoparticles-TiO_2 NPs were chosen as a potential dopant and were incorporated into tin oxide-SnO_2 matrix for the formation of nanocomposite structure. The schematic illustration of the model for the synthesized nanocomposite films was presented in Fig. 7.11 (a). The chapter is divided in the following sections. Section 8.1, covers the results of different characterizations of as received TiO_2 NPs used for the formation of tin oxide based nanocomposite thin films. The presence of nanoparticles in the dispersed solution, average particle size and phases of studied TiO_2 NPs, which were obtained from TEM and Raman analyses will be described. The experimental conditions followed during the deposition of nanocomposite films will be shortly described in section 8.2. Section 8.3, emphasizes on incorporation of the dopant NPs into SnO_2 matrix with the aim of obtaining enhanced electrical properties in the produced nanocomposite films. For this purpose different thin films were prepared. The results obtained from different characterizations (EDS, Raman, and XRD) of synthesized TiO_2 NPs-SnO_2 nanocomposite thin films will be discussed here. In particular, the emphases is given to the confirmation of the presence of NPs into grown SnO_2 films. Furthermore, another alternative thin film synthesis technique namely *"droplet casting"* will be introduced and the results obtained from this technique will also be discussed in comparison with sprayed films. Finally, the chapter will be summarized with remarks and outlook in section 8.4.

8.1 TiO_2-nanoparticles (NPs)

TiO_2 NPs were synthesized in Lotus synthesis, a project partner for this work. The nanoparticles were received as a dispersion solution in a bottle with a composition shown in Tab. 8.1.

Table 8.1: Anatase TiO_2 nanoparticles dispersed in acidic water

components	weight percentage (wt%)	PH	Particle Size	TiO_2 phase
Titanium (IV) oxide	20	< 1	10 - 20 nm	Anatase
Water	>75			
Nitric Acid	<5			

To confirm the presence of TiO_2 NPs and identify the particle size, the received nanoparticles were examined on transmission electron microscope (TEM) by spreading the NPs dispersion on holey carbon copper grids. The resulting TEM images are presented in Fig. 8.1. The TEM images confirmed the presence of TiO_2 NPs having round shape structure. In addition, it was noticed that the nanoparticles were crystallized with an average particle size in the range of 10-25nm and are surrounded by semicrystalline polymeric agglomerate. This can be seen in the bottom left image of Fig. 8.1. The source of the polymeric agglomerate is not clear to the author but suspected that it could relate to the synthesis process of the nanoparticles.

Evidently, titanium dioxide films are very responsive to Raman experiments [261, 262, 263, 264]. Thus, to confirm the presence of TiO_2 NPs in the received dispersed solution bottle and to further identify the phase of TiO_2 NPs, the nanoparticles were examined in Raman spectroscopy. To prepare the samples for Raman experiment, the NPs dispersion was deposited on fused silica using droplet casting technique, see Fig. 8.2 (a). In droplet casting technique, the pipette is first filled with nanoparticles solution and the latter is transferred drop by drop in to the surface of substrate. During deposition the substrate was heated to 140 °C, which allows evaporation of water and nitric acid (HNO_3)[1] of dispersed solution. In order to evaporate the remaining organic species and to transform the phase of TiO_2 NPs, some of the produced layers were post annealed in air at 800 °C. Both as deposited and post annealed layers were then examined in Raman spectroscopy.

[1]N.B. the boiling point of nitric acid (HNO_3) is $\approx$ 83 °C

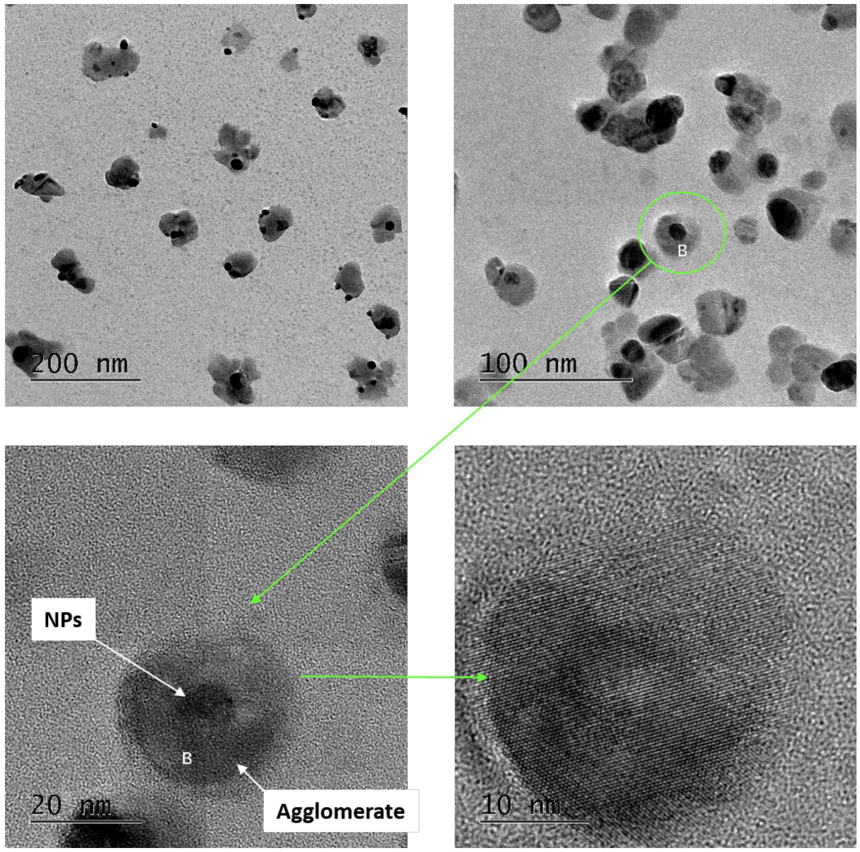

Figure 8.1: *Transmission electron microscope (TEM) images of as received TiO_2 NPs. The images confirmed the presence of crystalline, round shaped nanoparticles. In addition, semi-crystalline polymeric agglomerate have been observed encircling the NPs.*

The experimentally observed Raman spectra of TiO_2 NPs are presented in Fig. 8.2 (b). In the figure, Raman spectra of as deposited layer (blue), post annealed at 800 °C (red), and that of fused silica substrate (black) are represented. The characteristic of anatase TiO_2 includes: three E_g modes at 148.4, 193.96, and 635.94 cm^{-1}, one B_{1g} at 394.1 cm^{-1} and one A_{1g} 488.62 cm^{-1}, which were observed on both as deposited and annealed layers [265, 266]. As can be seen in the same figure, the Raman band at 148.4 cm^{-1} is very intense and sharp. For the sample annealed at 800 °C, E_g mode at 441.5 cm^{-1} and A_{1g} at 611 cm^{-1} of rutile TiO_2 was as well observed, which indicates the transformation of some of anatase to rutile phase of TiO_2 NPs and the formation of mixed polymorphs [267, 268], see the insert of Fig. 8.2 (c).

In summary, both TEM and Raman analyses confirmed the presence of TiO_2 NPs in the dispersed solution with a particle size ranging from 10-25 nm. In addition, TEM images reveal the presence of undesirable polymeric agglomerate, which encapsulated the nanoparticles.

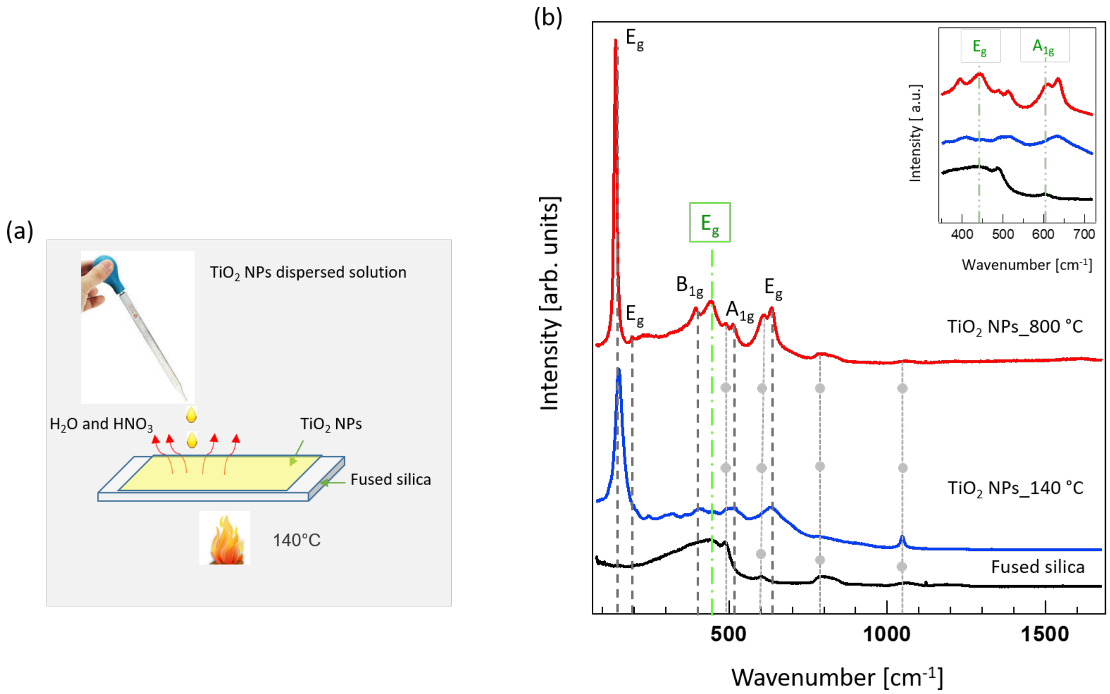

Figure 8.2: *(a), Schematic illustration of droplet casting technique for the production of TiO_2 NPs layers; (b), Raman spectra of TiO_2 NPs layers deposited on fused silica at 140 °C (blue) using droplet casting technique. Raman spectra of a layer post annealed at 800 °C is also represented (red). Additional Raman spectra of fused silica also shown for comparison (black). The typical Raman bands, which are the characteristics of anatase and rutile TiO_2 are represented by gray and green dashed lined respectively. In addition, peaks corresponding to fused silica are represented by dashed lines with a circle. The insert shows the magnified view of the two rutile Raman band structures after annealing treatment.*

8.2 Sample Preparation

The (TiO_2NPs-SnO_2) nanocomposite thin films were prepared by using homemade ultrasonic spray pyrolysis deposition system by mixing the NPs to the tin precursor of dibutyltin diacetate (DBTDA). The working principle of the setup is described in subsection 4.1.3. Different substrates were used during sample preparation namely, Si wafer, Corning C1737 borosilicate glass, and fused silica glasses, for the freedom of performing different characterizations. During deposition of the samples, the growth temperature was set at 500 °C, which resulted in a substrate surface temperature of 420 °C. This temperature setting was kept constant for all depositions. The deposition parameters followed during the preparation of different TiO_2 NPs incorporated SnO_2

nanocomposite films is summarized in Tab. 8.2.

Table 8.2: Deposition parameters of TiO_2NPs - SnO_2 nanocomposite thin films

TiO_2NPs - SnO_2 nanocomposite thin films							
Sample	SnO_2		TiO_2		Solvent	spray deposition	
	Precursor	conc. (m/l)	dopant	conc. (m/l)		Temp.	Time (min.)
SnO_2	DBTDA	0.1	-		ethanol	420 °C	45
TiO_2-SnO_2	DBTDA	0.1	TiO_2	0.001	ethanol	420 °C	30
TiO_2-SnO_2	DBTDA	0.1	TiO_2	0.001	ethanol	420 °C	45

8.3 TiO_2 NPs incorporation on SnO_2 films

The morphology and elemental composition of nominally undoped and nanoparticle incorporated SnO_2 thin films prepared on Si wafer substrate were examined by field emission gun-scanning electron microscope (FEG-SEM) and energy dispersive spectroscopy (EDS) analyzer equipped with SEM system. The results of these analyses is presented in Fig. 8.3. The SEM images of these films do not show any appreciable difference in both morphology and grain size except some of the grains look porous in the sample produced by adding acidic TiO_2 NPs in the tin precursor solution. This porosity of grains could be assigned to the acidic nature of TiO_2 NPs dispersion.

To confirm the incorporation of TiO_2 NPs into the grown SnO_2 films, the probed samples were examined in EDS by using acceleration voltage of V= 20 keV[2], see Fig. 8.3(c). The EDS spectra revealed, the expected titanium (Ti) peaks at respective energies of 0.45 and 4.51 keV are not observed for the sample prepared with addition of TiO_2 NPs into the precursor solution (Ti-Sn-O). On the other hand, the peaks corresponding to SnO_2 appear for both samples. Therefore, it is evident that EDS does not confirm the presence of TiO_2 NPs in the grown films.

[2]The applied voltage was very high so intense Si peak corresponding to Si wafer substrate was observed. Usually to avoid the spectra from substrate, lower acceleration voltage of ≈ 5-6 keV is used.

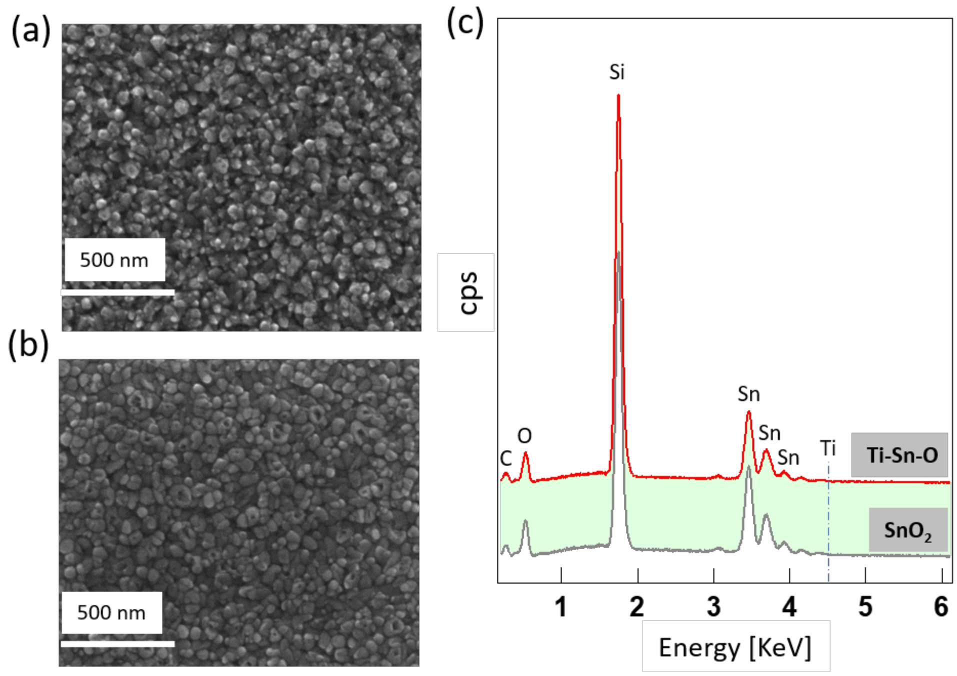

Figure 8.3: *The SEM images of (a) nominally undoped SnO_2, (b) nanocomposite film produced from NPs mixed Sn precursor solution (here it is represented as Ti-Sn-O), and (c) EDS spectra of the respective samples.*

As mentioned in section 8.1, TiO_2 NPs are very responsive to Raman experiments. Thus, to confirm the incorporation of TiO_2 NPs, as deposited TiO_2-SnO_2 nanocomposite sample and the same sample post annealed at 200 °C were examined by Raman spectroscopy, see Fig. 8.4. For comparison, Raman spectra of undoped SnO_2 with and without post annealing treatment are as well plotted in the same figure. In addition, the spectra of TiO_2 NPs layer post annealed at 800 °C and fused silica and corning glass substrates are also presented in same figure for comparison.

The Raman spectra of both as deposited and post annealed TiO_2 NPs-SnO_2 systems do not confirm the presence of TiO_2 NPs, since the most intense E_g mode Raman band at 148.4 cm^{-1} [265] was not seen on both as deposited and post annealed samples. The Raman shift of the most important bands of SnO_2 observed in nominally undoped and TiO_2 incorporated (Ti-Sn-O) SnO_2 films includes: E_g mode 476 cm^{-1}, A_{1g} mode 638 cm^{-1}, and B_{2g} mode at 782 cm^{-1} [269, 270]. However, the intensities of these modes are very weak in all examined samples, see Fig. 8.4. In addition, B_{2g} mode at 782 cm^{-1} was overlapped with Si-O stretching of the substrate. Here as well, the Raman spectroscopy does not confirm the presence of TiO_2 NPs in the studied nanocomposite films.

Furthermore, additional experiment of grazing incidence XRD (GIRXD) was performed

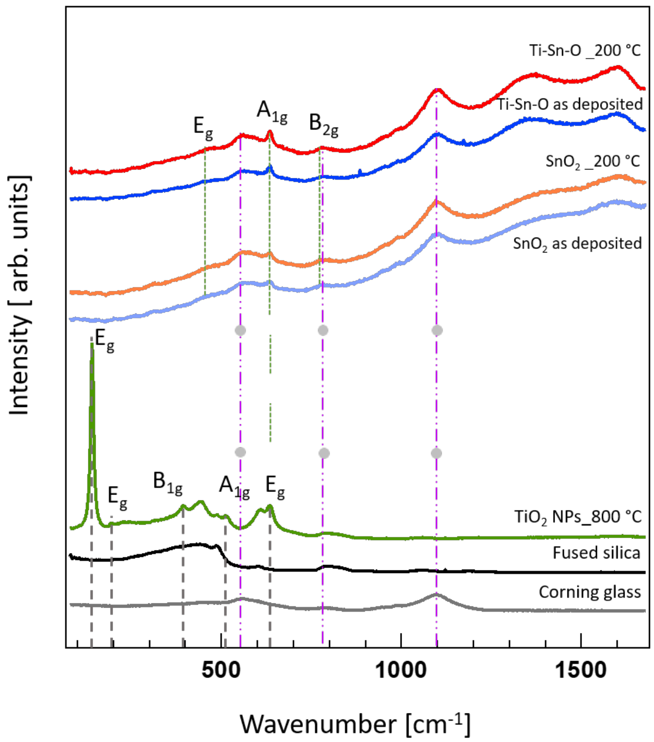

Figure 8.4: *Raman spectra of the sample prepared from TiO_2 NPs incorporated SnO_2 precursor solution deposited at 420 °C on corning glasses (Ti-Sn-O, blue) using spray pyrolysis technique. After deposition, the same sample was heat treated at 200 °C (Ti-Sn-O, red) in air and Raman spectra of undoped SnO_2 sample together with the spectra of post annealed sample also represented for comparison. The spectra of TiO_2 NPs layer post annealed at 800 °C, fused silica and corning glass substrates are also represented for visual comparison of the spectra. The typical Raman bands, which are characteristics of anatase TiO_2 are represented by gray lines and the green dashed lines represent the SnO_2 spectra. In addition, the peaks corresponding to corning glass are represented by dashed pink lines with a circle.*

.

in order to observe the diffraction pattern of TiO_2 from the probed nanocomposite sample. For this purpose, TiO_2-SnO_2 system, which post annealed at 200 °C and as deposited nominally undoped tin oxide sample were used. The XRD patterns of these samples are presented in Fig. 8.5. The diffraction patterns belonging to SnO_2 (PDF 00-041-1445) are assigned in the top of each peak. ICDD patterns of both anatase (PDF 00-021-1272) and rutile (PDF 00-021-1276) TiO_2 are represented by green and blue dashed lines respectively for reference.

For TiO_2-SnO_2 system, the diffraction peaks belonging to both anatase and rutile phases of TiO_2 were not observed, instead the diffraction peaks belonging to SnO_2 reflections

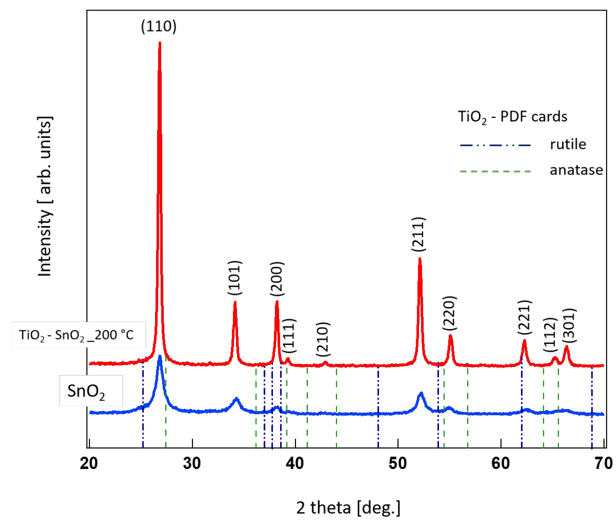

Figure 8.5: *(a) Grazing incidence-XRD (GIXRD) spectra of as deposited nominally undoped SnO_2 and TiO_2-SnO_2 system, which was post annealed in air at 200 °C. The diffraction peaks corresponding to SnO_2 are assigned on the top of each diffraction peaks (PDF SnO_2 00-041-1445), while anatase TiO_2 are marked with dashed green line (PDF TiO_2 anatase 00-021-1272), and dashed black lines for rutile TiO_2 (PDF TiO_2 rutile 00-021-1276).*

were seen with sharper and intense diffraction peaks compared to that of as deposited SnO_2 film. This indicates that the post annealing treatment improves the crystallinity of TiO_2-SnO_2 system. Here as well, GIXRD experiments do not confirm the presence of TiO_2 NPs in the grown nanocomposite films.

Different characterizations (EDS, Raman spectroscopy, and GIXRD) of the probed nanocomposite thin films synthesized by ultrasonic spray pyrolysis setup do not confirm the presence of TiO_2 NPs into the growing SnO_2 matrix. This might be related to the configuration of spray pyrolysis setup. In the setup (see Fig. 4.9), the substrates were mounted upside down and the sprayed mists were transported from the bottom of the chamber against gravity. Thus, this could lead to a transportation problem of nanoparticles and can result mainly in the synthesis of SnO_2 layer in the growing film. Therefore, it is not possible to test the modulation doping effect of TiO_2 NPs embedded tin oxide nanocomposite thin films under this condition.

In order to avoid the transportation problem, additional nanocomposite films were synthesized by drop casting technique[3] using the same precursor solution to those samples synthesized by spray pyrolysis.

[3] The description about the technique can be found in section 8.1.

During the synthesis of films[4], the substrate temperature was kept at 140 °C and afterwards the produced films were post annealed at 500 °C in air for 1 hour. The Raman spectra, optical image and EDS of the studied sample are shown in Fig. 8.6. After post annealing treatment, the films were not continuous throughout the layer surface. This can be seen in the optical image[5] of the same sample (Fig. 8.6(b)), in which the discontinuities are represented by different regions. Region (R1) represents the uncovered substrate region, Region (R3) represents fully covered continuous films region, and region (R2) represents the intermittent region.

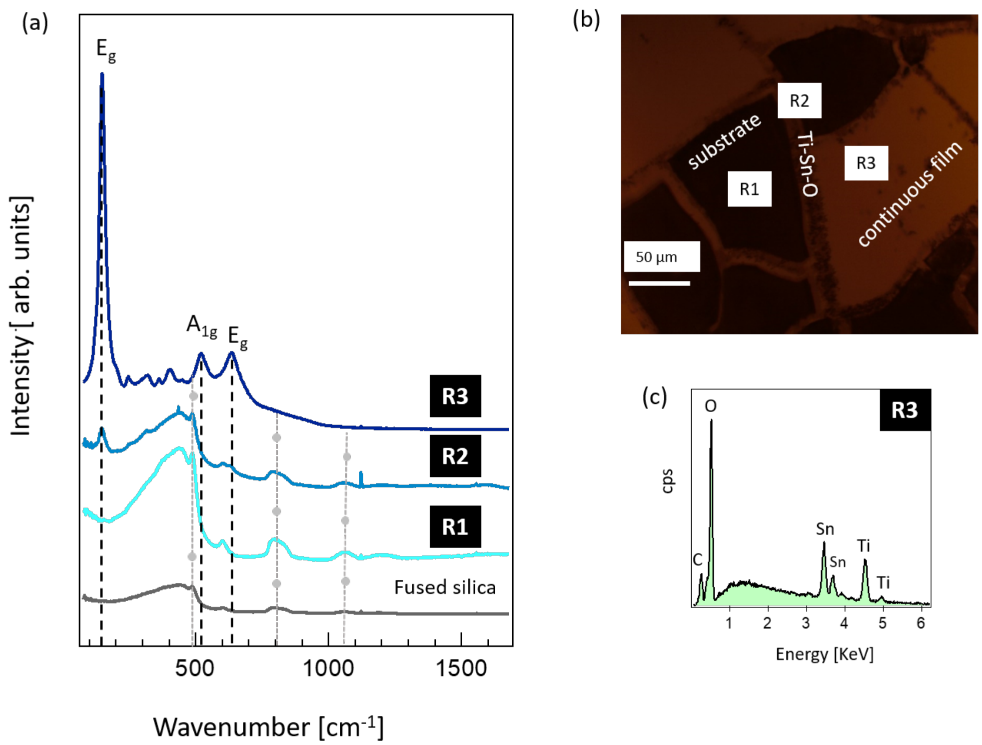

Figure 8.6: *Examination of TiO_2NPs - SnO_2 nanocomposite film prepared by pipette casting technique, which was synthesized on fused silica substrate at 140 °C and further post annealed at 500 °C for 1 hour (a), Raman spectra of the probed sample, since the produced film was not a continuous layer different regions are associated to different Raman spectra; (b), Optical image of the probed sample in reflection mode, in which R1 represent substrates or polymer agglomerate, R3 represents continuous nanocomposite layer, and R2 represents the intermittent region; and (c), EDS of the same film probed only in the continuous regime.*

The studied sample was further examined in Raman spectroscopy on the different regions (R1, R2, and R3), see Fig. 8.6 (a). For comparison the spectra of fused silica substrate is

[4] By drop casting technique

[5] the optical image was taken in reflection mode

also represented. The spectra of region R1 resembles that of fused silica substrate. This is true as the optical image also shows no film coverage in this region. In region R2, E_g mode Raman band at 148.4 cm^{-1} starts to appear and in region R3 the E_g intensifies as the film fully covers the substrate.

In conclusion, droplet casting method allowed us to incorporate TiO_2 NPs into SnO_2 matrix and formation of nanocomposite thin films. However, the produced films lack continuity and further investigation of the composite structure was not possible. In order to produce continuous nanocomposite films, selecting of the proper tin precursor is needed. In addition, finding alternative deposition technique, which can produce the desired nanocomposite structure is required.

8.4 Summary, Conclusion, and outlook

In this chapter, the chemical approach of defect modulation doping is tested on nanocomposite thin films. The main goal of this work was to produce nanoparticle incorporated nanocomposite thin films with the prospect of studding the electrical properties of the produced films in order to examine the influence of embedded nanoparticles. For this motive, different thin films were synthesized from DBTDA tin precursor in ethanolic solution and additional acidic TiO_2 NPs using spray pyrolysis and droplet casting.

Water dispersed TiO_2 NPs (which also contain small percentage of nitric acid) were received from Lotus synthesis, a project partner in this work. The TEM and Raman spectroscopy confirmed the presence of TiO_2 NPs within the dispersed solution with an average particle size in the range of 10-25 nm.

Different nanocomposite films were synthesized by using ultrasonic spray pyrolysis setup. The produced thin films were examined by several characterization techniques to confirm the incorporation of TiO_2 NPs into the grown films.

- The SEM images of nanocomposite films do not show any appreciable difference with nominally undoped tin oxide film. In addition, EDS of the same sample does not show any peak related to elemental Ti.

- Raman experiments as well do not confirm the presence any phase of TiO_2 NPs, knowing that this technique is very responsive to any form TiO_2 systems.

- The GIXRD patters of studied films do no show reflection corresponding to any crystalline phase of TiO_2 NPs.

Therefore, it is reasonable to conclude that for the thin films synthesized by ultrasonic spray pyrolysis setup the nanoparticles were not incorporated into growing films. In addition, their were some concerns regarding usage of the received TiO_2 NPs in the system:

- The dispersed solution contains few percentage of nitric acid.

  - First, as can be seen in Tab. 8.2 ethanol was used as a solvent for the preparation of precursor solution. The mixture of nitric acid and solvents (ethanol or methanol) could be a potential explosive [271].

  - Secondly, it was not possible to use the effective SnO_2 precursor namely-$SnCl_4$.

$5H_2O$ for this study. This is due to the acidic byproduct of precursor (HCl), which can react with nitric acid and form *aqua regia*.

- TEM images of TiO_2 NPs revealed the presence of encapsulating polymeric agglomerates. Thus, the nanoparticles are not active and the encapsulation may prevent the doping effect of nanoparticles, if the nanoparticles were embedded in the grown tin oxide films.

Another concern was the configuration of spray setup, in which the substrates were mounted upside down and sprayed mists were transported upward against gravity. This could made the transportation of nanoparticles difficult. Alternately, additional films were prepared by droplet casting technique from the same precursor solution. Raman and EDS analyses confirmed the presence of dopant TiO_2 NPs in the grown films. However, the films prepared by this technique suffers discontinuity. Thereby, further analysis of the nanocomposite structure was not possible.

In conclusion, the synthesis of nanocomposite films was the first step to test the modulation doping effect of TiO_2 NPs into tin oxide films. This was not the case as TiO_2 NPs do not embedded into the grown films in the current spray pyrolysis setup [6]. Improvement of the current spray pyrolysis setup and and of alternative thin film deposition techniques may result in the desired embedded structure. In addition, non acidic nanoparticles are would be more pertinent in order to avoid the problems mentioned above.

[6] more detailed description about the possible problems of current deposition chamber configuration can be found in section 10.6

Chapter 9

SnO_2-Al_2O_3 Demixed Composite Thin Films

In this chapter the concept of modulation doping is tested on Al_2O_3-SnO_2 demixed composite films, in which Al_2O_3 is used as a potential dopant. For this purpose, different composite thin films were prepared from SnO_2 and Al_2O_3 precursor solutions by ultrasonic spray pyrolysis technique. Schematic illustration of the model for demixed composite structure is shown in Fig. 7.11 (b). The chapter is divided in the following sections.

Section section 9.1 shortly describes the experimental conditions followed during the composite film production. Section 9.2 is devoted for confirming the formation of demixed phases of Al_2O_3 and SnO_2 in the composite structure. For this purpose, different structural characterizations (SEM, EDS, EPMA, XRD, TEM, and FTIR) on as deposited as well post annealed samples were performed. The optical properties of the studied samples will be discussed in section 9.3. Section 9.4 covers the electrical studies of the probed samples. The electrical study of the probed samples is covered in section 9.4. Finally, the chapter will be summarized and concluded in section 9.5.

Part of the results of this chapter have been published in the journal *Molecules* [272].

9.1 Sample Preparation

The demixed composite films were prepared by using homemade ultrasonic spray pyrolysis deposition method on different substrates, namely Si wafer, Corning C1737 borosilicate glass, fused silica glasses, and SiO_2/ Si wafer. Different types of substrates were used in order to have flexibility in performing different characterizations. The working principle of the setup was explained earlier in subsection 4.1.3. The tin precursor was $SnCl_4 \cdot 5(H_2O)$ dissolved in methanol with a fixed concentration of 0.1 M. Aluminum precursor was aluminum acetylacetonate-Al(acac)$_3$, which was added into the precursor solution in different concentrations: 0.0005, 0.001, 0.0015, 0.002, 0.0025, 0.005, 0.01, and 0.015 M. This corresponds to the Al/(Al+Sn) atomic ratio in a precursor solution of 0%, 0.5%, 1%, 1.37%, 1.96%, 2.44%, 4.76%, 9.1%, and 13.04%. During deposition of the samples, the growth temperature was set at 500 °C, which resulted in a substrate surface temperature of 420 °C. This temperature setting was kept constant for all depositions. The deposition parameters followed during the preparation of different Al_2O_3 - SnO_2 demixed composite films are summarized in Tab. 9.1.

In Tab. 9.1, other than the deposition conditions additional information about the deposition rate, the film thicknesses, and cationic Al % in the grown films are included. The film thicknesses are extracted from the SEM cross-section of the films grown on Si wafer substrate. The deposition rates are calculated using these thickness values. The Al/(Al+Sn) atomic ratio are calculated from the results obtained from EPMA analysis, which will be described more in detail in section 9.2.

For the sake of simplicity for presenting the results and further interpretation and discussion, sample identification is given here by using Al/(Al+Sn) results from EPMA, presented in Tab. 9.1. Undoped tin oxide will be named as nominally undoped SnO_2 or 0. The films grown with incorporation of Al(acac)$_3$ in the precursor solution are differentiated as SnO_2 :Al-XX, with XX corresponding to the cationic Al concentration in the films (example, SnO_2 :Al-0.2, SnO_2 :Al-1.8, and SnO_2 :Al-5.2).

Table 9.1: Deposition parameters of Al_2O_3 - SnO_2 demixed composite films.

Al_2O_3 - SnO_2 demixed composite films										
Sample		SnO_2		Al_2O_3		Solvent	Spray deposition			
Al/(Al+Sn) solution (%)	Al/(Al+Sn) Film (%)	Precursor	Conc. (m/l)	Precursor	Conc. (m/l)		Temp. (°C)	Time (min.)	Rate (nm/min)	Film thickness (nm)
0	-	$SnCl_4.5(H_2O)$	0.1	-	-	methanol	420	45	15	670
0.5	0.15	$SnCl_4.5(H_2O)$	0.1	$Al(acac)_3$	0.005	methanol	420	25	10.4	260
1	0.2	$SnCl_4.5(H_2O)$	0.1	$Al(acac)_3$	0.01	methanol	420	30	11.3	340
1.37	0.3	$SnCl_4.5(H_2O)$	0.1	$Al(acac)_3$	0.015	methanol	420	25	10.4	260
1.96	0.4	$SnCl_4.5(H_2O)$	0.1	$Al(acac)_3$	0.02	methanol	420	25	11.6	290
2.44	1.64 ± 0.08	$SnCl_4.5(H_2O)$	0.1	$Al(acac)_3$	0.025	methanol	420	30	6.7	200
4.76	1.8 ± 0.08	$SnCl_4.5(H_2O)$	0.1	$Al(acac)_3$	0.05	methanol	420	45	14.66	660
9.1	3.8 ± 0.2	$SnCl_4.5(H_2O)$	0.1	$Al(acac)_3$	0.1	methanol	420	45	17.7	800
13.04	5.2 ± 0.5	$SnCl_4.5(H_2O)$	0.1	$Al(acac)_3$	0.15	methanol	420	45	13	580

9.2 Structural Study

In order to evaluate the incorporation of aluminum in the SnO_2 thin films energy dispersive X-ray spectroscopy (EDS) measurements were performed on the films deposited on Si wafer substrates. The results are presented in Fig. 9.1 (a). In order to reduce the contribution of Si-wafer substrate in the spectra of films, the EDS measurements were performed at lower accelerating voltage of 6 keV, which allows to investigate a depth which corresponds well with the layer thickness. The energy of the detected elements are summarized in Tab. 9.2. EDS confirmed the presence of Al in the deposited thin oxide thin films. The aluminum peak at 1.486 keV intensifies as the amount of aluminum in the precursor solution increases, as shown in the magnified image of Fig. 9.1 (a). SnO_2 :Al-1.64 sample shows additional intensified peak around 1.7 keV, which is Si from the substrate. This is due to the fact that the sample is thin enough and using 6 keV accelerated voltage enables to reach the substrate surface.

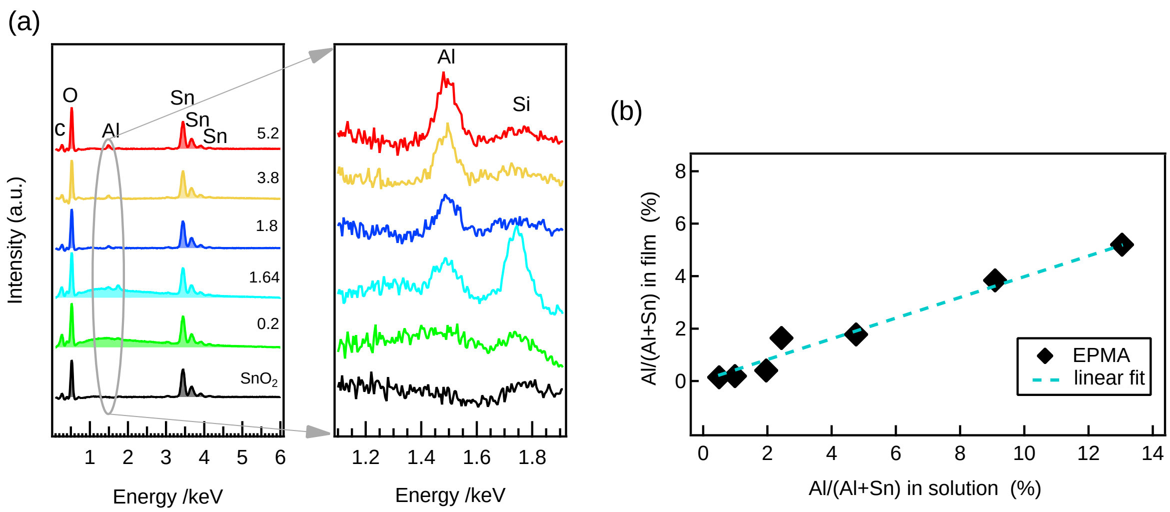

Figure 9.1: *(a) EDS spectra at 6 keV of different SnO_2 :Al thin films prepared on Si wafer substrates. In the right, magnified spectra of the same films around 1.5 keV is shown to see the evolution of Al peak; (b) relative Al content as obtained from EPMA analyses compared to the amount of Al in the precursor solution. A dashed line represents the linear relationship.*

Furthermore, the same samples were probed by another elemental analysis technique, namely Electron Probe Micro-Analyzer (EPMA, Cameca SX50 system equipped with wavelength dispersive spectrometers). The aluminum incorporation in each individual samples were quantified by this technique. EPMA measurements were performed at three different electron beam acceleration voltages (11, 16, and 22 keV) and the data were analyzed using the Stratagem program dedicated to the analysis of thin films [273].

Table 9.2: Energy table for EDS analysis of Al_2O_3 - SnO_2 composite films in keV

Element	$\mathbf{K}_\alpha$	$\mathbf{L}_\alpha$	$\mathbf{L}_\beta$
Tin- Sn	25.271	3.443	3.663
Silicon - Si	1.739	-	-
Aluminum-Al	1.486	-	-
Oxygen- O	0.525	-	-
Carbon- C	0.277	-	-

EPMA also confirmed the presence of aluminum in the studied films. The Al/(Al+Sn) atomic ratio obtained from EPMA is presented in Tab. 9.1 and the same results are plotted versus Al/(Al+Sn) atomic ratio of the starting solution, see Fig. 9.1 (b). The aluminum content in the produced films is only about ∼1/3 of that in the precursor solution. This suggests, under the current deposition conditions, that tin oxide is more efficiently deposited than aluminum incorporation.

The morphology of the studied films were examined in scanning electron microscopy (SEM)[1] operating at the voltage that varies from 5-20 keV. The top view SEM images of nominally undoped SnO_2 and different SnO_2 :Al films prepared on Si wafer substrates are shown in Fig. 9.2. The thicknesses of these films were estimated from the SEM cross-section measurements and are displayed in Tab. 9.1. The thickness variations among these films are mainly due to different deposition times (25, 30, and 45 min) and a slight variation of average flow rate of the precursor solution (2-2.3 mL/min). The produced films are all crystalline and significant morphological changes are observed upon the amount of Al incorporation. A similar trend has been observed for the films prepared on the other substrates.

The SEM image of nominally undoped SnO_2 film clearly reveals the polycrystalline nature of the films as well as the presence of extended planar twin defects crossing the entire grains. Moreover, the density of these defects is high as several extended twin defects can be identified within individual grains. Similar observations have been reported by different researchers for SnO_2 films produced by spray pyrolysis and the density of twins increased with increasing the concencentration of tin precursor $SnCl_4.5(H_2O)$ [274, 275, 276], along with an increase of deposition rate. It is important to note that these twin boundaries are not desirable for electrical properties of SnO_2 films as they are considered as additional electron scattering sites [277].

[1]The working principle of SEM system is discussed in subsubsection 4.2.1.3

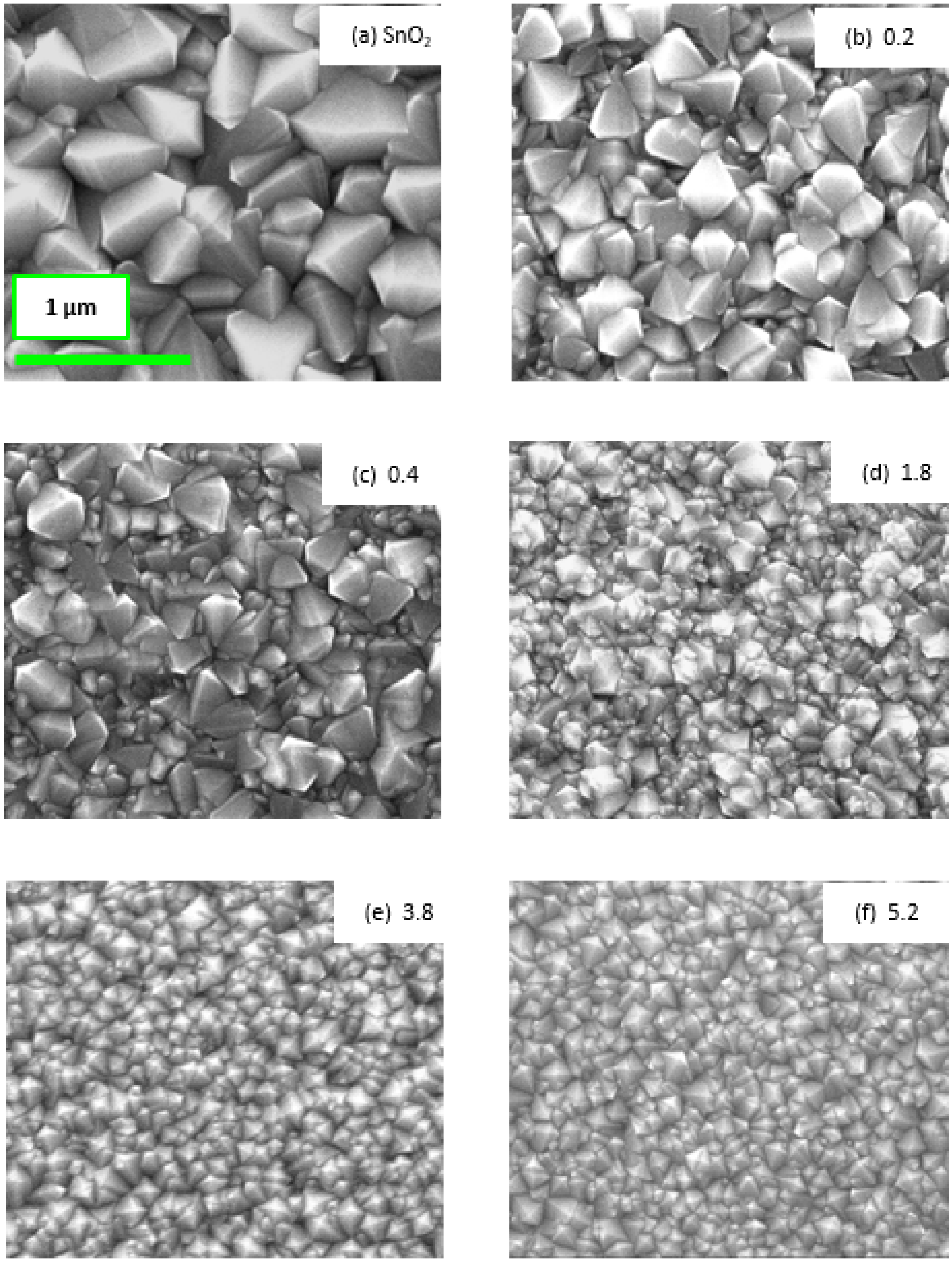

Figure 9.2: *Top-view FEG-SEM images of nominally undoped SnO_2 and different Al-doped SnO_2 thin films deposited on silicon wafer. (a) represents the pure SnO_2, while (b)-(f) corresponding to Al-doped films with the number associated with each image is the measured atomic ratio (Al/Al+Sn) in the films. All images have the same scale of 1 µm and the green scale bar presented in image (a) is identical for all samples.*

The density of planar defects decreased considerably upon Al incorporation, they have been seen in the SnO_2 :Al-0.2 and -0.4 films, see image (b) and (c) of Fig. 9.2. For the higher Al content films (1.8-5.2), the lamellar twins are not present anymore. Due to the presence of both grains and twin boundaries in nominally undoped SnO_2 and some Al incorporated films, it is important to distinguish between the grain size (L_g) and crystallite size (L_c) of the films .

The grain size (L_g) of the studied films was determined from the top view of SEM images shown in Fig. 9.2 by using digital image processing imageJ software. The average and the biggest grain size of these films are plotted for different compositions of SnO_2 :Al thin films, see Fig. 9.3. The visual observation of SEM images of Fig. 9.2 and the grain size plots of Fig. 9.3 shows the L_g of produced films decreased consistently with increasing Al_2O_3 concentration in the precursor solution. This could result from a thermodynamically favored heterogeneous nucleation of small grains induced by Al incorporation. Similar observations have been reported by Sinha et al. [278], Ahmed et al. [279], and Moharrami et al. [280].

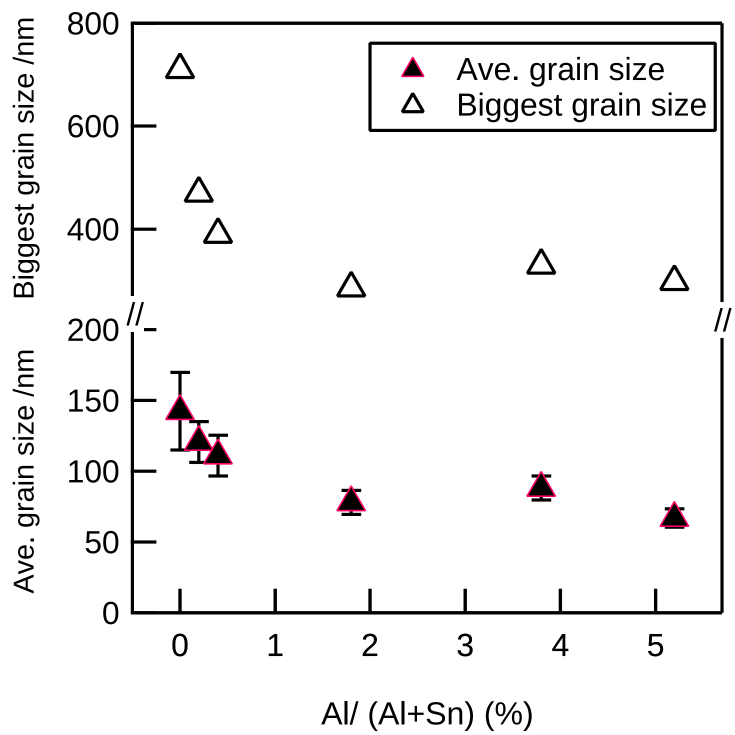

Figure 9.3: *The change of average grain size versus Al cationic ratio in the film for different compositions of* SnO_2 *:Al thin films obtained by using the digital image processing ImageJ software. The error bars show the standard deviation of the grain size distribution. The size of the biggest grain within the same films are also represented.*

Nominally undoped SnO_2 have an average grain size of 142 ± 27 nm with the biggest grain of the same film exhibit a size of 710 nm, which indicates there is upto 6 times size difference in the grains of the same film. Similarly, for the highest Al content SnO_2 :Al-5.2 sample, the average grain size is 67 ± 6 nm with the biggest grain of 300 nm, which also shows there is upto 5 times grain size variation within the film. These results are supported by the SEM images of the same films shown in Fig. 9.4. In the images, the biggest grains are colored in violet, while some smaller grains are colored in sky blue for comparison. Undoped tin oxide (Fig. 9.4(a)) have the biggest grain size of 710 nm and smaller grains of as low as 100 nm, which indicates there is upto 7 times size variation within the grains of the same sample. Similarly, SnO_2 :Al-5.2 (Fig. 9.4(b)) show upto 8 times variation in the grain size within the film.

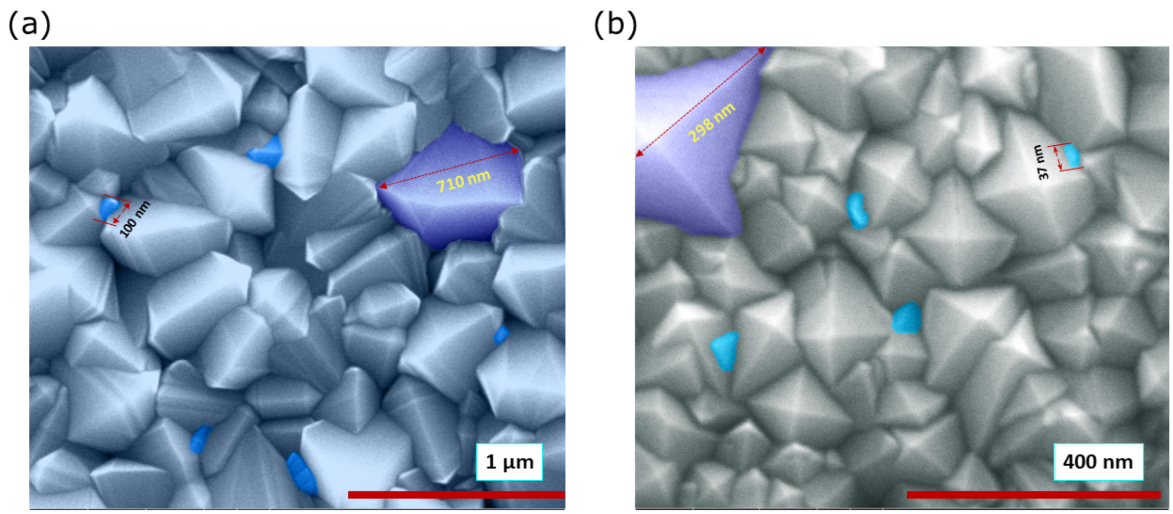

Figure 9.4: *Visual illustration of the grain size dispersion in the studied samples: SEM image of nominally undoped SnO_2 (a) and SnO_2:Al-5.2 (b). In both images the biggest grain is colored in violet, while some smaller grains are colored in sky blue for comparison.*

Figure Fig. 9.3 indicates that the Al composition within SnO_2:Al-5.2 films plays a key role in the grain size, more than the film thickness for instance. Indeed, the dependency of the average or biggest grain size exhibit a monotonous dependency and is rather independent from film thickness, at least in the range of 200–800 nm, see Tab. 9.1. The physical origin of these observations is probably a favored heterogeneous nucleation induced by Al incorporation in the film.

The EDS and EPMA experiments confirmed the presence of aluminum in the studied samples. Now the question is to identify whether Al is incorporated in SnO_2 films (Al elemental doping) or form different Al_2O_3 phase and forming demixed composite films. Thereby, in order to confirm the presence of crystalline phase of Al_2O_3 and identify different polymorphs of aluminum oxide, the studied films were examined by X-ray powder diffraction (XRD) in Bragg- Brento configuration. The detail working principle of XRD is explained in subsubsection 4.2.1.2.

The peak position of the diffraction patterns of studied films were shifted upto ≈0.168 °, see Fig. 9.5(a). This shift in peak position could have two explanations:

- **Z sample alignment**: For XRD analysis the probed samples must be positioned exactly at the center (in Z direction) of goniometer. If this is not the case, the sample alignment will not be good and the shift in the peak position would happen [281]. This shift depend on 2θ and it is more important at lower angles and almost not visible at higher angles [282, 283]. In order to correct this problem transition of data is not enough, rather calculating the shift due to a Z displacement using the following formula is required:

$$\Delta 2\theta(^\circ) = \frac{2 \times s \times cos(\theta)}{R} \times \frac{180}{\pi} \tag{9.1}$$

  where; $\Delta 2\theta$ is change in peak position, s is displacement of the sample , delta (2θ) is the shift of the position of the peak in 2θ and R is the instrument radius.

- **Offset on the detector**: the other possible reason for a shift in peak position could be due to a shift on the 2θ arm, that is shift on the position of the detector. This means when $\theta = 0$, $2\theta \neq 0$, with an offset on the position of the detector. This offset is constant for all the acquisitions and will be the same at both low and high angles. The correction for this problem is done to translate the data in 2 theta.

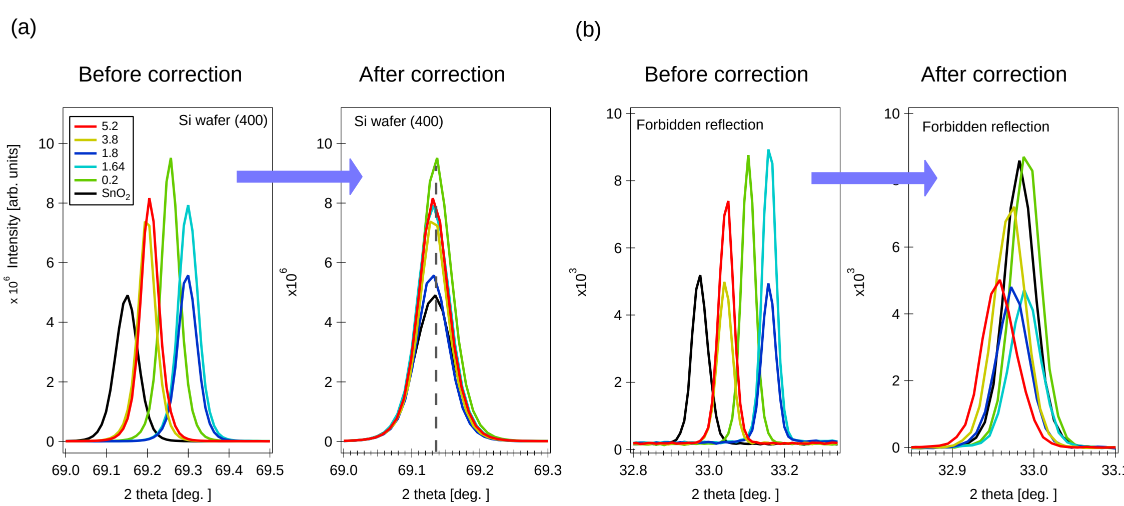

Figure 9.5: *Correction on X-ray reflections of the studied SnO_2:Al thin films by: (a), aligning the spectrum's according to Si (400) reflection at 69.132 ° (PDF- Si-00-027-1402) shown by vertical green dashed line and (b), forbidden reflection at 33 °.*

The correction on the peak position shifts of probed samples was possible by using well defined peak of crystalline substrate as reference. For this purpose, the probed

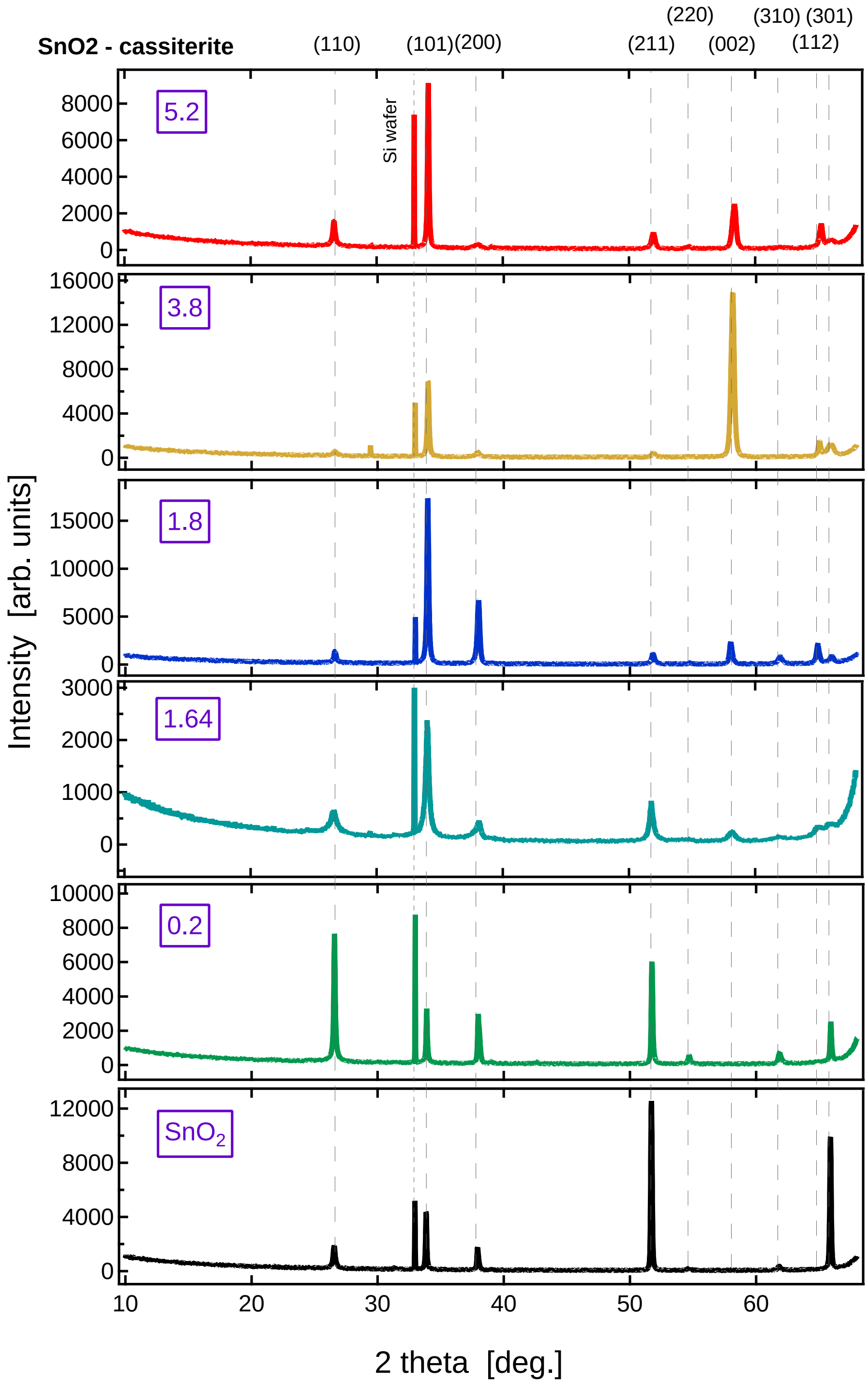

Figure 9.6: *Corrected X - ray diffraction (XRD) θ-2θ patterns of nominally undoped SnO_2 and different SnO_2:Al thin films with increasing Al content in the prepared samples using Si wafer substrate. In the same plot, the diffraction peaks corresponding to SnO_2 are marked with dashed lines (PDF-00-041-1445) and labeled with individual crystallographic orientation on the top.*

samples were prepared on Si wafer [110] substrate and Si (400) reflection with PDF card (Si-00-027-1402) was used as reference peak for correction. The diffraction peaks of Si (400) of probed samples around 69° before and after correction are shown in Fig. 9.5. Similarly, the forbidden reflection of Si (200) around 33° also represented in the same plot. However, generally speaking peak shift could have also another origin than instrumental: for instance change of lattice parameters, strains and so on.

The θ -2θ XRD diffraction patterns of undoped SnO_2 and different SnO_2:Al thin films collected between 10° and 70° (in 2θ scale) are shown in Fig. 9.6. In the same figure, the diffraction peaks corresponding to SnO_2 reflections are marked with dashed lines (PDF-00-041-1445) and labeled with individual crystallographic orientation on the top. In these diffraction patterns there was no crystalline peak corresponding to any polymorphs of Al_2O_3, rather big texturing have been observed upon change in Al_2O_3 concentration on the precursor solution.

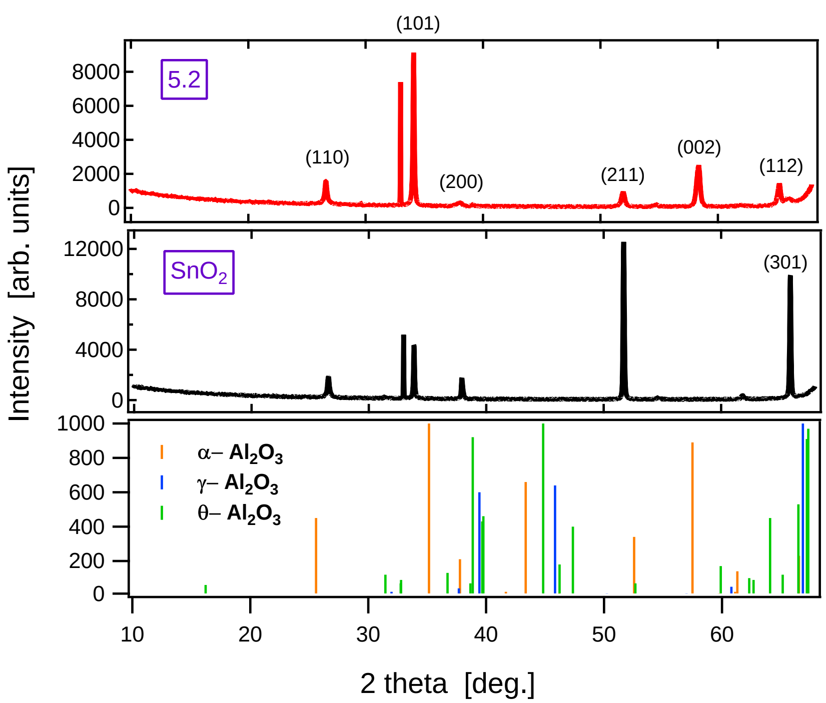

Figure 9.7: *θ - 2θ XRD patterns of pure SnO_2 and SnO_2:Al-5.2 samples. The diffraction peaks corresponding to SnO_2 are labeled in the top of reflection (PDF-00-041-1445): α- Al_2O_3 with orange line (PDF - 00-046-1212), γ - Al_2O_3 with blue line (PDF - 00-056-0457), and θ - Al_2O_3 with green line (PDF - 00-056-0456) standards are represented in the bottom plot.*

In order to check the presence of any kind of polymorphs of Al_2O_3 in the studied samples, the XRD patterns of undoped SnO_2 and the highest Al content SnO_2:Al-5.2 samples are compared in Fig. 9.7. In the figure, the important polymorphs of Al_2O_3, θ (PDF - 00-056-0456), γ (PDF - 00-056-0457), κ (PDF - 00-052-0803), and η (PDF -

00-056-0458) standards are represented. It is important to note that the probed samples were synthesized at 420 °C and XRD measurements are performed without further post annealing treatments. Thereby, the reflections of the stable α-phase is not expected in these films, since this stable phase can only appear at temperature higher than 1100 °C [284]. SnO_2:Al-5.2 does not show any reflection corresponding to any of the polymorphs of Al_2O_3, except the reflection at ≈58.3 °. This reflection could be assigned to (002) reflection of SnO_2 or (116) reflection of α-Al_2O_3. However, finding the reflection of α for as deposited films is unfortunate, thus the reflection must correspond to (002) SnO_2. Therefore, it is reasonable to argue there was no crystalline polymorphs of alumina. Amorphous Al_2O_3 still could be present in the films. One clear thing observed from XRD patterns of these two films is that there is a big texturing upon Al incorporation.

Furthermore, SnO_2:Al-5.2 sample was examined by TEM analysis in order to check the presence of crystalline Al_2O_3 in the grown films, see Fig. 9.8. This sample is chosen as it is the highest Al content film among the studied samples. The obtained diffraction rings are in a good agreement with the indices of SnO_2. However, there was no single diffraction ring matching the indices of crystalline alpha or other Al_2O_3 polymorphs.

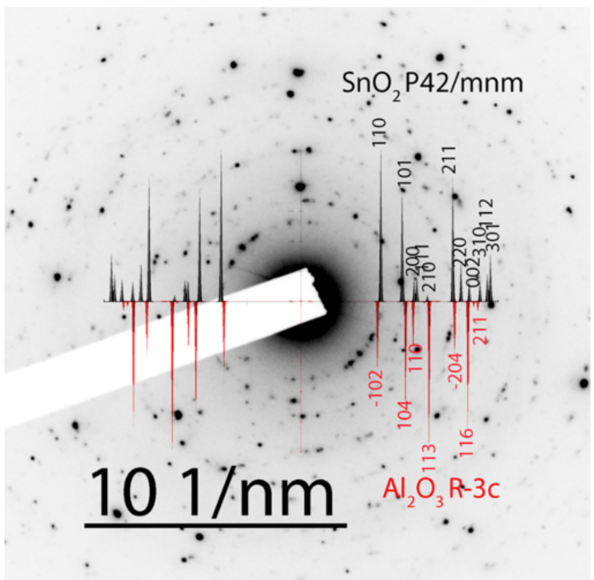

Figure 9.8: *TEM diffraction pattern of as deposited SnO_2:Al-5.2 sample prepared on Si wafer substrate with indices of SnO_2 (ICDD-00-041-1445) and α-Al_2O_3 (ICDD-00-046-1212).*

The XRD patterns of probed samples exhibit a systematic shift to higher degree and a broadening of the peaks upon increasing Al content in tin oxide films. To show this phenomenon, the (101) and (211) diffraction peaks were selected and plotted for all samples, see Fig. 9.9(a). For the (101) reflection, the peak position shifted from 33.84° for nominally undoped tin oxide to 34.089° for the SnO_2:Al-5.2 sample. Similarly, the

(211) reflection exhibited a shift of 0.23° to a higher angle for the SnO_2:Al-5.2 sample compared to nominally undoped tin oxide. In both reflections, black dashed arrows were used for visual guidance of the peaks shifting to higher angle. In addition, broadening of the peaks can clearly be observed in both reflections as the Al content increased in the prepared samples.

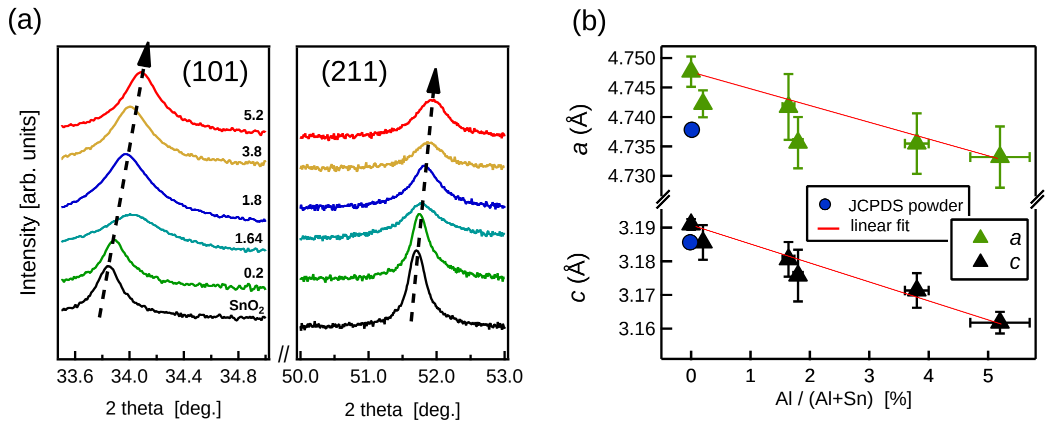

Figure 9.9: *(a), Broadening and shifting to the higher angles of XRD patterns of tin oxide thin films upon Al incorporation. Here, two dashed arrows are used to indicate that the Bragg peak position is continuously increased with increasing Al content in the grown films, (b), lattice constants a and c versus Al cationic (%) in the films. The lattice constants of standard JCPDS powder (PDF-00-041-1445) are also included for comparison. The linear interpolations (red lines) between SnO_2 and SnO_2:Al-5.2 films are plotted to show the linear relationship between lattice constant and Al concentrationin the films following Vegard's law.*

This shifting of the XRD peaks of tin oxide films upon increasing $Al(acac)_3$ concentration in the precursor solution is attributed to incorporation of Al into the SnO_2 lattice structure. In addition, the broadening of the peaks is related to the decrease of the grain size observed upon increasing the Al content. In six-fold coordination, the ionic radii of Al^{3+} (0.051 nm) is about 30% smaller than that of Sn^{4+} (0.071 nm), therefore it is compatible with the hypothesis that the Al dopant effectively substitutes the host atom without forming any secondary phase in the system. The overall lattice parameter is thus expected to decrease as more Al ions occupy the Sn sites, as indeed observed experimentally. Similar observations have been reported by Lee et al. [285] for Al content in the film (atomic %) varing from 0 to 8.2%, Ravichandran et al. [286] with Al concentration in the starting solution increasing from 0–30 atomic %, and Thirumurugan et al. [287] for 3 atomic % doping. In addition, the broadening of the XRD peaks indicates a diminution of crystal sizes.

The variation of lattice constants (a and c) of tin oxide films versus Al atomic (%) in the film is presented in Fig. 9.9(b). The lattice parameter's values a and c were determined from the Eq. 9.2 using (110), (101), (200), and (211) diffraction lines:

$$\frac{1}{d_{hkl}} = \sqrt{\frac{h^2 + k^2}{a^2} + \frac{l^2}{c^2}} \tag{9.2}$$

where d_{hkl} is the lattice parameter and h, k, and l are the Miller indices. The errors both in determining the lattice parameters from different diffraction lines and the Al atomic (%) from EPMA measurements are included in the plot. Without doping, the lattice constants of SnO_2 are: a = 4.74769 ± 0.0026 Åand c = 3.19093 ± 0.00164 Å, which are close to the standard SnO_2 powder (a = 4.73820 Åand c = 3.18710 Å). As the dopant concentration increases, both lattice constants decrease and the relative decrease in c is almost double that for a. To confirm whether the evolution of the lattice parameters upon doping follows Vegard's law [288, 289], which predicts a linear decrease of alloy lattice as the concentration of smaller size dopant increases, a linear fit has been plotted in Fig. 9.9(b). With a consideration of both the error bars of lattice parameters and Al atomic % of EPMA measurements, it can be considered that a and c follow Vegard's law rather well.

It has been stated that the electrical and optical properties of SnO_2 thin films depend on their preferential crystallographic orientations (i.e., texture) [290]. Thus, a deeper understanding and control of the structural ordering is important to better characterize these properties. The film texture strongly influences the grain boundary nature, which can affect the electrical mobility by scattering the free charge carriers. Additionally, the film texture governs the crystallographic orientation of the top facets and interface properties in heterojunctions. Interestingly, the preferred orientations are in turn governed by different physical mechanisms and this includes the following parameters by growth conditions, film thickness, type of substrate, nature of chemical precursors, and doping [274, 291, 292, 293].

As dopant ions substitute the host ions, the film growth orientation is altered as a result of mechanical strain induced in the lattice [294]. Here, the XRD patterns also show significant preferential orientations with Al incorporation into the tin oxide films. The change of texture coefficient C_{hkl} for thin oxide films upon Al incorporation has been calculated based on θ-2θ XRD measurements of Fig. 9.6. Only seven main peaks were taken into account: (110), (101), (200), (211), (002), (112), and (301). The texture analysis was quantitatively carried out from the $K\alpha_1$ component of each diffraction peak in the framework of the Harris method [184]. The texture coefficients C_{hkl} for each (hkl) crystallographic directions and degree of preferred orientation σ were respectively defined as the following in Eq. 9.3:

$$C_{hkl} = \frac{\frac{I_{hkl}}{I_{o,hkl}}}{\frac{1}{N}\Sigma_N \frac{I_{hkl}}{I_{o,hkl}}} \quad and \quad \sigma = \frac{\sqrt{\Sigma_N (C_{hkl}-1)^2}}{\sqrt{N}} \tag{9.3}$$

where; I_{hkl} is the intensity of (hkl) reflection of studied samples; $I_{o,hkl}$ is the intensity of the corresponding plane in the reference of powder (PDF 00-041-1445) from the International Center for Diffraction Data (ICDD), and N represents the number of reflections, in our case N=7.

Basically for randomly oriented samples, the texture coefficient and degree of preferred orientation equal 1 and 0, respectively. In contrast, for perfectly oriented grain samples along the (hkl) direction, the texture coefficient equals N for (hkl) planes (N=7 in our case) and 0 for other crystallographic planes and consequently the degree of preferred orientation is $\sqrt{N-1}$.

The pronounced structural reordering correlated with the evolution of texture coefficients for each (hkl) crystallographic direction and the degree of preferred orientation of the studied films are shown in Fig. 9.10. For nominally undoped SnO_2, the (301) crystallographic orientation is dominant with a texture coefficient of 4.57 and the (211) crystallographic orientation also has a C_{hkl} of 1.45. In the case of SnO_2:Al -0.2 sample, (301) is still the dominant orientation with C_{hkl} of 2.16; in addition (200) and (211) crystallographic orientations revealed C_{hkl} of 1.83 and 1.43 respectively. In contrast, a texture change is observed for the SnO_2:Al -1.64 film. Here, the (101) crystallographic orientation becomes the dominant orientation with a C_{hkl} of 2.56. In addition (002), (211), and (200) orientations have C_{hkl} of 1.6, 1.1, and 1.1 respectively. For the SnO_2:Al-1.8 sample the texture changed again and (002) becomes the dominant orientation with a C_{hkl} of 2.27. Finally, it became the only dominant orientation for SnO_2:Al-3.8 and -5.2 films. As a result, polycrstalline SnO_2 thin films undergo a texture transition from (301) to (101), and then to (002) preferred cristallographic orientation upon increasing Al content in the grown films [295].

It is further shown that the relative intensity between different (hkl) Bragg reflections is strongly dependent on the amount of Al incorporated into the growing film. The degree of preferred orientation is drastically reduced from 1.53 in undoped SnO_2 to $\approx$0.88 for SnO_2:Al-0.2 film. It remained almost unchanged between SnO_2:Al-0.2 and SnO_2:Al-1.8 films, and then suddenly increased to 2.2 for the SnO_2:Al-3.8 film. Finally for the highest Al content SnO_2:Al-5.2 film, the degree of preferred orientation reduced to 1.4 as can be seen in the insert of Fig. 9.10.

Due to the presence of twin boundaries in nominally undoped SnO_2 and different SnO_2:Al films, it was important to distinguish between the grain size (L_g) and crystallite size

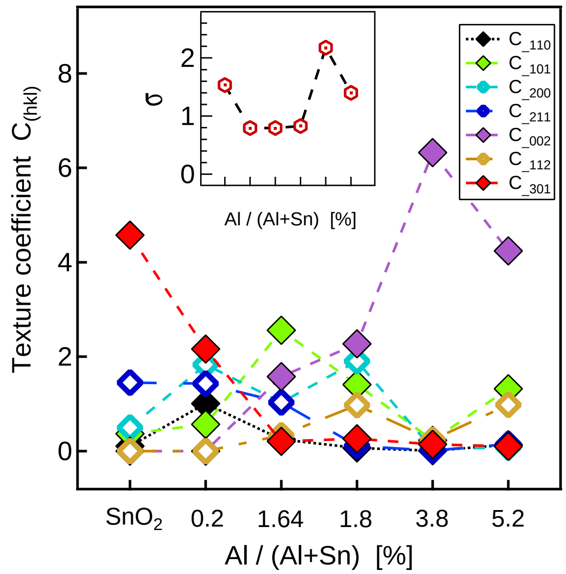

Figure 9.10: *The evolution of texture coefficients C_{hkl} calculated for tin oxide and different SnO_2:Al films plotted for SnO_2:Al different compositions. The color code of different crystallographic orientations (hkl), which are used to calculate C_{hkl} are represented in the legend. The plot for the degree of preferred orientation σ of the same films also shown in the insert. For better visual, the x-axis of the figures is not in a linear scale.*

(L_c) of studied films. The grain size was determined from the statistical analysis of the top view SEM images as discussed earlier in the beginning of this chapter. Meanwhile, crystallite size corresponds to the small coherent domains between two twin boundaries.

The crystal size is calculated using the Sherrer equation[296, 297] as shown in Eq. 9.4

$$L_c = \frac{K\lambda}{\beta cos(\theta)} \tag{9.4}$$

Where; L_c is the crystallite size, K is crystallite shape factor which has a typical value of about ≈ 0.9, λ is X-ray wavelength and is 1.5406 $\mathring{A}$, β is the full width at half maximum intensity of the peak in radian, and θ is the Bragg angle.

The crystallite size L_c calculated for tin oxide and different SnO_2:Al films is shown in the left figure of Fig. 9.11. For comparison, the film thicknesses extracted from the SEM cross-section of the probed samples is represented in the right image of the same figure. The average grain size shown in Fig. 9.3 is larger than that of L_c crystallites calculated by the Scherrer method, see Fig. 9.11. It should be noted that the average grain size is measured in the plane of the film at its surface, while the size of the crystallites is measured according to the depth of the film. This difference in size can be explained by the fact that the grains observed by SEM are composed of several crystallites. A crystallite is a domain in which crystallographic planes are coherent. Within the same grain, crystallites are separated by extensive defects, which have two dimensions, called twin boundaries. The grains, on the other hand, are separated by grain boundaries.

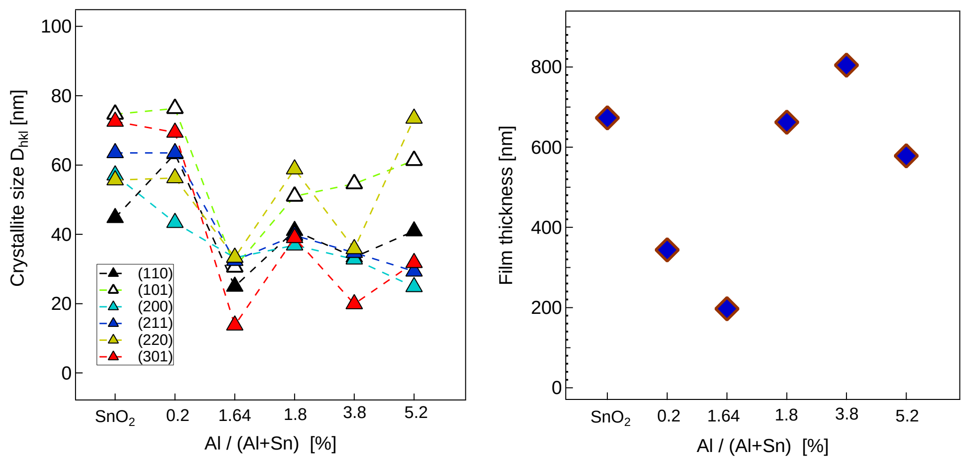

Figure 9.11: *(a), Evolution of crystallite size determined by Scherrer formula from XRD peak width as a function of* Al_2O_3 *-* SnO_2 *molar ratio (b), The film thickness of the same films extracted from the SEM crossection.*

Post Annealing Treatments

As it is revealed in the discussion above, the XRD patterns of as deposited films shown in Fig. 9.6 do not confirm the presence of crystalline Al_2O_3 phase, rather Al was effectively incorporated into SnO_2 lattice structure. Thus, further post annealing treatments are performed on the selected samples in order to see whether a crystalline alumina phase is measured after such treatments. For this purpose, undoped SnO_2, SnO_2:Al-0.15, -0.3, and -0.4 samples were chosen and post annealed at different temperature.

The post annealing treatments were performed at 900 and 1000 °C for 1 hour in atmospheric air. These temperatures were selected due to the fact that Al_2O_3 usually starts to crystallize at a temperature $\geq$ 600 °C and shows stable α- phase at a temperature only $\geq$ 1000 °C. Between these temperatures different metastable phases of Al_2O_3 could be observed [2]. The heat treated samples were then examined by different characterization techniques.

[2]more description about different polymorphs of Al_2O_3 can be found in subsection 3.3.1

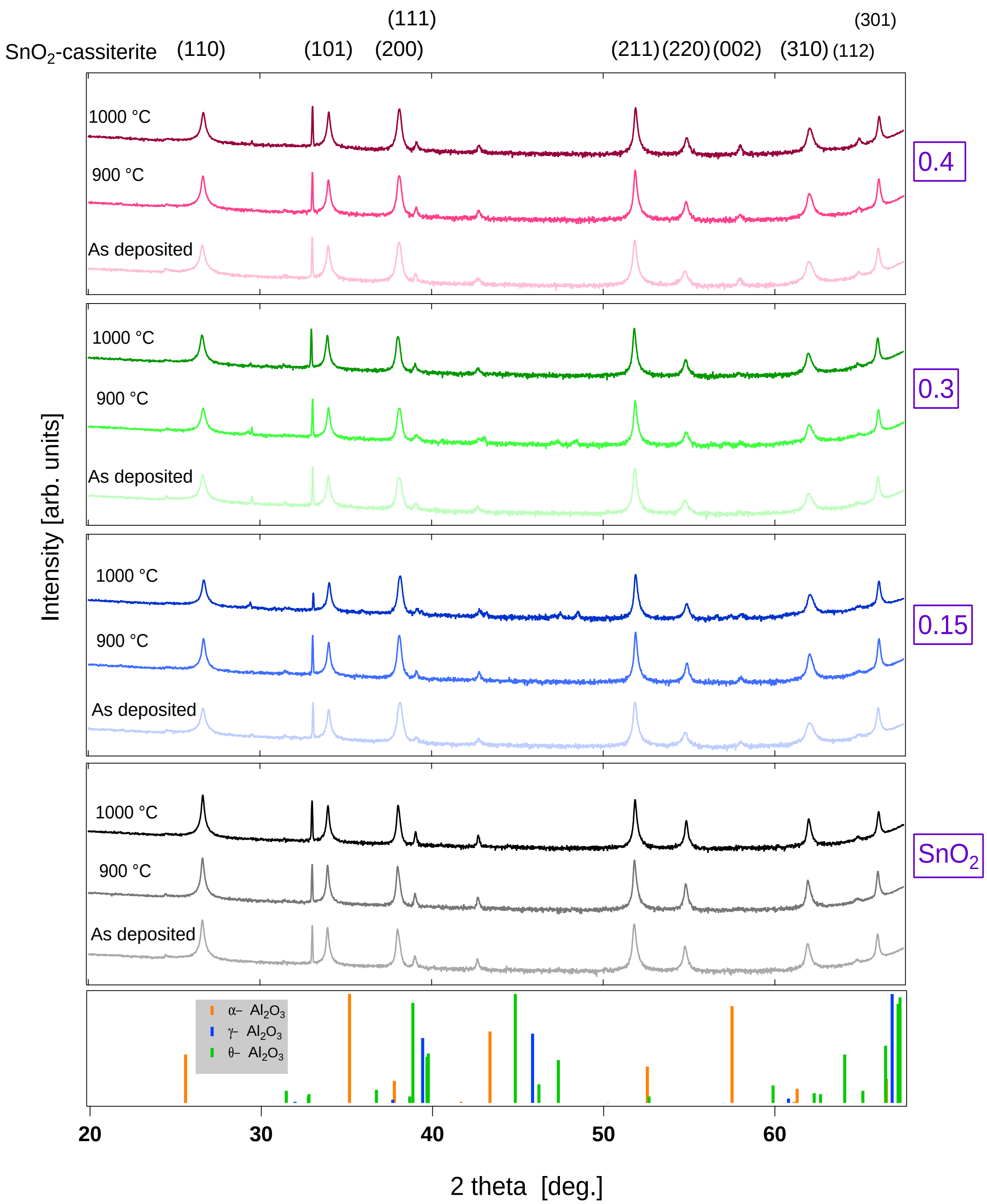

Figure 9.12: *θ - 2θ XRD patterns of as deposited films undoped SnO_2, SnO_2:Al-0.15, -0.3, and -0.4 together with the patterns of the same films after heat treatment at 900 and 1000 °C for 1 hour in air. The reference pdf cards of SnO_2 and different Al_2O_3 polymorphs are also represented.*

θ - 2θ XRD patterns of probed samples, which treated with different post annealing temperature are shown in Fig. 9.12. In addition, XRD patterns of as deposited films also represented for comparison. In the figure, the diffraction peak corresponding to SnO_2 are labeled in the top (PDF-00-041-1445), that of α- Al_2O_3 with orange line (PDF - 00-046-1212), θ - Al_2O_3 with green line (PDF - 00-056-0456), and γ - Al_2O_3 with blue line (PDF - 00-056-0457).

The heat treatment does not change the XRD patterns of nominally undoped SnO_2 sample, since there was no change in intensity or structural reordering upon heating. For SnO_2:Al-(0.15, 0.3, and 0.4) samples additional peak appeared at $\approx$57.89 ° in 2θ scale for both as deposited and post annealed samples. This reflection is more intense in 0.4 film. This peak could be attributed to (002) reflection of SnO_2 or (116) reflection of α-Al_2O_3. Since this reflection appears in both as deposited and heat treated samples, we can not assign the peak to (116) reflection of α- Al_2O_3 phase. Thereby, the XRD patterns of heat treated samples do not confirm the presence of crystalline Al_2O_3 phase in the probed samples.

Furthermore, SnO_2:Al-0.4 sample prepared on SiO_2/Si substrate and post annealed at 1000 °C (the highest Al content sample from the heat treated series) was examined by TEM electron diffraction and EDX experiments as shown in Fig. 9.13.

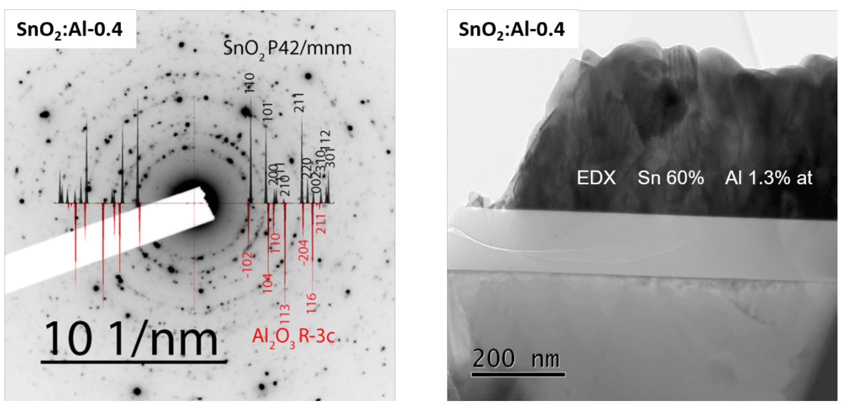

Figure 9.13: *(Left), TEM diffraction pattern of SnO_2:Al-0.4 sample prepared on SiO_2/Si substrate and post annealed at 1000 °C with indices of SnO_2 and α-Al_2O_3 (Right), EDX of the same sample which reveals the presence of Al 2.1% cataionic content.*

The diffraction rings of this film are in a good agreement with indices of SnO_2. In contrary, there was no diffraction ring matching the indices of α-Al_2O_3 or other alumina polymorphs. Thus, even though the sample was post annealed at 1000 °C, the TEM diffraction does not show a contribution associated to any polymorph of crystalline Al_2O_3. Actually at this annealing temperature, theta or alpha phases would be present [284, 298], which we do not see in our case. The possible reason for the observed absence of the diffraction rings of Al_2O_3 phases could be that the diffraction rings of SnO_2 and

Al_2O_3 are very close to each other. For example, the interreticular plane distance of SnO_2 (110) is 3.349 Å and that of Al_2O_3 (012) 3.48 Å; this is also true for other peaks. In addition, Al_2O_3 is in a very low quantity phase in the studied compositions. Hence, it is possible to have some spots of Al_2O_3 in the diffraction images but also it is difficult to identify them. The EDX analysis of the same sample revealed the presence of a 2.1% of Al as cationic content. Therefore it is reasonable to conclude that if not all, most of Al was incorporated into tin oxide lattice for the studied films.

FTIR

Films deposited on silicon wafer substrates were further examined by FTIR and the results are presented in Fig. 9.14. For better visual guidance all the spectra were

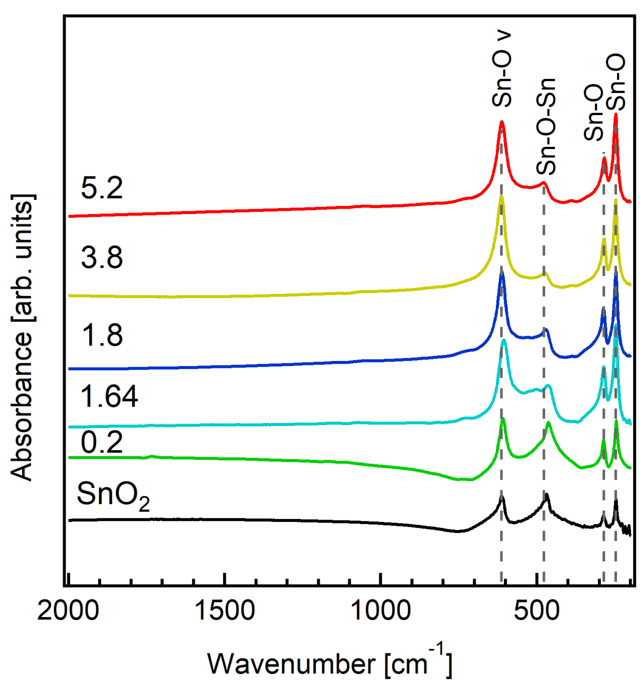

Figure 9.14: *Normalized FTIR spectra of nominally undoped and different Al-doped tin oxide thin films.*

normalized with the same intensity for the Si-O v band at 612.5 cm^{-1}. The spectra peaks present at 245, 282.5, and 612.5 cm^{-1} are assigned to the Sn-O vibration [279, 299], while a peak at 468.92 cm^{-1} is assigned to Sn-O-Sn stretching. Even though there was no independent peak observed which could be assigned to aluminum, Al incorporation has an influence on the broadening of Sn-O-Sn peaks and leads to a decrease of the relative intensity of the Sn-O-Sn stretching mode. This could be attributed to the formation of Sn-O-Al bonds. Actually Kumar and coworkers [300] reported similar broadening and attenuation of the Sn-O-Sn band as a function of increasing Al content in the SnO_2 thin films. Nevertheless, the exact position of Sn-O-Al band is not yet reported in literature nor on FTIR handbooks to the author knowledge.

9.3 Optical Study

Transmittance

The optical study of the probed samples was performed by measuring the total transmittance (T_{tot}) of SnO_2 and different SnO_2:Al films using perkin Elmer Lambda 950 spectrophotometer [3]. The total transmittance was measured between 250 - 2500 nm range as shown in the left image of Fig. 9.15. The total transmittance of bare glass substrate is also included for comparison. Virtually no shifting of the leading edge at short wavelengths, representing the onset of the leading optical band-to-band absorption (absorption edge), is observed upon Al doping. Thus, there was no blue-shift of the absorption edge.

The average total transmission of the probed samples in the visible (VIS) regime of 400-800 nm is plotted as shown in the right image of Fig. 9.15. In VIS regime the transmittance are in general high and are in the range of 72% - 81 %, which is important for TCO applications. In addition, in this regime there was not big difference in transmittance values. Meanwhile, in the near infrared (NIR) region above 1200 nm, a difference in plasma absorption between the samples is observed. Since aluminum is acting as an acceptor doping in SnO_2, a plasmon frequency shift towards the IR region is observed with increasing Al doping into the tin oxide films.

In the spectral range of relevant electromagnetic wavelengths for the applications in which TCOs are used (i.e flat screens, solar cells, etc.), free electrons dominate the electrical and optical properties. These properties can be described in a first approximation by the Drude free electron theory[301]. This theory often accounts for the measurable properties of TCOs, such as transmittance and reflectance, and their relationship to extrinsically controllable parameters (such as carrier concentration) and intrinsically uncontrollable

[3]The working principle of the spectrometer is discussed in subsubsection 4.2.1.5

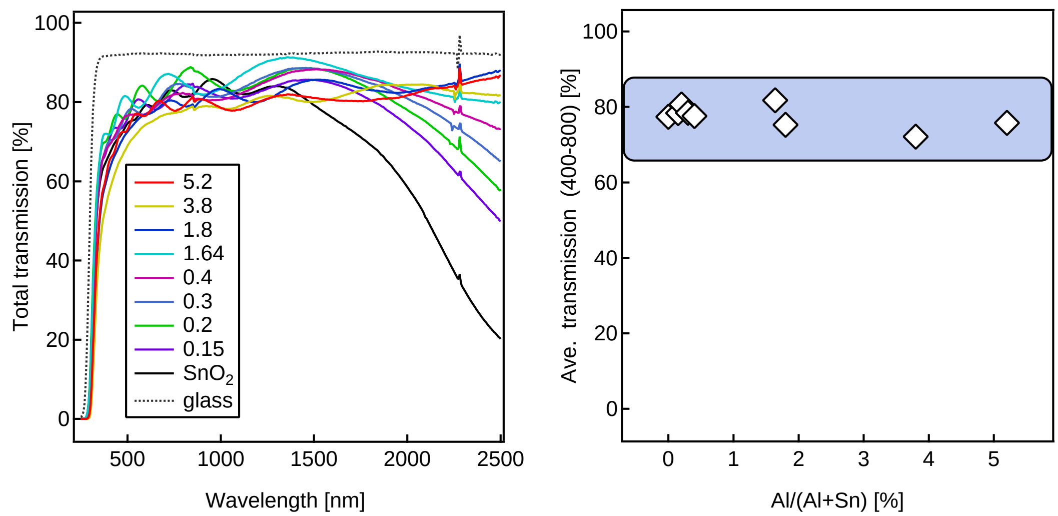

Figure 9.15: *(Left) Optical transmittance (T_{tot}) of nominally undoped SnO_2 and different SnO_2:Al thin films as a function of wavelength. The transmittance of bare glass is included for comparison,(right) Average total transmission of the same films in VIS regime of 400 - 800 nm.*

properties (such as crystal lattice and effective mass). The plasmon frequency shift towards higher wavelength observed upon Al doping is in a good agreement with the determined free carrier concentrations, see Fig. 9.18(c). Due to the fact that SnO_2 is naturally n-type TCO, the transmittance drop in NIR region is ascribed to plasmonic absorption. Doping with aluminum favors the creation of holes as low valence Al^{3+} cations substitute Sn^{4+} ones. For this reason Al^{3+} cations play the role of charge compensators and the transmittance in the INR region increases consequently, as shown by Fig. 9.15(a). The free carrier concentrations influence the resonant frequency of the plasma absorption according to the following relation within the framework of Drude theory[301]:

$$\omega_p = \sqrt{\frac{ne^2}{m^* \varepsilon_0 \varepsilon_\infty}} \tag{9.5}$$

where ω_p is plasma frequency, n is charge carrier density, e is elementary charge, m^* is carrier effective mass, ε_0 is vacuum permittivity, and ε_∞ is the value for the film dielectric constant at high frequencies.

For highly doped TCOs the plasmon energies are up to 1 eV, which is in the near infrared region of the electromagnetic spectrum. Due to the high number of free electrons, the incident infrared radiation is not transmitted but is rather reflected; this is a key feature for application of differently doped tin oxide thin films as low-emissivity window coatings.

Tauc plot and optical band gap

The widely accepted fundamental band gap of tin oxide is ≈ 3.6 eV [132, 133, 134]. The optical band gap of the probed samples were determined from the Tauc plot, which is the common way of determining the optical band gap of semiconductors. In this procedure, the absorption coefficient α_{opt} is calculated from the transmittance data. The Tauc plot $(\alpha_{opt}.E)^{1/r}$ is then plotted as a function of E, incident photon energy [302]. The exponent r depends on the type of fundamental optical transition across the band gap and it takes the value of 1/2 for direct allowed transition; which is the case for tin oxide. Extrapolating the linear onset of this plot into the base line gives the estimate optical band gap. In order to calculate the absorption coefficient α_{opt} the samples thicknesses were determined from the SEM crossection measurements.

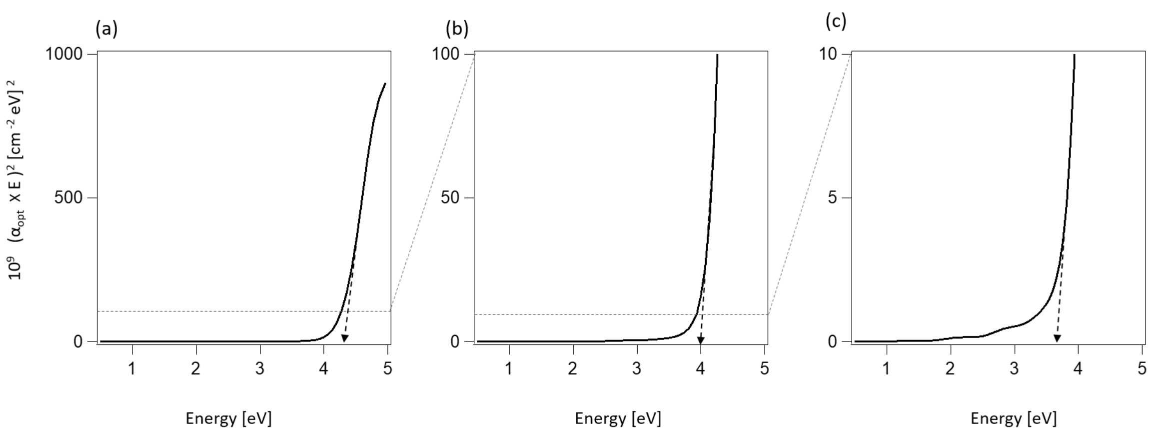

Figure 9.16: *The ambiguity of a Tauc plot is shown by plotting the same data of SnO_2:Al-0.3 film, but choosing different ordinate cutoff values in each representation. The cutoff value decreases from (a) to (c), effectively magnifying the data with each step. The horizontal dashed line indicates the data range included in the next magnification. An arrow pointing at the X-axis indicates the Tauc gap determined by extrapolating the respective linear region. Based on the the chosen ordinate cutoff values, Tauc gaps of 4.3 eV (a), 4 eV (b), and 3.67 eV (c) can be derived by this method.*

For undoped SnO_2 the optical band gap determined from the Tauc plot varies from 3.6 eV to 4.1 eV, with most of reporting values ≈4 eV [303, 304]. While, for antimony - doped tin oxide (ATO) films the band gaps are often increased, which is attributed to a Burstein -Moss shift. For highly doped samples, the band gaps upto 4.4 eV [305] have been reported. However, the absolute values are in conflict.

This difference in band gaps between studies is mostly caused by the lack of reference point; particularity it is not well defined where to extrapolate data linearly. This problem is visualized in Fig. 9.16. Here, absorption coefficients directly calculated from the transmittance spectrum of SnO_2:Al-0.3 film are plotted to determine the direct band gap. The full plot is shown in (a), the data in ordinate cut off at 10^{11} $(eV/cm)^2$ shown in (b), and that of cut off at 10^{10} $(eV/cm)^2$ (c). (b) and (c) are essentially increasing magnifications of (a). The resulting optical band gap are 4.3 eV in case (a), 4.0 eV in case (b), 3.67 eV in (c). Considering the overall shape of the data, extrapolation of linear region clearly must depend on which part of the curve is considered. Similar observation has been reported by Weidner [9] on nominally undoped tin oxide thin films, in which the optical band gap changes from 5.3 eV to 3.8 eV upon change ordinate cut off from 10^{12} $(eV/cm)^2$ and 10^{10} $(eV/cm)^2$. This variation indicates the lack of a reference point for this optical characterization method.

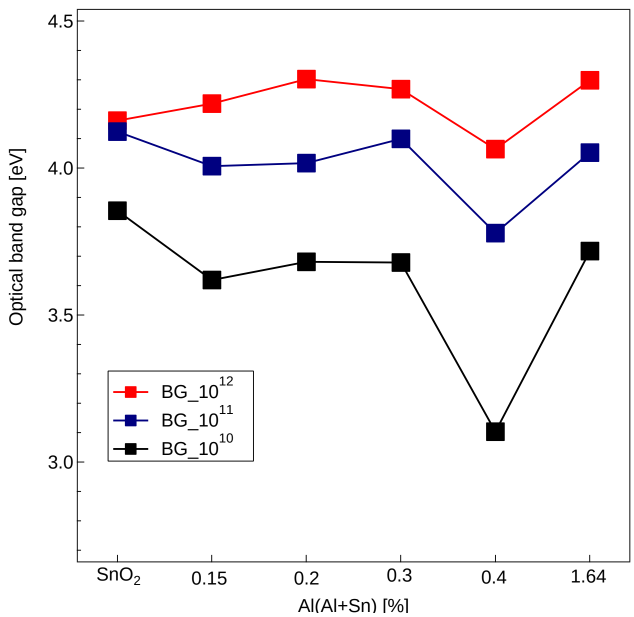

Figure 9.17: *The optical band gap extracted from Tauc plot of Al_2O_3 - SnO_2 systems with different Al_2O_3 to SnO_2 molar ratio. Each sample have three different band gaps by choosing ordinate cutoff values from 10^{10} to 10^{12}. For better visual, the x-axis of this figure is not in a linear scale.*

The optical band gap of probed samples determined from Tauc plots with the data in ordinate cut off at 10^{12} , 10^{11}, and 10^{10} $(eV/cm)^2$ are plotted as function of increasing aluminum content in the precursor solution, see Fig. 9.17. In general the band gaps decreased in all cases with lowering the ordinate cut off values. In addition, the band gaps slightly decreased by increasing alumina concentration and SnO_2:Al-0.4 sample exhibit the lowest band of all the series. The band gaps of SnO_2:Al-1.8, -3.8, and -5.2 films was not calculated due to the films were too insulating and it was not possible to get their thicknesses in a SEM crossection.

9.4 Electrical Study

Conductivity of nominally undoped and the different Al-doped SnO_2 thin films is provided in Fig. 9.18(a). Hall effect results of the same films are also displayed in Fig. 9.18(b) for the carrier mobility and (c) for the carrier concentration. Due to the experimental limitations of the Hall effect setup used, no Hall effect could be measured for the doped films above SnO_2:Al -1.64.

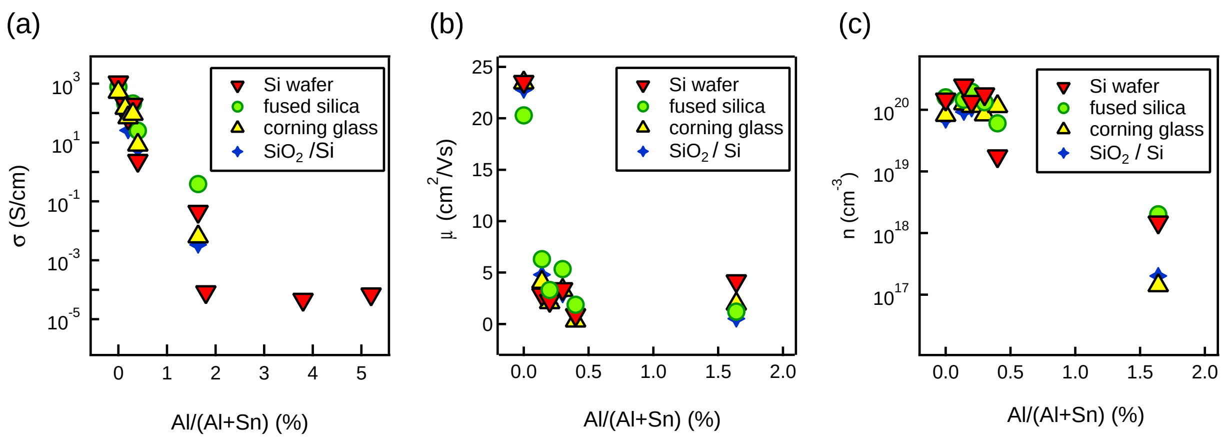

Figure 9.18: *(a),Conductivity ; (b) Hall mobility and; (c) Hall concentration of nominally undoped SnO_2 and SnO_2:Al thin films with different compositions prepared on different substrates of Si wafer, fused silica, corning glass, and SiO_2/Si. Hall measurements were possible only for samples with composition up to SnO_2:Al-1.64.*

The nominally undoped tin oxide films prepared on different substrates have a conductivity of $\approx 1.1 \times 10^3$ S/cm. Surprisingly, this value is at least two orders of magnitude higher than the conductivity of undoped SnO_2 films reported in literature. For magnetron sputtered films, the reported conductivity varies from 10^{-5} to 10^0 S/cm depending on the different deposition conditions[8, 306]. Similarly, SnO_2 films prepared by PLD have conductivity values of $\leq 4.5 \times 10^1$ S/cm [307], and that of sol-gel exhibit values $\leq 10^0$ S/cm [308]. The higher conductivity obtained for the thin films studied here (deposited by spray pyrolysis) is probably related to the tin precursor used namely, $SnCl_4.5(H_2O)$. Since chlorine has one less 2p orbital to fill than oxygen, substitution of O^{2-} ions by

Cl^- ions leads to an increase of free electrons per SnO_2 unit formula. For every chlorine substitution a tin atom retains an extra 5s electron which enters the conduction band of the lattice [276, 309]. In addition, oxygen vacancies are deep donors in SnO_2[122, 310], which can not be easily ionized and contribute to the electrical conduction. Eventually, we were not able to detect chlorine on our samples using different physicochemical analysis techniques.

In order to address the actual role of the incorporated chlorine atoms with respect to the electrical properties, Messad et al. [276] performed Rutherford back scattering (RBS) analyses on spray deposited SnO_2 films from $SnCl_4$ precursor to determine the bulk chloride concentration (n_{Cl^-}) and compared it with the Hall carrier concentration (n) of the same films. Their results showed that for unintentionally doped SnO_2 films deposited with precursor concentration of 0.1 M and substrate temperature between 400 and 550 °C, the chlorine ion concentration (n_{Cl^-}) and Hall concentration (n) have the same values. Thus, they concluded that with these experimental conditions the carrier density can be even identified with chlorine content. Meanwhile, at a deposition temperature higher than 550 °C, the n_{Cl^-} decreased with increasing substrate temperature. This is due to the breakage of Sn-Cl bonds with increasing temperature, as it was evident with Auger electron spectroscopy (AES) [311] and Secondary ion mass spectroscopy (SIMS) [312] observations. Eventhough they [276] successfully demonstrated the incorporation of chlorine ions, under the same deposition conditions, they measured a conductivity of 6×10^1 S/cm. This is in fact 2 orders of magnitude lower that the conductivity reported in the present work for nominally undoped films.

As it is discussed in the previous section of this chapter, several characterizations of the probed samples confirmed that Al is incorporated into tin oxide films rather than making different Al_2O_3 phase and forming demixed composite structure. Thereby, for Al doped films the scenario is different. Since Al^{3+} ions substitute Sn^{4+}, a hole is generated per SnO_2 molecule and compensates an existing carrier electron. Thus, the conductivity of tin oxide films does not improve upon Al incorporation. The conductivity of SnO_2:Al decreases consistently with increasing Al content due to the presence of compensating holes and for the highest Al content (1.8, 3.8, and 5.2) films the conductivity drops to $\sim 10^{-4}$ S/cm.

Hall effect measurements were possible only for the films with composition upto SnO_2:Al -1.64, the last three films in the series being too resistive and thus impossible to be measured with our system. Hall mobility exhibits a pronounced reduction with small Al incorporation. It decreased from ≈23 cm^2/Vs for undoped films to ≈5 cm^2/Vs for SnO_2:Al - 0.15 samples. With further increasing Al concentration up to SnO_2:Al -1.64, the mobility stayed in the following range: 1- 5 cm^2/Vs. This reduction in mobility could be attributed to the change in micro-structure of the films upon Al incorporation due to the grain size reduction for instance. Conversely, the carrier concentration was not affected in low Al content films with value of $\approx 1 \times 10^{20}$ cm^{-3}, being obtained for doping values up to 0.3. Then it decreased for the SnO_2:Al -0.4 film and finally dropped by 3 orders of magnitude $\approx 1 \times 10^{17}$ cm^{-3} for SnO_2:Al-1.64 samples.

As we have seen in the morphological study, aluminum incorporation resulted in a heterogeneous nucleation of smaller grains which leads to the formation of more grain boundaries, which act as a potential barrier and reduce carrier mobility. Therefore, the observed reduction in mobility is reasonable. At the same time Al doping favors the creation of holes as low valence Al^{3+} cations substitute Sn^{4+} ones. The created holes then compensate the existing carrier electrons and charge carrier density decreases. This is supported by the results of Hall effect measurements as carrier concentration decreased by up to 3 orders of magnitude only by incorporation of 1.64 % of Al.

Some reports claim [279, 286] that for a high enough Al doping of tin oxide, the type inversion of conductivity could have been observed. This would mean, having a tin oxide thin film with p-type conductivity. Mohagheghi et al. reported this transition can take place close to 8 % of Al incorporated into their films [313]. Meanwhile, in our Hall effect results we did not see such a type inversion behavior, probably because our SnO_2:Al thin films did not have high enough Al content.

9.5 Summary, Conclusion and Outlook

In this chapter, the chemical approach of defect modulation doping was tested. The aim of this work was to produce demixed crystalline Al_2O_3-SnO_2 composite films and examine the modulation effect of the system. For this purpose, different films were synthesized from $SnCl_4.5(H_2O)$ and $Al(acac)_3$ precursors by using ultrasonic spray pyrolysis setup. Results obtained from different characterizations of studied films are summarized here:

- The first important thing to confirm for the synthesized films were the formation of demixed crystalline phases of Al_2O_3 and SnO_2 in the composite structure. Different characterizations were performed to confirm the presence of crystalline Al_2O_3 in tin oxide matrix. XRD, TEM-EXD and XPS measurements of as deposited and post annealed films do not confirm the presence of crystalline alumina phase in the binary system.

- In the other hand EDS, EPMA, and TEM results confirmed the presence on Al into the synthesized films. Thus, Al^{3+} was incorporated into tin oxide lattice by substituting Sn^{4+} rather than formation of crystalline alumina. Incorporation of Al tuned the properties of probed SnO_2 thin films.

  - Al incorporation changes the morphology of tin oxide films and the grain size reduced consistently with increasing Al concentration.

  - Al incorporation leads texturing of tin oxide films and shifted the XRD reflections. The shifting and broadening of the reflections increases with increasing Al concentration.

  - Generally, Al incorporation does not change the optical transmittance of studied samples in the visible regime, which have a values in range of ≈ 72 - 81 %. While, in near infrared (NIR) regime the transmittance increases with increasing Al content by shifting the plasmon frequency towards NIR region. This is due to the fact that Al act as an acceptor doing in tin oxide films and reduced the carriers concentration.

  - The incorporation of Al into SnO_2 lattice structure does not improve the conductivity of tin oxide films. This occurs when Al^{3+} substitute Sn^{4+}, then holes are generated and Al acts as an acceptor doping. For high concentration of Al in the produced films, the conductivity of tin oxide film decreased up to 8 orders of magnitude compared to nominally undoped tin oxide samples.

In conclusion, the expected demixed binary composite system was not realized. Thereby, it was not possible to test defet modulation doping. Increasing the alumina content in the precursor solution could be one way to obtained the desired demixed composite system. Moharrami et al. [280] reported the formation of binary system for Al doping levels $\geq$ 40 at %

In this work it is clearly demonstrated the incorporation of Al into tin oxide films tuned the properties of tin oxide films. Similarly, it is possible to tune the properties of fluorine doped tin oxide (FTO) thin films by incorporation of Al.

Chapter 10

Al_2O_3 NPs-SnO_2 Nanocomposite Thin Films

This chapter is focused on incorporation of nanoparticles into tin oxide films to produce nanocomposite thin films with the purpose of testing defect modulation doping. Al_2O_3 nanoparticles (NPs) were chosen as dopant phase and incorporated into tin oxide matrix. Schematic illustration of a model for synthesized nanocomposite films is shown in Fig. 7.11 (a). The chapter is divided in the following sections.

Section 10.1 describes the characterization of different commercial Al_2O_3 nanoparticles (water dispersed, isopropanol dispersed and powder forms), to identify the phase of Al_2O_3 NPs and determine the size of the particles. The experimental conditions followed during deposition of nanocomposite thin films will be shortly described in section 10.2. In section 10.3, results of different structural characterizations of the probed samples are presented. The main goal of the section is to confirm the incorporation of Al_2O_3 NPs into the grown film. The morphological, composition, and XRD studies of nominally undoped tin oxide and different Al_2O_3 NPs-SnO_2 nanocomposite films will be discussed. In 10.4, the optical study of different nanocomposite thin films will be presented. Section 10.5, will focus on electrical studies of the studied samples. Finally, the chapter will be summarized in section 10.6 with remarks and outlook.

10.1 Al_2O_3 nanoparticles

Different commercial alumina nanoparticles (Al_2O_3 NPs) were used in this work as dopant material for the preparation of tin oxide based nanocomposite thin films. The received nanoparticles were in water dispersion, isopropanol dispersion, and powder forms. The detail description for each form of alumina nanoparticles is given in Tab. 10.1.

Table 10.1: Gamma(γ)-Al_2O_3 nanoparticles in different forms

Material	Gamma(γ)-Al_2O_3	Gamma(γ)-Al_2O_3	Gamma(γ)-Al_2O_3
Form	aqueous dispersion	aqueous dispersion	powder
Dispersion	water	isopropanol	-
Particle size (nm)	10	15	40-50
Particle wt %	20	10	-
Supplier	US Res. Nanomat. Inc.	US Res. Nanomat. Inc.	Alfa Aesar

In order to confirm the presence of nanoparticles and identify the particle size, both as received water and isopropanol dispersed Al_2O_3 NPs were examined by TEM, see Fig. 10.1. In both cases, the TEM analyses confirmed the presence of alumina nanoparticles. For water dispersion, well defined rod like crystalline particles were observed as can be seen in Fig. 10.1 (a). The particle size was much larger than what was written in the label of the received bottle with particle size up to $\geq$50 nm was observed. Meanwhile, for isopropanol dispersion semi-crystalline round shape particles were observed, see Fig. 10.1 (b). These particles are not completely crystalline as some amorphous regions are observed.

All forms of commercial Al_2O_3 nanoparticles used in this work were labeled as gamma phase, to confirm the presence of this phase, the subjected nanoparticles were examined in XRD. For XRD analyses, the samples were prepared from both water and isopropanol dispersion's of Al_2O_3 NPs by droplet casting technique [1]. The XRD patterns of these layers confirmed the presence of gamma(γ)-Al_2O_3 NPs in the dispersed solution as the XRD reflections match well with reference γ-alumina PDF card (00-056-0457), as revealed by Fig. 10.2.

[1]schematic illustration and description of this technique can be found section 8.1

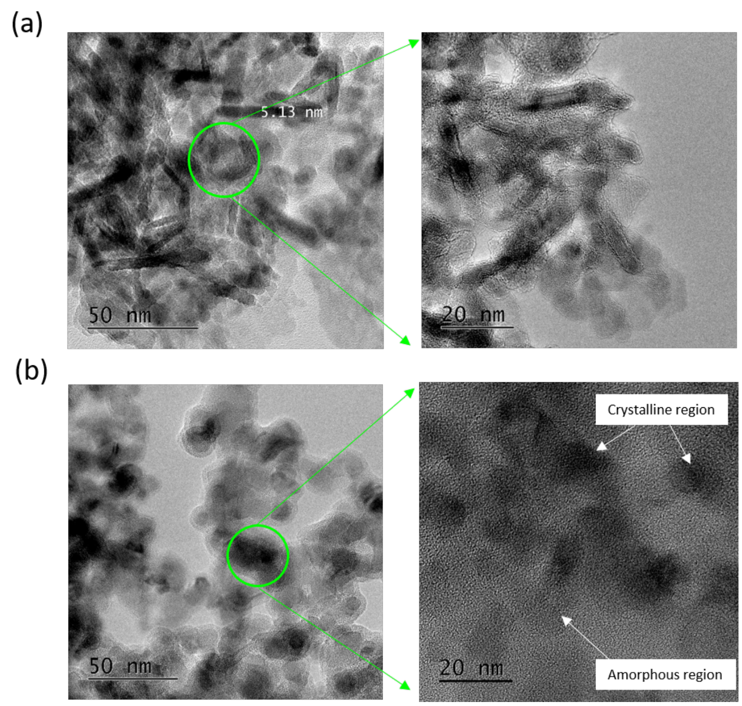

Figure 10.1: *TEM images of as received Al_2O_3 NPs (a), Al_2O_3 NPs in water dispersion and (b), Al_2O_3 NPs in isopropanol dispersion. White arrows are indicating either amorphous or crystalline regions of isopropanol dispersed NPs.*

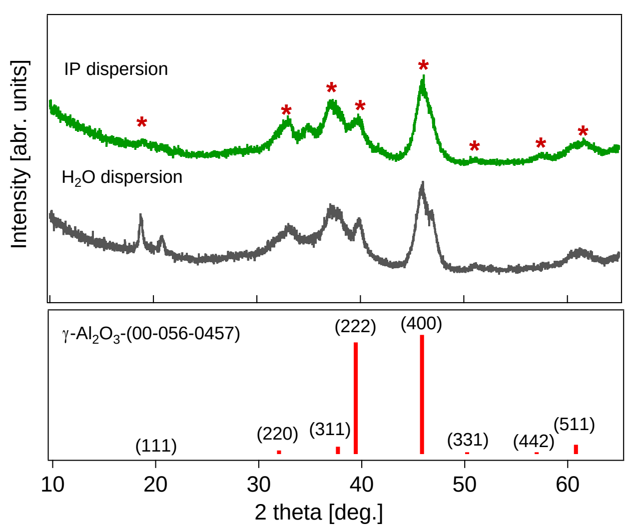

Figure 10.2: *XRD diffractograms for water and isopropanol dispersed gamma Al_2O_3 NPs-gels prepared by droplet casting of the NPs. The ICDD database pattern for gamma-alumina with reference no. 00-056-0457 is also represented.*

Therefore, TEM and XRD experiments confirmed the presence of γ-Al_2O_3 NPs both in water and isopropanol dispersion. Similar confirmations have been reported for powder nanoparticles during the PhD work of Zhang [314].

10.2 Sample Preparation

Different tin oxide based nanocomposite thin films were prepared by using homemade ultrasonic spray pyrolysis deposition method on different substrates, namely Si wafer, Corning C1737 borosilicate glass, fused silica glasses, and SiO_2/ Si wafer. These different substrates were chosen for flexibility of performing different characterizations. The working principle of the setup is explained in subsection 4.1.3. The tin precursor was $SnCl_4.5(H_2O)$ dissolved in methanolic solution with a fixed concentration of 0.1 M. Al_2O_3 NPs were used as a potential dopant material. Different forms of Al_2O_3 NPs were used (isopropanol dispersion, water dispersion, and powder form) and were added into the tin precursor solution in different $\left(\frac{Al_2O_3}{SnO_2}\right)$ molar ratio: 0.25, 0.5, and 1. During deposition of the samples, the growth temperature was set at 500 °C, which resulted in a substrate surface temperature of 420 °C. This temperature setting was kept constant for all depositions. The deposition time was kept 60 minutes for most of prepared samples. In order to distinguish the effect of nanoparticles and their parent dispersant, additional sample was prepared using the same volume of dopant (for water dispersed Al_2O_3 NPs) but without inclusion of NPs, that is using the same volume of deionized water.

The deposition parameters followed during the preparation of different Al_2O_3 NPs-SnO_2 nanocomposite thin films are summarized in Tab. 10.2. In the table, additional information about the deposition rate and the film thicknesses are presented. The film thicknesses are extracted from the SEM cross-section of the films grown on Si wafer substrate. The deposition rates are calculated using these thickness values.

For the sake of simplicity for presenting the results and for further discussion, sample identification is given here. Undoped tin oxide will be named as nominally undoped SnO_2. Different nanocomposite thin films are distinguished by the form of NPs (water dispersed-H_2O, isopropanol dispersed-IP, and powder) used and the $\left(\frac{Al_2O_3}{SnO_2}\right)$ molar ratio added into tin oxide precursor solution: SnO_2, IP-0.25, IP-0.5, H_2O-0.25, H_2O-0.5, H_2O-1, and powder-1.

Table 10.2: Deposition parameters of Al_2O_3 NPs embedded in SnO_2 nanocomposite thin films.

Al_2O_3 NPs embedded in SnO_2 (ASO) nanocomposite thin films									
Sample	SnO_2		Al_2O_3 NPs		Solvent	Spray deposition			
	Precursor	Conc. (m/l)	Precursor	(Al_2O_3/SnO_2) molar ratio		Temp. °C	Time (min.)	Rate (nm/min)	Thickness (nm)
SnO_2	$SnCl_4.5(H_2O)$	0.1	-	-	methanol	420	60	20.5	1230
gray SnO_2-H_2O	$SnCl_4.5(H_2O)$	0.1	H_2O	10ml	methanol	420	60	11	660
ASO-IP → 0.25	$SnCl_4.5(H_2O)$	0.1	IP disp.	0.25	methanol	420	60	11.3	676
ASO-IP → 0.5	$SnCl_4.5(H_2O)$	0.1	IP disp.	0.5	methanol	490	60	11.23	674
ASO-H_2O → 0.25	$SnCl_4.5(H_2O)$	0.1	H_2O disp.	0.25	methanol	420	60	13	775
ASO-H_2O → 1	$SnCl_4.5(H_2O)$	0.1	H_2O disp.	1	methanol	420	120	2.2	548
ASO-H_2O → 1	$SnCl_4.5(H_2O)$	0.1	H_2O disp.	1	methanol	420	120	2.2	260
ASO-H_2O → 1	$SnCl_4.5(H_2O)$	0.1	H_2O disp.	1	methanol	492	165	3.83	633
ASO → 1	$SnCl_4.5(H_2O)$	0.1	powder	1	methanol	492	60	8.8	524

10.3 Structural Study

The top view SEM images of nominally undoped SnO_2 and different Al_2O_3 NPs-SnO_2 nanocomposite thin films prepared using Al_2O_3 NPs precursors as dopant phase in different forms and different Al_2O_3 to SnO_2 molar ratio are presented in Fig. 10.3. In addition, SEM image of SnO_2 film produced by addition of 10 ml of deionized water in the precursor solution (this is the same volume as that of the dopant used for production of H_2O-0.5 sample, but without NPs inclusion).

In general with the visual assessment of the probed samples, there is very slight difference in the morphology between undoped tin oxide and different Al_2O_3 NPs incorporated thin films. The difference might be due to difference in deposition rate and film thickness of the probed samples, see Tab. 10.2. The extended planar twin defects are observed in all the studied samples. The same defects have been observed on the films prepared using $Al(acac)_3$ as dopant phase, see section 9.2.

Due to the presence of these twin boundaries in the probed samples it is important to distinguish between the grain size (L_g) and crystal size (L_c) of the films.

The grain size was determined following the same procedure described in section 9.2. The average and the biggest grain size of these films are plotted as a function of the nanocomposite films produced from different forms of Al_2O_3 NPs and having different (Al_2O_3/SnO_2) molar ratio, Fig. 10.4. Nominally undoped SnO_2 and SnO_2-H_2O samples shows very comparable morphology and have similar average and biggest grain size. The isopropanol dispersed IP-0.25 and -0.5 samples show similar average and biggest grain sizes. For water dispersion nanocomposite films, both the visual observation of the SEM images (see, Fig. 10.3) and the average grain size shown in Fig. 10.4 indicates grain sizes decrease with increasing NPs concentration in the precursor solution. For H_2O-1 sample (image (g)), more smaller grains are seen in visual observation and the average grain size is the lowest from water dispersion series. This sample also has a film thickness of only 260 nm, which is roughly half of the thickness of other studied samples. Additional thicker (633 nm thick) sample with the same concentration of H_2O-1 was also prepared, in which the bigger grains dominated the microstructure and show similar microstructure as undoped tin oxide films, see image (g) of Fig. 10.3. The sample prepared from the powder NPs shows comparable morphology and grain size when compared to the other films.

Nominally undoped tin oxide films have an average grain size of 264 $\pm$ 45 nm with the biggest grain of the same sample exhibit a size of 710 nm, which indicate there is up to 3.5 times size difference in the grains of the same film, see Fig. 10.4 (b). Similarly,

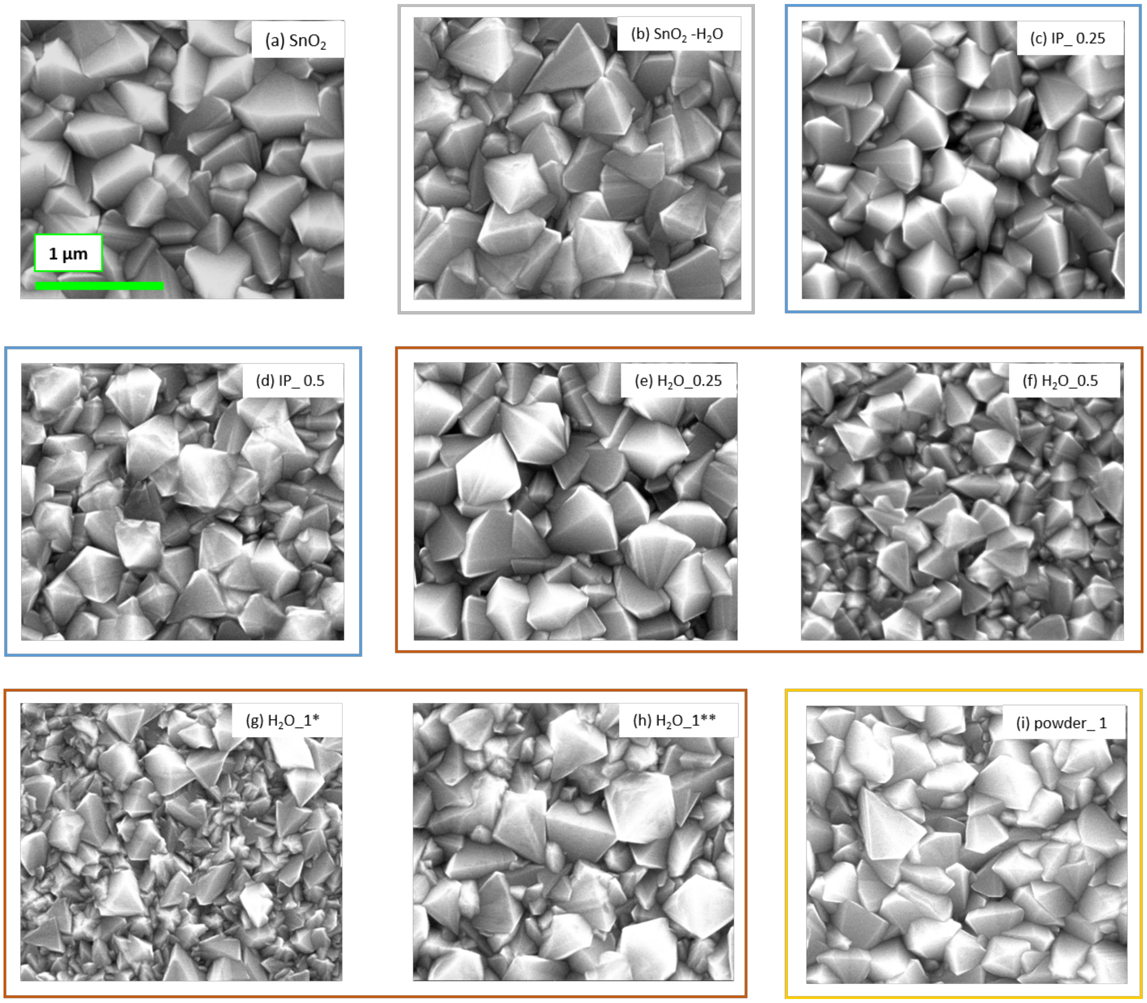

Figure 10.3: *Top view SEM image of nominally undoped SnO_2 and different Al_2O_3NPs-SnO_2 nanocomposite thin films prepared using Al_2O_3 NPs dopants in different forms and different (Al_2O_3 to SnO_2) molar ratio: (a), nominally undoped SnO_2 (b), SnO_2-H_2O (the same volume as the dopant of H_2O-0.5 sample but using dionized water only without NPs inclusion) (c), Isopropanol dispersion-0.25 (d),Isopropanol dispersion-0.5 (e), H_2O dispersion-0.25 (f), H_2O dispersion-0.5 (g), H_2O dispersion-1 *, longer deposition time of 2 hrs (h), H_2O dispersion-1 ** longer deposition time of 2.45 hrs, and (i), Al_2O_3 NPs in powder form-1. All images have the same scale of 1 μ and the green scale bar presented in image (a) can be used for all samples.*

SnO_2-H_2O films show comparable average and biggest grain size to that of undoped tin oxide. From this we can say that the addition of deionized water in the precursor solution does not affect the morphology and grain size of tin oxide films. The isopropanol dispersed IP-0.25 and -0.5 samples exhibit the same average grain size of 180$\pm$13 nm and biggest grain of $\approx$550 nm. Thus, addition of different concentration NPs does not change the morphology and grain size. In contrast, the concentration of NPs in the precursor solution shows an effect on the morphology and grain size of water dispersed films. The average grain size decreases from 190 ± 40 nm to 100 ± 10 nm for the films H_2O-0.25 and H_2O-1, respectively. When considering the largest grain, these films exhibit a size dispersion of up to ≈4 times within the same sample. Powder dispersed sample also exhibit similar trend of size dispersion as the other studied samples, see Fig. 10.3 and Fig. 10.4 for comparison.

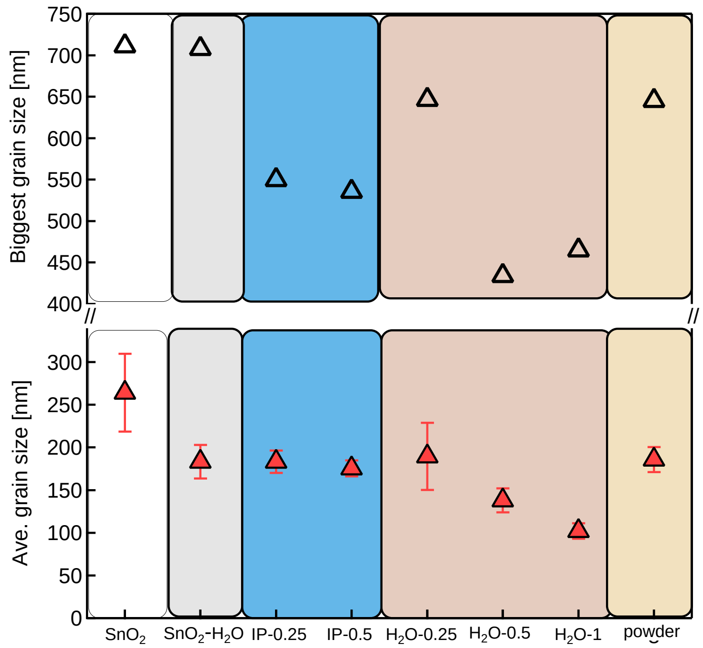

Figure 10.4: *The average grain size (bottom) of undoped SnO_2 and different Al_2O_3 NPs-SnO_2 nanocomposite systems produced using different forms and concentration of gamma-Al_2O_3 NPs as dopant phase. The error bar indicates the standard deviation of the grain size distribution. The size of the biggest grain (top) of the same films are also represented. Different forms of Al_2O_3 NPs are colored differently for better visual.*

In order to confirm the incorporation of dopant, Al_2O_3 NPs into the grown tin oxide thin films, the probed samples were examined in energy dispersive X-ray spectroscopy (EDS). The EDS spectra of nominally undoped SnO_2 and different Al_2O_3 NPs-SnO_2 nanocomposite thin films deposited on Si wafer substrate are shown in Fig. 10.5. In addition, the spectra measured at the conductive carbon tape, which used to attach the sample to the sample holders is included for comparison. The measurements were performed in two different acceleration voltages of 6 and 15 keV.

At an acceleration voltage of 6 keV, Al peak was not seen in any of Al_2O_3 NPs-SnO_2 systems, see Fig. 10.5 (b). While, at 15 keV small shoulders of Al peaks have been seen for all Al_2O_3-SnO_2 thin films, see Fig. 10.5 (c). However, the same shoulder appears for the spectra of carbon tape with the same energy and the same intensity. Therefore,

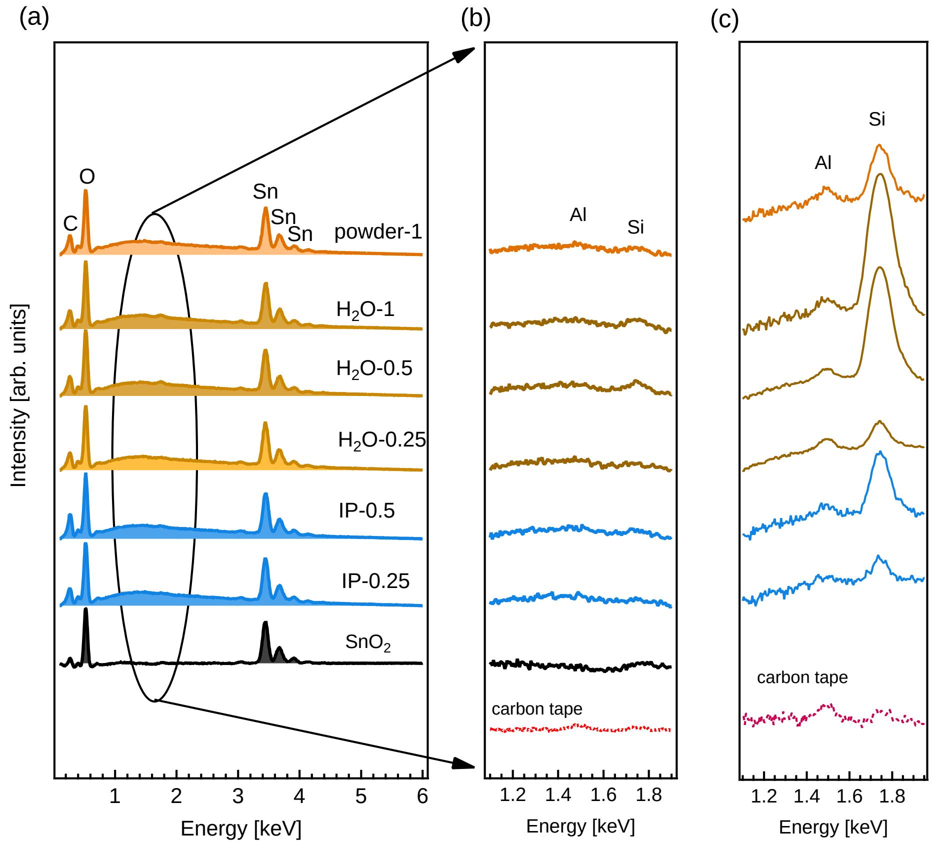

Figure 10.5: *(a), Energy dispersive X-ray spectroscopy spectra of undoped SnO_2 and different Al_2O_3 NPs-SnO_2 thin films prepared using Al_2O_3 NPs as a dopant phase in different forms and different (Al_2O_3 to SnO_2) molar ratio when probed at an acceleration voltage of 6 keV; (b), magnified spectra of the same films around 1.5 keV region; and (c), the magnified view of the same region probed at higher acceleration voltage of 15 keV. The spectrum measured on the conductive carbon tape contact is included for comparison. Different forms of Al_2O_3 NPs are colored differently for better visual.*

Al peaks observed when the voltage of 15 keV is used can not be attributed to Al_2O_3 NPs, which could be embedded into the grown tin oxide tin films, rather it is originated from the sample holder of the instrument. Thus, the EDS analyses do not confirm the presence of alumina nanoparticles into the studied films.

In order to confirm the incorporation of Al_2O_3 NPs, the studied samples were examined in XRD. The θ-2θ XRD diffraction patterns of nominally undoped SnO_2 and different Al_2O_3 NPs-SnO_2 nanocomposite thin films collected between 20° and 70° (in 2θ scale) are shown in Fig. 10.6. The diffraction pattern of SnO_2-H_2O sample is not included in the figure, as there was not alumina nanoparticles incorporated into the precursor solution. The diffraction peaks corresponding to SnO_2 reflections (PDF-00-041-1445) are

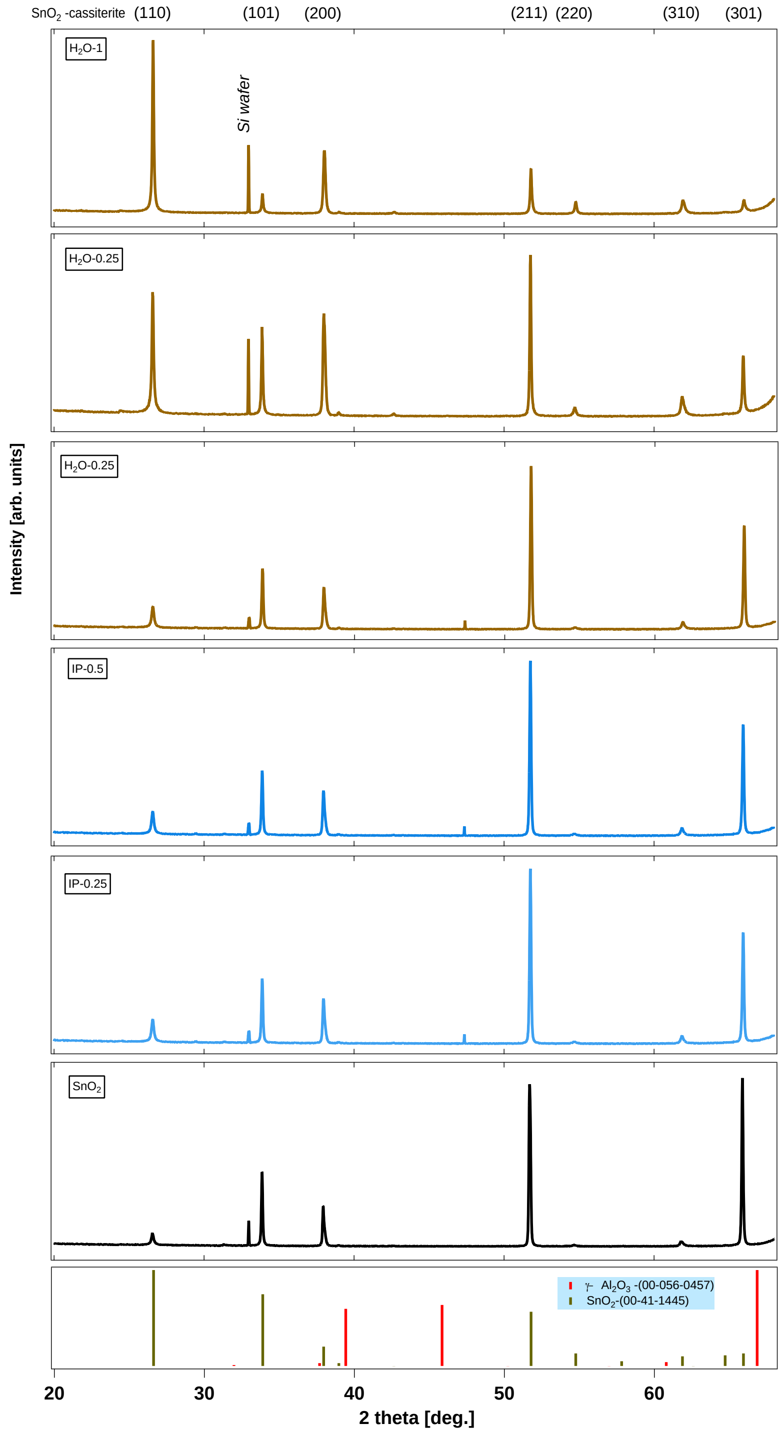

Figure 10.6: *The XRD diffractograms for undoped tin oxide and different Al_2O_3 NPs-SnO_2 thin films prepared using water and isopropanol dispersed gamma-Al_2O_3 NPs with different (Al_2O_3 to SnO_2) molar ratio.*

presented at the top of individual peaks. ICDD database pattern for gamma-alumina with reference no. 00-056-0457 is also represented in the Fig. 10.6.

The diffraction patterns of undoped SnO_2 and isopropanol (IP-0.25, IP-0.5) and water (H_2O-0.25, -0.5, and -1) based nanocomposite films are in a good agreement with cassiterrite SnO_2 (PDF-00-041-1445). However, there was no single reflection corresponding to γ-Al_2O_3 or any other polymorph of alumina. Therefore, the XRD analyses also do not confirm the incorporation of Al_2O_3 NPs. Although, the texturing of the films was observed.

The evolution of texture coefficient-C_{hkl} for different Al_2O_3 NPs-SnO_2 nanocomposite films are calculated based on θ -2θ XRD measurements of Fig. 10.6. Here, the texture analysis was quantitatively analysed using Harris method [184] with Eq. 4.8 by considering five main and independent diffraction peaks: (110), (101), (200), (211), and (301); whose indices are indicated in the legends of Fig. 10.6. In addition, the degree of preferred orientation σ was also calculated [2] according to Eq. 9.3. The calculated texture coefficient and degree of preferred orientation of the probed samples is plotted as a function of different nanocomposite thin fin films produced froms different form of Al_2O_3 and having different (Al_2O_3/SnO_2) molar ratio in the precursor solution, see Fig. 10.7.

For nominally undoped SnO_2, (301) crystallographic orientation is dominant with texture coefficient of 3.36 and the other orientations have C_{hkl} <1. In isopropanol dispersion series, for IP-0.25 sample (301) crystallographic orientation is dominant orientation C_{hkl} of 1.92. (200) and (211) crystallographic orientations also have C_{hkl} of 1.22 and 1.13 respectively. Similarly, for IP-0.5 sample (301) is still the dominant orientation with C_{hkl} of 2.37. These isopropanol series have almost identical change in C_{hkl} as that of undoped films. In water dispersion series, H_2O-0.25 sample (301) crystallographic orientation is still dominant with C_{hkl} of 2.77. Meanwhile, for H_2O-0.5 sample, (200) crystallographic orientation becomes the dominant orientation with C_{hkl} of 1.73 and (301) has also C_{hkl} of 1.42. For H_2O-1 sample, the C_{hkl} of (200) crystallographic orientation increased to 2.3. The texture study reveals that undoped tin oxide, isopropanol dispersion series and H_2O-0.25 have the same dominant crystallographic orientation of (301). While, for H_2O-0.5 and -1 samples the texture changed into (200) orientation. Since EDS and XRD do not confirm the incorporation of NPs, the change in texture can not be assigned to Al_2O_3 NPs incorporation.

The degree of preferred orientations of the same films is plotted as a function of sample types as shown in insert of Fig. 10.7. The degree of preferred orientation is reduced

[2]Description about texture coefficient C_{hkl} and degree of preferred orientation σ with the formulas used to calculate them can be found in section 9.2

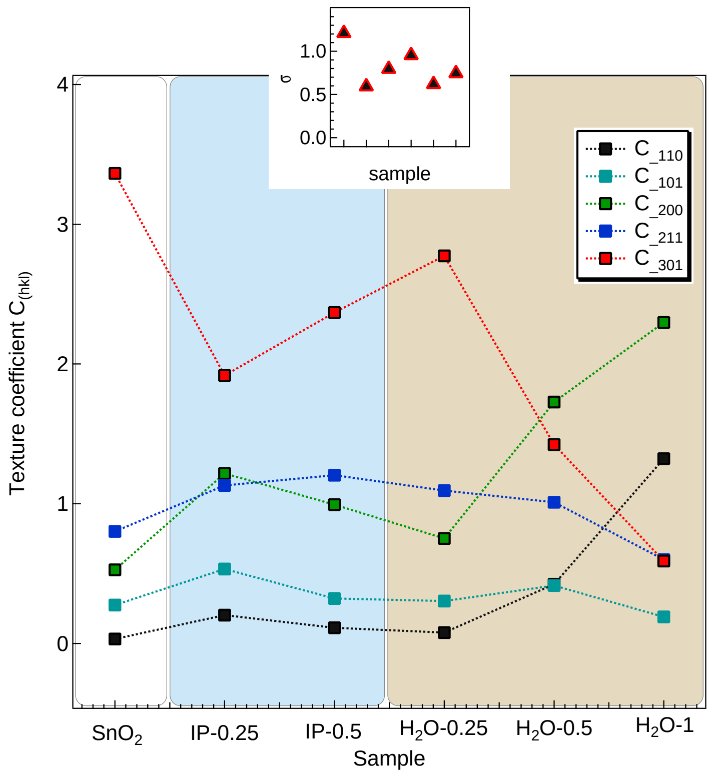

Figure 10.7: *Evolution of texture coefficients of Al_2O_3 NPs-SnO_2 nanocomposite thin films produced using water and isopropanol dispersed gamma-Al_2O_3 NPs in different (Al_2O_3/SnO_2) molar ratio in the precursor solution. The color code of different crystallographic orientations (hkl), which was used to calculate C_{hkl} is represented in the legend. The degree of preferred orientation of the same samples is represented in the insert.*

from 1.2 in undoped tin oxide to 0.6 for IP-0.25 and slightly increased to ≈0.8 for IP-0.5 sample. It further increases to 0.95 for H_2O-0.25 and slightly decreased to ∼0.7 for H_2O-0.5 and -1 samples.

Even though, the EDS and XRD analyses do not confirm the incorporation of Al_2O_3 NPs into tin oxide thin films; there have been changes in crystallographic orientation of the films. Since the samples are prepared in a similar deposition condition and there was no alumina nanoparticles incorporation, the source of texturing can be related to different film thicknesses of the studied samples.

Since the planar twin defects were observed in all SEM images the probed samples (see Fig. 10.3), it is important to distinguish between the grain size (L_g) and crystallite size (L_c) of studied films. Grain sizes were determined from the statistical analysis of the top view SEM images as described earlier in this chapter. Meanwhile, crystallite size corresponds to the small coherent domains between two twin boundaries. The

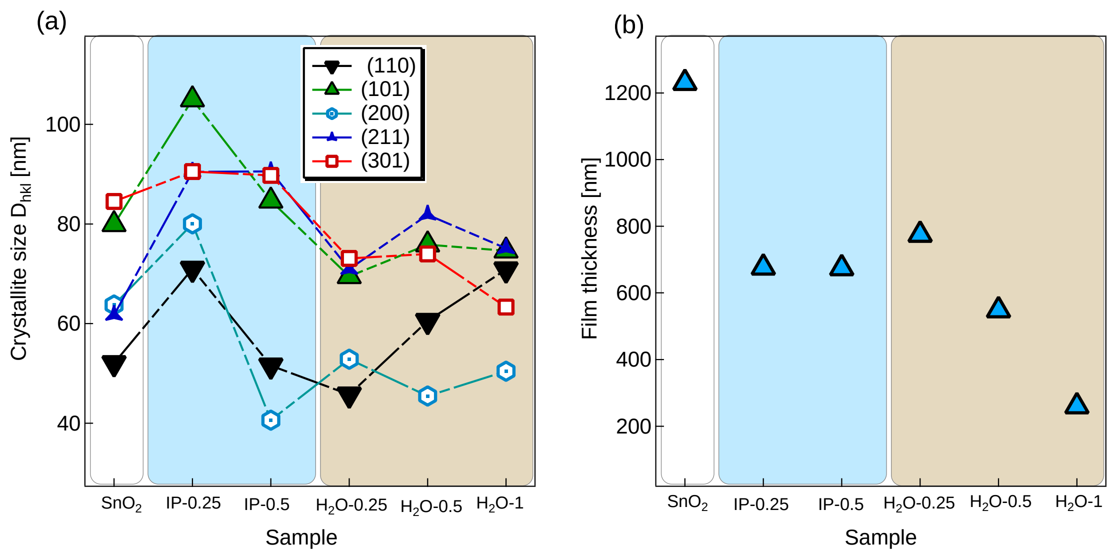

Figure 10.8: *(a)Evolution of crystallite size D_{hkl} determined by Scherrer formula from XRD peak width of different Al_2O_3 NPs - SnO_2 systems. The color code of different crystallographic orientations (hkl), which was used to calculate D_{hkl} is represented in the legend; (b), The film thicknesses of the same films extracted from SEM crossection.*

crystal size was calculated using the Sherrer equation [296, 297] as shown in Eq. 9.4 and the evolution of crystallite size on different probed films is shown in Fig. 10.8. For comparison, the film thickness extracted from SEM crossection of the same film is shown in Fig. 10.8(b) . The film thicknesses were extracted only for the samples prepared on Si wafer substrate. Similarly, the deposition rates of the same films calculated in Tab. 10.2 are based on the same thickness extracted from the SEM crossection. In general, the crystallite size is lower for H_2O incorporated samples compared to IP dispersion film. This is consistent with the evolution of grain size in Fig. 10.4.

10.4 Optical Study

The optical study of the probed samples was performed by measuring the total transmittance (T_{tot}) of undoped SnO_2 and different Al_2O_3 NPs-SnO_2 thin films using perkin Elmer Lambda 950 spectrophotometer. The total transmittance was measured between 250-2500 nm wavelength range as shown in the left image of Fig. 10.9. The total transmittance of bare glass substrate measured in the same regime is also included for comparison. There was no shift of the leading edge at short wavelength for most of samples, except H_2O-1 sample (shift to the lower energy). Therefore, there was no blue-shift of the absorption edge for most of the films except H_2O-1.

The average transmittance of probed samples in the visible region of 400-800 nm is plotted as shown in the right image Fig. 10.9. In this regime, the transmittance of probed samples are generally high, in the range of 70- 80 %.

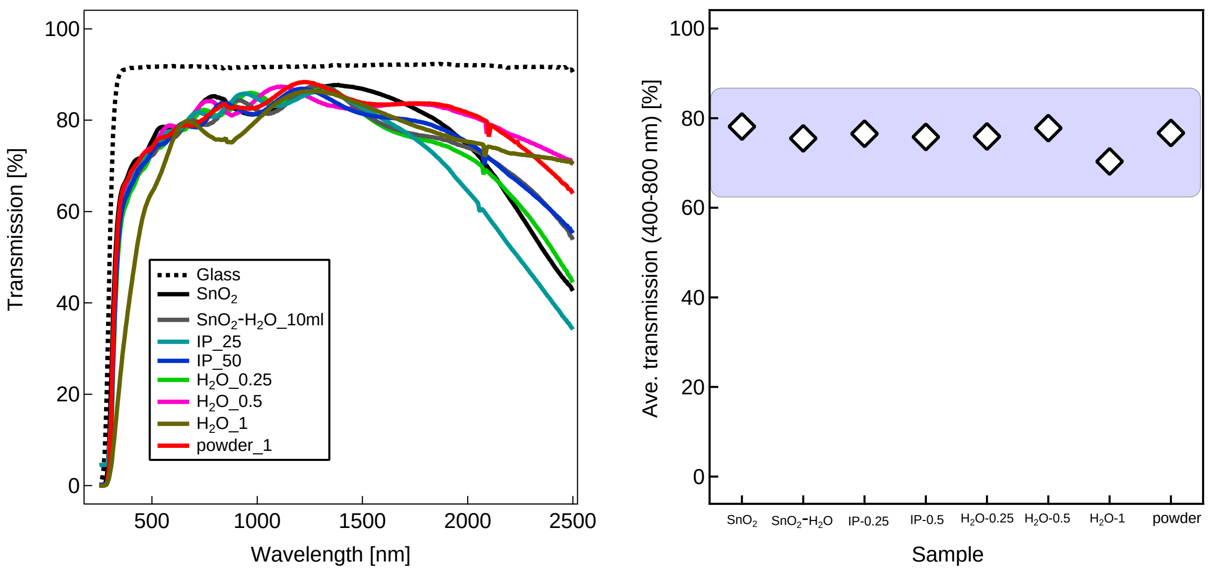

Figure 10.9: *(left) Optical transmission (T_{tot}) in 250 - 2500 nm range plotted for different Al_2O_3 NPs- SnO_2 thin films using Al_2O_3 NPs in different forms and different Al_2O_3 to SnO_2 molar ratio. The transmittance of bare glass substrate is included for comparison; (right), An average total transmission of the same samples in visible regime of 400 -800 nm.*

Compared to undoped tin oxide, the films produced by adding different Al_2O_3 NPs in the tin precursor solution have a slight different transmittance in near infrared (NIR) region. The films with isopropanol dispersion series (IP-0.25 and -0.5), the transmittance increases with increasing the NPs concentration in the precursor solution. Similarly, the films with water dispersion series (H_2O-0.25, -0.5, and 1), the transmittance increases with increasing alumina nanoparticles concentration in the precursor solution. The powder-1 and SnO_2-H_2O samples also show higher transmittance value compared to undoped tin oxide film. These changes in transmittance values are associated to the shift of plasmon frequency towards NIR region. Since, the Al_2O_3 NPs are not incorporated into the grown tin oxide films and the films are prepared in similar deposition conditions, the change in transmittance of NIR can be attributed to the difference in film thickness of the studied samples.

The optical band gap of probed samples determined from Tauc plots [3] with the data in ordinate cut off at 10^{11} and 10^{10} $(eV/cm)^2$ are plotted as function Al_2O_3 NPs-SnO_2 nanocomposite films produced using different forms of Al_2O_3 NPs and different (Al_2O_3/SnO_2) molar ratio, see Fig. 10.10. In general, the band gaps decreased in all cases with lowering the ordinate cut off values. For water dispersion series, the band gap slightly decreased and at H_2O-1 lowest band gap exhibited. For isopropanol dispersion films and powder incorporated sample shows the similar optical band gap.

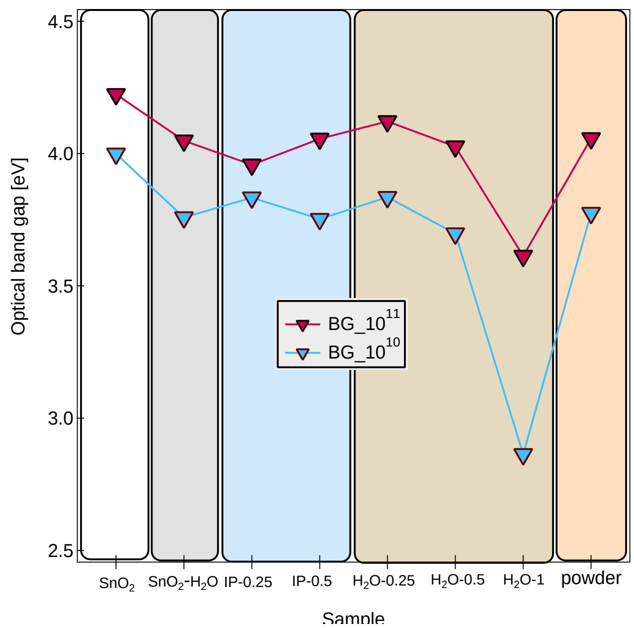

Figure 10.10: *The optical band gap extracted from Tauc plot of the studied samples. The films produced from the different forms of Al_2O_3 NPs added into the precursor solution are colored differently for better visual.*

10.5 Electrical Study

Conductivity of nominally undoped and different Al_2O_3-SnO_2 nanocomposite films prepared by using different forms of gamma-Al_2O_3 NPs and different (Al_2O_3 to SnO_2) molar ratio deposited on different substrates (Si wafer, fused silica, corning glass, and SiO_2/Si) is presented in Fig. 10.11(a). Hall effect results of the same films is presented in Fig. 10.11(b) for carrier concentration and Fig. 10.11(c) for carrier mobility.

[3] The description on how to extract optical band gap from Tauc plot can be found in section 9.3

Different structural characterizations of the probed samples revealed that Al_2O_3 NPs are not incorporated into the grown films and the desired nanocomposite films were not produced. Thereby, the change in electrical properties among these samples can not be attributed to the embedding of nanoparticles in the grown films. Here in description of the results and discussion the amount of nanoparticles added into the precursor solution are considered.

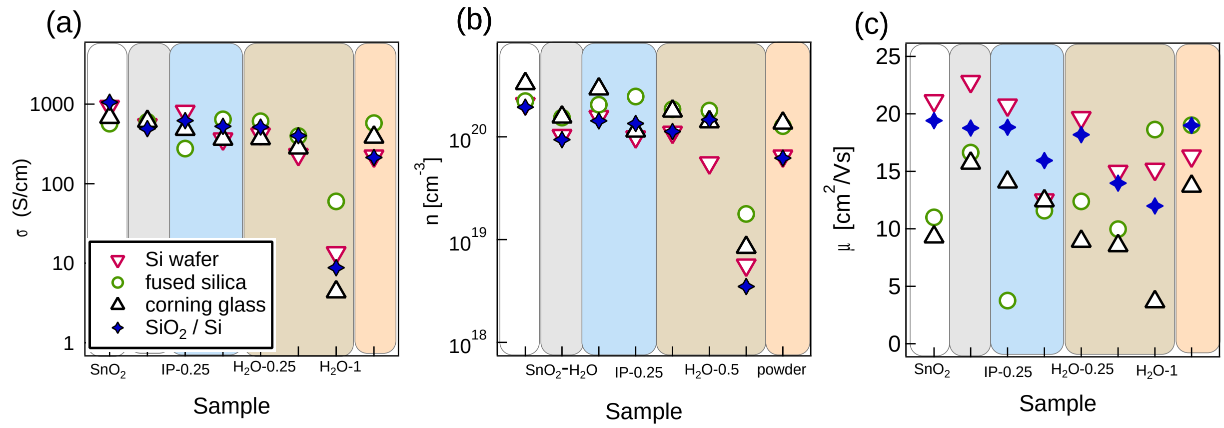

Figure 10.11: *(a) Conductivity; (b), carrier concentration and (c), carrier mobility of undoped tin oxide and different Al_2O_3-SnO_2 nanocomposite films prepared by using different forms of gamma-Al_2O_3 NPs and different (Al_2O_3 to SnO_2) molar ratio. The type of substrates used in the probed samples are represented in the legend.*

The conductivity of nominally undoped tin oxide was in the range of ≈ 600-1110 S/cm for different substrates. For isopropanol dispersion series, conductivity values differ in the range of ≈ 270 - 810 S/cm for different substrates. For the water dispersion series (H_2O-0.25, -0.5, and 1), the conductivity decreases with increasing alumina NPs concentrations in the tin precursor solution. H_2O-1 sample exhibits the lowest conductivity values of ≈5-60 S/cm from the studied films. The samples prepared using powder NPs have comparable conductivity values to those isopropanol series.

The Hall effect measurements reveal that the conductivity changes are mostly due to carrier concentration. The carrier concentrations are in the range of $\approx 5 \times 10^{19}$ cm^{-3} and 3×10^{20} cm^{-3} for most of the films except H_2O-1, which show lower carrier concentration of upto one order of magnitude. On the other hand, the Hall mobilities show scattering results among the same compositions prepared in different substrates, which have the values in the range of 3 to 25 cm^2/Vs.

The incorporation of nanoparticles into the grown tin oxide films was the preliminary task to test defect modulation doping effect of Al_2O_3 NPs on tin oxide films. However, the nanoparticles are not incorporated, as it is evident from different characterization. Thus, it is not possible to test modulation doping.

10.6 Summary, Conclusion, and Outlook

In this chapter, the chemical approach of defect modulation doping was tested by incorporating Al_2O_3 nanoparticles into tin oxide thin films. For this purpose different forms of Al_2O_3 NPs were used as dopant phase and series of samples were prepared by using ultrasonic spray pyrolysis setup.

The first step to test the modulation doping effect of Al_2O_3 NPs in tin oxide films is the confirmation of the presence of nanoparticles into the grown films. For this purpose, the studied samples were probed by several characterization techniques (EDS, XRD, and XPS) to confirm the incorporation of Al_2O_3 NPs into tin oxide matrix. Eventually, none of these techniques confirm the presence of alumina nanoparticles in the probed samples.

Discussion of the different reasons explaining the absence of Al_2O_3 nanoparticles in the grown films.

Their are several reasons, which could explain why the nanoparticles were not incorporated into growing tin oxide thin films. Some of the reasons will be discussed here.

One of the possible reason could be the following: the nanoparticles introduced in the precursor solution may not exist in atomized droplets of mist, rather they may stay in the bottom of solution pot. In this way the generated mist could only contain tin oxide precursor droplets. However, since the atomization was performed in ultrasonic transducer, sedimentation of nanoparticles into the bottom of solution pot may not the probable condition.

The other possible reason for incorporation problem of nanoparticles into growing film could be related to the transport of generated droplets. Aerosol transport of droplets is one of the important processing step for spray pyrolysis deposition and is discussed below.

Aerosol Transport of Droplets

After the formation of mist, droplets are transported with the aim of having as many droplets as possible reaching the surface of substrate. During the transport of droplets, they experience physical and chemical changes as depicted in schematic diagram of Fig. 4.7. As the droplet traverses the ambient, there are four main forces simultaneously acting on it, which determine the path of droplets. Those forces are gravitational, electrical, thermophoretic and stokes force [315], as described below:

- **Gravitational force** (F_g), is the force pulling the droplet downward. The size of this force depends on the mass of traveling droplet, which is a function of its volume and density. Assuming the droplets have spherical shape, the gravitational force is given by Eq. 10.1.

$$F_g = m_d g = \frac{4\pi}{3}\rho_d r^3 g \tag{10.1}$$

  where: m_d is mass of droplet, g is acceleration due to gravity, ρ_d is droplet density, and r is radius of the droplet.

  Depending on the configuration of spray pyrolysis setup, this gravitational force could be the main *driving* or *retarding* force of droplet transport. For the configuration when droplets travel from the top to bottom to reach substrate surface, the gravitational force is the driving force for droplet transport. While, for the configurations in which the droplets travel from bottom to top, gravitational force contributes as retarding force against the ascending transport of droplets. In both conditions the effect of this force is more pronounced for larger droplets/particles.

- **Electrical force** (F_E) is applicable to spray pyrolysis systems which include an additional electric source governing the droplet's trajectory. Ultrasonic atomizers are electrically driven, whereby an electric generator is vibrated at ultrasonic frequencies. Similarly, electrostatic discharge (ESD) atomizers use a strong electric force at the liquid - gas interface to generate charged droplets. Thus, for spray deposition using ultrasonic and ESD atomizers, electrical force is one of the main component which drives the droplets transport and is given by Eq. 10.2.

$$F_e = q_d E \tag{10.2}$$

  where, E is the generated electric field strength and q_d is the droplet charge. This droplet charge depends on temporal change of the droplet and is given by Eq. 10.3:

$$q_d = q_{max}\frac{t}{t+t_0} \quad (r \gg 1\mu m) \quad with \;\; q_{max} = 8\pi\sqrt{\gamma\varepsilon_0 r^3} \;\; and \;\; t_0 = \frac{4}{bdivE} \tag{10.3}$$

where, γ is liquid -gas surface tension, ε_0 is the electrical permitivity, and b is ionic mobility.

- **Stokes force** (F_s) is the drag experienced by the droplet due to the air resistance in the ambient [316]. The force is caused by the friction between the droplet and air molecules. The stokes force depends on the particle's velocity and size. Thus, large droplets which move with a high velocity will experience the largest retarding force according to Eq. 10.4:

$$F_s = 6\pi\eta_a r(v_d - v_a)\Big(1 + \frac{3}{8}Re\Big) \tag{10.4}$$

where, η_a is the viscosity of air, r is the droplet radius, v_d is the droplet velocity, v_a is the air velocity, and R_e is Reynolds number. For spherical particles, the Reynolds number is given by

$$R_e = \frac{2r(v_d - v_a)\rho_a}{\eta_a} \tag{10.5}$$

where, ρ_a is the density of air. Since $\frac{3}{8}R_e$ term in Eq. 10.4 is small ($\frac{3}{8}R_e \ll 1$), it is often excluded from Stokes force calculations.

- **Thermophoretic force** (F_t) is a retarding force, causing droplets to significantly decrease their velocity as they approach the heated substrate. The air temperature increases steeply due to the forced convection effect of the air flow when close to the heated substrate. Since the thermophoretic force depends on the thermal gradient in the transport environment, it will have no effect on the droplet movement, when it is several ($\sim$ 5 - 7) nm away from the substrate [317]. However, in high thermal gradient region, the thermophoretic force begins to dominate. This is true for pressure spray deposition (PSD) systems where the main driving force is gravity; however, for ESD systems, the electrical force is often stronger than the thermophoretic force. Therefore, the motion of the droplet within the "thermal zone" would not change significantly, but the increased temperature would have other effects on the droplet, such a reduction in size due to droplet evaporation into the "thermal zone" region. The equation governing the strength of the thermophoretic force is given by Eq. 10.6

$$F_t = \frac{3\pi\eta_a^2 r}{\rho_a}.\frac{\bigtriangledown(T_d)}{T_a} \tag{10.6}$$

where η_a is the viscosity of air, r is the droplet radius, T_d is the droplet temperature, T_a is the air temperature, ρ_a is the density of the air, and $\bigtriangledown$ (T_d) is

$$\bigtriangledown(T_d) = \frac{3k_a}{2k_a^2 + k_d}.\bigtriangledown(T_a) \tag{10.7}$$

where, k_a and k_d are the thermal conductivities of the air and the droplet, respectively. It should be mentioned that Eq. 10.6 is only valid for droplets whose radius is much larger that the mean free path of the air molecules.

In this work ultrasonic spray deposition chamber is used. In the deposition chamber the substrates were mounted upside down and the generated mists of droplets were transported upward against gravity to reach the substrate surface, see Fig. 4.9. Thus, the incorporation problem of nanoparticles could partially be attributed to the transportation of mists.

Assuming the generated droplets contain alumina nanoparticles and taking into account the configuration of the setup, transport of droplets plays an important role in incorporation of nanoparticles into growing film. As discussed earlier, the path of droplets is determined by different forces. Since the droplets are traveling upward, gravitational force F_g will act as retarding force and its effect is more pronounced for larger droplets. Seeing that the generated droplets were transported by applying compressed air (7.5 mm of H_2O), which is not bigger than the possible stokes forces, stokes forces may have big impact in this condition. In the other hand, electrical force applied during droplet generation could be considered as driving force for the droplet transport.

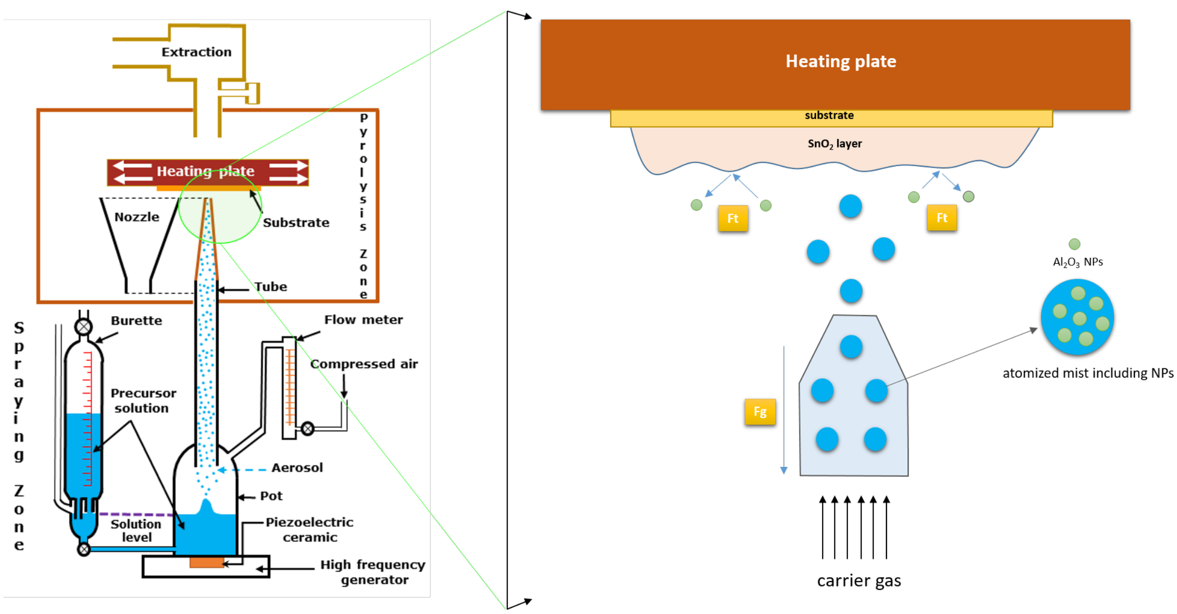

Figure 10.12: *Left: Schematic illustration for ultrasonic spray pyrolysis setup used in this work; Right : magnified view of pyrolysis zone, which includes spray nozzle, atomized droplets with Al_2O_3 NPs, Al_2O_3 NPs, heating plate, substrate, and growing tin oxide film. In the plot important forces acting on traveling droplets, Fg - gravitational force and Ft - thermophoretic are also be represented.*

During this work all the samples were prepared at deposition temperature of ≈420 °C.

Similarly, in spraying zone (droplet generation area), the temperature was around ≈50 - 60 °C[4]. In such a way the incoming droplets will face big thermophoretic retarding force F_t when they reach substrate surface. This is due to high temperature gradient and this will prevent the nanoparticles from incorporating into the growing thin film.

These scenarios are schematically illustrated in Fig. 10.12. In the figure, the full scale deposition setup is shown in left. While, the magnified view of pyrolysis zone with representation of important forces acting on droplets is shown in the right figure. First, it is assumed that the droplets contain Al_2O_3 NPs and are transported upward with the help of compressed air. The gravitational force - F_g will act as retarding force as indicated by downward arrow in the figure. During deposition, the distance between nozzle head and substrate surface was only ≈1.5 cm, so temperature gradient will play an important role here. Due to strong thermophoretic force, the incoming naoparticles could bounce back from the surface of the film than physically adsorbed into the film, see the right figure.

If the nanoparticles were reaching the substrate surface they would be adsorbed physically into the growing film. Generally, when neutral species or radicals impinging onto the growing film surface, they can adsorbed at the surface according to their sticking coefficient s and form an *adsorbate*. This sticking coefficient s describes the probability for the incoming particle to loose its kinetic energy via energy transfer to the atoms of the solid and to become trapped in a bound state at the surface. This bound surface state can be a physisorbed or chemisorbed state; in the physisorbed state the binding energy is typically $<$ 500 meV. The binding force is promoted via dipole–dipole interactions (van der Waals force). In the chemisorbed state the binding energy is typically $>$ 500 meV and the adsorbed species forms a chemical bond (covalent or ionic) with the substrate [318]. For alumina nanoparticles the phenomena would be only physisorption.

In summary, we have seen that incorporation of nanoparticle (Al_2O_3 NPs and TiO_2 NPs[5]) using the current spray pyrolysis setup and deposition condition is not easy. The nanoparticles may not be present into atomized droplets. If they would be present inside the droplets, they could face different forces, which act against them during transport. Finally, if they reach substrate surface, they may not be adsorbed due to high temperature gradient or too weak bond with van der Waals (vdW) interactions.

In conclusion, care must be given in all three steps of spray pyrolysis deposition. During atomization, the power and frequency must be tuned in a way that nanoparticles are present within the formed droplets. During transport, the acting forces must be used as driving force and reduce the impact of retarding forces. Finally, other deposition

[4] Heats are generated during atomization of droplets by ultrasonic transducer.

[5]this is the case of chaper 8

conditions must also be controlled in order to see the desired nanocomposite structure. Preparation of nanocomposite thin films by other alternative techniques could also be considered. Electro spray pyrolysis (ESP) and sol gel techniques could be an alternative for the sample fabrication technique.

Closing Remarks and Outlook

This study investigated the novel doping strategy for semiconductor materials, namely *defect modulation doping*, which has the potential to circumvent conductivity limits both in regard to charge carrier density and charge carrier mobility. The strategy uses two chemically and structurally dissimilar materials, which do not have to be conductive by their own. With the band alignment and Fermi level pinning in the doping material of these materials it is possible to obtain Fermi levels outside the doping limits in the host material.

In this work, it was attempted to demonstrate the defect modulation doping concept for different transparent conducting oxide (TCO) materials. For this purpose, the study was divided into two parts by the approaches followed experimentally. The first part deals with a *physical approach* and the second part with a *chemical approach*. The main findings from both approaches are summarized in detail in the subsections below.

The physical approach

In this approach the viability of defect modulation doping was tested by using different ultra thin defective and amorphous wide band gap insulators namely, Al_2O_3 and SiO_2 as the potential dopant and deposited on the surfaces of TCOs (In_2O_3 and Sn-doped In_2O_3). As a result, conduction electrons are induced in the interface near region of the TCOs, which enhance the electrical properties. The important results found from ITO/ALD-Al_2O_3, In_2O_3/ALD-Al_2O_3, and In_2O_3/sputtered SiO_2 systems are summarized below with the future outlook:

- **ITO/ALD-Al_2O_3**

  Ultra thin Al_2O_3 deposited by atomic layer deposition (ALD) technique was used as a potential dopant and coated on Sn-doped In_2O_3 thin films prepared in different conditions in order to induce conduction electrons in the interface near region of ITO. ALD-Al_2O_3 was chosen as the Fermi energy is $\approx$ 4.5 eV above valence band maximum and by combining with ITO the Fermi energy is expected to shift upward in the doped interface. The study was developed by correlating the microstructural, interfacial and electrical studies. In addition, several post deposition treatments were performed in order to discriminate different effects, which govern the changes of carrier concentration and mobility. The obtained results emphasize the following key points.

By deposition of 5-cycles of ALD-Al_2O_3, the Fermi energy in ITO was expected to raise to E_F - $E_{VB} \geq 4$ eV. However, this was not the case as the Fermi energies of ITO films corresponded only to E_F - $E_{\mathrm{V}B} \approx 3.2 \pm 0.2$ eV after alumina deposition. The discrepancy between the expected and the measured Fermi energies is explained by the formation of a very narrow space charge region at the surface of highly doped ITO. If this is narrower than the depth probed by XPS, the Fermi level directly at the interface cannot be observed.

The conductivity and Hall effect measurements reveal that alumina deposition results in an increase of conductivity on most of ITO thin films prepared in different deposition conditions. This was mostly due to an increase of carrier concentrations. However, the upside obtained from the coating was moderate. In addition, the Al_2O_3 coverage resulted a in chemical reduction of ITO.

Realization of defect modulation doping was not possible on ITO films covered with 5-cycles of ALD-Al_2O_3. This was mostly related to the deposition conditions followed during the coverage of Al_2O_3 layers at 200 °C. At this temperature, the diffusion of compensating oxygen interstitial defects is not suppressed. Therefore, oxygen interstitials can diffuse towards the interface and screen the potential difference induced by the high Fermi energy at the interface. Annealing experiments confirmed that oxygen defects are sufficiently mobile at 200 °C.

In order to overcome this problem, a low temperature deposition process with very low oxygen activity could be an option. If low temperature deposition is applied for ITO, the inherently small grain size of low-temperature grown films has to be overcome, as this clearly limits the carrier concentration. The use of seed layers, such as the recently demonstrated Fe_2O_3 might be the solution for this as it enhance the crystallinity of ITO. On the other hand, performing ALD deposition at lower temperature is also still possible. However, care must be given as the ALD deposition must be done at the temperature within the *"ALD of Al_2O_3 window"* in order to avoid condensation and incomplete reactions.

- **In_2O_3/ALD-Al_2O_3**

  Here, undoped In_2O_3 thin films were used as a TCO host and coated with ALD-Al_2O_3 for testing defect modulation doping. In_2O_3 was prepared with different conditions like ITO, in order to discriminate the governing factors for the changes in the carrier concentrations and mobility. Al_2O_3 layers were deposited with different numbers of ALD-cycles, to see the influence of Al_2O_3 layer thickness on the doped interface.

  Al_2O_3 deposition does not bring the Fermi energy of In_2O_3 to the expected value of E_F - E_{VB} $\geq$ 4 eV, but limited to E_F - E_{VB} $\approx$ 2.9 eV $\pm$ 0.1 eV. Here as well, the formation of a very narrow space charge region explains the obtained lower Fermi energies at the doped interface.

  Conductivity and Hall effect measurements revealed that Al_2O_3 deposition results an increase of conductivity of In_2O_3 thin films. This was mostly due to an increase of carrier concentration. The systematic study on the influence of Al_2O_3 layer thickness on the near surface and bulk properties of In_2O_3 revealed that an enhancement of electrical properties occurs up to 10-cycles of ALD. For 10-cycles of Al_2O_3 deposition, the carrier concentration increased upto a factor of 2.5.

  In a nutshell, In_2O_3/ALD-Al_2O_3 thin films indicate that defect modulation doping effect occurs and results in a moderate enhancement of electrical properties. However, in order to improve the interface properties and firmly prove the modulation doping effect, more detailed studies are required on the doped interface.

- **In_2O_3/sputtered SiO_2**

  In this case, a different wide band gap material, namely SiO_2, was used as a potential dopant and deposited on the surface of undoped In_2O_3 thin films. SiO_2 layers were reactively sputtered from a silicon target, which results in partially reduced silicon dioxide, represented as SiO_{2-x}. The reduction of SiO_2 can come from either vacancies of oxygen (V_O) or silicon interstitials (Si_i). These defects then should generate a Fermi level pinning in the upper half of the band gap ($\geq$ 4.5 eV). Therefore, combining In_2O_3 with a very thin layer of reduced SiO_{2-x} should also result in a high Fermi level position at the In_2O_3 surface higher than the doping limit.

  For these purpose different $\approx$2 nm thick SiO_{2-x} layers were deposited on the top of 20 nm thick In_2O_3 thin films deposited at 400 °C. SiO_{2-x} were deposited either at room temperature (RT) or at 400 °C and by adding 0.6% to 5 % of O_2 in the sputtering gas in order to obtain different stochiometries of the reduced layer.

By the deposition of partially reduced SiO_{2-x}, the Fermi energies in the produced In_2O_3 thin films were expected to shift upward, even beyond the doping limit. However, the photoemission experiments revealed that this is not the case for SiO_{2-x} coverage both at RT and 400 °C. Thus, SiO_{2-x} does not induce the desired increase of Fermi energy at the surfaces of In_2O_3 thin films.

The bulk conductivity and Hall effect measurement revealed that coating of ≈2 nm SiO_{2-x} does not bring the desired improved electrical properties on In_2O_3 thin films. This can be explained by, on one hand, the impact of oxygen species on the surface of In_2O_3 during SiO_{2-x} deposition. This can counteract the defect modulation doping by reducing the concentration of oxygen vacancies in In_2O_3. This is valid for SiO_{2-x} depositions at both temperatures, since the In_2O_3 films were only 20 nm thick. On the other hand, SiO_{2-x} does not show the suitable intrinsic defects (V_O or/and Si_i), which can pin the Fermi energy in the upper half of the band gap.

The energy band alignment at the In_2O_3/SiO_2 interface is characterized by a large valence band discontinuity of $\triangle E_{VB} \sim 1.4$ eV, which is comparable to the interface of ITO/ALD-Al_2O_3 ($\triangle E_{VB} \approx 1$ eV) [38]. In addition, the Fermi level position in the SiO_2 is pinned at ∼5.8 eV. This suggests that silicon dioxide still has a potential to be a dopant material for demonstrating defect modulation doping. Therefore, further optimization of the deposition conditions and careful investigation of the interface is needed in order to achieve the desired Fermi level pinning by the defect.

The chemical approach

In this approach different nanocomposite thin films were prepared using ultrasonic spray pyrolysis deposition. To test the defect modulation doping, two different routes were followed: embedding of nanoparticles into TCO host matrix and formation of two demixed phases with one phase to be the potential dopant. In the first route, TiO_2 nanoparticles (NPs) and Al_2O_3 NPs were chosen as dopant phases and were deposited together with SnO_2 TCO host precursors. Meanwhile, for the second route the mixture of $SnCl_4 \cdot 5(H_2O)$ and $Al(acac)_3$ precursors solution in different composition were used to produce SnO_2/Al_2O_3 demixed composite films.

- **SnO_2/TiO_2 NPs nanocomposite**

  These nanocomposite thin films were synthesized from dibutyltin diacetate (DBTDA) precursor for tin oxide and TiO_2 NPs as a dopant phase. Both are mixed in different composition using ethanol solution. The TiO_2 NPs were dispersed in acidic water solution with particle size in range of 10-25 nm and have small percentage of nitric acid (NHO_3). The precursor solutions were then utilized in spray pyrolysis deposition.

Different physicochemical characterizations of the synthesized films revealed that TiO_2 NPs were not incorporated into the grown tin oxide thin films and embedding was not possible. In addition, there were some concerns on usage of the dopant nanoparticles.

- The presence of nitric acid inside TiO_2 NPs dispersion was problematic:
  * Firstly, it can readily react with the solvents (ethanol and methanol) used in making precursor solutions. The mixture of nitric acid and these solvents could be a potential explosive.
  * Secondly, the tin oxide precursor used for this study was DBTDA, which is less effective compared to $SnCl_4 \cdot 5(H_2O)$ precursor in terms of desired film properties. DBTDA was chosen to avoid the possible reaction between nitric acid and acidic byproduct of SnO_2 precursor $SnCl_4.5(H_2O)$, that is HCl which can form aqua regia.
- TiO_2 NPs also had encapsulating polymeric agglomerates. Hence, the nanoparticles are not active and the encapsulation may prevent the doping effect of nanoparticles.

- **SnO_2/Al_2O_3 NPs nanocomposite**

  Since there were issues with TiO_2 nanoparticles other potential dopants of Al_2O_3 NPs were selected and different thin films were prepared using spray pyrolysis deposition with the aim of embedding Al_2O_3 NPs into the TCO host. Three different forms of γ-Al_2O_3 NPs were used, namely water dispersed, isopropanol dispersed, and powder forms with average particle sizes of 10 nm, 15 nm, and 40 nm respectively. $SnCl_4 \cdot 5(H_2O)$ was used as tin precursor and mixed together with the dopant NPs in different compositions in methanol solution. Different physicochemical characterizations of the probed samples revealed that the desired nanocomposite structure was not obtained as Al_2O_3 NPs did not embed in the tin dioxide thin films.

  As it is mentioned above, under the deposition conditions followed during this work and the used deposition chamber setup, embedding of the nanoparticles (both TiO_2 and Al_2O_3) in the SnO_2 TCO host was not possible by ultrasonic spray pyrolysis deposition. There are several reasons why this was not possible and some of the most prominent causes are described below with some suggestions of possible solutions.

Nanoparticles: TiO_2 NPs were encapsulated in polymeric agglomerates and contains nitric acid in the dispersed solution. Therefore, finding of the suitable TiO_2 NPs, which are solvent/process friendly and free of encapsulating layers are necessary. Finding the right surface active agents (surfactants) for removing the agglomerates is still an option. The situation was different for Al_2O_3 NPs. In this case, the NPs suffered sedimentation during both preparation of precursors solutions and inside the solution pot of the spray setup. Accordingly, this could affect the transportation of nanoparticles into the substrate surface.

Spray pyrolysis setup configuration: in the current spray setup configuration, substrates were mounted upside down and the sprayed mists were transported upward against gravity. This could make the transportation and embedding of nanoparticles difficult. Therefore, in order to successfully embed the NPs, further adjusting of the spray setup configuration is needed. In addition, using alternative thin film synthesis techniques including electro-spraying, sol-gel, and spin coatings are still an option. In this case, also finding the right precursors and deposition conditions are required.

- **SnO_2/Al_2O_3 demixed composite films**

  For this approach, the aim was to produce nanocomposite thin films contain two demixed phases of TCO matrix and insulator dopant phase. For this purpose, $SnCl_4 \cdot 5(H_2O)$ and $Al(acac)_3$ precursors in different compositions were used in methanolic solution. The produced thin films were then characterized by different physicochemical analysis and summarized below:

  - To confirm the formation of demixed crystalline phases of SnO_2 and Al_2O_3, different characterizations of XRD, TEM, and XPS were performed. None of these analysis did confirm the presence of a crystalline alumina phase in the binary system. On the other hand, different structural characterizations confirmed the presence of Al in the synthesized films. Thus, Al^{3+} was incorporated into the tin dioxide lattice by substituting Sn^{4+} rather than formation of crystalline alumina. Incorporation of Al tuned the properties of probed SnO_2 thin films. The important results obtained from different characterizations of the studied films are summarized below:

    * Al incorporation changes the morphology of tin dioxide films and resulted in a reduction of grain size with increasing Al concentration in the grown films.

* Al incorporation also resulted in a structural reordering of tin dioxide by a texture transition from (301) to (101), and then to (002) upon increasing Al content in the grown films.

* The optical transmittance of tin oxide was not changed in the visible region by Al incorporation with an average transmittance of 72-81 % being obtained. Meanwhile, in the near infrared region, a difference in plasmonic absorption is observed in all samples: the plasmon frequency shifted towards the IR region as a function of Al doping concentration.

* Since Al^{3+} substitutes Sn^{4+} in SnO_2 lattice structure, the electron concentration is reduced and electrical properties of tin dioxide films did not improve.

– In conclusion, the expected demixed binary composite materials was not realized. As a future outlook, following points could be taken into considerations. Since only 6 % Al was incorporated into the prepared films, increasing the Al content in the grown films would still be an option to get the secondary Al_2O_3 phase. Using of other deposition techniques including sol gel or spin coating methods together with suitable different precursors are still an option.

Importance

The results of this study illustrate different attempts followed in order to resolve one of the biggest challenges in the area of TCO semiconductors researches, enhancement of their electrical properties. As the approach is based on near surface properties, it has a great importance to fully realize the range of potential device applications, in particular, for the usage of TCOs as contacts, sensors and in nanoscale materials, where the surface to bulk ratio is much higher than in conventional films. With further utilization of the modulation doping process, the nanocomposite approach could be promising. This can allow to obtain high quality TCOs with low budget and scalable spray pyrolysis deposition.

Bibliography

[1] S. Zhang, S.-H. Wei, and A. Zunger, "Microscopic Origin of The Phenomenological Equilibrium "Doping Limit Rule" in n-type III-V Semiconductors," *Physical Review Letters*, vol. 84, no. 6, p. 1232, 2000. (cited on pages XV and XVI.)

[2] W. Walukiewicz, "Intrinsic Limitations to The Doping of Wide-Gap Semiconductors," *Physica B: Condensed Matter*, vol. 302, pp. 123–134, 2001. (cited on pages XV and 16.)

[3] R. Dingle, "XCIV. Scattering of Electrons and Holes by Charged Donors and Acceptors in Semiconductors," *The London, Edinburgh, and Dublin Philosophical Magazine and Journal of Science*, vol. 46, no. 379, pp. 831–840, 1955. (cited on pages XV and 23.)

[4] T. Minami, "Transparent conducting oxide semiconductors for transparent electrodes," *Semiconductor Science and Technology*, vol. 20, no. 4, p. S35, 2005. (cited on pages XV and 14.)

[5] K. Ellmer, "Past achievements and future challenges in the development of optically transparent electrodes," *Nature Photonics*, vol. 6, no. 12, p. 809, 2012. (cited on pages XV and XVI.)

[6] E. Fortunato, D. Ginley, H. Hosono, and D. C. Paine, "Transparent Conducting Oxides for Photovoltaics," *MRS Bulletin*, vol. 32, no. 3, pp. 242–247, 2007. (cited on pages XV, 30, and 31.)

[7] R. Dingle, H. Störmer, A. Gossard, and W. Wiegmann, "Electron Mobilities in Modulation-Doped Semiconductor Heterojunction Superlattices," *Applied Physics Letters*, vol. 33, no. 7, pp. 665–667, 1978. (cited on pages XVI, 23, 32, 33, 34, 35, and 36.)

[8] M. Weidner, A. Fuchs, T. J. Bayer, K. Rachut, P. Schnell, G. K. Deyu, and A. Klein, "Defect Modulation Doping," *Advanced Functional Materials*, p. 1807906, 2019. (cited on pages XVI, 40, 41, 42, 108, 118, 123, 139, and 211.)

[9] M. Weidner, "Fermi Level Determination in Tin Oxide by Photoelectron Spectroscopy: Relation to Optoelectronic Properties; Band Bending at Surfaces and Interfaces; modulation doping," Ph.D. dissertation, Technische Universität Darmstadt, 2016. (cited on pages XVI, 40, 41, 43, and 210.)

[10] R. Enderlein and N. J. Horing, *Fundamentals of Semiconductor Physics and Devices*. World Scientific, 1997. (cited on page1.)

[11] H. Lüth and H. Ibach, *Solid-State Physics: An Introduction to Principles of Materials Science*, 4th ed. Springer-Verlag Berlin Heidelberg, 2009. (cited on page1.)

[12] A. Klein, "Transparent Conducting Oxides: Electronic Structure–Property Relationship From Photoelectron Spectroscopy With In Situ Sample Preparation," *Journal of The American Ceramic Society*, vol. 96, no. 2, pp. 331–345, 2013. (cited on pages 1, 16, 17, 18, 19, 20, 30, 67, 82, 102, 108, and 134.)

[13] J. Deuermeier, "Origins of Limited Electrical Performance of Polycrystalline Cu_2O Thin-Film Transistors," Ph.D. dissertation, Universidade NOVA De Lisboa (Portugal), 2016. (cited on pages 1, 68, and 71.)

[14] A. M. H. Fuchs, "Der Frontkontakt der CdTe-Dünnschichtsolarzelle: Charakterisierung und Modifizierung von Puffer-und Fensterschichten und deren Grenzflächen," Ph.D. dissertation, Technische Universität Darmstadt, 2015. (cited on pages 1 and 10.)

[15] W. Heisenberg, "Uber den Anschaulichen Inhalt der quantentheoretischen Kinematik und Mechanik," *Z. Phys.*, vol. 43, pp. 172–198, 1927. (cited on page2.)

[16] W. Pauli, "Über den zusammenhang des Abschlusses der Elektronengruppen im Atom mit der Komplexstruktur der Spektren," *Zeitschrift für Physik*, vol. 31, no. 1, pp. 765–783, 1925. (cited on page2.)

[17] F. Kröger and H. Vink, "Relations between the concentrations of imperfections in crystalline solids," in *Solid State Physics*. Elsevier, 1956, vol. 3, pp. 307–435. (cited on page7.)

[18] A. Zunger, "Practical Doping Principles," *Applied Physics Letters*, vol. 83, no. 1, pp. 57–59, 2003. (cited on page9.)

[19] S. Zhang, S.-H. Wei, and A. Zunger, "A Phenomenological Model for Systematization and Prediction of Doping Limits in II–VI and I–III–VI_2 Compounds," *Journal of Applied Physics*, vol. 83, no. 6, pp. 3192–3196, 1998. (cited on page9.)

[20] J. Robertson and S. Clark, "Limits to Doping in Oxides," *Physical Review B*, vol. 83, no. 7, p. 075205, 2011. (cited on pages 11 and 16.)

[21] M. V. Frischbier, H. F. Wardenga, M. Weidner, O. Bierwagen, J. Jia, Y. Shigesato, and A. Klein, "Influence of Dopant Species and Concentration on Grain Boundary Scattering in Degenerately Doped In_2O_3 Thin Films," *Thin Solid Films*, vol. 614, pp. 62–68, 2016. (cited on pages 15, 109, 112, 116, 120, 122, and 124.)

[22] G. Masetti, M. Severi, and S. Solmi, "Modeling of Carrier Mobility Against Carrier Concentration in Arsenic-, Phosphorus-, and Boron-Doped Silicon," *IEEE Transactions on Electron Devices*, vol. 30, no. 7, pp. 764–769, 1983. (cited on pages 15 and 23.)

[23] D. Chattopadhyay and H. Queisser, "Electron Scattering by Ionized Impurities in Semiconductors," *Reviews of Modern Physics*, vol. 53, no. 4, p. 745, 1981. (cited on pages 15 and 23.)

[24] K. L. Hoyer, A. H. Hubmann, and A. Klein, "Influence of dopant segregation on the work function and electrical properties of Ge-doped in comparison to Sn-doped In_2O_3 thin films," *Physica Status Solidi (a)*, vol. 214, no. 2, p. 1600486, 2017. (cited on page15.)

[25] S. Zhang and J. E. Northrup, "Chemical Potential Dependence of Defect Formation Energies in GaAs: Application to Ga Self-Diffusion," *Physical Review Letters*, vol. 67, no. 17, p. 2339, 1991. (cited on pages 16 and 18.)

[26] S. Zhang, S.-H. Wei, and A. Zunger, "A Phenomenological Model for Systematization and Prediction of Doping Limits in II–VI and I–III–VI_2 Compounds," *Journal of Applied Physics*, vol. 83, no. 6, pp. 3192–3196, 1998. (cited on page16.)

[27] P. Ágoston, P. Erhart, A. Klein, and K. Albe, "Geometry, Electronic Structure and Thermodynamic Stability of Intrinsic Point Defects in Indium Oxide," *Journal of Physics: Condensed Matter*, vol. 21, no. 45, p. 455801, 2009. (cited on pages 17, 18, 50, 140, and 142.)

[28] S. Lany and A. Zunger, "Dopability, Intrinsic Conductivity, and Nonstoichiometry of Transparent Conducting Oxides," *Physical Review Letters*, vol. 98, no. 4, p. 045501, 2007. (cited on pages 18 and 50.)

[29] P. Ágoston, C. Körber, A. Klein, M. J. Puska, R. M. Nieminen, and K. Albe, "Limits For n-Type Doping in In_2O_3 and SnO_2: A Theoretical Approach by First-Principles Calculations Using Hybrid-Functional Methodology," *Journal of Applied Physics*, vol. 108, no. 5, p. 053511, 2010. (cited on page18.)

[30] G. González, T. Mason, J. Quintana, O. Warschkow, D. E. Ellis, J.-H. Hwang, J. P. Hodges, and J. Jorgensen, "Defect Structure Studies of Bulk and Nano-Indium-Tin Oxide," *Journal of Applied Physics*, vol. 96, no. 7, pp. 3912–3920, 2004. (cited on pages 18 and 46.)

[31] N. Yamada, I. Yasui, Y. Shigesato, H. Li, Y. Ujihira, and K. Nomura, "Donor Compensation and Carrier-Transport Mechanisms in Tin-Doped In_2O_3 Films Studied by Means of Conversion electron Spectroscopy and Hall effect Measurements," *Japanese Journal of Applied Physics*, vol. 39, no. 7R, p. 4158, 2000. (cited on page18.)

[32] P. Erhart, K. Albe, and A. Klein, "First-Principles Study of Intrinsic Point Defects in ZnO: Role of Band Structure, Volume Relaxation, and Finite-Size Effects," *Physical Review B*, vol. 73, no. 20, p. 205203, 2006. (cited on page18.)

[33] S. w. Lee, Y.-W. Kim, and H. Chen, "Electrical Properties of Ta-doped SnO_2 Thin Films Prepared by The Metal–Organic Chemical-Vapor Deposition Method," *Applied Physics Letters*, vol. 78, no. 3, pp. 350–352, 2001. (cited on page18.)

[34] H. Ohta, M. Orita, M. Hirano, H. Tanji, H. Kawazoe, and H. Hosono, "Highly Electrically Conductive Indium–Tin– Oxide Thin Films Epitaxially Grown on Yttria-Stabilized Zirconia (100) By Pulsed-Laser Deposition," *Applied Physics Letters*, vol. 76, no. 19, pp. 2740–2742, 2000. (cited on pages 18 and 36.)

[35] Y. Gassenbauer, R. Schafranek, A. Klein, S. Zafeiratos, M. Hävecker, A. Knop-Gericke, and R. Schlögl, "Surface States, Surface Potentials, and Segregation at Surfaces of Tin-Doped In_2O_3," *Physical Review B*, vol. 73, no. 24, p. 245312, 2006. (cited on pages 18, 47, 106, 109, 124, 136, 137, and 143.)

[36] P. Cox, R. Egdell, C. Harding, W. Patterson, and P. Tavener, "Surface Properties of Antimony Doped Tin (IV) Oxide: S Study by Electron Spectroscopy," *Surface Science*, vol. 123, no. 2-3, pp. 179–203, 1982. (cited on page18.)

[37] I. Sieber, N. Wanderka, I. Urban, I. Dörfel, E. Schierhorn, F. Fenske, and W. Fuhs, "Electron Microscopic Characterization of Reactively Sputtered ZnO Films with Different Al-Doping Levels," *Thin Solid Films*, vol. 330, no. 2, pp. 108–113, 1998. (cited on page18.)

[38] T. J. Bayer, A. Wachau, A. Fuchs, J. Deuermeier, and A. Klein, "Atomic Layer Deposition of Al_2O_3 onto Sn-doped In_2O_3: Absence of Self-Limited Adsorption During Initial Growth by Oxygen Diffusion From The Substrate and Band Offset Modification By Fermi Level Pinning in Al_2O_3 ," *Chemistry of Materials*, vol. 24, no. 23, pp. 4503–4510, 2012. (cited on pages 18, 19, 41, 42, 70, 71, 72, 106, 107, 108, 136, 137, 139, 144, and 242.)

[39] D. S. Ginley and J. D. Perkins, "Handbook of Transparent Conductors." Springer, 2011. (cited on pages 20, 21, 22, and 24.)

[40] J. Y. Seto, "The Electrical Properties of Polycrystalline Silicon Films," *Journal of Applied Physics*, vol. 46, no. 12, pp. 5247–5254, 1975. (cited on pages 20, 21, 22, and 112.)

[41] G. Baccarani, B. Ricco, and G. Spadini, "Transport Properties of Polycrystalline Silicon Films," *Journal of Applied Physics*, vol. 49, no. 11, pp. 5565–5570, 1978. (cited on pages 21 and 22.)

[42] T. Kamins, "Polycrystalline Silicon For Integrated Circuit Applications," *Boston/Dordrecht/Lancaster*, pp. 158–159, 1988. (cited on page22.)

[43] E. Conwell and V. Weisskopf, "Theory of Impurity Scattering in Semiconductors," *Physical Review*, vol. 77, no. 3, p. 388, 1950. (cited on pages 22 and 23.)

[44] W. Zawadzki, *Mechanisms of Electron Scattering in Semiconductors*. Zakład Narodowy imienia Ossolińskich Wydawnictwo Polskiej Akademii Nauk, 1979. (cited on page22.)

[45] T. Pisarkiewicz, K. Zakrzewska, and E. Leja, "Scattering of Charge Carriers in Transparent and Conducting Thin Oxide Films With a Non-Parabolic Conduction Band," *Thin Solid Films*, vol. 174, pp. 217–223, 1989. (cited on page22.)

[46] J. Bellingham, W. Phillips, and C. Adkins, "Intrinsic Performance Limits in Transparent Conducting Oxides," *Journal of Materials Science Letters*, vol. 11, no. 5, pp. 263–265, 1992. (cited on page23.)

[47] W. Shockley *et al.*, *Electrons and Holes in Semiconductors: With Applications to Transistor Electronics*. van Nostrand New York, 1950. (cited on page23.)

[48] I. Dakhovsky, T. Polyanskaya, A. Samoilovich, and Y. Shmartsev, "Electron Mobilty in Heavly Doped Semiconductors," *Sov Phys Semiconductors*, vol. 4, no. 11, pp. 1857–1861, 1971. (cited on page23.)

[49] D. Klaassen, "A Unified Mobility Model For Device Simulation—I. Model Equations and Concentration Dependence," *Solid-State Electronics*, vol. 35, no. 7, pp. 953–959, 1992. (cited on page23.)

[50] P. Ebert, T. Zhang, F. Kluge, M. Simon, Z. Zhang, and K. Urban, "Importance of Many-Body Effects in The Clustering of Charged Zn Dopant Atoms in GaAs," *Physical Review Letters*, vol. 83, no. 4, p. 757, 1999. (cited on page23.)

[51] C. Erginsoy, "Neutral Impurity Scattering in Semiconductors," *Physical Review*, vol. 79, no. 6, p. 1013, 1950. (cited on page24.)

[52] K. Ellmer and R. Mientus, "Carrier Transport in Polycrystalline Transparent Conductive Oxides: A Comparative Study of Zinc Oxide and Indium Oxide," *Thin Solid Films*, vol. 516, no. 14, pp. 4620–4627, 2008. (cited on page24.)

[53] D. Dexter and F. Seitz, "Effects of dislocations on mobilities in semiconductors," *Physical Review*, vol. 86, no. 6, p. 964, 1952. (cited on page24.)

[54] B. Pödör, "Electron Mobility in Plastically Deformed Germanium," *physica Status Solidi (b)*, vol. 16, no. 2, 1966. (cited on page24.)

[55] D. S. Ginley, H. Hosono, D. C. Paine *et al.*, "Handbook of transparent conductors," 2010. (cited on pages 25 and 30.)

[56] J. Bardeen and W. Shockley, "Deformation Potentials and Mobilities in Non-polar crystals," *Physical Review*, vol. 80, no. 1, p. 72, 1950. (cited on page25.)

[57] J. D. Zook, "Piezoelectric Scattering in Semiconductors," *Physical Review*, vol. 136, no. 3A, p. A869, 1964. (cited on page26.)

[58] N. Preissler, O. Bierwagen, A. T. Ramu, and J. S. Speck, "Electrical Transport, Electrothermal Transport, and Effective Electron Mass in Single-Crystalline In_2O_3 Films," *Physical Review B*, vol. 88, no. 8, p. 085305, 2013. (cited on pages 26, 27, 112, and 122.)

[59] E. Burstein, "Anomalous Optical Absorption Limit in InSb," *Physical Review*, vol. 93, no. 3, p. 632, 1954. (cited on page27.)

[60] H. Liu, V. Avrutin, N. Izyumskaya, Ü. Özgür, and H. Morkoç, "Transparent Conducting Oxides for Electrode Applications in Light Emitting and Absorbing Devices," *Superlattices and Microstructures*, vol. 48, no. 5, pp. 458–484, 2010. (cited on page28.)

[61] I. Hamberg and C. G. Granqvist, "Evaporated Sn-doped In_2O_3 Films: Basic Optical Properties and Applications to Energy-Efficient Windows," *Journal of Applied Physics*, vol. 60, no. 11, pp. R123–R160, 1986. (cited on pages 29 and 136.)

[62] M. Oshima, Y. Takemoto, and K. Yoshino, "Optical and Electrical Characterization of FTO Films Grown by Spray Pyrolysis Method," *Physica Status Solidi c*, vol. 6, no. 5, pp. 1124–1126, 2009. (cited on page28.)

[63] B.-Z. Dong, H. Hu, G.-J. Fang, X.-Z. Zhao, D.-Y. Zheng, and Y.-P. Sun, "Comprehensive Investigation of Structural, Electrical, and Optical Properties for ZnO: Al Films Deposited at Different Substrate Temperature and Oxygen Ambient," *Journal of Applied Physics*, vol. 103, no. 7, p. 073711, 2008. (cited on page28.)

[64] S. Shirakata, T. Sakemi, K. Awai, and T. Yamamoto, "Electrical and Optical Properties of Large Area Ga-doped ZnO Thin Films Prepared by Reactive Plasma Deposition," *Superlattices and Microstructures*, vol. 39, no. 1-4, pp. 218–228, 2006. (cited on page28.)

[65] Y. Yang, S. Jin, J. E. Medvedeva, J. R. Ireland, A. W. Metz, J. Ni, M. C. Hersam, A. J. Freeman, and T. J. Marks, "CdO as The Archetypical Transparent Conducting Oxide. Systematics of Dopant Ionic Radius and Electronic Structure Effects on Charge Transport and Band Structure," *Journal of The American Chemical Society*, vol. 127, no. 24, pp. 8796–8804, 2005. (cited on page28.)

[66] K. Ellmer, A. Klein, and B. Rech, *Transparent Conductive Zinc Oxide: Basics and Applications in Thin Film Solar Cells. Springer Series in MaterialsS cience, 104*. Springer, 2008. (cited on page29.)

[67] C. G. Granqvist, "Transparent conductors as solar energy materials: A panoramic review," *Solar Energy Materials and Solar Cells*, vol. 91, no. 17, pp. 1529–1598, 2007. (cited on page30.)

[68] N. Yamazoe, J. Fuchigami, M. Kishikawa, and T. Seiyama, "Interactions of tin oxide surface with O_2, H_2O and H_2," *Surface Science*, vol. 86, pp. 335–344, 1979. (cited on page30.)

[69] N. Barsan, D. Koziej, and U. Weimar, "Metal oxide-based gas sensor research: How to?" *Sensors and Actuators B: Chemical*, vol. 121, no. 1, pp. 18–35, 2007. (cited on page30.)

[70] L. L. Chang and K. Ploog, *Molecular Beam Epitaxy and Heterostructures*. Springer Science & Business Media, 2012, vol. 87. (cited on pages 32 and 33.)

[71] R. Dingle, *Semiconductors and Semimetals: Applications of Multiquantum Wells, Selective Doping, and Superlattices.* Academic Press, 1988. (cited on page33.)

[72] M. Henini, *Molecular Beam Epitaxy: From Research to Mass Production.* Newnes, 2012. (cited on page33.)

[73] J. Wiley, "Semiconductors and Semimetals Transport Phenomena," *Academic, New York*, vol. 10, 1975. (cited on page34.)

[74] S. Calnan and A. Tiwari, "High Mobility Transparent Conducting Oxides For Thin Film Solar Cells," *Thin Solid Films*, vol. 518, no. 7, pp. 1839–1849, 2010. (cited on page35.)

[75] G. J. Exarhos and X.-D. Zhou, "Discovery-Based Design of Transparent Conducting Oxide Films," *Thin Solid Films*, vol. 515, no. 18, pp. 7025–7052, 2007. (cited on page35.)

[76] Y. Shigesato, S. Takaki, and T. Haranoh, "Electrical and Structural Properties of Low Resistivity Tin-Doped Indium Oxide Films," *Journal of Applied Physics*, vol. 71, no. 7, pp. 3356–3364, 1992. (cited on page36.)

[77] K. Ellmer, "Magnetron Sputtering of Transparent Conductive Zinc Oxide: Relation Between The Sputtering Parameters and The Electronic Properties," *Journal of Physics D: Applied Physics*, vol. 33, no. 4, p. R17, 2000. (cited on page36.)

[78] M. Lorenz, E. Kaidashev, H. Von Wenckstern, V. Riede, C. Bundesmann, D. Spemann, G. Benndorf, H. Hochmuth, A. Rahm, H.-C. Semmelhack *et al.*, "Optical and Electrical Properties of Epitaxial (Mg, Cd)$_X$Zn$_{1-X}$O, ZnO, and ZnO:(Ga, Al) Thin Films on C-Plane Sapphire Grown by Pulsed Laser Deposition," *Solid-State Electronics*, vol. 47, no. 12, pp. 2205–2209, 2003. (cited on page36.)

[79] T. Koida, H. Fujiwara, and M. Kondo, "Reduction of Optical Loss in Hydrogenated Amorphous Silicon/Crystalline Silicon Heterojunction Solar Cells By High-Mobility Hydrogen-Doped In_2O_3 Ttransparent Conductive Oxide," *Applied Physics Express*, vol. 1, no. 4, p. 041501, 2008. (cited on page36.)

[80] C. H. Mueller, E. T. Croke, and S. A. Alterovitz, "High Electron Mobility in SiGe/Si n-MODFET Structures on Sapphire Substrates," *Electronics Letters*, vol. 39, no. 18, pp. 1353–1354, 2003. (cited on page36.)

[81] S. Gökden, "Mobility of Two-Dimensional Electrons in an AlGaN/GaN Modulation-Doped Heterostructure," *Physica Status Solidi (a)*, vol. 200, no. 2, pp. 369–377, 2003. (cited on page36.)

[82] K. Ellmer, "Resistivity of Polycrystalline Zinc Oxide Films: Current Status and Physical Limit," *Journal of Physics D: Applied Physics*, vol. 34, no. 21, p. 3097, 2001. (cited on page36.)

[83] K. Ellmer and G. Vollweiler, "Electrical Transport Parameters of Heavily-Doped Zinc Oxide and Zinc Magnesium Oxide Single and Multilayer Films Heteroepitaxially Grown on Oxide Single Crystals," *Thin Solid Films*, vol. 496, no. 1, pp. 104–111, 2006. (cited on pages 36 and 37.)

[84] I. Rauf, "Low Resistivity and High Mobility Tin-Doped Indium Oxide Films," *Materials Letters*, vol. 18, no. 3, pp. 123–127, 1993. (cited on page37.)

[85] Rauf, IA, "A Novel Method For Preparing Thin Films With Selective Doping in A Single Evaporation Step," *Journal of Materials Science Letters*, vol. 12, no. 24, pp. 1902–1905, 1993. (cited on page37.)

[86] D. Cohen and S. Barnett, "Predicted Electrical Properties of Modulation-Doped ZnO-Based Transparent conducting Oxides," *Journal of Applied Physics*, vol. 98, no. 5, p. 053705, 2005. (cited on pages 37, 38, and 39.)

[87] J. J. Robbins and C. A. Wolden, "High Mobility Oxides: Engineered Structures to Overcome Intrinsic Performance Limitations of Transparent Conducting Oxides," *Applied Physics Letters*, vol. 83, no. 19, pp. 3933–3935, 2003. (cited on page39.)

[88] H. Chin, I. Cheng, C. Li, Y. Wu, J. Chen, W. Lu, and W. Lee, "Electrical Properties of Modulation-Doped RF-Sputtered Polycrystalline MgZnO/ZnO Heterostructures," *Journal of Physics D: Applied Physics*, vol. 44, no. 45, p. 455101, 2011. (cited on page39.)

[89] R. Schafranek, S. Li, F. Chen, W. Wu, and A. Klein, "$PbTiO_3/SrTiO_3$ interface: energy band alignment and its relation to the limits of fermi level variation," *Physical Review B*, vol. 84, no. 4, p. 045317, 2011. (cited on page40.)

[90] Y.-J. Zhao, C. Persson, S. Lany, and A. Zunger, "Why can $CuInSe_2$ be readily equilibrium-doped n-type but the wider-gap $CuGaSe_2$ cannot?" *Applied Physics Letters*, vol. 85, no. 24, pp. 5860–5862, 2004. (cited on page40.)

[91] C. Körber, V. Krishnakumar, A. Klein, G. Panaccione, P. Torelli, A. Walsh, J. Da Silva, S.-H. Wei, R. Egdell, and D. Payne, "Electronic structure of In_2O_3 and sn-doped In_2O_3 by hard x-ray photoemission spectroscopy," *Physical Review B*, vol. 81, no. 16, p. 165207, 2010. (cited on page40.)

[92] K. Zhang, R. Egdell, F. Offi, S. Iacobucci, L. Petaccia, S. Gorovikov, and P. King,

"Microscopic origin of electron accumulation in In_2O_3," *Physical Review Letters*, vol. 110, no. 5, p. 056803, 2013. (cited on page41.)

[93] M. Weidner, J. Brötz, and A. Klein, "Sputter-deposited polycrystalline tantalum-doped SnO_2 layers," *Thin Solid Films*, vol. 555, pp. 173–178, 2014. (cited on page41.)

[94] J. Deuermeier, T. J. Bayer, H. Yanagi, A. Kiazadeh, R. Martins, A. Klein, and E. Fortunato, "Substrate reactivity as the origin of fermi level pinning at the Cu_2O/ALD-Al_2O_3 interface," *Materials Research Express*, vol. 3, no. 4, p. 046404, 2016. (cited on pages 41, 108, and 139.)

[95] S. Hillmann, K. Rachut, T. J. Bayer, S. Li, and A. Klein, "Application of atomic layer deposited Al_2O_3 as charge injection layer for high-permittivity dielectrics," *Semiconductor Science and Technology*, vol. 30, no. 2, p. 024012, 2015. (cited on pages 41, 108, 136, and 139.)

[96] J. Weber, A. Janotti, and C. Van de Walle, "Native Defects in Al_2O_3 and Their Impact on III-V/Al_2O_3 Metal-Oxide-Semiconductor-Based Devices," *Journal of Applied Physics*, vol. 109, no. 3, p. 033715, 2011. (cited on pages 41, 61, 151, and 170.)

[97] A. Klein, "Energy band alignment in chalcogenide thin film solar cells from photoelectron spectroscopy," *Journal of Physics: Condensed Matter*, vol. 27, no. 13, p. 134201, 2015. (cited on page42.)

[98] S. Li, F. Chen, R. Schafranek, T. J. Bayer, K. Rachut, A. Fuchs, S. Siol, M. Weidner, M. Hohmann, V. Pfeifer *et al.*, "Intrinsic Energy Band Alignment of Functional Oxides," *Physica Status Solidi (RRL)-Rapid Research Letters*, vol. 8, no. 6, pp. 571–576, 2014. (cited on pages 42, 108, and 139.)

[99] M. Marezio, "Refinement of The Crystal Structure of In_2O_3 at Two Wavelengths," *Acta Crystallographica*, vol. 20, no. 6, pp. 723–728, 1966. (cited on page45.)

[100] H. Hosono and D. C. Paine, *Handbook of Transparent Conductors*. Springer Science & Business Media, 2010. (cited on page46.)

[101] S. Z. Karazhanov, P. Ravindran, P. Vajeeston, A. Ulyashin, T. Finstad, and H. Fjellvåg, "Phase Stability, Electronic Structure, and Optical Properties of Indium Oxide Polytypes," *Physical Review B*, vol. 76, no. 7, p. 075129, 2007. (cited on page46.)

[102] R. Shannon, "New High Pressure Phases Having the Corundum Structure," *Solid*

State Communications, vol. 4, no. 12, pp. 629–630, 1966. (cited on page46.)

[103] A. Reid and A. Ringwood, "High-Pressure Scandium Oxide and Its Place in The Molar Volume Relationships of Dense Structures of M_2X_3 and ABX_3 type," *Journal of Geophysical Research*, vol. 74, no. 12, pp. 3238–3252, 1969. (cited on page46.)

[104] C. T. Prewitt, R. D. Shannon, D. B. Rogers, and A. W. Sleight, "C Rare Earth Oxide-Corundum Transition and Crystal Chemistry of Oxides Having The Corundum Structure," *Inorganic Chemistry*, vol. 8, no. 9, pp. 1985–1993, 1969. (cited on page46.)

[105] M. Sorescu, L. Diamandescu, D. Tarabasanu-Mihaila, and V. Teodorescu, "Nanocrystalline Rhombohedral In_2O_3 Synthesized by Hydrothermal and Postannealing Pathways," *Journal of Materials Science*, vol. 39, no. 2, pp. 675–677, 2004. (cited on page46.)

[106] A. Gurlo, P. Kroll, and R. Riedel, "Metastability of Corundum-Type In_2O_3," *Chemistry-a European Journal*, vol. 14, no. 11, pp. 3306–3310, 2008. (cited on page46.)

[107] P. Parent, H. Dexpert, G. Tourillon, and J.-M. Grimal, "Structural Study of Tin-Doped Indium Oxide Thin Films Using X-Ray Absorption Spectroscopy and X-Ray Ddiffraction I. Description of The Indium Site," *Journal of The Electrochemical Society*, vol. 139, no. 1, pp. 276–281, 1992. (cited on page47.)

[108] A. Walsh, J. L. Da Silva, S.-H. Wei, C. Körber, A. Klein, L. Piper, A. DeMasi, K. E. Smith, G. Panaccione, P. Torelli *et al.*, "Nature of The Band Gap of In_2O_3 Revealed by First-Principles Calculations and X-Ray Spectroscopy," *Physical Review Letters*, vol. 100, no. 16, p. 167402, 2008. (cited on pages 47, 48, 106, 138, 139, 157, and 165.)

[109] R. Weiher and R. Ley, "Optical Properties of Indium Oxide," *Journal of Applied Physics*, vol. 37, no. 1, pp. 299–302, 1966. (cited on pages 47 and 48.)

[110] A. Klein, "Electronic Properties of In_2O_3 Surfaces," *Applied Physics Letters*, vol. 77, no. 13, pp. 2009–2011, 2000. (cited on pages 47 and 139.)

[111] V. Scherer, C. Janowitz, A. Krapf, H. Dwelk, D. Braun, and R. Manzke, "Transport and Angular Resolved Photoemission Measurements of The Electronic Properties of In_2O_3 Bulk Single Crystals," *Applied Physics Letters*, vol. 100, no. 21, p. 212108, 2012. (cited on page47.)

[112] O. Mryasov and A. Freeman, "Electronic Band Structure of Indium Tin Oxide and Criteria For Transparent Conducting Behavior," *Physical Review B*, vol. 64, no. 23, p. 233111, 2001. (cited on page48.)

[113] P. Erhart, A. Klein, R. G. Egdell, and K. Albe, "Band Structure of Indium Oxide: Indirect Versus Direct Band Gap," *Physical Review B*, vol. 75, no. 15, p. 153205, 2007. (cited on page48.)

[114] F. Fuchs and F. Bechstedt, "Indium-Oxide Polymorphs From First Principles: Quasiparticle electronic states," *Physical Review B*, vol. 77, no. 15, p. 155107, 2008. (cited on pages 48, 157, and 165.)

[115] "Electrical Properties of In_2O_3, author=De Wit, JHW, journal=Journal of Solid State Chemistry, volume=8, number=2, pages=142–149, year=1973, publisher=Elsevier." (cited on page48.)

[116] J. De Wit, G. Van Unen, and M. Lahey, "Electron Concentration and Mobility in In_2O_3," *Journal of Physics and Chemistry of Solids*, vol. 38, no. 8, pp. 819–824, 1977. (cited on pages 48, 140, and 167.)

[117] J. De Wit, "The High Temperature Behavior of In_2O_3," *Journal of Solid State Chemistry*, vol. 13, no. 3, pp. 192–200, 1975. (cited on pages 48, 140, and 167.)

[118] R. Weiher, "Electrical Properties of Single Crystals of Indium Oxide," *Journal of Applied Physics*, vol. 33, no. 9, pp. 2834–2839, 1962. (cited on page48.)

[119] J. De Wit, "Structural Aspects and Defect Chemistry in In_2O_3," *Journal of Solid State Chemistry*, vol. 20, no. 2, pp. 143–148, 1977. (cited on page50.)

[120] G. B. González, "Investigating the Defect Structures in Transparent Cconducting Oxides Using X-ray and Neutron Scattering Techniques," *Materials*, vol. 5, no. 5, pp. 818–850, 2012. (cited on page50.)

[121] P. Ágoston and K. Albe, "Formation Entropies of Intrinsic Point Defects in Cubic In_2O_3 From First-Principles Density Functional Theory Calculations," *Physical Chemistry Chemical Physics*, vol. 11, no. 17, pp. 3226–3232, 2009. (cited on page50.)

[122] P. Ágoston, K. Albe, R. M. Nieminen, and M. J. Puska, "Intrinsic n-Type Behavior in Transparent Conducting Oxides: A Comparative Hybrid-Functional Study of In_2O_3 , SnO_2, and ZnO," *Physical Review Letters*, vol. 103, no. 24, p. 245501, 2009. (cited on pages 50, 57, and 212.)

[123] A. Gassmann, S. V. Yampolskii, A. Klein, K. Albe, N. Vilbrandt, O. Pekkola, Y. A. Genenko, M. Rehahn, and H. von Seggern, “Study of Electrical Fatigue by Defect Engineering in Organic Light-Emitting diodes,” *Materials Science and Engineering: B*, vol. 192, pp. 26–51, 2015. (cited on pages 51 and 140.)

[124] “Determination of The Solubility of Tin in Indium Oxide Using In Situ and Ex Situ X-Ray Diffraction, author=Gonzalez, GB and Mason, TO and Okasinski, JS and Buslaps, T and Honkimaki, V,” *Journal of the American Ceramic Society*, vol. 95, no. 2, pp. 809–815, 2012. (cited on page50.)

[125] G. Frank and H. Köstlin, “Electrical Properties and Defect Model of Tin-Doped Indium Oxide Layers,” *Applied Physics A*, vol. 27, no. 4, pp. 197–206, 1982. (cited on page51.)

[126] J.-H. Hwang, D. Edwards, D. Kammler, and T. Mason, “Point Defects and Electrical Properties of Sn-oped In-Based Transparent Conducting Oxides,” *Solid State Ionics*, vol. 129, no. 1-4, pp. 135–144, 2000. (cited on pages 52 and 53.)

[127] L. Gracia, A. Beltrán, and J. Andrés, “Characterization of The High-Pressure Structures and Phase Transformations in SnO_2. A Density Functional Theory Study,” *The Journal of Physical Chemistry B*, vol. 111, no. 23, pp. 6479–6485, 2007. (cited on page55.)

[128] W. H. Baur, “Über die verfeinerung der kristallstrukturbestimmung einiger vertreter des rutiltyps: TiO_2, SnO_2, GeO_2 und MgF_2,” *Acta Crystallographica*, vol. 9, no. 6, pp. 515–520, 1956. (cited on page54.)

[129] O. Byl and J. T. Yates, “Anisotropy in The Electrical Conductivity of Rutile TiO_2 in The (110) Plane,” *The JJournal of Physical Chemistry B*, vol. 110, no. 46, pp. 22 966–22 967, 2006. (cited on page54.)

[130] E. Chao, J. Fahey, J. Littler, and D. Milton, “Stishovite, SiO_2, a Very High Pressure New Mineral From Meteor Crater, Arizona,” *Journal of Geophysical Research*, vol. 67, no. 1, pp. 419–421, 1962. (cited on page54.)

[131] S. Das and V. Jayaraman, “SnO_2: A Comprehensive Review on Structures and Gas Sensors,” *Progress in Materials Science*, vol. 66, pp. 112–255, 2014. (cited on page55.)

[132] A. Schleife, J. Varley, F. Fuchs, C. Rödl, F. Bechstedt, P. Rinke, A. Janotti, and C. Van de Walle, “Tin Dioxide From First Principles: Quasiparticle Electronic States and Optical Properties,” *Physical Review B*, vol. 83, no. 3, p. 035116, 2011. (cited on pages 55, 56, and 209.)

[133] D. Fröhlich, R. Kenklies, and R. Helbig, “Band-Gapa ssignment in SnO_2 by Two-Photon Spectroscopy,” *Physical Review Letters*, vol. 41, no. 25, p. 1750, 1978. (cited on pages 55, 56, and 209.)

[134] T. Nagata, O. Bierwagen, M. E. White, M.-Y. Tsai, and J. S. Speck, “Study of The Au Schottky Contact Formation on Oxygen Plasma Treated n-Type SnO_2 (101) Thin Films,” *Journal of Applied Physics*, vol. 107, no. 3, p. 033707, 2010. (cited on pages 55, 56, and 209.)

[135] H. Odaka, S. Iwata, N. Taga, S. Ohnishi, Y. Kaneta, and Y. Shigesato, “Study on Electronic Structure and Optoelectronic Properties of Indium Oxide by First-Principles Calculations,” *Japanese Journal of Applied Physics*, vol. 36, no. part 1, pp. 5551–5554, 1997. (cited on page55.)

[136] P. Barbarat and S. Matar, “First-Principles Investigations of The Electronic, Optical and Chemical Bonding Properties of SnO_2,” *Computational Materials Science*, vol. 10, no. 1-4, pp. 368–372, 1998. (cited on page56.)

[137] K. Mishra, K. Johnson, and P. Schmidt, “Electronic Structure of Antimony-Doped Tin oxide,” *Physical Review B*, vol. 51, no. 20, p. 13972, 1995. (cited on page56.)

[138] W. Göpel, K. Schierbaum, H.-D. Wiemhöfer, and J. Maier, “Defect Chemistry of Tin (IV)-Oxide in Bulk and Boundary Layers,” *Solid State Ionics*, vol. 32, pp. 440–443, 1989. (cited on page57.)

[139] J. Maier and W. Göpel, “Investigations of The Bulk Defect Chemistry of Polycrystalline tin (IV) Oxide,” *Journal of Solid State Chemistry*, vol. 72, no. 2, pp. 293–302, 1988. (cited on page57.)

[140] S. Samson and C. Fonstad, “Defect Structure and Electronic Donor Levels in Stannic Oxide Crystals,” *Journal of Applied Physics*, vol. 44, no. 10, pp. 4618–4621, 1973. (cited on page57.)

[141] Lee, Choong-Ki and Cho, Eunae and Lee, Hyo-Sug and Seol, Kwang Soo and Han, Seungwu, “Comparative Study of Electronic Structures and Dielectric Properties of Alumina Polymorphs by First-Principles Methods,” *Physical Review B*, vol. 76, no. 24, p. 245110, 2007. (cited on pages 58 and 60.)

[142] K. Wefers and C. Misra, “Oxides and Hydroxides of Aluminum,” 1987. (cited on page59.)

[143] M. Kronberg, “Plastic Deformation of Single Crystals of Sapphire: Basal Slip and Twinning,” *Acta Metallurgica*, vol. 5, no. 9, pp. 507–524, 1957. (cited on page59.)

[144] J. Bilde-Sørensen, B. Lawlor, T. Geipel, P. Pirouz, A. Heuer, K. Lagerlo *et al.*, "On Basal Slip and Basal Twinning in Sapphire (α-Al_2O_3)—I. Basal Slip Revisited," *Acta Materialia*, vol. 44, no. 5, pp. 2145–2152, 1996. (cited on page59.)

[145] A. Bourdillon, S. El-Mashri, and A. Forty, "Application of TEM Extended Electron Energy Loss Fine Structure to The Study of Aluminium Oxide Films," *Philosophical Magazine A*, vol. 49, no. 3, pp. 341–352, 1984. (cited on page59.)

[146] I. Levin and D. Brandon, "Metastable Alumina Polymorphs: Crystal Structures and Transition Sequences," *Journal of The American Ceramic Society*, vol. 81, no. 8, pp. 1995–2012, 1998. (cited on page59.)

[147] D. Liu, S. Clark, and J. Robertson, "Oxygen Vacancy Levels and Electron Transport in Al_2O_3," *Applied Physics Letters*, vol. 96, no. 3, p. 032905, 2010. (cited on page60.)

[148] R. H. French, "Electronic Band Structure of Al_2O_3, with Comparison to Alon and AIN," *Journal of The American Ceramic Society*, vol. 73, no. 3, pp. 477–489, 1990. (cited on page60.)

[149] H. Momida, T. Hamada, Y. Takagi, T. Yamamoto, T. Uda, and T. Ohno, "Theoretical Study on Dielectric Response of Amorphous Alumina," *Physical Review B*, vol. 73, no. 5, p. 054108, 2006. (cited on page60.)

[150] E. O. Filatova and A. S. Konashuk, "Interpretation of the changing the band gap of Al_2O_3 depending on its crystalline form: connection with different local symmetries," *The Journal of Physical Chemistry C*, vol. 119, no. 35, pp. 20 755–20 761, 2015. (cited on page60.)

[151] B. Ealet, M. Elyakhloufi, E. Gillet, and M. Ricci, "Electronic and crystallographic structure of γ-alumina thin films," *Thin Solid Films*, vol. 250, no. 1-2, pp. 92–100, 1994. (cited on page60.)

[152] V. Afanas' ev, M. Houssa, A. Stesmans, and M. Heyns, "Band Alignments in Metal–Oxide–Silicon Structures with Atomic-Layer Deposited Al_2O_3 and ZrO_2," *Journal of Applied Physics*, vol. 91, no. 5, pp. 3079–3084, 2002. (cited on page61.)

[153] M. Aguilar-Frutis, M. Garcia, and C. Falcony, "Optical and electrical properties of aluminum oxide films deposited by spray pyrolysis," *Applied Physics Letters*, vol. 72, no. 14, pp. 1700–1702, 1998. (cited on page61.)

[154] K. Wasa, M. Kitabatake, and H. Adachi, *Thin Film Materials Technology: Sputtering of Control Compound Materials.* Springer Science & Business Media, 2004.

(cited on page64.)

[155] M. Ohring, *Materials Science of Thin Films.* Elsevier, 2001. (cited on page64.)

[156] P. F. Michel, "Coating by Cathode Disintegration," Feb. 7 1939, uS Patent 2,146,025. (cited on page64.)

[157] K. Wasa and S. Hayakawa, "Low Pressure Sputtering System of The Magnetron Type," *Review of Scientific Instruments*, vol. 40, no. 5, pp. 693–697, 1969. (cited on page64.)

[158] J. S. Chapin, "The Planar Magnetron," *Research Development*, vol. 25, no. 1, pp. 37–40, 1974. (cited on page64.)

[159] Y. Gassenbauer, "Untersuchung der elektronischen und chemischen oberflächeneigenschaften von zinn-dotiertem indium-oxid im hinblick auf die funktion in organischen leuchtdioden," Ph.D. dissertation, TU Darmstadt, Berlin, January 2007. [Online]. Available: http://tubiblio.ulb.tu-darmstadt.de/29769/ (cited on page68.)

[160] R. L. Puurunen, "Surface Chemistry of Atomic Layer Deposition: A Case Study For The Trimethylaluminum/Water Process," *Journal of Applied Physics*, vol. 97, no. 12, p. 9, 2005. (cited on pages 67, 68, 70, 71, and 72.)

[161] T. Kääriäinen, D. Cameron, M.-L. Kääriäinen, and A. Sherman, *Atomic layer deposition: principles, characteristics, and nanotechnology applications.* John Wiley & Sons, 2013. (cited on page69.)

[162] V. Miikkulainen, M. Leskelä, M. Ritala, and R. L. Puurunen, "Crystallinity of Inorganic Films Grown By Atomic Layer Deposition: Overview and General Trends," *Journal of Applied Physics*, vol. 113, no. 2, p. 2, 2013. (cited on pages 70 and 72.)

[163] O. Sneh, R. B. Clark-Phelps, A. R. Londergan, J. Winkler, and T. E. Seidel, "Thin Film Atomic Layer Deposition Equipment for Semiconductor Processing," *Thin Solid Films*, vol. 402, no. 1-2, pp. 248–261, 2002. (cited on page72.)

[164] J. Viguie and J. Spitz, "Chemical Vapor Deposition at Low Temperatures," *J. Electrochem. Soc*, vol. 122, no. 4, pp. 585–588, 1975. (cited on pages 73 and 74.)

[165] W. Siefert, "Properties of Thin In_2O_3 and SnO_2 Films Prepared by Corona Spray Pyrolysis, and a Discussion of The Spray Pyrolysis Process," *Thin Solid Films*, vol. 120, no. 4, pp. 275–282, 1984. (cited on page74.)

[166] M. Girtan, H. Cachet, and G. Rusu, “On the physical properties of indium oxide thin films deposited by pyrosol in comparison with films deposited by pneumatic spray pyrolysis,” *Thin Solid Films*, vol. 427, no. 1-2, pp. 406–410, 2003. (cited on page75.)

[167] D. Zaouk, Y. Zaatar, A. Khoury, C. Llinares, J.-P. Charles, and J. Bechara, “Fabrication of tin oxide (SnO_2) thin film by electrostatic spray pyrolysis,” *Microelectronic Engineering*, vol. 51, pp. 627–631, 2000. (cited on page75.)

[168] G. Caccioppoli, B. Clausen, C. Bonjour, and P. Pralong, “Fabrication of Metal Powders by Ultrasonic Atomization,” *Materiaux*, vol. 100, pp. 1–4, 2002. (cited on page76.)

[169] E. Lierke and G. Griesshammer, “The Formation of Metal Powders by Ultrasonic Atomization of Molten Metals,” *Ultrasonics*, vol. 5, no. 4, pp. 224–228, 1967. (cited on page76.)

[170] B. Vukasinovic, M. K. Smith, and A. Glezer, “Mechanisms of Free-Surface Breakup in Vibration-Induced Liquid Atomization,” *Physics of Fluids*, vol. 19, no. 1, p. 012104, 2007. (cited on page76.)

[171] R. J. Lang, “Ultrasonic Atomization of Liquids,” *The journal of The Acoustical Society of America*, vol. 34, no. 1, pp. 6–8, 1962. (cited on page76.)

[172] S. Hüfner, “Photoelectron Spectroscopy: Principles and Applications,” 1995. (cited on pages 79 and 80.)

[173] H. Hertz, “Ueber einen einfluss des ultravioletten lichtes auf die electrische entladung,” *Annalen Der Physik*, vol. 267, no. 8, pp. 983–1000, 1887. (cited on page79.)

[174] A. Einstein, “Über einen die erzeugung und verwandlung des lichtes betreffenden heuristischen gesichtspunkt,” *Annalen Der Physik*, vol. 322, no. 6, pp. 132–148, 1905. (cited on pages 79 and 81.)

[175] K. Siegbahn and K. Edvarson, “β-Ray Spectroscopy in the Precision Range of 1: 105,” *Nuclear Physics*, vol. 1, no. 8, pp. 137–159, 1956. (cited on page79.)

[176] S. Hüfner, “Photoelectron Spectroscopyprinciples and Applications,” Tech. Rep., 2003. (cited on pages 79 and 104.)

[177] D. Woodruff and T. Delchar, “Modern Techniques of Surface Science,” 1994. (cited on page79.)

[178] M. Cardona and L. Ley, "Photoemission in Solids I," *Photoemission in Solids I: General Principles*, 1978. (cited on page79.)

[179] M. P. Seah and W. Dench, "Quantitative Electron Spectroscopy of Surfaces: A Standard Data Base For Electron Inelastic Mean Free Paths in Solids," *Surface and Interface Analysis*, vol. 1, no. 1, pp. 2–11, 1979. (cited on page82.)

[180] M. S. (eds.), *Practical Materials Characterization*, 1st ed. Springer-Verlag New York, 2014. (cited on pages 84, 85, and 86.)

[181] A. Guinier, *X-Ray Diffraction: In Crystals, Imperfect Crystals, and Amorphous Bodies*, 1st ed. Dover Publications, Paris, France, 1994. (cited on pages 84 and 85.)

[182] B. E. Warren, *X-ray Diffraction*. Dover Publications, Inc ..., New York, 1990. (cited on page85.)

[183] K. N. Stoev and K. Sakurai, "Review on Grazing Incidence X-ray Spectrometry and Reflectometry," *Spectrochimica Acta Part B: Atomic Spectroscopy*, vol. 54, no. 1, pp. 41–82, 1999. (cited on page86.)

[184] G. Harris, "X. quantitative Measurement of Preferred Orientation in Rolled Uranium Bars," *The London, Edinburgh, and Dublin Philosophical Magazine and Journal of Science*, vol. 43, no. 336, pp. 113–123, 1952. (cited on pages 86, 200, and 227.)

[185] P. D. File *et al.*, "Joint committee on Powder Diffraction Standards," *ASTM, Philadelphia, Pa*, pp. 9–185, 1967. (cited on page87.)

[186] P. D. L. R. (auth.), *Scanning Electron Microscopy: Physics of Image Formation and Microanalysis*, 2nd ed., ser. Springer Series in Optical Sciences 45. Springer-Verlag Berlin Heidelberg, 1998. (cited on pages 87 and 88.)

[187] A. Zoubir, *Raman Imaging: Techniques and Applications*. Springer, 2012, vol. 168. (cited on page89.)

[188] L. H. D. Norman B. Colthup and S. E. W. (Auth.), *Introduction to Infrared and Raman Spectroscopy*, 3rd ed. Academic Press, Boston, 1990. (cited on pages 89 and 90.)

[189] E. H. Hall, "On a new Action of The Magnet on Electric Currents," *American Journal of Mathematics*, vol. 2, no. 3, pp. 287–292, 1879. (cited on page91.)

[190] M. Grundmann, "The Physics of Semiconductors." 2010. (cited on page92.)

[191] D. A. Neamen, "Semiconductor Physics and Devices: Basic Principles," 2011. (cited on page92.)

[192] M. V. Hohmann, A. Wachau, and A. Klein, "In Iitu Hall Effect and Conductivity Measurements of ITO Thin Films," *Solid State Ionics*, vol. 262, pp. 636–639, 2014. (cited on pages 94, 114, and 124.)

[193] M. Frischbier, "Die elektrischen eigenschaften von indiumoxid-dünnschichten: in-situ hall-effekt-messungen zur aufklärung des einflusses von punktdefekten und korngrenzen," Ph.D. dissertation, Technische Universität Darmstadt, 2015. (cited on pages 91, 94, and 123.)

[194] L. Van der Pauw, "A Method of Measuring Specific Resistivity and hall effect of discs of arbitrary shape," *Philips Research Reports*, vol. 13, pp. 1–9, 1958. (cited on page94.)

[195] G. K. Deyu, J. Hunka, H. Roussel, J. Brötz, D. Bellet, and A. Klein, "Electrical properties of low-temperature processed sn-doped in_2o_3 thin films: The role of microstructure and oxygen content and the potential of defect modulation doping," *Materials*, vol. 12, no. 14, 2019. (cited on page102.)

[196] Y. Gassenbauer, A. Wachau, and A. Klein, "Chemical and electronic properties of the ITO/Al_2O_3 interface," *Physical Chemistry Chemical Physics*, vol. 11, no. 17, pp. 3049–3054, 2009. (cited on pages 106, 107, and 136.)

[197] J. F. Moulder, "Handbook of X-ray photoelectron spectroscopy," *Physical Electronics*, pp. 230–232, 1995. (cited on pages 106, 136, and 159.)

[198] Y. Gassenbauer and A. Klein, "Electronic and chemical properties of tin-doped indium oxide (ITO) surfaces and ITO/ZnPc interfaces studied in-situ by photoelectron spectroscopy," *The Journal of Physical Chemistry B*, vol. 110, no. 10, pp. 4793–4801, 2006. (cited on pages 106 and 136.)

[199] R. Egdell, J. Rebane, T. Walker, and D. Law, "Competition between initial-and final-state effects in valence-and core-level X-ray photoemission of Sb-doped SnO_2," *Physical Review B*, vol. 59, no. 3, p. 1792, 1999. (cited on pages 106 and 136.)

[200] V. Christou, M. Etchells, O. Renault, P. Dobson, O. Salata, G. Beamson, and R. Egdell, "High resolution X-ray photoemission study of plasma oxidation of indium–tin–oxide thin film surfaces," *Journal of Applied Physics*, vol. 88, no. 9, pp. 5180–5187, 2000. (cited on pages 106 and 136.)

[201] R. Egdell, T. Walker, and G. Beamson, "The screening response of a dilute electron gas in core level photoemission from Sb-doped SnO_2," *Journal of Electron Spectroscopy and Related Phenomena*, vol. 128, no. 1, pp. 59–66, 2003. (cited on pages 106 and 136.)

[202] P. King, T. D. Veal, F. Fuchs, C. Y. Wang, D. Payne, A. Bourlange, H. Zhang, G. R. Bell, V. Cimalla, O. Ambacher *et al.*, "Band gap, electronic structure, and surface electron accumulation of cubic and rhombohedral In_2O_3," *Physical Review B*, vol. 79, no. 20, p. 205211, 2009. (cited on pages 106, 107, 148, and 149.)

[203] P. King, T. Veal, D. Payne, A. Bourlange, R. Egdell, and C. McConville, "Surface electron accumulation and the charge neutrality level in In_2O_3," *Physical Review Letters*, vol. 101, no. 11, p. 116808, 2008. (cited on pages 107, 148, and 149.)

[204] O. Bierwagen, "Indium oxide—a transparent, wide-band gap semiconductor for (opto) electronic applications," *Semiconductor Science and Technology*, vol. 30, no. 2, p. 024001, 2015. (cited on pages 107 and 149.)

[205] T. Berthold, J. Rombach, T. Stauden, V. Polyakov, V. Cimalla, S. Krischok, O. Bierwagen, and M. Himmerlich, "Consequences of plasma oxidation and vacuum annealing on the chemical properties and electron accumulation of In_2O_3 surfaces," *Journal of Applied Physics*, vol. 120, no. 24, p. 245301, 2016. (cited on pages 107, 148, and 149.)

[206] M. Batzill and U. Diebold, "The surface and materials science of tin oxide," *Progress in Surface Science*, vol. 79, no. 2-4, pp. 47–154, 2005. (cited on page107.)

[207] J.-M. Themlin, M. Chtaïb, L. Henrard, P. Lambin, J. Darville, and J.-M. Gilles, "Characterization of tin oxides by X-ray-photoemission spectroscopy," *Physical Review B*, vol. 46, no. 4, p. 2460, 1992. (cited on page107.)

[208] Y. Gassenbauer and A. Klein, "Electronic surface properties of rf-magnetron sputtered In_2O_3: Sn," *Solid State Ionics*, vol. 173, no. 1-4, pp. 141–145, 2004. (cited on page107.)

[209] D. Briggs and M. Seah, *Practical surface analysis: by Auger and X-ray photoelectron spectroscopy*. Wiley, 1983. (cited on page107.)

[210] S. Siol, J. C. Hellmann, S. D. Tilley, M. Graetzel, J. Morasch, J. Deuermeier, W. Jaegermann, and A. Klein, "Band alignment engineering at Cu_2O/ZnO heterointerfaces," *ACS Applied Materials & Interfaces*, vol. 8, no. 33, pp. 21 824–21 831, 2016. (cited on page108.)

[211] R. Giesecke, R. Hertwig, T. J. Bayer, C. A. Randall, and A. Klein, "Modification of the schottky barrier height at the RuO_2 cathode during resistance degradation of Fe-doped $SrTiO_3$," *Journal of the American Ceramic Society*, vol. 100, no. 10, pp. 4590–4601, 2017. (cited on page108.)

[212] S. Sze, "Physics of semiconductor devices," 1981. (cited on page109.)

[213] S. Harvey, T. O. Mason, Y. Gassenbauer, R. Schafranek, and A. Klein, "Surface versus bulk electronic/defect structures of transparent conducting oxides: I. Indium oxide and ITO," *Journal of Physics D: Applied Physics*, vol. 39, no. 18, p. 3959, 2006. (cited on pages 109, 135, 136, and 143.)

[214] J. Maier, *Physical chemistry of ionic materials: ions and electrons in solids*. John Wiley & Sons, 2004. (cited on page109.)

[215] P. K. Song, H. Akao, M. Kamei, Y. Shigesato, and I. Yasui, "Preparation and crystallization of tin-doped and undoped amorphous indium oxide films deposited by sputtering," *Japanese Journal of Applied Physics*, vol. 38, no. 9R, p. 5224, 1999. (cited on page110.)

[216] J. Bellingham, W. Phillips, and C. Adkins, "Electrical and optical properties of amorphous indium oxide," *Journal of Physics: Condensed Matter*, vol. 2, no. 28, p. 6207, 1990. (cited on pages 110 and 114.)

[217] R. Khanal, D. B. Buchholz, R. P. Chang, and J. E. Medvedeva, "Composition-dependent structural and transport properties of amorphous transparent conducting oxides," *Physical Review B*, vol. 91, no. 20, p. 205203, 2015. (cited on pages 110 and 112.)

[218] J.-O. Park, J.-H. Lee, J.-J. Kim, S.-H. Cho, and Y. K. Cho, "Crystallization of indium tin oxide thin films prepared by RF-magnetron sputtering without external heating," *Thin Solid Films*, vol. 474, no. 1-2, pp. 127–132, 2005. (cited on page110.)

[219] D. Mattox, "Particle bombardment effects on thin-film deposition: A review," *Journal of Vacuum Science & Technology A: Vacuum, Surfaces, and Films*, vol. 7, no. 3, pp. 1105–1114, 1989. (cited on page110.)

[220] A. Klein and F. Säuberlich, "Surfaces and interfaces of sputter-deposited ZnO films," in *Transparent Conductive Zinc Oxide*. Springer, 2008, pp. 35–78. (cited on page112.)

[221] N. Sommer, J. Hüpkes, and U. Rau, "Field emission at grain boundaries: Modeling

the conductivity in highly doped polycrystalline semiconductors," *Physical Review Applied*, vol. 5, no. 2, p. 024009, 2016. (cited on page112.)

[222] J. E. Medvedeva, D. B. Buchholz, and R. P. Chang, "Recent advances in understanding the structure and properties of amorphous oxide semiconductors," *Advanced Electronic Materials*, vol. 3, no. 9, p. 1700082, 2017. (cited on pages 112, 114, and 116.)

[223] C. Lohaus, C. Steinert, G. Deyu, J. Brötz, W. Jaegermann, and A. Klein, "Enhancing electrical conductivity of room temperature deposited Sn-doped In_2O_3 thin films by hematite seed layers," *Applied Physics Letters*, vol. 112, no. 15, p. 152105, 2018. (cited on pages 112, 117, and 131.)

[224] J. Deuermeier, H. F. Wardenga, J. Morasch, S. Siol, S. Nandy, T. Calmeiro, R. Martins, A. Klein, and E. Fortunato, "Highly conductive grain boundaries in copper oxide thin films," *Journal of Applied Physics*, vol. 119, no. 23, p. 235303, 2016. (cited on page112.)

[225] P. Ágoston and K. Albe, "Ab initio modeling of diffusion in indium oxide," *Physical Review B*, vol. 81, no. 19, p. 195205, 2010. (cited on pages 113, 124, 140, 142, and 167.)

[226] J. Crank, "The mathematics of diffusion," *Oxford University Press, Oxford*, 1975. (cited on page116.)

[227] G. Gregori, R. Merkle, and J. Maier, "Ion conduction and redistribution at grain boundaries in oxide systems," *Progress in Materials Science*, vol. 89, pp. 252–305, 2017. (cited on page120.)

[228] M. Groner, F. Fabreguette, J. Elam, and S. George, "Low-temperature Al_2O_3 atomic layer deposition," *Chemistry of Materials*, vol. 16, no. 4, pp. 639–645, 2004. (cited on page120.)

[229] M. Kot, C. Das, Z. Wang, K. Henkel, Z. Rouissi, K. Wojciechowski, H. J. Snaith, and D. Schmeisser, "Room-temperature atomic layer deposition of Al_2O_3: Impact on efficiency, stability and surface properties in perovskite solar cells," *ChemSusChem*, vol. 9, no. 24, pp. 3401–3406, 2016. (cited on page120.)

[230] D. B. Buchholz, L. Zeng, M. J. Bedzyk, and R. P. Chang, "Differences between amorphous indium oxide thin films," *Progress in Natural Science: Materials International*, vol. 23, no. 5, pp. 475–480, 2013. (cited on pages 142 and 144.)

[231] D. B. Buchholz, Q. Ma, D. Alducin, A. Ponce, M. Jose-Yacaman, R. Khanal, J. E.

Medvedeva, and R. P. Chang, “The structure and properties of amorphous indium oxide,” *Chemistry of Materials*, vol. 26, no. 18, pp. 5401–5411, 2014. (cited on pages 142 and 144.)

[232] G. Pacchioni, L. Skuja, and D. L. Griscom, *Defects in SiO_2 and related dielectrics: science and technology*. Springer Science & Business Media, 2012, vol. 2. (cited on page152.)

[233] R. Alfonsetti, L. Lozzi, M. Passacantando, P. Picozzi, and S. Santucci, “XPS studies on SiO_x thin films,” *Applied Surface Science*, vol. 70, pp. 222–225, 1993. (cited on pages 152, 159, and 161.)

[234] M. R. Holmes, S. Liu, J. Keeley, M. Jenkins, K. Leake, H. Schmidt, and A. R. Hawkins, “Hollow waveguides with low intrinsic photoluminescence fabricated with PECVD silicon nitride and silicon dioxide films,” *IEEE Photonics Technology Letters*, vol. 23, no. 20, pp. 1466–1468, 2011. (cited on page152.)

[235] P. Panek, K. Drabczyk, A. Focsa, and A. Slaoui, “A comparative study of SiO_2 deposited by PECVD and thermal method as passivation for multicrystalline silicon solar cells,” *Materials Science and Engineering: B*, vol. 165, no. 1-2, pp. 64–66, 2009. (cited on page152.)

[236] A. Mahdjoub, “Graded refraction index antireflection coatings based on silicon and titanium oxides,” *Semiconductor Physics Quantum Electronics & Optoelectronics*, 2007. (cited on page152.)

[237] B. E. Deal and C. R. Helms, *The physics and chemistry of SiO_2 and the Si-SiO_2 interface*. Springer Science & Business Media, 2013. (cited on page152.)

[238] R. A. Devine, “The physics and technology of amorphous SiO_2.” (cited on page152.)

[239] R. Mozzi and B. Warren, “The structure of vitreous silica,” *Journal of Applied Crystallography*, vol. 2, no. 4, pp. 164–172, 1969. (cited on page152.)

[240] R. Bell and P. Dean, “The structure of vitreous silica: validity of the random network theory,” *Philosophical Magazine*, vol. 25, no. 6, pp. 1381–1398, 1972. (cited on page152.)

[241] R. Salh, “Defect related luminescence in silicon dioxide network: a review,” 2011. (cited on pages 153, 154, and 155.)

[242] I. Fanderlik, *Silica glass and its application*. Elsevier, 2013. (cited on pages 153 and 154.)

[243] J. Waber and D. T. Cromer, "Orbital radii of atoms and ions," *The Journal of Chemical Physics*, vol. 42, no. 12, pp. 4116–4123, 1965. (cited on page153.)

[244] M. A. Stevens-Kalceff, "Electron-irradiation-induced radiolytic oxygen generation and microsegregation in silicon dioxide polymorphs," *Physical Review Letters*, vol. 84, no. 14, p. 3137, 2000. (cited on page154.)

[245] R. Weeks, "Paramagnetic resonance of lattice defects in irradiated quartz," *Journal of Applied Physics*, vol. 27, no. 11, pp. 1376–1381, 1956. (cited on page154.)

[246] L. Skuja, M. Hirano, H. Hosono, and K. Kajihara, "Defects in oxide glasses," *Physica Status Solidi (c)*, vol. 2, no. 1, pp. 15–24, 2005. (cited on pages 154 and 155.)

[247] H. Hosono, Y. Abe, H. Imagawa, H. Imai, and K. Arai, "Experimental evidence for the Si-Si bond model of the 7.6-eV band in SiO_2 glass," *Physical Review B*, vol. 44, no. 21, p. 12043, 1991. (cited on page155.)

[248] Y. Li and W. Ching, "Band structures of all polycrystalline forms of silicon dioxide," *Physical Review B*, vol. 31, no. 4, p. 2172, 1985. (cited on page156.)

[249] E. Calabrese and W. B. Fowler, "Electronic energy-band structure of α quartz," *Physical Review B*, vol. 18, no. 6, p. 2888, 1978. (cited on page156.)

[250] J. R. Chelikowsky and M. Schlüter, "Electron states in α-quartz: A self-consistent pseudopotential calculation," *Physical Review B*, vol. 15, no. 8, p. 4020, 1977. (cited on page156.)

[251] S. Nekrashevich and V. Gritsenko, "Electronic structure of silicon dioxide (a review)," *Physics of The Solid State*, vol. 56, no. 2, pp. 207–222, 2014. (cited on page156.)

[252] C. G. Van de Walle and J. Neugebauer, "Universal alignment of hydrogen levels in semiconductors, insulators and solutions," *Nature*, vol. 423, no. 6940, p. 626, 2003. (cited on page156.)

[253] C. G. Van de Walle, "Universal alignment of Hydrogen Levels in Semiconductors and Insulators," *Physica B: Condensed Matter*, vol. 376, pp. 1–6, 2006. (cited on pages 156, 157, and 158.)

[254] Y. Xu and M. A. Schoonen, "The Absolute Energy Positions of Conduction and Valence Bands of Selected Semiconducting Minerals," *American Mineralogist*, vol. 85, no. 3-4, pp. 543–556, 2000. (cited on pages 157 and 158.)

[255] L. Schlapbach and A. Züttel, "Hydrogen-storage materials for mobile applications," in *Materials for sustainable energy: a collection of peer-reviewed research and review articles from nature publishing group*. World Scientific, 2011, pp. 265–270. (cited on page158.)

[256] Y. Yamashita, K. Namba, Y. Nakato, Y. Nishioka, and H. Kobayashi, "Spectroscopic observation of interface states of ultrathin silicon oxide," *Journal of Applied Physics*, vol. 79, no. 9, pp. 7051–7057, 1996. (cited on page159.)

[257] A. Thøgersen, J. H. Selj, and E. S. Marstein, "Oxidation effects on graded porous silicon anti-reflection coatings," *Journal of The Electrochemical Society*, vol. 159, no. 5, pp. D276–D281, 2012. (cited on page159.)

[258] J. Waldrop, R. Grant, S. Kowalczyk, and E. Kraut, "Measurement of semiconductor Heterojunction Band Discontinuities by X-ray Photoemission Spectroscopy," *Journal of Vacuum Science & Technology A: Vacuum, Surfaces, and Films*, vol. 3, no. 3, pp. 835–841, 1985. (cited on page164.)

[259] G. V. Rao, F. Säuberlich, and A. Klein, "Influence of Mg Content on the Band Alignment at Cd s/Zn, Mg)O Interfaces," *Applied Physics Letters*, vol. 87, no. 3, p. 032101, 2005. (cited on page164.)

[260] N. Richard, L. Martin-Samos, G. Roma, Y. Limoge, and J.-P. Crocombette, "First principle study of neutral and charged self-defects in amorphous SiO_2," *Journal of Non-Crystalline Solids*, vol. 351, no. 21-23, pp. 1825–1829, 2005. (cited on pages 167 and 168.)

[261] H. Tang, K. Prasad, R. Sanjines, P. Schmid, and F. Levy, "Electrical and optical properties of TiO_2 anatase thin films," *Journal of Applied Physics*, vol. 75, no. 4, pp. 2042–2047, 1994. (cited on page176.)

[262] S. Balaji, Y. Djaoued, and J. Robichaud, "Phonon confinement studies in nanocrystalline anatase-TiO_2 thin films by micro raman spectroscopy," *Journal of Raman Spectroscopy*, vol. 37, no. 12, pp. 1416–1422, 2006. (cited on page176.)

[263] K. Bange, C. Ottermann, O. Anderson, U. Jeschkowski, M. Laube, and R. Feile, "Investigations of TiO_2 films deposited by different techniques," *Thin Solid Films*, vol. 197, no. 1-2, pp. 279–285, 1991. (cited on page176.)

[264] I. Oja, A. Mere, M. Krunks, R. Nisumaa, C.-H. Solterbeck, and M. Es-Souni, "Structural and electrical characterization of TiO_2 films grown by spray pyrolysis," *Thin Solid Films*, vol. 515, no. 2, pp. 674–677, 2006. (cited on page176.)

[265] T. Ohsaka, F. Izumi, and Y. Fujiki, "Raman spectrum of anatase, TiO_2," *Journal of Raman Spectroscopy*, vol. 7, no. 6, pp. 321–324, 1978. (cited on pages 177 and 180.)

[266] W. Zhang, Y. He, M. Zhang, Z. Yin, and Q. Chen, "Raman scattering study on anatase TiO_2 nanocrystals," *Journal of Physics D: Applied Physics*, vol. 33, no. 8, p. 912, 2000. (cited on page177.)

[267] T. Mazza, E. Barborini, P. Piseri, P. Milani, D. Cattaneo, A. L. Bassi, C. Bottani, and C. Ducati, "Raman spectroscopy characterization of TiO_2 rutile nanocrystals," *Physical Review B*, vol. 75, no. 4, p. 045416, 2007. (cited on page177.)

[268] S. Porto, P. Fleury, and T. Damen, "Raman spectra of TiO_2, MgF_2, ZnF_2, FeF_2, and MnF_2," *Physical Review*, vol. 154, no. 2, p. 522, 1967. (cited on page177.)

[269] R. Katiyar, P. Dawson, M. Hargreave, and G. Wilkinson, "Dynamics of the rutile structure. III. lattice dynamics, infrared and raman spectra of SnO_2," *Journal of Physics C: Solid State Physics*, vol. 4, no. 15, p. 2421, 1971. (cited on page180.)

[270] J. Scott, "Raman spectrum of SnO_2," *The Journal of Chemical Physics*, vol. 53, no. 2, pp. 852–853, 1970. (cited on page180.)

[271] A. Mc Adams and S. Krop, "Injury and death from red fuming nitric acid," *Journal of the American Medical Association*, vol. 158, no. 12, pp. 1022–1024, 1955. (cited on page185.)

[272] G. K. Deyu, D. Muñoz-Rojas, L. Rapenne, J.-L. Deschanvres, A. Klein, C. Jiménez, and D. Bellet, "Sno_2 films deposited by ultrasonic spray pyrolysis: Influence of al incorporation on the properties," *Molecules*, vol. 24, no. 15, 2019. (cited on page187.)

[273] V. Sammelselg, J. Aarik, A. Aidla, A. Kasikov, E. Heikinheimo, M. Peussa, and L. Niinist, "Composition and thickness determination of thin oxide films: comparison of different programs and methods," *Journal of Analytical Atomic Spectrometry*, vol. 14, no. 3, pp. 523–527, 1999. (cited on page190.)

[274] V. Consonni, G. Rey, H. Roussel, B. Doisneau, E. Blanquet, and D. Bellet, "Preferential orientation of fluorine-doped SnO_2 thin films: The effects of growth temperature," *Acta Materialia*, vol. 61, no. 1, pp. 22–31, 2013. (cited on pages 191 and 200.)

[275] J. Bruneaux, H. Cachet, M. Froment, and A. Messad, "Correlation between structural and electrical properties of sprayed tin oxide films with and without

fluorine doping," *Thin Solid Films*, vol. 197, no. 1-2, pp. 129–142, 1991. (cited on page191.)

[276] A. Messad, J. Bruneaux, H. Cachet, and M. Froment, "Analysis of the effects of substrate temperature, concentration of tin chloride and nature of dopants on the structural and electrical properties of sprayed SnO_2 films," *Journal of Materials Science*, vol. 29, no. 19, pp. 5095–5103, 1994. (cited on pages 191 and 212.)

[277] G. Rey, C. Ternon, M. Modreanu, X. Mescot, V. Consonni, and D. Bellet, "Electron scattering mechanisms in fluorine-doped SnO_2 thin films," *Journal of Applied Physics*, vol. 114, no. 18, p. 183713, 2013. (cited on page191.)

[278] S. Sinha, S. Ray, and I. Manna, "Effect of Al doping on structural, optical and electrical properties of SnO_2 thin films synthesized by pulsed laser deposition," *Philosophical Magazine*, vol. 94, no. 31, pp. 3507–3521, 2014. (cited on page193.)

[279] S. F. Ahmed, S. Khan, P. Ghosh, M. Mitra, and K. Chattopadhyay, "Effect of al doping on the conductivity type inversion and electro-optical properties of SnO_2 thin films synthesized by sol-gel technique," *Journal of Sol-Gel Science and Technology*, vol. 39, no. 3, pp. 241–247, 2006. (cited on pages 193, 206, and 213.)

[280] F. Moharrami, M. Bagheri-Mohagheghi, H. Azimi-Juybari, and M. Shokooh-Saremi, "Structural, electrical, optical, thermoelectrical and photoconductivity properties of the SnO_2–Al_2O_3 binary transparent conducting films deposited by the spray pyrolysis method," *Physica Scripta*, vol. 85, no. 1, p. 015703, 2011. (cited on pages 193 and 215.)

[281] A. Jesche, M. Fix, A. Kreyssig, W. Meier, and P. Canfield, "X-ray diffraction on large single crystals using a powder diffractometer," *Philosophical Magazine*, vol. 96, no. 20, pp. 2115–2124, 2016. (cited on page195.)

[282] B. O'Connor, D. Li, and B. Hunter, "The importance of the specimen displacement correction in rietveld pattern fitting with symmetric reflection-optics diffraction data," *Advances in X-Ray Analysis*, vol. 44, pp. 96–102, 2001. (cited on page195.)

[283] E. Zolotoyabko, *Basic concepts of X-ray diffraction*. John Wiley & Sons, 2014. (cited on page195.)

[284] C.-K. Lee, E. Cho, H.-S. Lee, K. S. Seol, and S. Han, "Comparative study of electronic structures and dielectric properties of alumina polymorphs by first-principles methods," *Physical Review B*, vol. 76, no. 24, p. 245110, 2007. (cited on pages 198 and 205.)

[285] S.-H. Lee, J.-M. Choi, J.-H. Lim, J. Park, and J.-S. Park, "A study on the thermoelectric properties of ALD-grown aluminum-doped tin oxide with respect to nanostructure modulations," *Ceramics International*, vol. 44, no. 2, pp. 1978–1983, 2018. (cited on page199.)

[286] K. Ravichandran and K. Thirumurugan, "Type inversion and certain physical properties of spray pyrolysed SnO_2: Al films for novel transparent electronics applications," *Journal of Materials Science & Technology*, vol. 30, no. 2, pp. 97–102, 2014. (cited on pages 199 and 213.)

[287] K. Thirumurugan, K. Ravichandran, R. Mohan, S. Snega, S. Jothiramalingam, and R. Chandramohan, "Effect of solvent volume on properties of SnO_2: Al films," *Surface Engineering*, vol. 29, no. 5, pp. 373–378, 2013. (cited on page199.)

[288] L. Vegard and H. Dale, "VIII. Untersuchungen über mischkristalle und legierungen," *Zeitschrift für Kristallographie-Crystalline Materials*, vol. 67, no. 1-6, pp. 148–162, 1928. (cited on page200.)

[289] A. R. Denton and N. W. Ashcroft, "Vegard's law," *Physical Review A*, vol. 43, no. 6, p. 3161, 1991. (cited on page200.)

[290] K. Chopra, S. Major, and D. Pandya, "Transparent conductors—a status review," *Thin Solid Films*, vol. 102, no. 1, pp. 1–46, 1983. (cited on page200.)

[291] C. Agashe, M. Takwale, B. Marathe, and V. Bhide, "Structural properties of SnO_2: F films deposited by spray pyrolysis," *Solar Energy Materials*, vol. 17, no. 2, pp. 99–117, 1988. (cited on page200.)

[292] G. Gordillo, L. Moreno, W. De la Cruz, and P. Teheran, "Preparation and characterization of SnO_2 thin films deposited by spray pyrolysis from $SnCl_2$ and $SnCl_4$ precursors," *Thin Solid Films*, vol. 252, no. 1, pp. 61–66, 1994. (cited on page200.)

[293] M. Fantini, I. Torriani, and C. Constantino, "Influence of the substrate on the crystalline properties of sprayed tin dioxide thin films," *Journal of Crystal Growth*, vol. 74, no. 2, pp. 439–442, 1986. (cited on page200.)

[294] E. Gilardi, E. Fabbri, L. Bi, J. L. Rupp, T. Lippert, D. Pergolesi, and E. Traversa, "Effect of dopant–host ionic radii mismatch on acceptor-doped barium zirconate microstructure and proton conductivity," *The Journal of Physical Chemistry C*, vol. 121, no. 18, pp. 9739–9747, 2017. (cited on page200.)

[295] C. V. Thompson, "Structure evolution during processing of polycrystalline films,"

Annual Review of Materials Science, vol. 30, no. 1, pp. 159–190, 2000. (cited on page201.)

[296] P. Scherrer, "Bestimmung der inneren struktur und der größe von kolloidteilchen mittels röntgenstrahlen," in *Kolloidchemie Ein Lehrbuch*. Springer, 1912, pp. 387–409. (cited on pages 202 and 229.)

[297] J. I. Langford and A. Wilson, "Scherrer After Sixty Years: A Survey and Some New results in The Determination of Crystallite Size," *Journal of Applied Crystallography*, vol. 11, no. 2, pp. 102–113, 1978. (cited on pages 202 and 229.)

[298] S. D. Ponja, I. P. Parkin, and C. J. Carmalt, "Synthesis and material characterization of amorphous and crystalline (α-) Al_2O_3 via aerosol assisted chemical vapour deposition," *RSC Advances*, vol. 6, no. 105, pp. 102 956–102 960, 2016. (cited on page205.)

[299] B. Zhang, Y. Tian, J. Zhang, and W. Cai, "The FTIR studies of SnO_2: Sb (ATO) films deposited by spray pyrolysis," *Materials Letters*, vol. 65, no. 8, pp. 1204–1206, 2011. (cited on page206.)

[300] C. Kumar, N. Mishra, A. Kumar, M. Bhatt, P. Chaudhary, and R. Singh, "Structural investigation of nanomixed $xSnO_2$ –Al_2O_3 synthesized by sol–gel route," *Applied Nanoscience*, vol. 6, no. 7, pp. 1059–1064, 2016. (cited on page207.)

[301] T. J. Coutts, D. L. Young, and X. Li, "Characterization of transparent conducting oxides," *MRS Bulletin*, vol. 25, no. 8, pp. 58–65, 2000. (cited on pages 207 and 208.)

[302] J. Tauc, R. Grigorovici, and A. Vancu, "Optical properties and electronic structure of amorphous germanium," *Physica Status Solidi (b)*, vol. 15, no. 2, pp. 627–637, 1966. (cited on page209.)

[303] B. Stjerna, E. Olsson, and C. Granqvist, "Optical and electrical properties of radio frequency sputtered tin oxide films doped with oxygen vacancies, F, Sb, or Mo," *Journal of Applied Physics*, vol. 76, no. 6, pp. 3797–3817, 1994. (cited on page209.)

[304] G. Sanon, R. Rup, and A. Mansingh, "Band-Gap Narrowing and Band Structure in Degenerate Tin oxide (SnO_2) Films," *Physical Review B*, vol. 44, no. 11, p. 5672, 1991. (cited on page209.)

[305] B. Stjerna, C. G. Granqvist, A. Seidel, and L. Häggström, "Characterization of rf-sputtered SnO_x thin films by electron microscopy, hall-effect measurement,

and mössbauer spectrometry," *Journal of Applied Physics*, vol. 68, no. 12, pp. 6241–6245, 1990. (cited on page209.)

[306] C. Körber, P. Ágoston, and A. Klein, "Surface and bulk properties of sputter deposited undoped and Sb-doped SnO_2 thin films," *Sensors and Actuators B: Chemical*, vol. 139, no. 2, pp. 665–672, 2009. (cited on page211.)

[307] H. Kim and A. Pique, "Transparent conducting Sb-doped SnO_2 thin films grown by pulsed-laser deposition," *Applied Physics Letters*, vol. 84, no. 2, pp. 218–220, 2004. (cited on page211.)

[308] A. Maddalena, R. Dal Maschio, S. Dire, and A. Raccanelli, "Electrical conductivity of tin oxide films prepared by the sol-gel method," *Journal of Non-Crystalline Solids*, vol. 121, no. 1-3, pp. 365–369, 1990. (cited on page211.)

[309] C. A. Vincent, "The nature of semiconductivity in polycrystalline tin oxide," *Journal of The Electrochemical Society*, vol. 119, no. 4, pp. 515–518, 1972. (cited on page212.)

[310] J. E. Swallow, B. A. Williamson, T. J. Whittles, M. Birkett, T. J. Featherstone, N. Peng, A. Abbott, M. Farnworth, K. J. Cheetham, P. Warren *et al.*, "Self-compensation in transparent conducting F-doped SnO_2," *Advanced Functional Materials*, vol. 28, no. 4, p. 1701900, 2018. (cited on page212.)

[311] K. H. Kim and C. G. Park, "Electrical properties and gas-sensing behavior of SnO_2 films prepared by chemical vapor deposition," *Journal of The Electrochemical Society*, vol. 138, no. 8, pp. 2408–2412, 1991. (cited on page212.)

[312] J. Ferron and R. Arce, "Anomalous incorporation of fluorine in tin oxide films produced with the pyrosol method," *Thin Solid Films*, vol. 204, no. 2, pp. 405–411, 1991. (cited on page212.)

[313] M.-M. Bagheri-Mohagheghi and M. Shokooh-Saremi, "The influence of al doping on the electrical, optical and structural properties of SnO_2 transparent conducting films deposited by the spray pyrolysis technique," *Journal of Physics D: Applied Physics*, vol. 37, no. 8, p. 1248, 2004. (cited on page213.)

[314] S.-T. Zhang, "Study of fluorine-doped tin oxide (FTO) thin films for photovoltaics applications," Ph.D. dissertation, Technische Universität, Darmstadt, 2017. (cited on page220.)

[315] W. Siefert, "Corona spray pyrolysis: a new coating technique with an extremely enhanced deposition efficiency," *Thin Solid Films*, vol. 120, no. 4, pp. 267–274,

1984. (cited on page234.)

[316] N. Fuchs, “The mechanics of aerosols,” 1964. (cited on page235.)

[317] L. Filipovic, *Topography simulation of novel processing techniques.* LuE, TU Wien, 2012. (cited on page235.)

[318] A. von Keudell, “Surface processes during thin-film growth,” *Plasma Sources Science and Technology*, vol. 9, no. 4, p. 455, 2000. (cited on page237.)

List of Abbreviations

AC	Alternating current
AES	Auger electron spectroscopy
ALD	Atomic layer deposition
AZO	Al-doped zinc oxide
CB	Conduction band
CBM	Conduction band minimum
CVD	Chemical vapor deposition
DAISY-MAT	DArmstadt Integrated SYstem for MATerial research
DC	Direct current
DOS	Density of states
DFT	Density functional theory
EDS	Energy- dispersive spectroscopy
EDX	Energy -dispersive X-ray spectroscopy
EPMA	Electron probe micro-analyzer
FTIR	Fourier-transform infrared Spectroscopy
FTO	F-doped tin oxide
GIXRD	Grazing incidence X-ray diffraction
GPC	Growth per cycle
ICCD	International center of diffraction data
IR	Infrared
ITO	Sn-doped indium oxide
LCD	Liquid crystal display
MFC	Mass flow controller
MS	Magnetron sputtering
NIR	Near-infrared
NPs	Nanoparticles
PES	Photoelectron spectroscopy
PLD	Pulsed laser deposition
PVD	Physical vapor deposition
RBS	Rutherford back scattering

RF	Radiofrequency
RT	Room temperature
sccm	Standard cubic centimeters per minute
SE	secondary electrons
SEM	Scanning electron microscopy
SIMS	Secondary ion mass spectroscopy
SnO_2:Al	Al-doped tin oxide
TEM	Transmission electron microscopy
TMA	Trimethylaluminum
TCO	Transparent Conducting Oxide
UHV	Ultrahigh vacuum
UPS	Ultraviolet photoelectron spectroscopy
UV	Ultraviolet
VB	Valence band
VIS	Visible region
VBM	Valence band maximum
XPS	X-ray photoelectron spectroscopy
XRD	X-ray diffraction

Symbols and Physical Quantities

α	absorption coefficient
B	magnetic field
d	film thickness
$\mathrm{D}(E)$	density of states
d_{hkl}	distance of lattice planes hkl
e	elementary charge
E	energy
ε	electric field
E_{A}	acceptor level
E_{a}	activation energy
E_{B}	binding energy (referenced to E_{F})
$E_{\mathrm{C}B}$	conduction band
E_{D}	donor level
E_{F}	Fermi energy
ΔE_f	defect formation energy
E_{F}-$E_{\mathrm{V}B}$	valence band maximum with respect to the Fermi energy
E_{g}	energy band gap
$E_{\mathrm{S}EE}$	secondary electron edge
$E_{\mathrm{V}B}$	valence band
$\Delta E_{\mathrm{V}B}$	valence band discontinuity
ε_0	permittivity of vacuum
ε_{r}	relative permittivity
E_{g}	energy band gap
$\mathrm{F}(E)$	Fermi-Dirac distribution
h	plank constant
hkl	Miller indices
I	electric current or intensity
K	Boltzmann constant
λ_{e}	inelastic mean free path of electrons

λ	wave length
μ	charge carrier mobility
N	density of states
n	free electron carrier concentration
N_{A}	density of acceptors
N_{A}^{-}	density of ionized acceptors
N_{D}	density of donors
N_{D}^{+}	density of ionized donors
p	free hole carrier concentration
q	charge
R	resistance
n	free electron carrier concentration
N_{A}	density of acceptors
R_{H}	Hall coefficient
r_{R}	Hall factor
ρ	charge density
O_i	oxygen interstitials
σ	conductivity
T	Temperature
$\mathrm{T_s}$	substrate temperature
τ	scattering time
θ	diffraction angle (XRD) or emission angle (XPS)
V_{H}	Hall Voltage
V_{O}	oxygen vacancy
Φ	work function
Φ_{bb}	amount of band bending
Φ_{B}	Schottky barrier height
$\Phi_{instrument}$	work function of the instrument
Φ_{sample}	work function of the sample
W	width of the space charge region
X	electron affinity

Acknowledgment

This acknowledgment begins with my true gratitude towards my supervisors **Prof. Andreas Klein** and **Prof. Daniel Bellet** as well as **Dr. David Munoz Rojas** for giving me this amazing opportunity on work in their working group towards the preparation of my PhD. I am grateful for the assistance you provide me and meticulous guidance of my doctoral thesis. It was a great pleasure to be part of both groups.

During my thesis, I am particularly grateful to Carmen Jiménez and Jean-Luc Deschanvers for their help on experimental setup, sample characterizations and many fruitful scientific discussions during my stay in LMGP, which has formed a significant part of my thesis.

Many thanks for my colleagues in the ESM division for a great team work: the old hands Andi, Philipp, Hans and Christian for the crucial introduction to the experimental setups and procedures. The same is true for other ESMs: Raf, Yanick, Priya, Binxang, Kathi and Nicole. It was great time to do science with you guys. This extend to my old group surface science division and Prof. Wolfram Jaegermann for the pleasant working atmosphere. Thank you Joachim Brötz for measuring some of my samples with XRD. Thank you Marga Lang for the kind help with organizational work, which could be complicated as science.

It was a great pleasure to get to know and work with all the great people in Grenoble. I thank Franz Bruckert, Michèle San Martin, Josiane Viboud and Virginie Charrière for their help concerning the administrative and technical issues. I thank Hervé Roussel, Laetitia Rapenne, and Odette Chaix for XRD, TEM and Raman measurements. Thank you Matthieu Jouvert for the technical support. I am thankful for all other members of LMGP who have contributed to my work/living life.

Thank you all other EJD-FunMaters, we had such a great time in each doctoral school meetings and other reunions. I wish the best for all of you.

My acknowledgment extend to my host for the last four years in Reinheim, Gabriele and Herbert of Haus Gobi, who have been literally my second family in Germany. I am grateful for lots of good memories in your house.

A special thanks to my all old friends in Trento, Zee family and Aweke. Thank you my new friends in Darmstadt and Grenoble especially to the great people I met in LMGP (Sara, Eugene, Joao, Viet, Dorina and all of you not mentioned here) you were ideal company to take my mind off from work and explore France.

Last but not least, I would like to thank my family. Aschu and Geze you are my rock. Enatiye this is for you. All this is possible by the grace of God and his mother.